Exploring the Effects of Secondary Interactions for Magnetic Applications

Author:

Brodie Matheson

Supervisor:

Prof. Mark Waterland

A thesis submitted in fulfilment of the requirements for the degree of

Doctor of Philosophy

in

Chemistry

School of Food Technology and Natural Sciences

Massey University

2025

Declaration of Authorship

I, Brodie Matheson, declare that this thesis titled, “Exploring the Effects of Secondary Interactions for Magnetic Applications” and the work presented in it are my own.

I confirm that:

- This work was done wholly or mainly while in candidature for the research degree of PhD in Chemistry at Massey University.
- Where I have consulted the published work of others, this is always clearly attributed.
- Where I have quoted from the work of others, the source is always given. With the exception of such quotations, this thesis is entirely my own work.
- I have acknowledged all main sources of help.
- All work presented in this thesis was completed by the author, except:
  - In collaboration with the University of Electro-Communications, Tokyo, Japan, Professor Takayuki Ishida and his students Shin-ichiro Takeshi, Liangcheng Lyu, and Rina Takano collected the magnetic data presented in Chapter 4. This includes the production of the susceptibility, magnetisation and Cole-Cole plots.
  - The collection of the X-ray data presented in this thesis was performed by Dr Tyson Dais and Marryllyn Donaldson.

Signed: 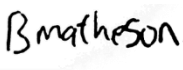

Date: 8th of November 2024

Abstract

The field of molecular magnetism has had a surge of interest in recent years due to the discovery of single molecule magnets (SMMs), which are species that possess magnetic properties that are entirely molecular in origin. Despite this research interest, SMMs are not yet at the stage where they can be implemented in modern technology. A key area requiring further insight is magneto-structural correlation, how the structural feature of the molecule effects the magnetic properties. In this regard, how secondary interactions can affect the magneto-structural properties of an SMM is worthy of further development in this field.

Herein, trinuclear heterometallic 3*d*/4*f* complexes are reported, which provide a framework for the manipulation of secondary interactions. A series of four-coordinate Ni^{II} complexes provides a necessary reference, possessing an absence of controllable second sphere interactions. A series of five-coordinate Cu^{II} complexes allows control of the axially bound species to effectively manipulate the secondary interactions. Our investigation into axially bound chloride, bromide, and nitrate anions are reported with the halide complexes being magnetically characterised. Two Cu_2Tb complexes possess ferromagnetic exchange between Cu and Ln ions as well as zero-field AC magnetic susceptibility, indicative of SMM behaviour. Analogous Cu_2Gd and Cu_2Er possess ferromagnetic and antiferromagnetic exchange respectively. Further analysis revealed that secondary interactions had a significant effect on the magneto-structural properties of these complexes, with the supramolecular architecture dominated by secondary interactions.

Attempts to develop a series with a six-coordinate 3*d* ion capable of exhibiting a greater array of secondary interactions were unsuccessful, with the hydrolysis of the ligand by a $MnCl_2$ catalysed reaction being the net result.

Finally, a tetranuclear Cu_3La complex is reported which provides an avenue for the comparison of a trinuclear and tetranuclear series.

Acknowledgements

First, I would like to express my gratitude to my original main supervisor, Dr. Paul Plieger, for all the support he has given me since I first entered postgraduate studies and giving me the chance to pursue a PhD. I would also like to thank Professor Mark Waterland, for stepping up and becoming my main supervisor when circumstances left me in need of one. Additionally, I would like to thank my co-supervisors Dr Gareth Rowlands and Dr Tyson Dais for their abundance of support especially with regards to organic synthesis and X-ray crystallography respectively.

I would like to thank our collaborator Professor Takayuki Ishida and his students from the University of Electro-Communications for carrying out magnetic characterisation of a number of the complexes presented in this thesis.

Special thanks goes out to all members past and present of the Plieger/Rowlands/Dais/Waterland groups for all their help and support, especially in these trying Covid times.

Finally, to my mum and dad, thank you for providing a 'low' rent place to live whilst I worked my way through this research.

Publication list

B. E. Matheson, T. N. Dais, M. E. Donaldson, G. J. Rowlands and P. G. Plieger. The importance of second sphere interactions on single molecule magnet performance. *Inorg. Chem. Front.*, 2023, **10**, 6427-6439

x

Contents

List of Figures

xx

List of Tables

List of Abbreviations and Symbols

3*d*	First row transition metal ion
4*f*	Lanthanide ion
Å	Angstrom
AC	Alternating Current
ATR-FTIR	Attenuated Total Reflectance Fourier Transform Infrared spectroscopy
B	Applied magnetic field
CFs	Crystal Fields
χ	Magnetic susceptibility
χ_M	Molar magnetic susceptibility
$\chi_M T$	Temperature dependent molar magnetic susceptibility
χ'	Frequency dependent in-phase magnetic susceptibility
χ''	Frequency dependent out-of-phase magnetic susceptibility
CHN	Carbon, Hydrogen, and Nitrogen elemental analysis
D	Axial Anisotropy parameter
DC	Direct Current
DFT	Density Functional Theory
EPR	Electron Paramagnetic Resonance Spectroscopy
ESI-MS	Electrospray Ionisation Mass Spectrometry
H	Magnetic field
I	Electric current
J	Heisenberg exchange coupling constant
K	Kelvin
Ln	Lanthanide
M	Magnetisation
M_s	Spin state quantum number
M–L–M	Metal–Ligand–Metal
MP	Melting Point
MRI	Magnetic Resonance Imaging
NMR	Nuclear Magnetic Resonance Spectroscopy
COSY	Correlated Spectroscopy
HMBC	Heteronuclear Multiple Bond Correlation
HMQC	Heteronuclear Multiple Quantum Coherence
OAM	Orbital Angular Momentum
QTM	Quantum Tunneling of Magnetisation
S	Total spin
SCXRD	Single Crystal X-ray Diffraction
SIM	Single Ion Magnet
SMM	Single Molecule Magnet
SOC	Spin-Orbit Coupling
SQUID	Superconducting Quantum Interference Device
T_b	Blocking temperature
TA-QTM	Thermally Assisted Quantum Tunneling of Magnetisation
^{t}Bu	*tert*-butyl group
TGA	Thermogravimetric Analysis
TM	Transition Metal
U_{eff}	Effective energy for reversal of magnetisation
XRD	X-ray Diffraction
ZFS	Zero-Field Splitting

Chapter 1

Introduction

1.1 Magnetism

Magnetism can arise from two sources, either electric current (*I*), or the spin magnetic moments of fundamental particles.[1] The movement of electrons through a wire causes a circular magnetic field perpendicular to the direction of the current. This type of magnetism is exploited to create powerful electromagnets, the uses of which include electric motors, MRI (Magnetic Resonance Imaging) and NMR (Nuclear Magnetic Resonance) applications.

The spin magnetic moments of atomic nuclei are typically many thousands of times smaller than that of the orbiting electrons and so are negligible with regards to the magnetic moment of an atom. At the atomic level there exists two types of magnetism: diamagnetism and paramagnetism, this influences how the atom interacts with a magnetic field. Diamagnetic atoms contain only paired electrons, thus have no magnetic moment, and will have a repulsive interaction with an applied magnetic field. Paramagnetic atoms have at least one unpaired electron, thus have a non-zero magnetic moment and will have an attractive interaction with an applied magnetic field.

Magnetism becomes more complicated with regards to bulk materials as new temperature dependent behaviour can occur. Ordinarily the net magnetism of a bulk material tends to be very weak due to the presence of diamagnetic atoms as well as the individual magnetic dipoles of atoms in a material being cancelled out due to the random orientation of these dipoles within the bulk material. However, when the material is subjected to a relatively strong magnetic field, the spins of the ground state electrons align with or against the direction of the magnetic field, resulting in different types of magnetism: Ferromagnetism, antiferromagnetism and ferrimagnetism (Figure 1.1). Ferromagnetism and antiferromagnetism occur when neighbouring magnetic dipoles align either parallel or antiparallel respectively. Ferrimagnetism occurs when neighbouring dipoles align antiparallel but have different magnitudes, resulting in a net magnetic dipole. This often occurs when there are different magnetic ions within the bulk

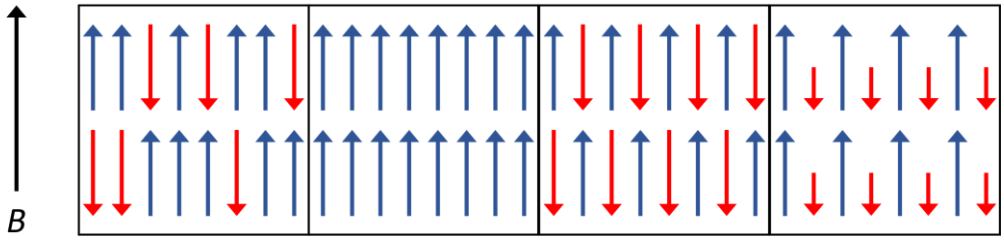

Figure 1.1 Representation of alignment of spins when subjected to an applied field (***B***), from left to right, in paramagnetic, ferromagnetic, antiferromagnetic, and ferrimagnetic materials.

material. The temperature dependence of these interactions is a result of the materials being able to retain their magnetisation in the absence of a magnetic field. This is due to the ordered alignment of the individual magnetic dipoles being energetically favourable over the disordered state. However, at temperatures above the Curie point for a material, the thermal energy is sufficient to overcome the energy minimising ordered state, resulting in a loss of magnetisation.[1,2]

1.1.1 Single Molecule Magnetism

Single molecule magnets (SMMs) are a class of discrete molecules which exhibit magnetic hysteresis and slow relaxation of magnetisation once removed from an external magnetic field.[3,4] SMMs differ from traditional magnets in that their magnetic domains are represented by a single molecule as opposed to the large number of spin-aligned atoms within the magnetic domain of a traditional bulk magnet. In a traditional magnet, the magnetic hysteresis is a result of the magnetic moments aligning parallel with one another to maintain a lowered energy state. In comparison, a SMMs magnetic properties are a result of a combination of metal-ligand interactions, the counterion employed, the ground state of the metal ions, and the magnetic isolation of the magnetic core by bulky organic ligands.

SMMs are commonly characterised by three parameters: the temperature dependent magnetic susceptibility ($\chi_M T$) , the effective barrier for reversal of magnetisation (U_{eff}), and the blocking temperature (T_b).[5,6] Temperature dependant magnetic susceptibility is a measure of how the SMM interacts with an external magnetic field, and the degree to which it can be magnetised (Figure 1.2). The shape of the DC magnetic susceptibility versus temperature can provide information on the type of magnetic interactions present in the sample. The blocking temperature T_b is the temperature below which magnetisation is retained, and as such would be the most sensible parameter for determining SMM performance. However, the exact definition of T_b often varies between groups with the more commonly utilised definitions being; the maximum temperature at which magnetic hysteresis is observed,[7,8] the temperature

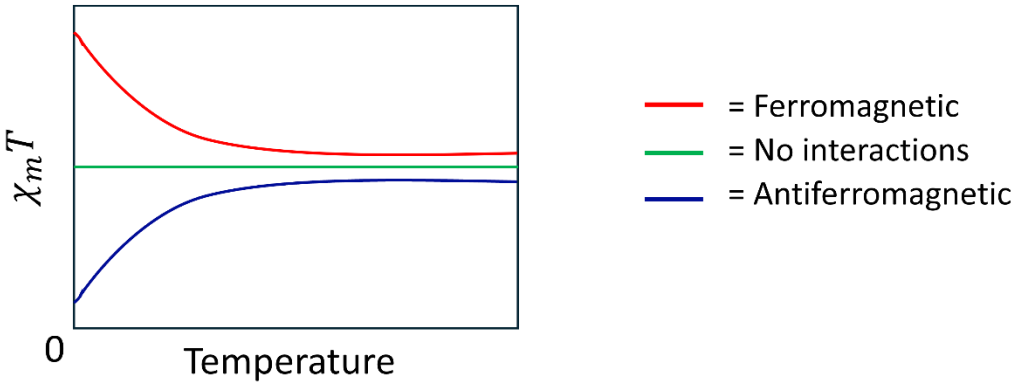

Figure 1.2: Representation of how the shape of the DC magnetic plots provides information on the magnetic interactions present in a complex.

corresponding to the maximum zero-field AC susceptibility,[9-12] and the temperature at which the relaxation time is equal to 100 seconds.[13-15] Furthermore, the exact definition used for T_b is not always present in publications, making comparisons of T_b between studies difficult.[16] Increasing this temperature has been the focus of many researchers in recent years, as getting this above liquid nitrogen temperature (77 K), and ideally to room temperature, is key for the applicability of an SMM.[17,18] In this regard, Guo *et al.* have recently made a breakthrough, with a SMM exhibiting a blocking temperature of 80 K.[19] This SMM consists of a central Dy^{III} ion axially coordinated by two Cp derivatives, Cp^* and Cp^{iPr5}, which are pentamethylcyclopentadienyl and penta-iso-propylcyclopentadienyl respectively.

The effective barrier to reversal of magnetisation U_{eff} represents the minimum amount of energy required to overcome the barrier for reversal of magnetisation, and as such is the parameter most directly related to SMM performance. For a simple approximation, U_{eff} can be represented by the equation

$$U = |D|S^2$$

Where *D* is the axial zero-field splitting parameter, and *S* is the total spin of the ground states of the magnetic centres. The sign of *D* is critical as it determines the type of magnetic anisotropy associated with *S*. A positive *D* represents easy-plane anisotropy and results in the $M_s = 0$, or $M_s = \pm ½$ for half integer *S*, state having the lowest energy, which means the magnetic phenomena associated with an SMM cannot exist.[3,5] A negative *D*, however, represents easy-axis anisotropy, which results in the $M_s = \pm S$ state having the lowest energy. This state is bistable which is a necessity for any molecule to exhibit SMM behaviour. A unique case comes in the form of Kramers ions, which are metal ions that have an odd number of ground state electrons, such as the Dy^{III} ion.[20] Due to time-reversal symmetry Kramers ions are guaranteed to have a bistable

ground state, resulting in molecules with Kramers ions can exhibit SMM behaviour regardless of the sign of D.[21]

The magnetisation and relaxation of an SMM can be described by the double well system where the $M_s = \pm S$ are shown as two separate wells (Figure 1.3). In the absence of an external magnetic field, all non-zero M_s levels are doubly degenerate. Upon applying a magnetic field parallel to the magnetisation axis, the $-M_s$ levels are stabilised and the $+M_s$ levels are destabilised, resulting in the saturation of the $+M_s$ level. Upon removal of the magnetic field, the U_{eff} represents the barrier that must be overcome to return the system to equilibrium. Thus, the higher this barrier, the longer the time for reversal of magnetisation and the more effective the SMM. It is the capability of an SMM to retain this magnetisation that makes it an attractive option for applications in molecular spintronics, quantum computing, and data storage.[22,23]

U_{eff} can also be obtained by fitting the temperature dependence of the relaxation time to an Arrhenius law. [24-26] Thus, U_{eff} provides information about the exponential relaxation regime, which is dominated by the Orbach process.[27,28] The Orbach process is a one phonon phenomenon where a series of sequential absorption of phonons 'over' the energy barrier is followed by a series of emissions, resulting in demagnetisation. At lower temperatures significant deviation from the Arrhenius law can be observed, which is often attributed to alternative relaxation methods such as direct processes and quantum tunnelling of magnetisation (QTM).[29,30] QTM is a phenomenon whereby the ground state electrons tunnel through the energy barrier, quenching the magnetisation. Additionally, Raman relaxation and thermally assisted quantum tunnelling of the magnetisation (TA-QTM) can operate over a wide temperature range, where Raman relaxation is akin to the Orbach process but occurs through virtual states and TA-QTM involves the thermal excitation of ground state electrons followed by quantum tunnelling (Figure 1.4). All this means that simply achieving a high U_{eff} will not necessarily lead to improved SMM performance.[31-35]

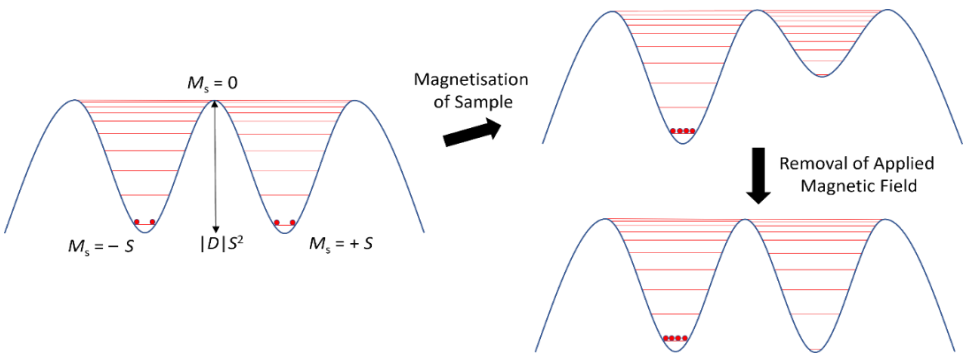

Figure 1.3: Schematic representation of, equilibrium of magnetisation in absence of external magnetic field (left), magnetisation of the material due to an applied magnetic field (top right), and retention of magnetism upon removal of the applied magnetic field (bottom right).

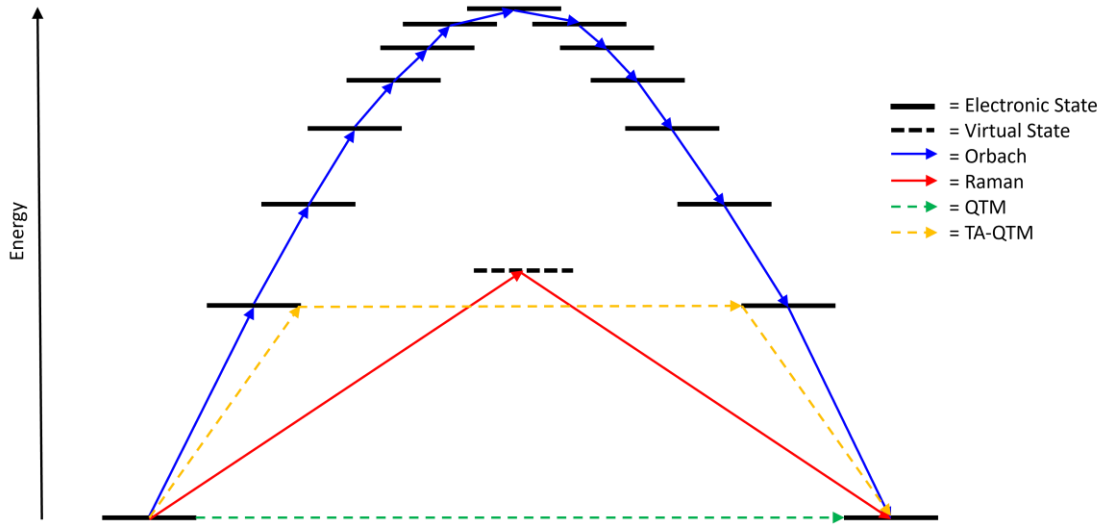

Figure 1.4: Schematic representation of the relaxation mechanisms typically present in SMMs.

1.1.2 Exchange Interactions

A major factor limiting the performance of SMMs is the presence of through-barrier relaxation processes, such as QTM, which quench the magnetisation without having to fully overcome the energy barrier, therefore minimising these processes is essential for developing high-end SMMs.[36,37] One of the key routes in reducing QTM is by utilising exchange pathways to couple adjacent metal centres together. A direct exchange interaction is identified as an electronic interaction between multiple metal centres. This occurs when partially occupied atomic orbitals of neighbouring metal centres overlap, resulting in an exchange of electronic or magnetic information between the coupled centres.[38] Superexchange interactions are similar, however instead of neighbouring metal centres being linked directly, they are linked through an intermediary bridging group. In this case a partially occupied atomic orbital on a metal centre overlaps with an atomic or molecular orbital on the bridging ligand, this orbital is also overlapping with an atomic orbital of another adjacent metal centre allowing the flow of electronic and magnetic information between the two coupled metal centres (Figure 1.5). Superexchange in polynuclear clusters can occur in two distinct ways, the type of which is dependent on the M–L–M bond angle. Antiferromagnetic exchange occurs when the M–L–M bond angle approaches 180° and is classified as either σ or π type, depending on which orbital of the ligand is involved. This is due to the Pauli exclusion principle prohibiting occupied orbitals from containing electrons of the same spin, thus the spin of the donated electron is opposite to that of the unpaired electron on the metal. Ferromagnetic exchange occurs when the M–L–M bond angle approaches 90°, thus many researchers hoping to achieve ferromagnetic

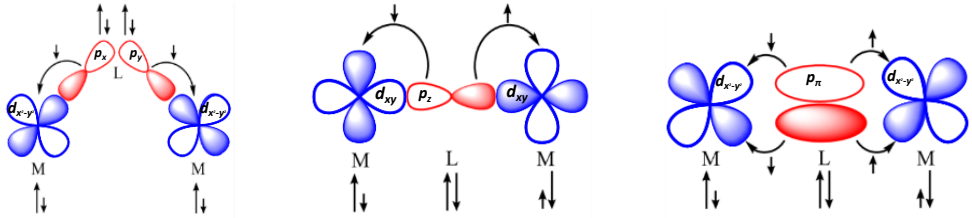

Figure 1.5: Schematic representation, of σ-type ferromagnetic (left), σ-type antiferromagnetic (centre), and π-type antiferromagnetic magnetic superexchange (right).

interactions aim for bond angles which favour it, however, when multiple superexchange pathways are present within a molecule, the antiferromagnetic exchange will dominate due to effects such as spin-orbit coupling (SOC).[31,38,39]The presence of exchange pathways can effectively reduce the probability of QTM by requiring the coupled metal centres to both simultaneously lose their magnetisation.[40]

1.2 Single Molecule Magnets

1.2.1 3*d* SMMs

The first SMM was reported in 1993 when Sessoli *et al.* showed the magnetic properties of an Mn_{12} cluster, $[Mn^{III}_8Mn^{IV}_4(OAc)_{16}(H_2O)_4O_{12}]\cdot 2AcOH\cdot 4H_2O$ the structure of which was first reported in 1980 by Lis *et al.* (Figure 1.6).[41,42] This molecule was the first to display molecular-

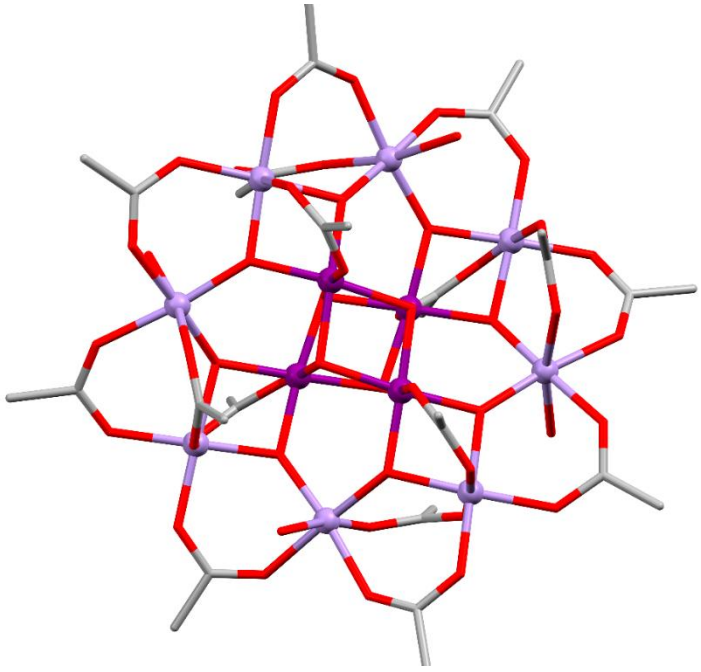

Figure 1.6: Crystal structure of Mn_{12}, first produced by Lis *et al*., hydrogen atoms have been omitted for clarity. Colour code: Mn^{III}, Mn^{IV}, C, and O, are in lilac, purple, grey, and red respectively.

based magnetic hysteresis and retention of magnetisation, which was present at temperatures below 4 K.

Mn_{12} consists of central tetrahedron of four Mn^{IV} ions surrounded by an octagon of eight Mn^{III} ions. Each Mn^{IV} ion is bridged to three Mn^{III} ions by two μ_3-oxide ions, the Mn^{III} ions are linked by μ_2-acetate ions with four water molecules capping four of the Mn^{III} ions. The Mn^{IV} ions, each with S = 3/2, are aligned opposite to the Mn^{III} ions, each with S = 2, giving a total ground spin state of S = 10. Through EPR measurements it was found that this complex possessed a large D value of -0.5 cm^{-1} caused by the Jahn-Teller distorted Mn^{III} ions, this resulted in an U_{eff} of approximately 60 K. It was more than a decade until an SMM was synthesised which had superior magnetic properties than Mn_{12}. 3*d* SMMs typically contain $Mn^{II/III/IV}$, $Fe^{I/II/III}$, or Co^{II} ions due to the unique magnetic properties these metals can provide. Metals with low spin, d^7, d^4 as well as d^9 electronic configurations, such as Mn^{III} tend to exhibit enhanced Jahn-Teller distortions which can result in large uniaxial magnetic anisotropy and so are better candidates for SMMs.[43]

Due to the quadratic dependence of U_{eff} on parameter S, a lot of initial attempts to improve upon Mn_{12} was to create large polynuclear clusters which had large spin ground states.[5] In this regard Ako *et al.* created a cluster $[Mn^{III}_{12}Mn^{II}_{7}(\mu_4\text{–}O)_8(\mu_3,\eta_1\text{–}N_3)_8(H\mathbf{J})_{12}(MeCN)_6]^{2+}$ $H_3\mathbf{J}$ = 2,6-bis(hydroxymethyl)-4-(methylphenol), which had a record-breaking ground state S = 83/2 (Figure 1.7)[44] However, it was found that this cluster had unexpectedly poor magnetic properties, with a U_{eff} = 5.8 K. It was later identified that the orientation of the Jahn-Teller axes of each metal centre needs to be colinear to promote anisotropy, thus with so many metal centres the total anisotropy of the system drastically decreased, resulting in poor magnetic

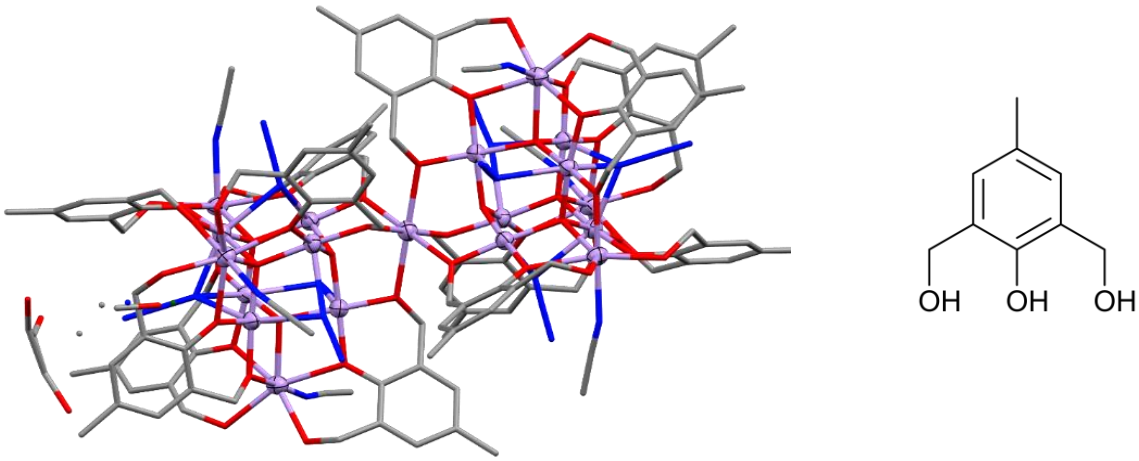

Figure 1.7: Crystal structure of the Mn_{19} cluster produced by Ako *et al.* (left), and the corresponding ligand (right). Hydrogen atoms have been omitted for clarity. Colour code: Mn, C, O, and N are purple, grey, red, and blue respectively.

properties. In a later report into SMMs through theoretical calculations Neese *et al.* identified that the parameter *S* was also related to the total anisotropy *D* through the equation:[5]

$$S \propto 1/D^2$$

Thus, U_{eff} is effectively independent on *S* with the total anisotropy being the deciding factor in the effectiveness of an SMM. One of the biggest issues with 3*d* SMMs is the quenching of the orbital angular momentum (OAM) by the ligand field and subsequent lowering of the SOC. This results in a lower *D* value for the system, and thus a lower energy barrier to the reversal of magnetisation.

As a result of these observations, researchers pivoted into creating SMMs with smaller numbers of magnetic ions which still displayed Jahn-Teller distortions, as well as developing a ligand field which did not quench OAM. An example of this is the work of Brechin *et al.* who developed a hexanuclear Mn^{III} cluster $[Mn^{III}_6O_2(Et\text{-}sao)_6(Bz(Me)_2)_2(EtOH)_6]$, [(Et-sao = 2-hydroxyphenylpropanone oxime), which produced a then record breaking U_{eff} = 86.4 K and a blocking temperature of 4.5 K (Figure 1.8).[45] This is owing to the anisotropy of the individual Mn^{III} ions aligning with one another, so as to not cancel out. In a different approach, Long *et al.* developed a linear dialkyl cobalt complex $Co^{II}(C(SiMe_2ONaph)_3)_2$ that minimised the effect of the ligand field (Figure 1.9). The ground state of this complex showed non-Aufbau filling of the d-

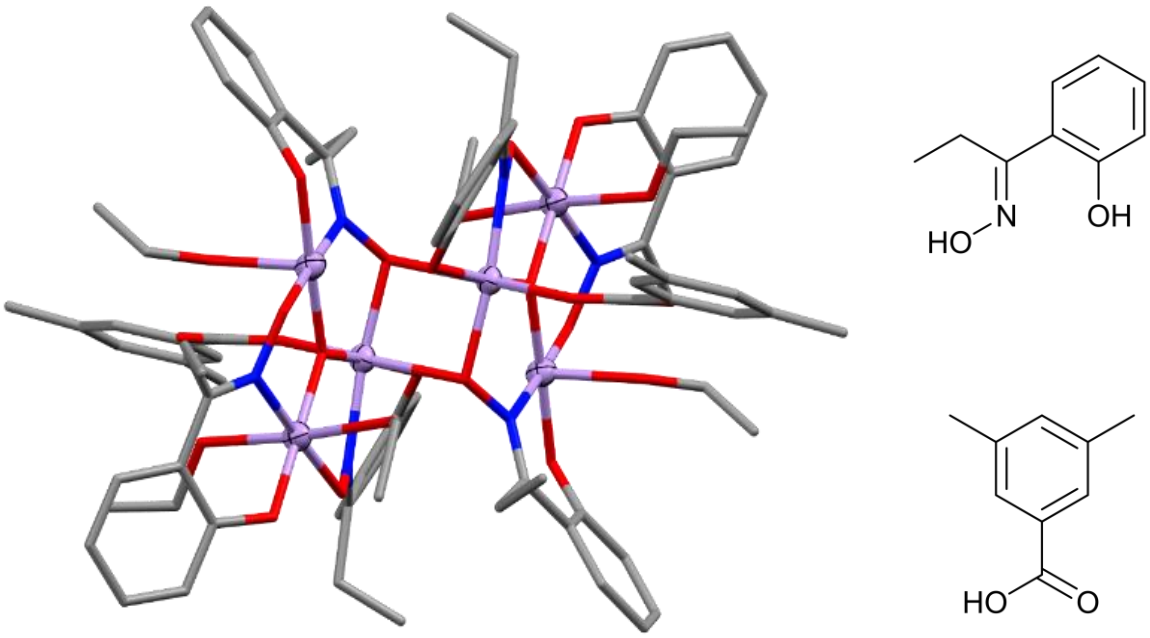

Figure 1.8: Crystal structure of the Mn^{III} complex produced by Brechin *et al.* (left), and corresponding ligand (right). Hydrogen atoms were omitted for clarity. Colour code: Mn, C, O, and N are purple, grey, red, and blue respectively.

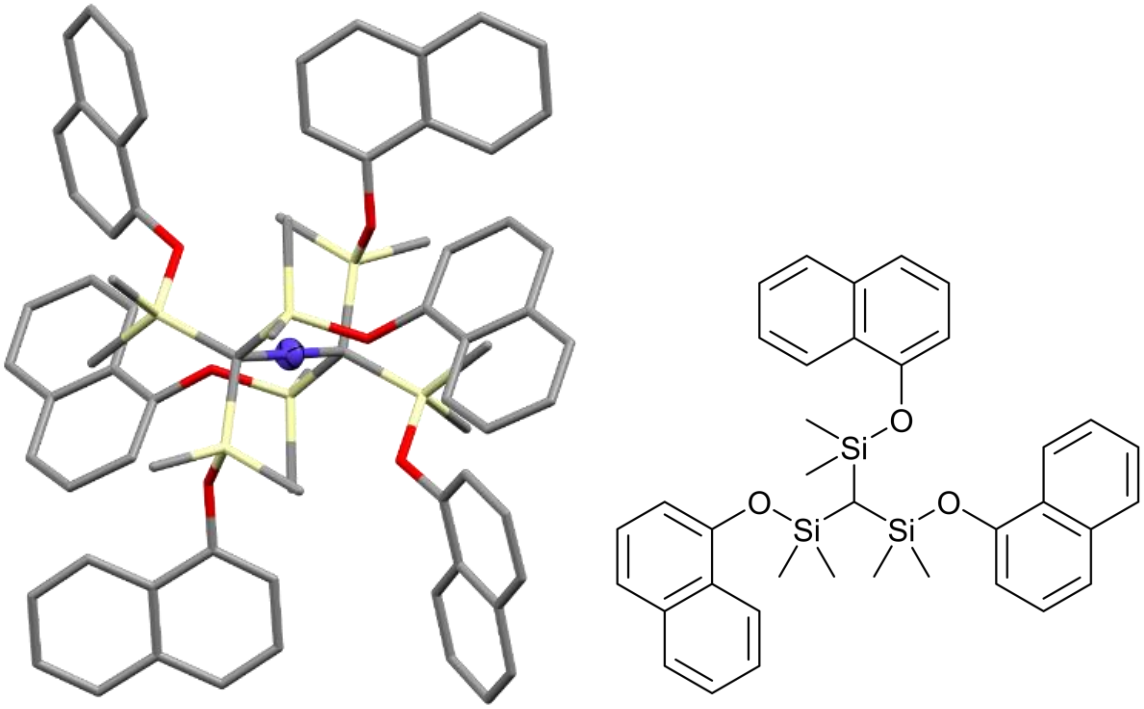

Figure 1.9: Crystal structure of the dialkyl Co^{II} complex produced by Long et al (left) and corresponding ligand (right). Hydrogen atoms have been omitted for clarity. Colour code: Co, Si, C, and O are indigo, beige, grey, and red respectively.

orbitals which resulted in an incredibly small ligand field. This essentially removed OAM allowing the complex to obtain a record U_{eff} of 647.5 K.[46]

1.2.2 4*f* SMMs

With the quenching of OAM being a major issue in 3*d* SMMs, some researchers looked to the f-block metals, namely lanthanides, as a potential source of high anisotropy for SMMs. The advantage of the lanthanides is that the 4*f* orbitals are 'shielded' by the fully occupied $5s^2$ and $5p^6$ orbitals. This means that interactions between the 4*f* orbitals and the ligand field are almost purely electrostatic in nature and thus the spin-orbit coupling (SOC) cannot be quenched as easily as for 3*d* ions. This invites the possibility of very high anisotropy in SMMs developed with lanthanides.[47]

The first 4*f* SMM was developed by Ishikawa *et al.* and utilised a sandwich coordination where two phthalocyanine ligands surround a central Ln^{III} metal (Figure 1.10).[48] Complexes using Tb^{III} and Dy^{III} produced U_{eff} values of 330.9 and 43 K respectively, which suggests that even a single lanthanide ion is enough to create an SMM. Due to the strong SOC the electron spin *S* is not the only source for the angular momentum, therefore when considering the magnetic properties of lanthanide based SMMs it is necessary to utilise SOC terms identified by the quantum number

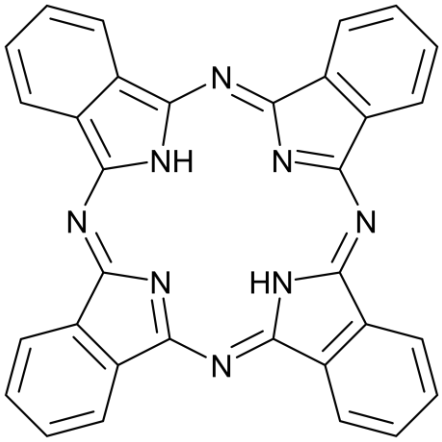

Figure 1.10: Structure of the phthalocyanine ligand utilised by Ishikawa et al.

J. *J* is represented by the vector summation of *L* and *S* and takes values in the range $L \pm S$. The splitting of these terms by the ligand field gives the sublevels M_J instead of M_S. Despite this difference, the design of 4*f* SMMs is analogous to that of 3*d* SMMs, the ground state should be the highest possible value of M_J, which can be accomplished when the ground state anisotropy is axial. The difference between M_J and $M_J = \pm 1$ should be maximised to increase U_{eff}, which would necessitate a rational design of the ligand field.

To this end in 2011 Rinehart *et al.* separated the Ln^{III} series into two classes, dependent on the shape of their electron density, either oblate or prolate (Figure 1.11).[47] This allowed for more

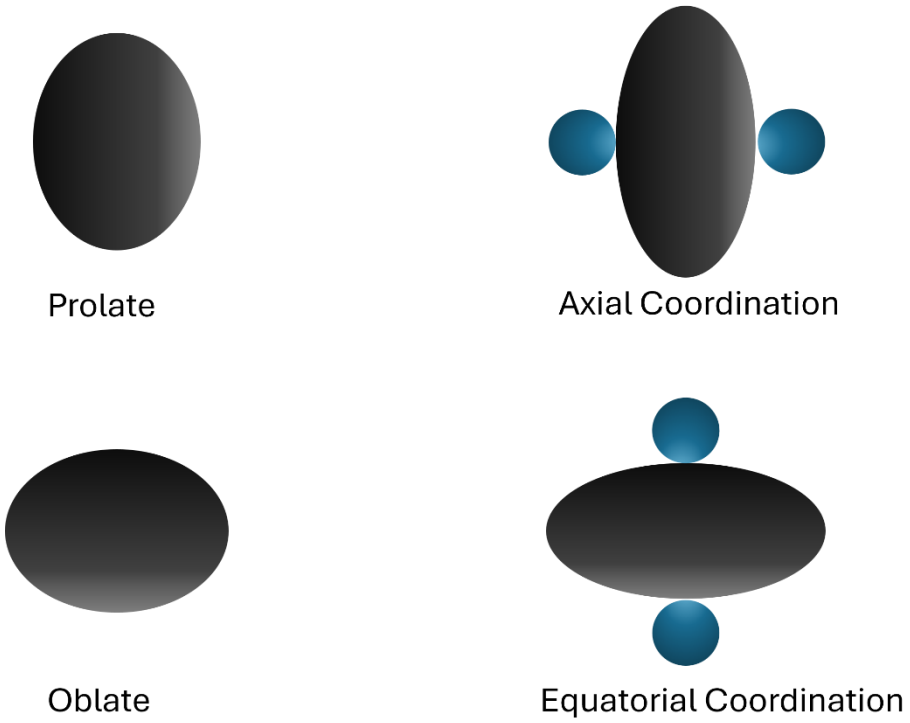

Figure 1.11: Schematic representation of how ligand coordination can enhance the anisotropy of lanthanide ions.

rational design of the ligand field. For oblate ions, ligands with greater electron density should be located axially, to minimise electronic interactions thus stabilising the ground state. Furthermore, if there are no ligands bound equatorially, the electron density will further expand along the plane the anisotropy is located, further enhancing it. For prolate ions, the inverse is true, with equatorially bound ligands being preferred. One notable exception is the case of Gd^{III}. Gd^{III} contains a total of 7 unpaired electrons, this results in an incredibly large ground state *S*, which would be ideal for a 3*d* SMM. However, Gd^{III} is completely isotropic, the individual spins cancel out giving a *J* of 0, meaning it will be ineffective in an SMM. Utilising this rational design idea in 2016 Gregson *et al.* synthesised the complex $K(18\text{-crown-6})(THF)_2[Dy(BIPM^{TMS})_2]$ where $BIPM^{TMS} = [C(PPh_2NSiMe_3)_2]_2$, which had a then record high U_{eff} of 812.69 K for mononuclear Dy^{III} based SMMs (Figure 1.12).[17]

The key to this is the strong axial C donors and weak equatorial N donors enhancing the anisotropy of the ion. Later that year Ding *et al.* synthesised the complex $[Dy(O^tBu)_2(py)_5](BPh_4)$ that achieved a U_{eff} of 1815 K, almost doubling the previous record, however the blocking temperature was only 14 K, not increasing at anywhere near the levels that U_{eff} was. This is due to the QTM, this is a big problem in lanthanides owing to the mixing of M_J states providing additional degeneracy and thus more routes for QTM to occur. QTM is one of the major reasons that a correlation between U_{eff} and B_T cannot be made.[49]

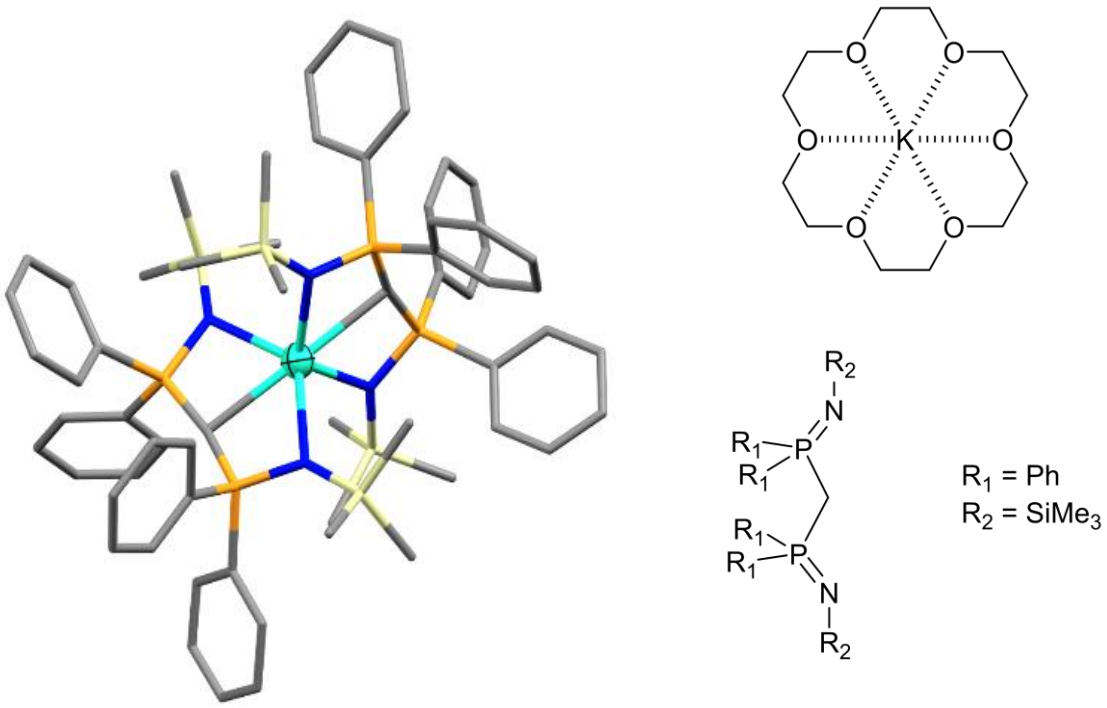

Figure 1.12: Crystal structure of the Dy^{III} complex synthesised by Gregson *et al.* (left), the 18-crown-6 molecule (top right), and the ligand $BIPM^{TMS}$ (bottom right). Hydrogen atoms have been omitted for the sake of clarity. Colour code: Dy, Si, P, C, and N are light blue, beige, orange, grey, and blue respectively.

1.2.3 3*d*/4*f* SMMs

In 2002 Wernsdorfer *et al.* identified the ability of magnetic superexchange between metal ions to modulate or even eliminate QTM effects.[40] In this case antiferromagnetic coupling between a dimer, involving six hydrogen bonds between six pyridine hydrogens on one unit and six chloride ions on the other unit, where each centre contained three Mn^{III} and one Mn^{IV} ion, was able to alter the magnetic properties of the SMM. This idea has since been used to try and combine the exchange interactions of 3*d* metal ions and the high single ion anisotropy of 4*f* metal ions, to create an SMM with a high U_{eff} and negligible QTM. Creating 3*d*/4*f* mixed metal systems can be challenging due to the lack of selectivity in coordination sites. This is because both ions are classified as 'hard acids' and thus prefer oxygen rich binding sites. The simplest way to get around this issue is through careful design of 'coordination pockets' which bind preferentially with atoms of appropriate sizes. Since 3*d* ions are much smaller than 4*f* ions, it is common to design ligands which have both small and large coordination pockets, to ensure selectivity.[3,50,51]

The first 3*d*/4*f* SMM was reported by Osa *et al.* in 2004 as the complex $[Cu^{II}\mathbf{J2}Tb^{III}(hfac)_2]_2$ where **J2** = 1-(2-hydroxybenzamido)-2-(2-hydroxy-3-methoxy-benzylideneamino)-ethane.[52] The ligand **J2** has a distinct 3*d* binding site, between the nitrogen and phenolic oxygen atoms, as well as a partial 4*f* binding site between a phenolic oxygen atom and the phenoxy oxygen atom, the $HFAC^-$ anion provides the rest of the coordination. This complex possessed a U_{eff} of 21 K and a T_B of 1.2 K. An SMM synthesised by Tong *et al.*, $[Co^{II}{}_2Dy^{III}(\mathbf{J3})_2H_2O)]NO_3$, **J3** = 2,2',2"-(((nitrilotris(ethan-2,1-diyl))tris(azanediyl))tris(methylene))tris-(4-bromophenol)), has achieved the record U_{eff} for a mixed metal 3*d*/4*f* SMM of 600 K (Figure 1.13).[53] By utilising techniques such as desolvation the researchers were able to induce small structural changes in the complex, altering the coordination environment, thus resulting in the record U_{eff}. However, they were unable to sufficiently quench the QTM and as a result no magnetic hysteresis was observed.

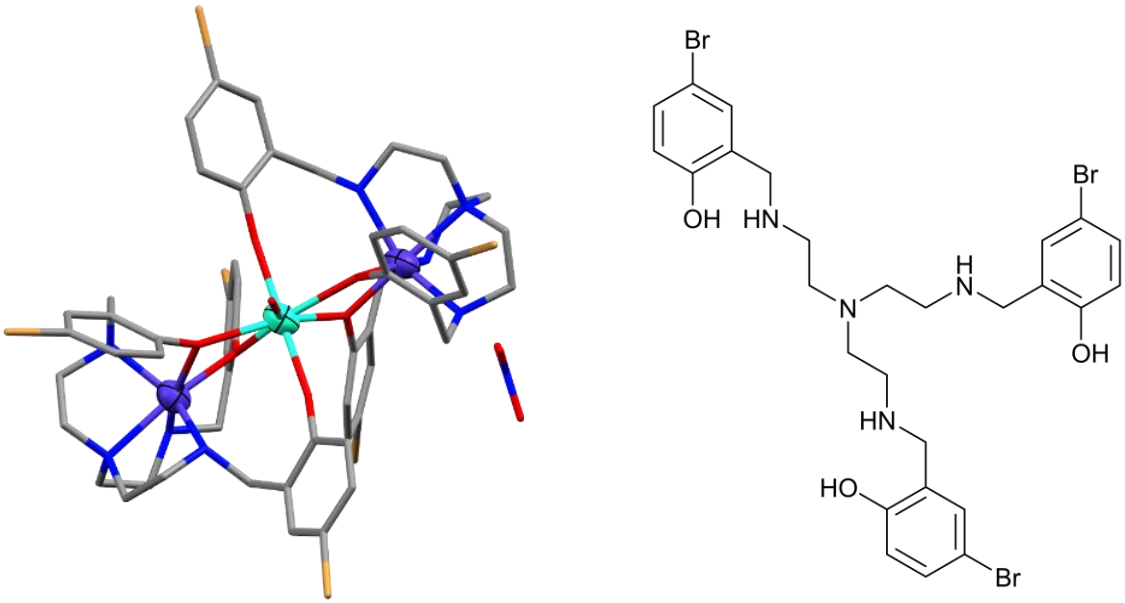

Figure 1.13: Crystal structure of the Co^{II}_2·Dy^{III} complex synthesised by Tong *et al.* (left) and the corresponding ligand (right). Hydrogen atoms have been omitted for clarity. Colour code: Dy, Co, Br, C, O, and N are indigo, cyan, light orange, grey, red, and blue respectively.

1.3 Secondary Interactions

Secondary interactions, consist of interactions that are not directly involved in the primary coordination sphere. Second sphere interactions are a subset of secondary interactions which requires one of the interacting parties to be part of a bound ligand. The two most common types of secondary interactions are steric effects and hydrogen bonding. Steric effects are due to electrostatic repulsion which results in molecules and atoms pushing neighbouring species away. Effective use of sterically bulky macrocyclic ligands has been explored by Tang *et al.,* in their quest to elucidate the relaxation mechanisms of SMMs.[54-57] These bulky ligands help to isolate the magnetic centres and reduce the crystal fields (CFs). With the addition of electron withdrawing substituents to the macrocycles Tang *et al.* were able to further weaken the equatorial crystal field, dramatically increasing SMM performance.[58] Hydrogen bonding interactions result in an attraction between hydrogen bond donor and acceptor species. This type of attraction is shared by similar interactions such as halogen bonding and π-π stacking interactions.

1.3.1 Effects of Secondary Interactions

The effects of secondary interactions on SMMs are numerous and varied, often involving the interplay of multiple types of interactions. Perhaps the most often mentioned secondary effect in the context of SMMs is the physical isolation of magnetic centres, which prevents interactions between adjacent magnetic centres, resulting in a reduction of the number of relaxation pathways present. This is most easily achieved by steric effects where sterically bulky ligands push neighbouring molecules apart and is represented in Figure 1.14 (A). Similarly, utilising secondary interactions to impose rigidity on a complex can result in a decrease in molecular vibrations, which then decreases the number of relaxation pathways.[59] Another subcategory of this involves magnetic dilution where most magnetically active ions in a sample are replaced with diamagnetic ions.[60] An effect utilising hydrogen bonding is shown in Figure 1.14 (B), where

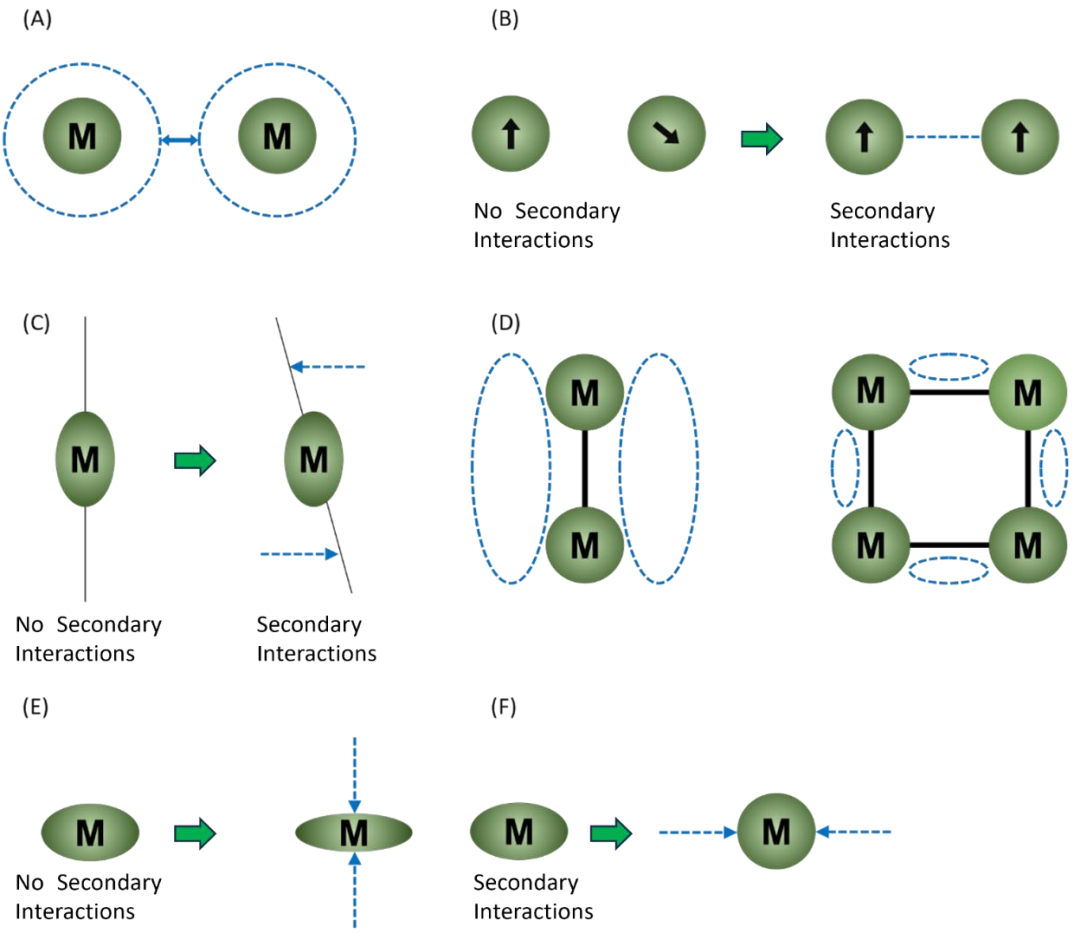

Figure 1.14: Representations of secondary effects (dashed lines represent the secondary interactions). (A) Isolation of adjacent magnetic centres. (B) Magnetic exchange mediated by hydrogen bonds. (C) Reorientation of the magnetic axis away from the ideal orientation. (D) Nuclearity of complexes can be determined by secondary interactions, predominantly steric effects. (E) Alteration of electron density by secondary interactions into a more favourable distribution. (F) Alteration of electron density by secondary interactions into a less favourable distribution.

hydrogen bonds mediate exchange between adjacent metal centres. This can result in an increase or decrease in QTM or even the presence of SMM behaviour. An effect that is often the result of multiple secondary interactions is the reorientation of the magnetic axis of the complex as represented in Figure 1.14 (C). This is often, but not exclusively, a negative effect and is a result of secondary interactions altering the orientation of the anisotropy axes and the symmetry axis of a molecule. This phenomenon has been thoroughly explored by Sessoli *et al.,* in their work on a series of Ln-DOTA complexes.[61-64] The nuclearity of SMMs is a sterically dominated effect. By utilising ligands with similar coordination sites, but differing steric bulk, it is possible to control the number and orientation of magnetic ions present in the complex, as shown in Figure 1.14 (D). Finally, the electron density of the magnetic centres can be affected by secondary interactions. This effect is the broadest as it often inolves the interplay of several secondary interactions and can be either positive or negative, as represented in Figure 1.14 (E) and (F) respectively, depending on whether the electron density is altered to enhance the intrinsic anisotropy of the magnetic centre or not.

1.3.2 Positive effects

There have been numerous cases where secondary interactions have been reported to enhance or even cause SMM behaviour.

Magnetic isolation

The most noted benefit of secondary interactions with regards to SMMs, is their ability to isolate the magnetic core, resulting in a decrease of the potential pathways for the relaxation of magnetisation. A prime demonstration of this is presented by Liu and co-workers who reported on a series of five binuclear dysprosium complexes featuring substituents with differing electronic and steric environments.[65] They synthesised the complexes, $[Dy_2(DMOMP)_2(TFNB)_4]\cdot Et_2O$ (**1**), $[Dy_2(DMOAP)_2(TFNB)_4]$ (**2**), $[Dy_2(DMOEP)_2(TTA)_4]$ (**3**), $[Dy_2(DMOEP)_2(BTFA)_4]$ (**4**) and $[Dy_2(DMOEP)_2(TFNB)_4]$ (**5**), where H-DMOMP = 2,6-dimethoxy-4-methylphenol, H-DMOAP = 3,5-dimethoxy-4-hydroxybenzaldehyde, H-DMOEP = methyl 3,5-dimethoxy-4-hydroxybenzoate, TTA = 2-thenoyltrifluoroacetone, BTFA = benzoyltrifluoroacetone, and TFNB = 4,4,4-trifluoro-1-(2-naphthyl)-1,3-butanedione. The reported U_{eff} values of the complexes under the optimal applied field are 38.9 K, 74.7 K, 20.0 K, 33.6 K and 97.3 K for complexes (**1**), (**2**), (**3**), (**4**), and (**5**), respectively. The structures of complexes (**3**), (**4**), and (**5**) are identical except for the terminal substituents of the β-diketonate. Liu *et al.* deduced that the vast difference in U_{eff} was due to the amount of conjugation and steric hindrance increasing from thiophene (**3**) to benzene (**4**) to naphthalene (**5**) in (Figure 1.15).

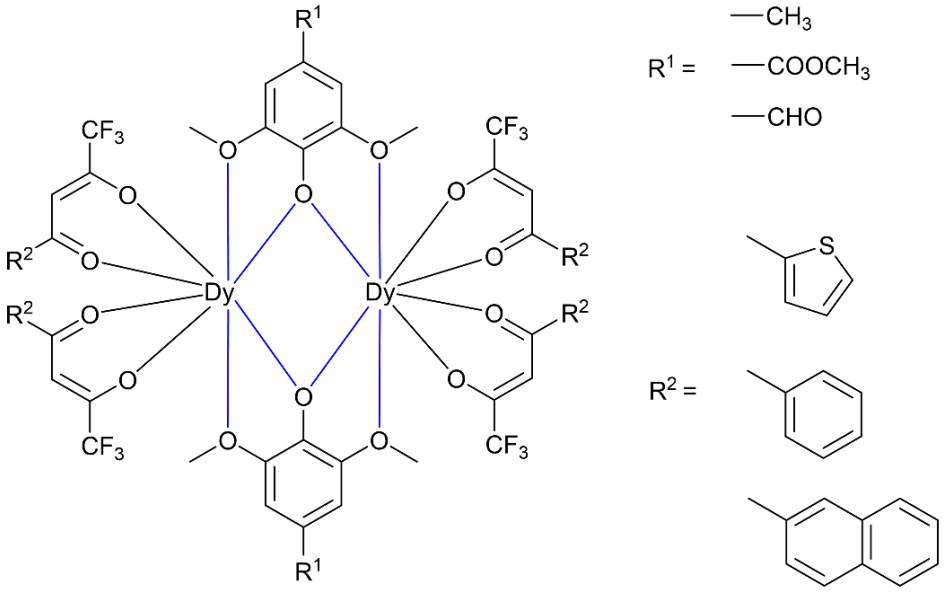

Figure 1.15: General structure of complexes reported by Liu *et al.* (**1**), $R^1 = CH_3$ R^2 = naphthalene, (**2**), R^1 = CHO R^2 = naphthalene, (**3**), $R^1 = COOCH_3$ R^2 = thiophene, (**4**), $R^1 = COOCH_3$ R^2 = benzene, (**5**), $R^1 = COOCH_3$ R^2 = naphthalene.

A similar phenomenon of magnetic isolation was explored by Petit *et al.* who synthesised the dinuclear cobalt complex $[Co^{II}_2(calix)_2]\cdot(Et_3NH)_2$ (**6**), where calix = *p-tert*-butylcalix[8]arene (Figure 1.16).[66] This study focused on identifying the role the second coordination sphere plays in quantifying the zero-field splitting (ZFS) on the cobalt sites. Through *ab initio* calculations the authors deduced that the effect of the second coordination sphere on the ZFS of the Co^{II} ions was twice that of the first coordination sphere, ΔE = 70.59 cm^{-1} and 30.55 cm^{-1} respectively. Additionally, it was discovered that half of the magnetic anisotropy of the Co^{II} ions is a result of the symmetry lowering effects of the calix[8]arene in the second coordination sphere.

Magnetic exchange mediation

The most direct way that secondary interactions can impact SMM performance is by mediating exchange coupling of adjacent metal ions. This is most commonly achieved through hydrogen-bonding which is used to couple adjacent metal centres in a manner similar to magnetic superexchange.[38] This can create an exchange bias which can alter QTM.[67]

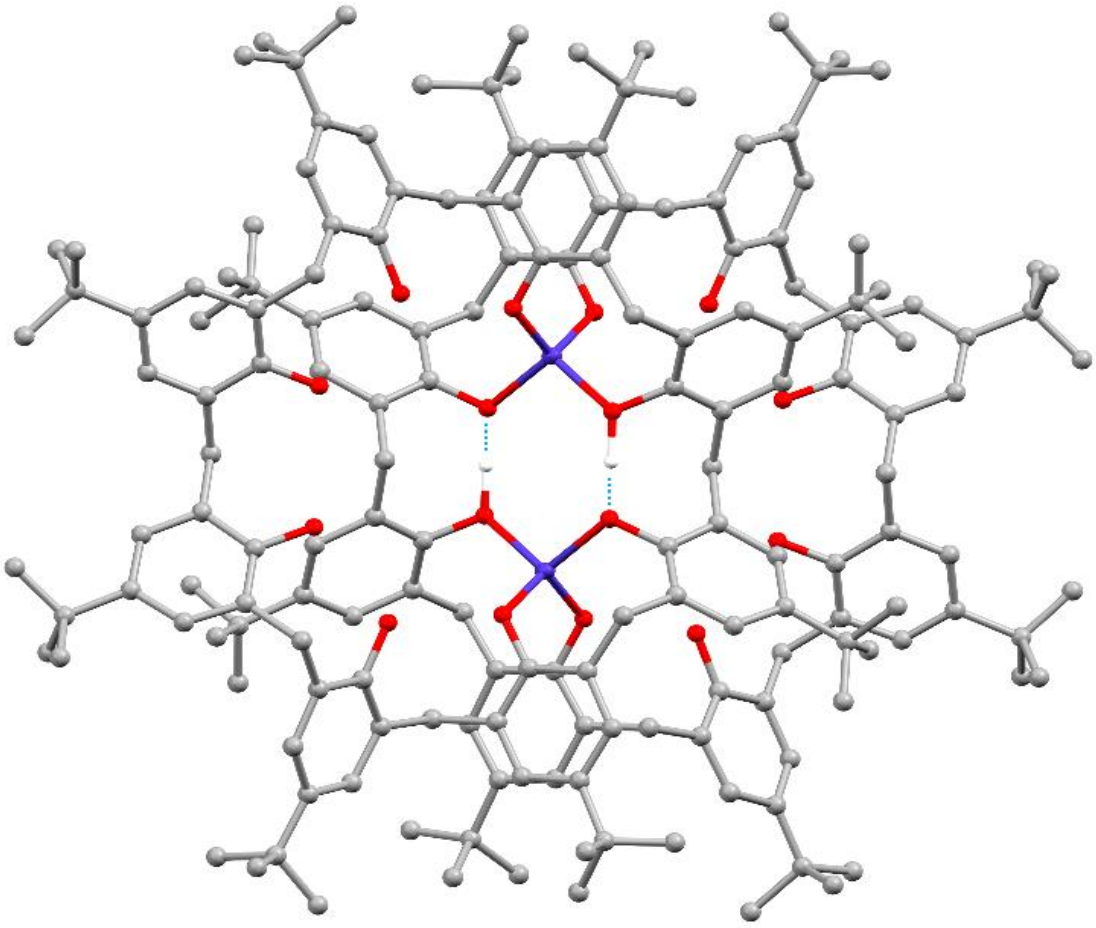

Figure 1.16: Structure of the complex (**6**) reported by Petit *et al.* Solvent molecules and non-interacting hydrogen atoms have been omitted for clarity. Colour code: Co, O, C, and H are purple, red, grey, and white respectively. Thermal ellipsoids of metal atoms shown at 30%.

The direct implications of hydrogen bonding on the magnetic relaxation dynamics of SMMs was investigated by Mitsuhashi *et al.*[68,69] who synthesised a series of three mononuclear four-coordinate cobalt complexes, $[Co(iml)_2]\cdot CH_3OH$ (**7**), $[Co(imn)_2]$ (**8**) and $[Co(thp)_2]$ (**9**), where iml = 2-(2-imidazolyl)phenol, imn = 2-(2-imidazolinyl)phenol, and thp = 2-(1,4,5,6-tetrahydropyrimidin-2-yl)phenol (Figure 1.17).[68] These three complexes differ by slight alterations in the conformation of the N-H groups. They found that the static magnetic properties of the complexes were comparable with axial zero field splitting parameters (D) of -42(11), -38(3) and -35(24) cm^{-1} for (**7**), (**8**), and (**9**), respectively. The dynamic magnetic properties revealed that only two of the complexes displayed frequency dependant in-phase (χ') and out-of-phase (χ'') signals between 1.9 – 8 K and 1.9 – 3.5 K for (**8**) and (**9**), respectively. Mitsuhashi *et al.* identified two reasons for this, firstly, (**7**) formed a two-dimensional hydrogen bonding network whilst (**8**) and (**9**) formed one-dimensional chains. The inter-sheet Co ⋯ Co

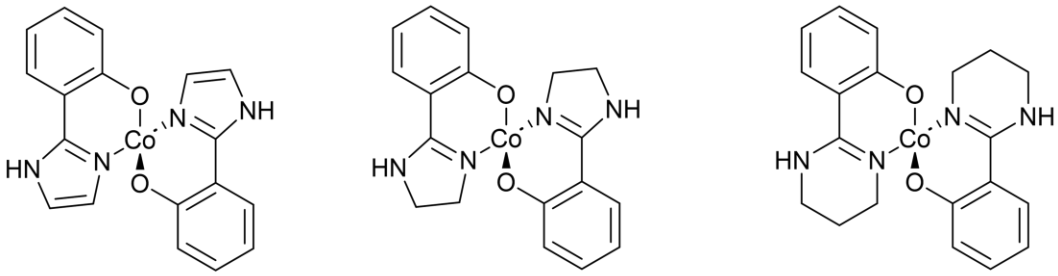

(**7**) (**8**) (**9**)

Figure 1.17: Structure of the complexes reported by Mitsuhashi *et al.*

distance in (**7**) (7.51 Å) is much shorter than the interchain distances in (**8**) and (**9**) (≥ ca. 9 Å). Mitsuhashi *et al.* surmised that since each Co^{II} ion is surrounded by more magnetic ions, dipolar interactions can enhance the QTM resulting in reduced SMM performance. Secondly, the closest Co···Co distance between two adjacent molecules for (**7**) is 7.03 Å whilst it is 6.05 Å and 6.36 Å for (**8**) and (**9**) respectively. Thus, the hydrogen-bonded chains of (**8**) and (**9**) can be regarded as a chain of dimers, in which the magnetic exchange coupling between SMMs works to supress QTM.

This same phenomenon was explored by Yang *et al.* who synthesised two trinuclear manganese complexes $[Mn^{III}_3O(Me\text{-}salox)_3(MeOH)_3(ClO_4)]\cdot MeOH$ (**10**) and $[Mn^{III}_3O(Ph\text{-}salox)_3(MeOH)_3(ClO_4)]\cdot 2MeOH$ (**11**) where HMe-salox = 2-hydroxyphenylethanone oxime and HPh-salox = (2-hydroxy-phenyl)(phenyl)methanone oxime.[67] Magnetic measurements revealed that both complexes displayed frequency dependant in-phase (χ') and out-of-phase (χ'') signals between 2 K and 7 K, with (**10**) showing an effective energy barrier of 58 K whilst complex (**11**) had an effective energy barrier of 42 K. An interesting difference was found in the stepwise magnetisation hysteresis loops of the complexes where the QTM steps of (**11**) were observed at fields of -0.52 T, -0.17 T, 0.16 T, 0.52 T, 0.87 T, 1.21 T, and 1.67 T, whereas those for complex (**12**) were observed at fields of 0 T and 0.7 T. This difference was attributed to the supramolecular environments each individual complex resides in. The less bulky complex (**10**) conforms to a 'tail to tail' arrangement of adjacent units which provides strong hydrogen bonding interactions between the binding ligand and a terminal MeOH ligand of neighbouring units (Figure 1.18). Complex (**11**) meanwhile, adopts a 'head to tail' arrangement providing a single hydrogen bonding interaction between a non-coordinated perchlorate anion and a terminal MeOH ligand. The presence of the strong hydrogen bonding interaction in complex (**10**) mediated a pathway for the exchange bias effect which in turn caused the QTM steps in the hysteresis loop.

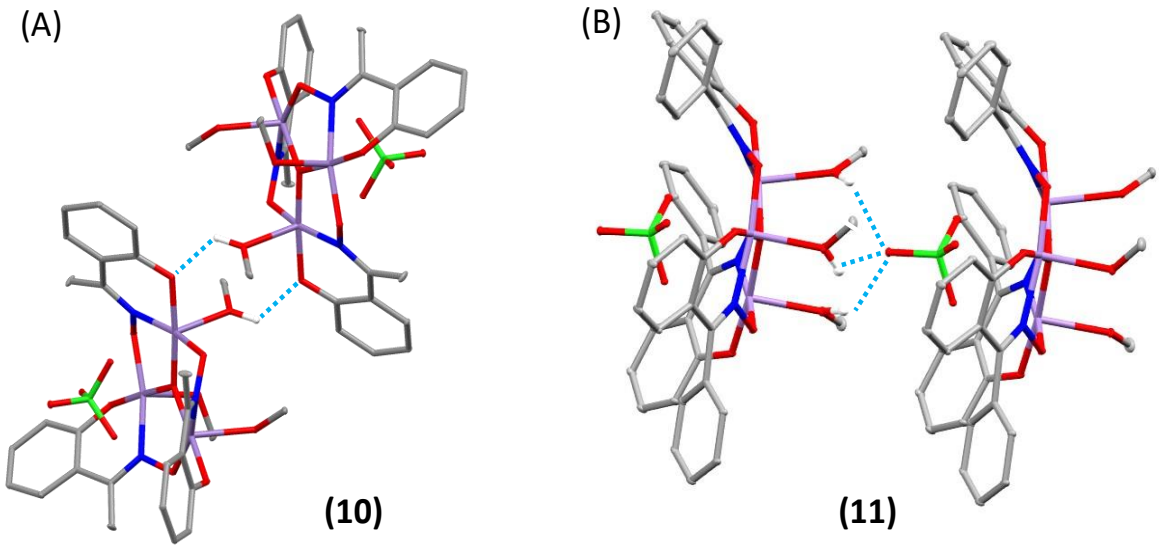

Figure 1.18: Structure of the two complexes reported by Yang *et al.* With the tail-tail arrangement (A) and the head to tail arrangement (B). Intermolecular interactions are shown by dashed red lines. Solvent molecules and non-interacting hydrogens have been omitted for clarity. Colour code: Mn, O, N, C, Cl, and H are lilac, red, blue, grey, green, and white respectively. Thermal ellipsoids shown at 15%.

Fournet *et al.* investigated the hydrogen bond-mediated magnetic coupling of a new member of the Mn_{12} family $[Mn_{12}O_{12}(O_2C(C_6H_4\text{-}p\text{-}F))_{16}(H_2O)_4]$ (**12**) which was the first of its family to display a three-dimensional ferromagnetic network.[70] Magnetic measurements taken on the complex revealed a U_{eff} of 59.3 K which is typical for the Mn_{12} family. There are two main types of intermolecular hydrogen bonds, one involving *ortho*-C-H···F units the other involving *meta*-C-H···F units. Fournet *et al.* further explain that due to the symmetry of and spins in the relevant manganese and fluorine orbitals, exchange interactions mediated by the hydrogen bonds were predominantly ferromagnetic for the *ortho* units and antiferromagnetic for the *meta* units. The overall result is a net ferromagnetic interaction due to the greater localisation of spin onto the *ortho* position.

Control over complex nuclearity

A less direct way that second sphere interactions can impact SMM performance is by controlling the nuclearity of resulting complexes. This is often achieved by utilising ligands that provide identical metal binding sites but different steric bulk. In this vein, Jiao *et al.* reported two complexes in 2018 which showed intramolecular ferromagnetic interactions.[71] A trinuclear $[Ni^{II}(4\text{-Clbpy})_2][(pzTp)Fe^{III}(CN)_3]_2{\cdot}4H_2O$ complex (**13**) and a tetranuclear $[Ni^{II}(4\text{-Clbpy})_2][(Tp^*)Fe^{III}(CN)_3]_2{\cdot}4CH_3OH{\cdot}2H_2O$ complex (**14**) where 4-Clbpy = 4,4'-dichloro-2,2'-bipyridine, pzTp = tetrakis(pyrazolyl)borate and Tp* = hydrotris-(3,5-dimethylpyrazol-1yl)borate. They proposed that the interaction between the bulky Tp*

units and the 4-Clbpy ligand resulted in the formation of a tetranuclear square complex. Magnetic studies performed on these two complexes revealed that the trinuclear complex (**13**) showed no SMM behaviour however, the tetranuclear complex (**14**) displayed frequency dependant in-phase (χ') and out-of-phase (χ'') signals between 1.9 K and 5 K, and an effective energy barrier of 62.31 K. This difference was put down to three factors: the larger spin ground state owing to the addition of an extra Ni^{II} ion, weaker intermolecular interactions removing pathways for magnetic relaxation, and stronger intramolecular ferromagnetic interactions due to the difference in Ni-N-C bond angles which dictates the degree of overlap between the magnetic orbitals of adjacent Ni^{II} and Fe^{II} ions.

Zhao and co-workers utilised two chiral pairs of weakly coordinating hexaazamacrocycles, one based on (1*R,*2*R/*1*S,*2*S*)-1,2-diphenylethylenediamine, and the other, on (1*R,*2*R/*1*S,*2*S*)-1,2-diaminocyclohexane in their report investigating the effects of steric hindrance on the performance of dysprosium single molecule magnets (Figure 1.19).[72] The mononuclear complexes were synthesised by using the bulkier 1,2-diphenylethylenediamine-based hexaazamacrocycle which resulted in two complexes, (**15**) and (**16**), displaying SMM behaviour with U_{eff} values of 800.0 K and 766.9 K, respectively. Two dinuclear complexes (**17**) and (**18**)

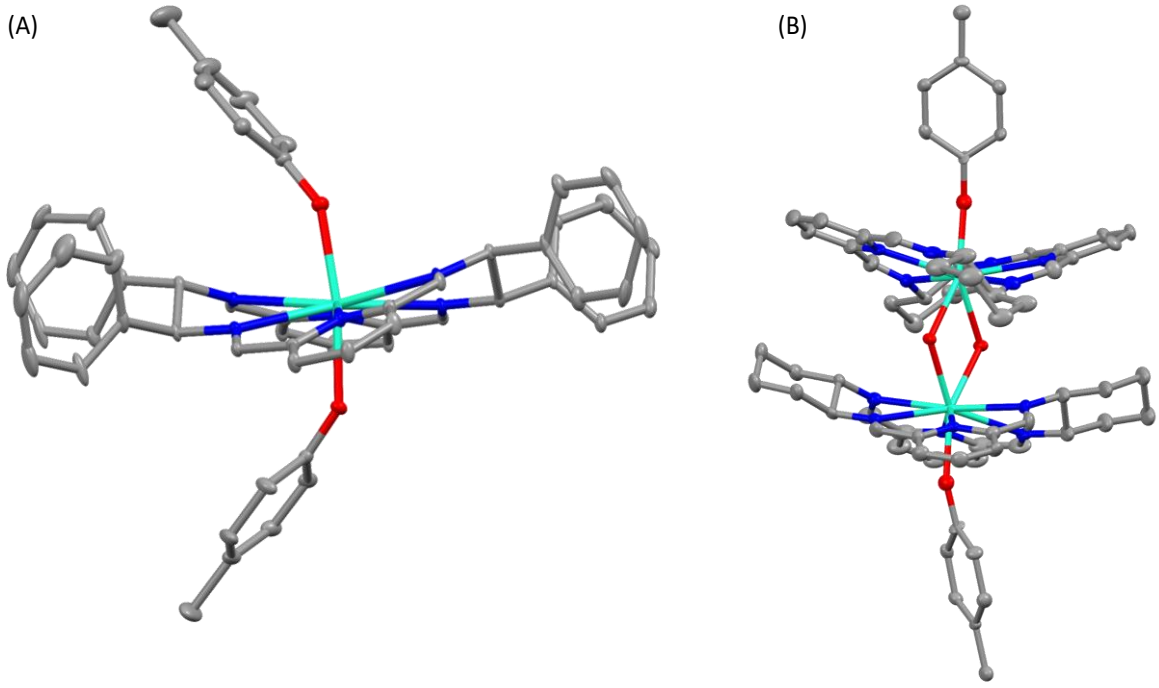

Figure 1.19: Structures of the mononuclear (A, **15**/**16**) and dinuclear (B, **17**/**18**) complexes reported by Zhao *et al.* Solvent molecules and hydrogen atoms have been omitted for clarity. Colour code: Dy, O, N, and C are cyan, red, blue, and grey respectively. Thermal ellipsoids shown at 15%.

which also displayed SMM behaviour were synthesised using the less sterically bulky 1,2-diaminocyclohexane based macrocycle. These complexes had U_{eff} values of 198.6 K and 230.2 K, respectively. The reason for the large difference between energy barriers was put down to the geometry of the magnetic cores. The Dy^{III} ions of the mononuclear complexes possess an almost perfect local D_{6h} geometry which enhances the axial crystal field. In contrast, the Dy^{III} ions of the dinuclear complexes possess a 'hula-hoop' geometry which weakens the axial crystal field reducing U_{eff}.

Reorientation of magnetic axis

An interesting way that secondary interactions have been shown to affect the magnetic properties of SMMs is by reorienting the magnetic axes. An example where this was beneficial is reported by Novitchi *et al.* The group developed two series of 3*d*-4*f* SMMs $[Cu^{II}Gd^{III}$**J4**$(NO_3)_3]\cdot 3.5THF$ (**19**), $[Cu^{II}Tb^{III}$**J4**$(NO_3)_3]\cdot 3.5THF$ (**20**) and $[Cu^{II}Dy^{III}$**J4**$(NO_3)_3]\cdot 3.5THF$ (**21**) $[(\mu_3\text{-}C_9H_3O_6)(Cu^{II}Gd^{III}$**J4**$(NO_3)_2)_3]\cdot 3THF$ (**22**), $[(\mu_3\text{-}C_9H_3O_6)(Cu^{II}Tb^{III}$**J4**$\text{-}(NO_3)_2)_3]\cdot 3THF$ (**23**) and $[(\mu_3\text{-}C_9H_3O_6)(Cu^{II}Dy^{III}$**J4**$\text{-}(NO_3)_2)_3]\cdot 3THF$ **(24)**. Where H_2**J4** = *N,N'*-bis (3-hydroxymethyl-5-methylsalicylidene)-1,3-diaminopropane.[73] The magnetic properties of the dysprosium complexes, (**21**) and (**24**), showed that the dinuclear complex (**21**) displayed magnetic hysteresis curves of low coercivity, whilst the hexanuclear cluster (**24**) was much larger; coercivity being a measure of how resistant the complex is to being demagnetised by an external magnetic field. Furthermore, the hysteresis curves of (**21**) were only open at 0.04 K whilst for (**24**) open at temperatures up to 1.1 K. Previous research done on similar complexes suggested that this difference was not a result of intramolecular magnetic interactions, since these were expected to be negligible.[74-76] Novitchi and co-workers deduced that intermolecular π-π stacking and hydrogen bonding interactions between two hexanuclear clusters resulted in a reorientation of the anisotropy axes of the lanthanide ions (Figure 1.20). This in turn caused the large change in SMM behaviour.

Changing electron density

Recent advances in SMM research have revealed that matching the electron density of the magnetic ion with an appropriate ligand field is essential to enhancing the magnetic properties of SMMs, especially those that are lanthanide based. A key example of this was shown by Zhang *et al.* who developed a series of four mononuclear dysprosium complexes $[Dy(tmpd)_3$(4,4'-dmpy)] (**25**), $[Dy(tffb)_3$(4,4'-dmpy)] (**26**), $[Dy(tffb)_3$(5,5'-dmpy)] (**27**), and $[Dy(tmpd)_3$(5,5'-dmpy)] (**28**), where tmpd = 4,4,4-trifluoro-1-(4-methoxyphenyl)-1,3-butanedione, tffb = 4,4,4- trifluoro-1-(4-fluorophenyl)-1,3-butanedione, 4,4'-dmpy = 4,4'- dimethyl-2,2'-bipyridyl, and 5,5'-dmpy =

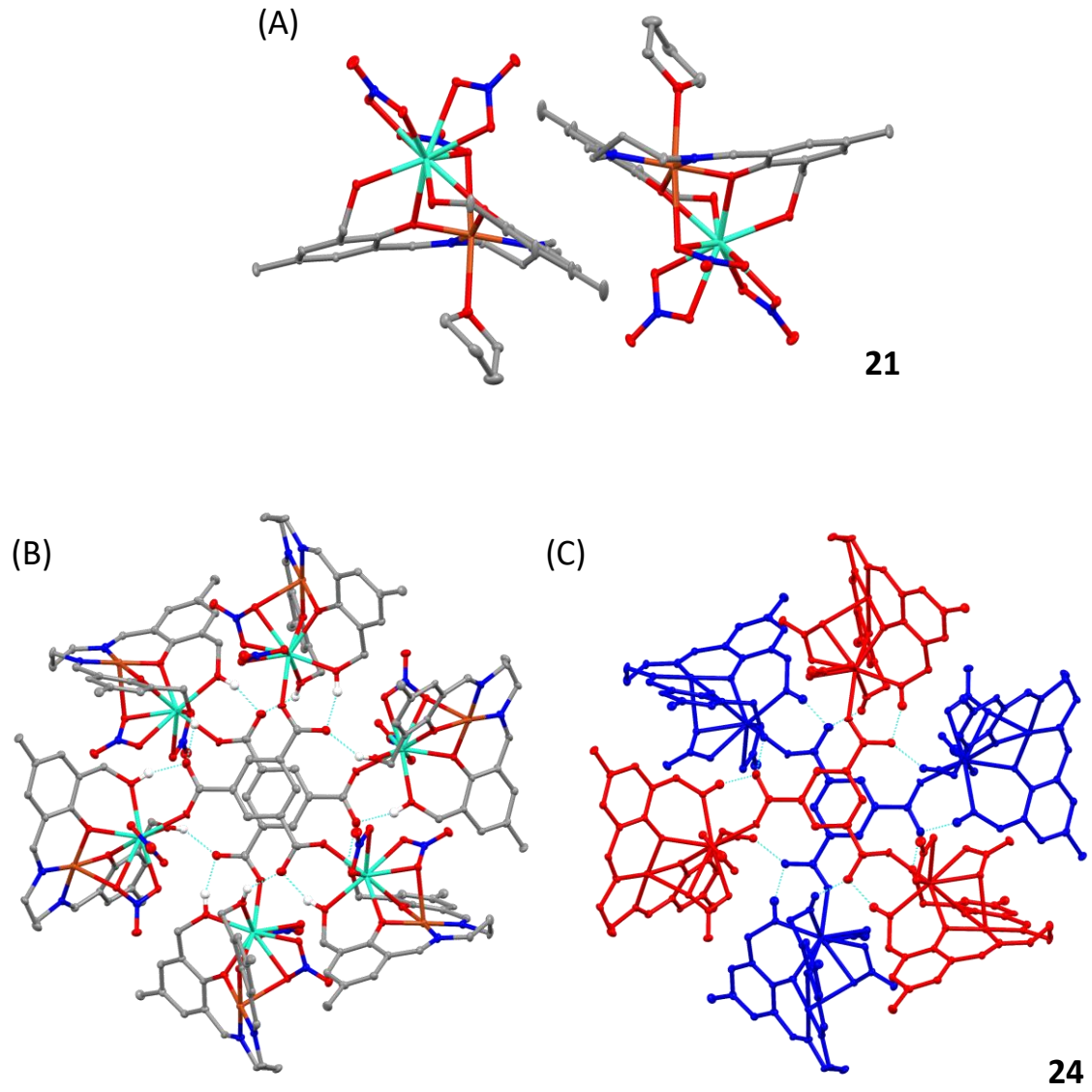

Figure 1.20: Structures of two molecules of the dinuclear (A) and hexanuclear (B, C) dysprosium complexes reported by Novitchi *et al.* Solvent molecules and non-interacting hydrogen atoms have been omitted for clarity. Hydrogen bonding interactions are shown by dashed cyan lines. Colour code: Dy, Cu, O, N, C, and H are cyan, orange, red, blue, grey, and white respectively. Thermal ellipsoids shown at 15%.

5,5'-dimethyl-2,2'-bipyridyl.[77] Magnetic measurements on these complexes revealed U_{eff} values of 66 K (**25**), 189 K (**26**), 115 K (**27**) and 205 K (**28**). Experimental and theoretical investigations revealed that the symmetry of the electron density distribution surrounding the central Dy^{III} ion is critical in regulating the slow relaxation of magnetisation. It was found that complex (**28**) had the strongest axial ligand field, which when coupled with the Dy^{III} ion's naturally oblate electron density resulted in the complex with the highest energy barrier to reversal of magnetisation. Furthermore, the lowest energy barrier was displayed by complex (**25**), which was found to have the shortest intermolecular Dy···Dy separation because of the presence of strong π–π stacking

interactions. This resulted in stronger dipolar interactions between the molecules which, in this case, increased QTM and thus a lower energy barrier for reversal of magnetisation.

Fellah *et al.* investigated the effects a non-coordinating alcohol group had on the magnetic properties of a series of four binuclear CuLn complexes, [Cu**J5**(H_2O)Gd(NO_3)$_2$(H_2O)$_2$]·NO_3 (**29**), [Cu**J5**(MeOH)Tb(NO_3)$_3$] (**30**), [Cu**J5**(MeOH)Dy(NO_3)$_3$] (**31**), and [Cu**J5**(H_2O)Dy(NO_3)$_3$] (**32**) where H_2**J5** = 1,3-bis(2-hydroxy-3-meythoxybenzlidene)propan-2-ol).[78] Of these complexes, only (**30**) displayed SMM properties with an U_{eff} barrier of 24.6 K. In all complexes, the alcohol group acts as a hydrogen bond donor for intermolecular interactions and a hydrogen bond acceptor for intramolecular interactions (Figure 1.21). The researchers noted that only the complexes (**30**) and (**31**), which contained a methanol molecule bound to the copper, displayed slow relaxation of magnetisation. Furthermore, they postulated that the intramolecular hydrogen bonding between the non-coordinated alcohol group and the apical ligand (H_2O or MeOH) could help stabilise the coordination with respect to the lability of this ligand. This in turn directly affected the magnetic properties of the reported complexes.

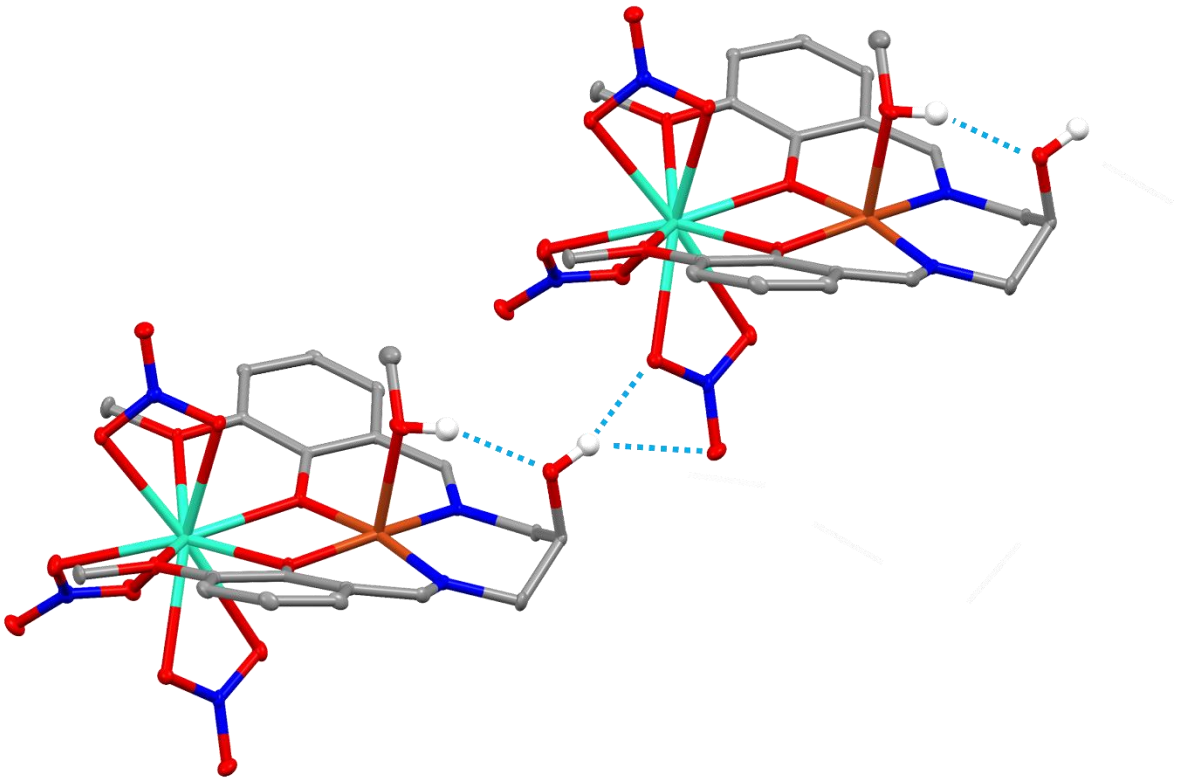

Figure 1.21: Structure of the terbium complex **(30)** reported by Fellah *et al.* with hydrogen bonding interactions depicted by dashed red lines. Non-interacting hydrogen atoms have been omitted for clarity. Colour code: Tb, Cu, O, N, C, and H are cyan, orange, red, blue, grey, and white respectively. Thermal ellipsoids shown at 15%.

1.3.3 Negative effects

In this section the impact secondary interactions can have to diminish or prevent SMM behaviour will be discussed. As one might expect, the negative effects of secondary interactions are far less commonly reported, with even fewer being the focus of the reported research.

Changing electron density

Secondary interactions which alter electron density on the magnetic centre can also quench the resultant magnetic properties. This happens by either providing various relaxation pathways for the reversal of magnetisation, most notably QTM; or, by reducing the magnetic anisotropy of the metal ion, reducing SMM performance. This effect was thoroughly investigated by Canaj and co-workers who synthesised two dysprosium SMMs $[Dy(H_2O)_5(HMPA)_2]Cl_3 \cdot HMPA \cdot H_2O$ (**33**) and $[Dy(H_2O)_5(HMPA)_2]I_3 \cdot 2HMPA$ (**34**), HMPA = hexamethylphosphoramide (Figure 1.22).[79] Magnetic studies revealed that the energy barrier for the reversal of magnetisation was 460 K (**33**) and 600 K (**34**). This difference was attributed to the large computed LoProp (Local properties)[80] charge of the chloride anion compared to the iodide anion. In practice, this resulted in a larger equatorial electron density for (**33**) which for a Dy^{III} ion results in a larger transverse ligand field and a resultant increase in QTM. Furthermore, they performed *ab initio* calculations to identify what effect removing anions/molecules in the second coordination sphere had on the magnetic properties of the complex. The result was an increase in the calculated energy barrier (U_{cal}) for reversal of magnetisation to a maximum of approximately 3100 K for the two-coordinate $[Dy(HMPA)_2]^{3+}$ model. This drastic increase was a result of the decreasing equatorial electron density and the increase in the axial crystal field as they moved to lower coordinate models.

A more conclusive example of the detrimental effects of changing the electron density was studied by Ramakant *et al.* who developed a series of lanthanide based 1D polymers $([Dy(\mathbf{J6})_2(H_2O)_4]\cdot 6Br)_n$ (**35**), $([Gd(\mathbf{J6})_2(H_2O)_4]\cdot 6Br)_n$ (**36**) and $([La(\mathbf{J6})_2(H_2O)_4]\cdot 6Br)_n$ (**37**) where **J6** = 3,3′,3′′-((2,4,6-trimethylbenzene-1,3,5-triyl)tris(methylene))tris(1-(carboxymethyl)-

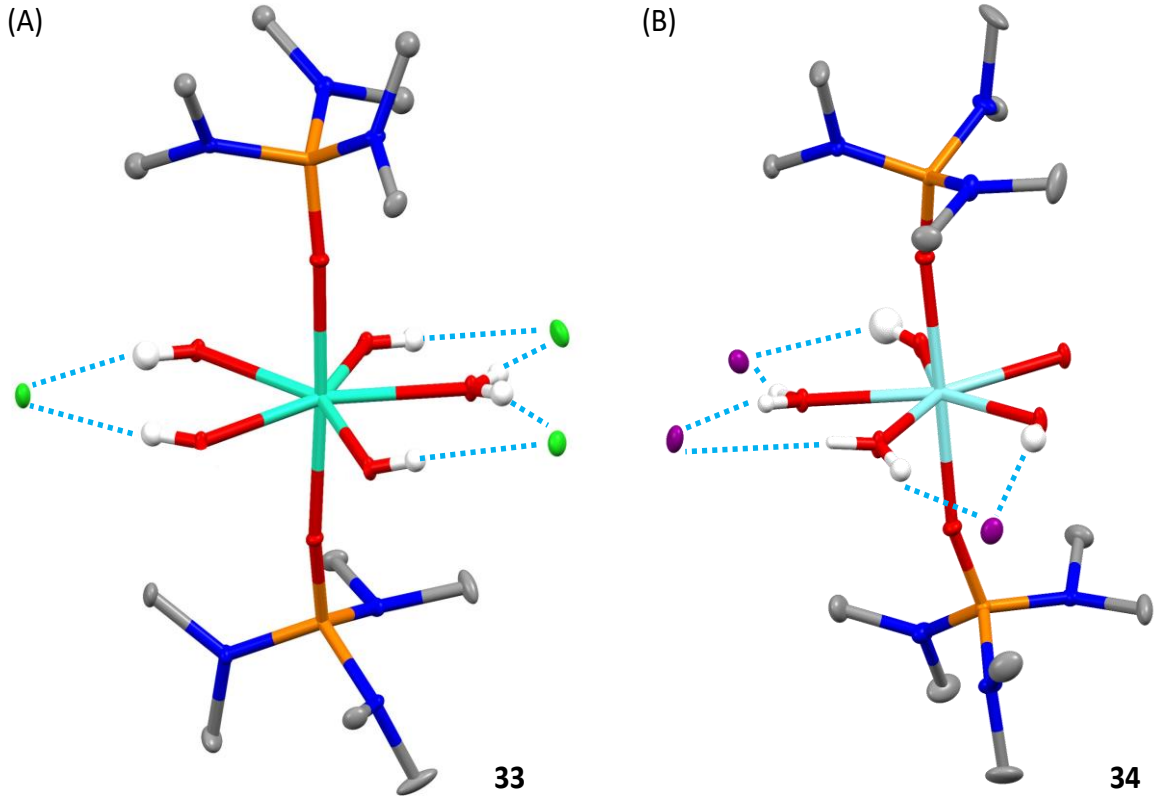

Figure 1.22: Diagram of the chloride containing complex (A) and the iodine containing complex (B) reported by Canaj *et al.* Solvent molecules and non-interacting hydrogens have been omitted for clarity. Hydrogen bonding interactions are shown as dashed red lines. Colour code: Dy, O, N, C, P, Cl, I, and H are cyan, red, blue, grey, orange, green, violet, and white respectively. Thermal ellipsoids shown at 15%.

benzimidazolium).[81] They found that (**35**) displayed some SMM behaviours whilst (**36**) and (**37**) did not, which is not unreasonable since La^{III} is diamagnetic and Gd^{III} is typically magnetically isotropic. The observed out-of-phase ac magnetic susceptibility (χ'') measurements on (**35**) showed frequency dependence between 1.9 K and 4.2 K however, there was no clear χ'' maxima within the experimental temperature and frequency ranges. This absence was a result of fast QTM bypassing the energy barrier. Through theoretical calculations they reasoned that hydrogen bonding interactions between bound water molecules and the bromide anions resulted in an increase in equatorial electron density, which resulted in an unfavourable crystal field and thus negatively affected the slow relaxation of magnetisation.

A case where the magnetic anisotropy of the metal centres was altered is reported by Yao *et al.* who investigated the effect of substituent size in a series of three dinuclear cobalt SMMs, $[((PyPz_3)Co)_2(DHBQ)](PF_6)_2$ (**38**), $[((PyPz_3)Co)_2(CA)](PF_6)_2$ (**39**) and $[((PyPz_3)Co)_2(BA)](PF_6)_2$ (**40**) where $PyPz_3$ = 2-(di(1*H*-pyrazol-1-yl)methyl)-6-(1*H*-pyrazol-1-yl)pyridine, DHBQ = 2,5-dihydro-1,4-benzoquinone, CA = chloraniline and BA = bromaniline (Figure 1.23).[82] Magnetic measurements revealed the energy barriers for reversal of magnetisation to be 117 K (**38**), 40.3

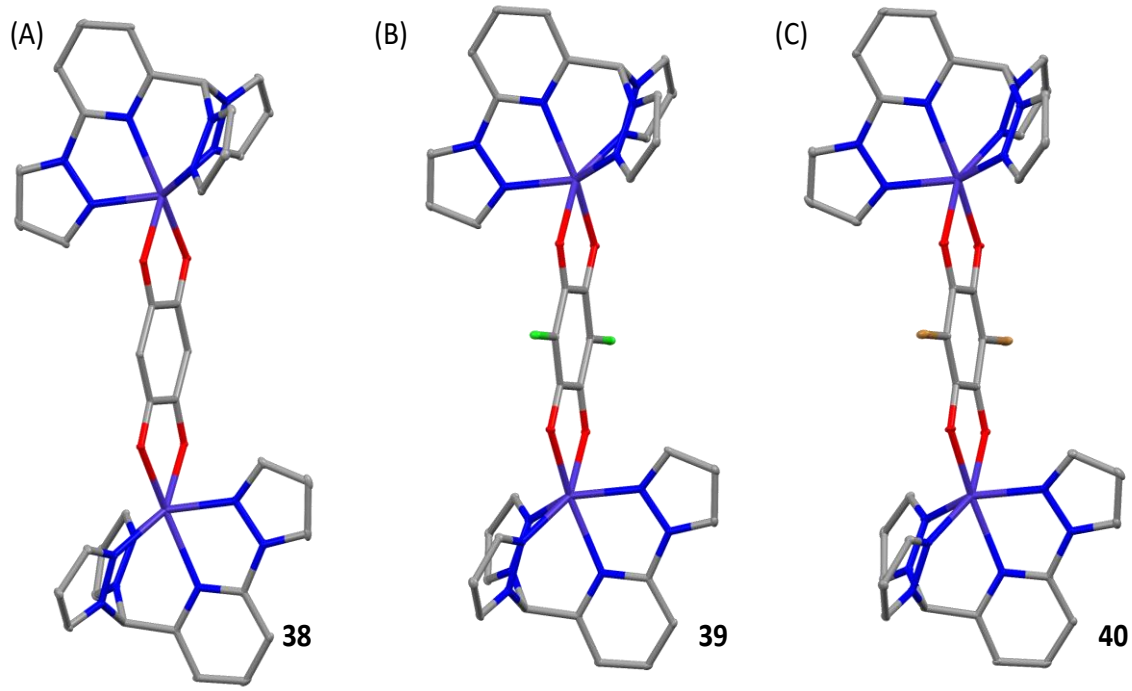

Figure 1.23: Structures of the three complexes reported by Yao *et al.* Solvent molecules and hydrogen atoms have been omitted for clarity. Colour code: Co, O, N, C, Cl, and Br are purple, red, blue, grey, green, and orange respectively. Thermal ellipsoids shown at 15%.

K (**39**) and 33.1 K (**40**). Analysis of the X-ray data revealed that the cobalt centres adopted a distorted trigonal prismatic geometry with this distortion becoming more pronounced the larger the substituent, (**38**) → (**39**) → (**40**). The corresponding magnetic analysis revealed that the more structurally distorted the complex, the lower the effective energy barrier. This was ascribed to the greater distortions increasing the rhombic anisotropy, which promoted QTM mechanisms.

Douib *et al.* recently reported an investigation on the effect that bulky anions had on the magnetic properties of a pair of chiral dysprosium SMMs.[83] The chiral pair of complexes [Dy((∓)hfc)$_3$(**J7**)]$_2$·C_7H_{16} (**41**) where hfc$^-$ = 3(heptafluoropropylhydroxymethylene)-(±)-camphorate) and **J7** = 4'-(4'''-pyridyl-*N*-oxide)-1,2':6'1''-bis-(pyrazolyl)pyridine), were dinuclear of the form 2M2L and possessed eight oxygens occupying the primary coordination sphere of the lanthanide ions. Six oxygens were provided by the coordinated hfc$^-$ anions and one each by the two bound ligands. Addition of the bulky BarF anion (BarF = tetrakis[3,5-bis(trifluoromethyl)phenyl]borate) resulted in the formation of the chiral pair of 1D coordination polymers [Dy((∓)hfc)$_2$(**J7**BarF)]$_n$·nCH_3NO_2 (**42**). The presence of the bulky anion caused partial dissociation of the hfc$^-$ anions from the metal centre, which resulted in the lanthanide ion having five oxygen and three nitrogen atoms occupying its coordination sites (Figure 1.24). They reported that the

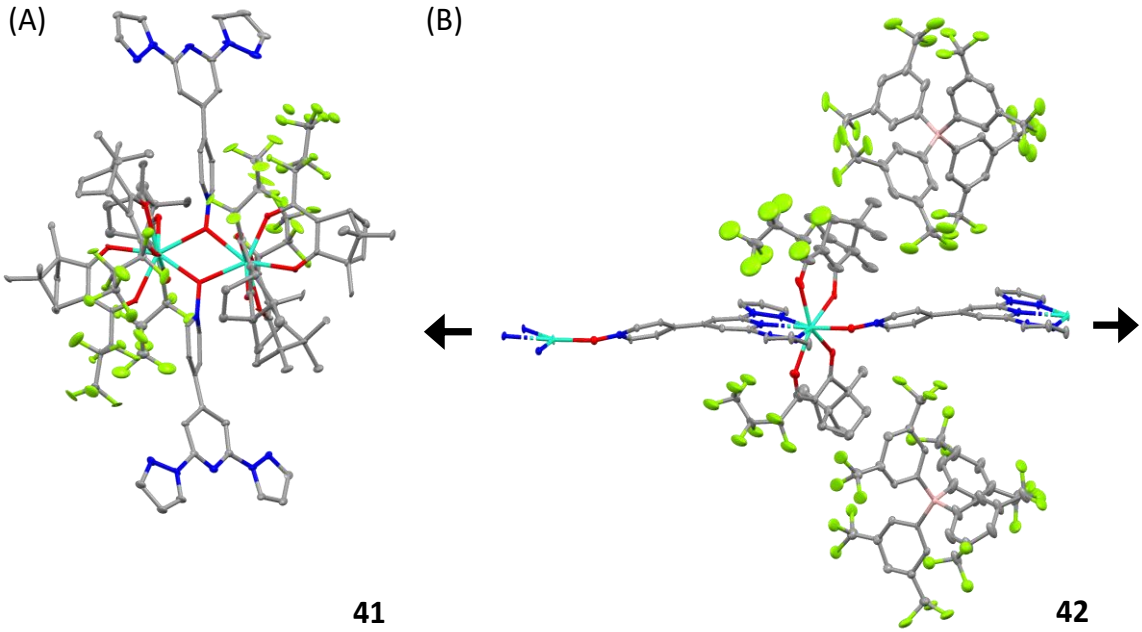

Figure 1.24: Structures of the dinuclear complex (A) and polymer complex (B) reported by Douib *et al.* Solvent molecules and hydrogen atoms have been omitted for clarity. Colour code: Dy, O, N, C, F, and B are cyan, red, blue, grey, lime, and pink respectively. Thermal ellipsoids shown at a 15% confidence level.

dinuclear complex (**41**) acts as a SMM with a blocking temperature of 4 K whilst the polymeric complex (**42**) acts as a one-dimensional assembly of field induced SMMs where the magnetic relaxation occurs through Raman processes. They attributed the enhanced SMM properties in the dinuclear complexes to the electronic distribution of the first coordination sphere better matching the oblate Dy^{III} ion when compared to the polymer complex.

Reorientation of magnetic axis

A combination of secondary interactions can result in the symmetry of the complex no longer aligning with the easy axis of magnetisation, hindering SMM behaviour. Alternatively, secondary effects can also reorient the magnetisation axis itself away from the principal symmetry axis of the molecule. Both result in a lowering of the energy barrier.

An example of the former was presented by Gil *et al.* who investigated how the secondary interactions caused by 18-crown-6 affected the SMM performance of two mononuclear dysprosium based complexes $[Dy(NCS)_3(H_2O)_5]\cdot 0.45(KSCN)(18\text{-crown-6})$ (**43**) and $[Dy(NO_3)_2(NCS)_3(H_2O)]\cdot(H_2O)(NH_4)_2\cdot 2(18\text{-crown-6})$ (**44**).[84] The effective energy barriers for reversal of magnetisation were determined to be 47 K for (**43**) and 65.9 K for (**44**). They went further and performed a series of theoretical calculations to identify the effects of all secondary

interactions resulting from the encapsulation by the crown ether. They found that hydrogen bonding interactions between bound water molecules and the crown ether had a detrimental effect on the magnetic anisotropy due to the water molecules being bound on the equatorial plane of the dysprosium anion. Furthermore, through *ab initio* calculations they found that by altering the electrostatic potential exerted by the crown ethers to align with the magnetic easy axis, they were able to enhance the magnetic properties. However, the mismatched symmetry axis of the crown ether molecules and the magnetic easy axis of the recorded complexes resulted in less optimal SMM performance.

Exploring the same phenomenon, Herchel and co-workers also investigated the effect of the second coordination sphere, specifically the effect that 18-crown-6 had, on the magnetic properties of two mononuclear lanthanide complexes $[Dy(NO_3)_3(H_2O)_3]\cdot$(18-crown-6) (**45**) and $[Er(NO_3)_3(H_2O)_3]\cdot$(18-crown-6) (**46**).[85] Due to the complicated relaxation pathways present, the experimentally determined energy barriers lie in the ranges 66 – 71 K (**45**) and 21 – 24 K (**46**). Theoretical calculations of each complex with and without the presence of the crown ethers (Figure 1.25) indicated that the calculated energy barriers for the complexes without crown ethers present were 143 K (**45'**) and 42 K (**46'**) whilst with the crown ethers they were 57 K (**45**) and 16 K (**46**). This was attributed to the reorientation of the magnetisation axis, demonstrating that the second coordination sphere has the capability to drastically reduce the magnetic performance of SMMs.

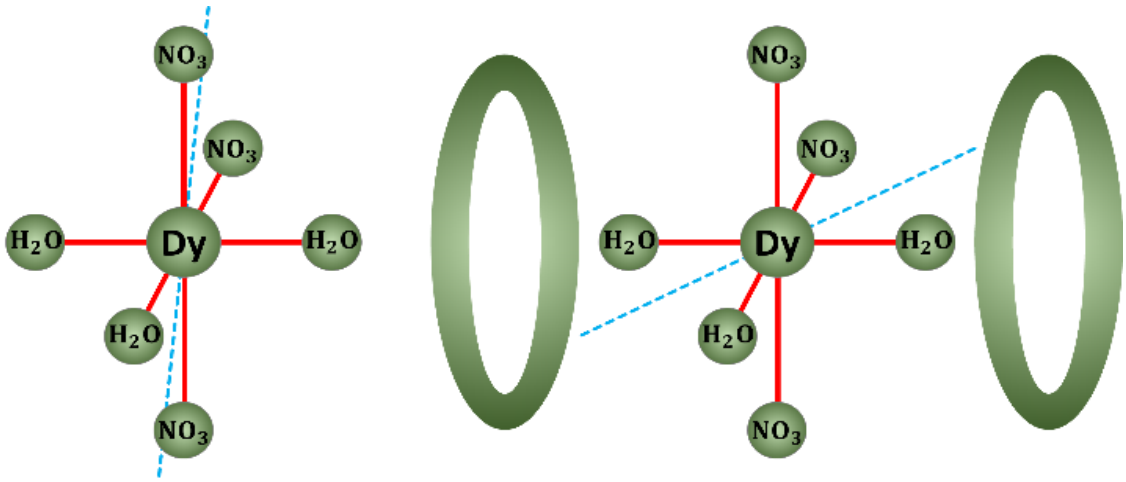

Figure 1.25: Effect of 18-crown-6 on the magnetic axis as reported by Herchel *et al.,* blue line represents the magnetic axis.

1.3.4 Other effects

Secondary interactions can influence SMMs through ways that don't directly impact the magnetic properties. For example, secondary interactions are the dominant forces behind crystal packing and the formation of supramolecular architectures, where control of these could prove beneficial in the development of future SMMs.[86,87]

Exploring this, Sushila *et al.* synthesised five mononuclear lanthanide complexes [(Nd**J8**$_2$)(Et$_3$NH)]·THF (**47**), [(Tb**J8**$_2$)(Et$_3$NH)]·THF (**48**), [(Dy**J8**$_2$)(Et$_3$NH)]·THF (**49**), [(Nd**J9**$_2$)(Et$_3$NH)]·THF/H$_2$O (**50**) and [(Tb**J9**$_2$)(Et$_3$NH)]·THF/H$_2$O **(51)**. Where H$_2$**J8** = 2-bis(2-hydroxy-3,5-dichlorobenzyl)aminomethylpyridine and H$_2$**J9** = 2-bis(2-hydroxy-3,5-dibromobenzyl)aminomethylpyridine).[88] The complexes are essentially isostructural however, only the dysprosium containing complex (**49**) showed SMM behaviour with U_{eff} of 13.45 K. A notable trend of this series is that the overall coordination environment of the magnetic centre was invariant to the halogen used. This is a result of the hydrogen/halogen bonding interplay, which controls the overall crystal packing, being largely independent of the halogen present. However, the individual molecules do show subtle variations in order to cope with the stereo-electronic requirements when different halides are present.

Schmitz *et al.* reported on the magnetic properties of two self-assembling supramolecular architectures ([Dy(OAc)$_3$(H$_2$O)$_3$][Dy(H$_2$O)$_3$(prop·SMe)$_3$][H$_2$O⊂Cr$_3$Dy$_6$(OAc)$_{12}$(H$_2$bda)$_3$(gly)$_3$(ox)$_3$(prop·SMe)$_3$]$_2$(H$_2$O))·12H$_2$O·1.5MeCN (**52**) and ([Tb(OAc)$_3$(H$_2$O)$_3$][Tb(H$_2$O)$_3$(prop·SMe)$_3$] [H$_2$O⊂Cr$_3$Tb$_6$(OAc)$_{12}$(H$_2$bda)$_3$(gly)$_3$(ox)$_3$(prop·SMe)$_3$]$_2$(H$_2$O))·11.25H$_2$O·1.5MeCN (**53**) where Hprop·SMe = 3-(methylthio)propionic acid; H$_2$bda = *N*-butyldiethanolamine; ox = oxalate^{2-}; gly = glycolate^{2-}.[89] The recorded energy barriers were 11.9 K (**52**) and 4.9 K (**53**). The overall structures of each complex have dimensions of ca. 17 × 12 Å, which is comprised of distinct molecules which self-assembled and are maintained by purely intramolecular hydrogen bonds. They postulated that the formation of the supramolecular architecture was likely templated by cooperative hydrogen bonds of a central trio of water molecules in a manner which resembles polyoxovanadate chemistry.[90]

1.4 Schiff Base Complexes

Schiff base ligands are among the most popular types of ligands used in the synthesis of 3*d*-4*f* metal complexes.[78,91-96] Schiff bases were discovered in 1864 by Hugo Schiff and are a sub-class

of imine with the general form $R_1R_2C=NR_3$ where $R_3 \neq H$.[97] They are commonly made via the condensation of a primary amine with either an aldehyde, producing an aldimine; or a ketone, producing a ketimine. This reaction proceeds by the nucleophilic addition of the amine to the carbonyl, giving an intermediate hemiaminal, which upon dehydration produces the imine. The resultant imine can be easily hydrolysed back to their initial precursors under acidic conditions. The popularity of Schiff base condensation reactions for the synthesis of 3*d*-4*f* metal complexes ligands is due to the vast variety of primary amines and carbonyl-based compounds that can be coupled, providing a huge library of potential coordination environments. On top of this, Schiff base reactions impart a lot of functionality with a single reaction, providing a simple synthetic route for researchers. Schiff bases are often classified by the number of donor atoms provided in the compound with mono-, bi-, tri-, and tetra- dentate coordination sites being the most popular (Figure 1.26).[92,98]

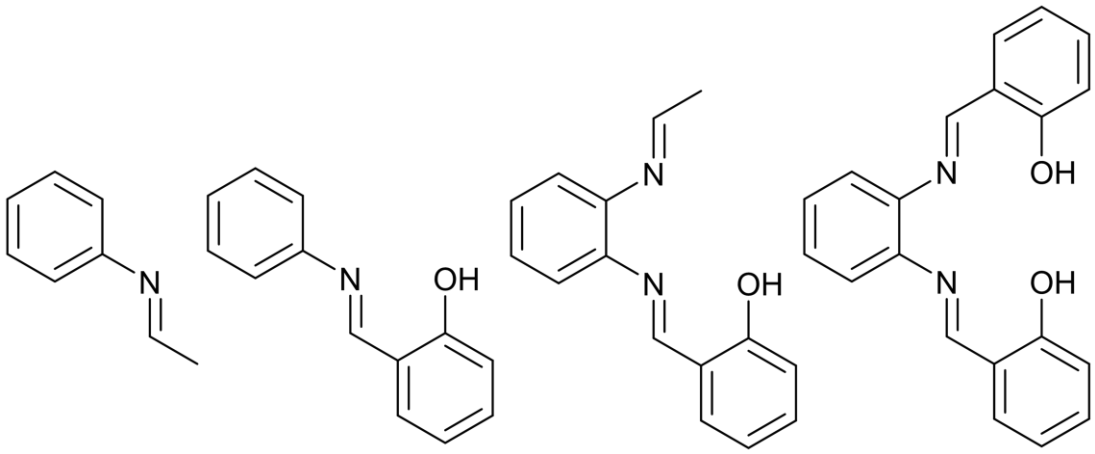

Figure 1.26: From left to right, examples of monodentate, bidentate, tridentate and tetradentate Schiff base ligands.

1.4.1 Salen/Salphen-type Schiff bases

Within the class of Schiff base ligands, salen and salphen type Schiff base ligands are among the most widely employed.[94,99] These ligands are derived from salicylaldehyde derivatives and various diamines, this produces an inner N_2O_2 coordination environment, which is ideal for binding 3*d* metal.[100]

The aromatic structure of salphen-type ligands imparts rigidity into the system, which enhances the bridging and chelating potential of the ligand allowing the formation of stable metal complexes. By utilising salicylaldehyde derivatives such as o-vanillin, an outer O_4 coordination environment can also be created, which is capable of coordinating to the larger 4*f* metal ions.[78,101,102] This allows the 3*d* and 4*f* metal ions to be bound simultaneously, with the phenolic

oxygen atoms linking the two metal centres. This type of construction was utilised by Vrablova *et al.* who synthesised a series of Ni–Ln (Ln= Ce^{III}, Gd^{III} and Dy^{III}) with a ligand formed by the Schiff base condensation of *o*-vanillin with ethylene diamine (Figure 1.27).[102]

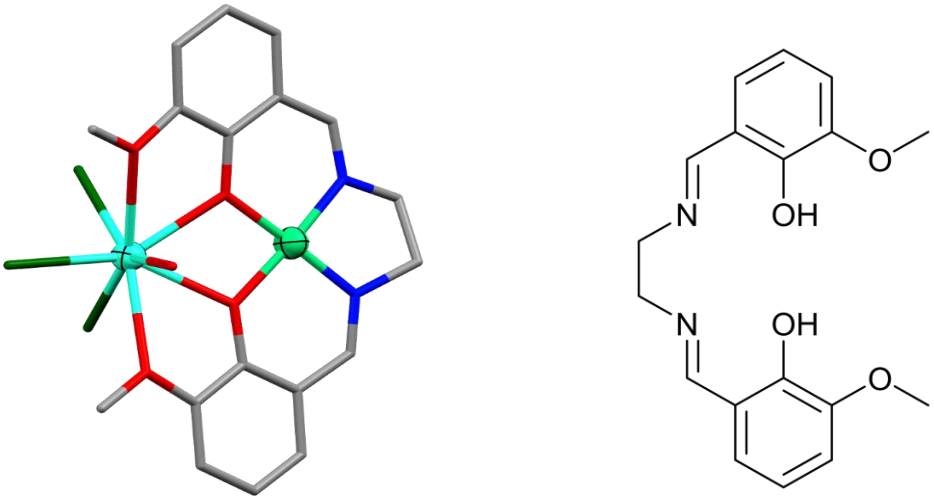

Figure 1.27: Crystal structure of the Ni-Dy complex, synthesised by Vrablova et al (left) and the corresponding ligand (right). Hydrogen atoms have been omitted for clarity. Colour code: Dy = cyan, N = light green, Cl = green, C = grey, O = red, and N = blue.

AC magnetic measurements of the resulting complexes found that all three displayed slow relaxation of magnetisation, even the isotropic Gd^{III} system. This is thought to occur due to the unsymmetric *fac* arrangement of chlorido ligands onto the Ln ion.

The Plieger group has previously utilised salicylaldehyde derivatives, specifically the 3-bromomethyl-5-*tert*-butylsalicylaldehyde subunit as a building block for the synthesis of a series of Ni^{II} based defective dicubane complexes (Figure 1.28).[103] By introducing slight structural

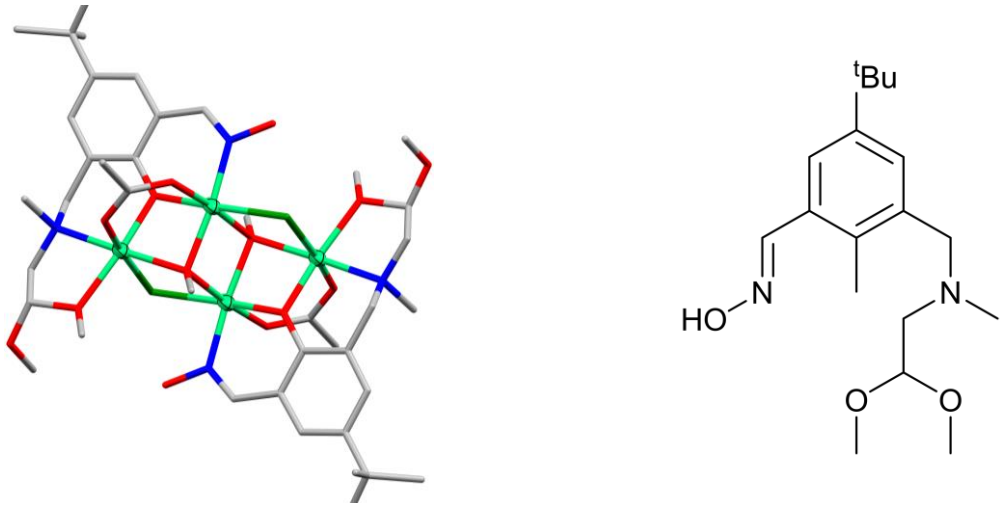

Figure 1.28: Crystal structure for a $Ni^{(II)}_4$ dicubane complex synthesised by Woodhouse (left) and the corresponding ligand (right). Hydrogen atoms have been omitted for clarity. Colour code: Ni = light green, Cl = green, C = grey, O = red, and N = blue.

changes, different coordinating anions and lattice solvent molecules, the coordination environment of subsequent complexes is altered allowing for tuning of the magnetic properties of these complexes.[104]

1.5 Research Aims

The aims of the research presented in this thesis are to investigate the effects that secondary interactions can have on the magnetic and structural properties of polynuclear metallic complexes. Particular attention is paid to how second sphere effects influenced exchange interactions between adjacent metal ions by altering the M–L–M bond angles.

Chapter 2 covers our investigation into the design of a ligand system capable of tuning the strength of secondary interactions with the initial attempts focusing on an asymmetrical 5-*tert*-butylsalicylaldehyde based structure. This design would place a *3d* and a *4f* metal in close proximity, giving a chance to elucidate the extent of any exchange interactions.

Two series of heterometallic 3*d*–4*f* complexes will be developed utilising the symmetric salphen based ligand (H_6**L1**). The salphen ligand structure explored throughout this thesis provides an attractive basis for the investigation of secondary interactions as they pertain to single molecule magnetism. The ease of functionalisation of the central diamine through either Schiff-base condensation or Suzuki coupling provides a convenient route for the tuning of secondary interactions.

Chapter 3 explores a series of nickel complexes which consist of two Ni^{II}-H_4**L1** subunits bound to a central Ln^{III} ion. The nickel ions adopt a square planar geometry which provides an opportunity to explore the magnetic and structural properties of the system, more specifically the SIM characteristics, without the effects of secondary interactions.

Chapter 4 investigates a series of complexes which utilise a square pyramidal Cu^{II} ion. This provides an avenue for investigation of secondary interactions, primarily hydrogen bonding, through different bound anions or co-ligands. Successful complexations will be characterised through SCXRD, ESI-MS, ATR-IR, TGA and magnetic analyses to determine the physical, structural, and magnetic properties of the systems.

Chapter 5 briefly covers the attempts made to synthesise complexes involving other transition metal ions, namely Co^{II}, Zn^{II}, $Fe^{II/III}$, and Mn^{II}. However, most of these attempts failed to produce any complexes detectable through the mentioned analyses whilst reactions between H_6**L1** and Mn^{II} resulted in the hydrolysis of the ligand. Chapter 5 also covers our research into a second,

bulkier, salphen-based ligand (H_6**L2**), which will be developed and put through an identical complexation and characterisation process to investigate the effect that other secondary interactions such as π-π stacking and steric effects will have on these systems (Figure 1.29).

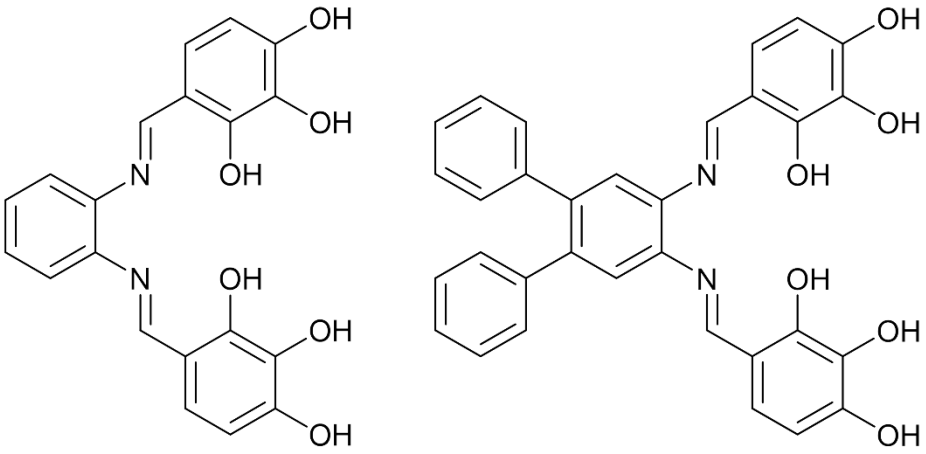

Figure 1.29: Structure of the two ligands H_6**L1** (left) and H_6**L2** (right) investigated throughout the course of this thesis.

Chapter 2

Ligand Design and Synthesis

2.1 General Details

All starting materials and analytical grade solvents obtained from commercial sources were used without purification unless otherwise stated. MeOH was dried according to the procedure of Lund and Bjerrum then stored over 3 Å molecular sieves for a week prior to use.[105] THF was passed through alumina columns then stored over 3 Å molecular sieves for a week prior to use. All reactions were carried out under ambient conditions in acetone washed glassware unless otherwise stated. All complexation and crystallisation attempts were performed at RT in ambient conditions, unless otherwise stated.

All organic compounds have been characterised by ^{1}H NMR, ESI-MS/HR-MS, MP, and ATR-IR where possible with new organic compounds fully characterised with ^{1}H, ^{13}C, COSY, HMQC, and HMBC spectra. The metallic complexes have been characterised by a combination of SCXRD, ATR-IR, ESI-MS/HR-MS, CHN elemental analysis, TGA, MP, and magnetic susceptibility measurements. A number of the complexes reported in this thesis have only been characterised by SCXRD and ESI-MS due to the small amount of material produced.

All NMR spectra were collected at RT on a Bruker-500 Avance instrument, with the ^{1}H shift of the solvent used as an internal standard. ESI-MS spectra were collected on a Dionex UltiMate 3000. HR-MS were collected on a ThermoScientific Q Exactive Focus Hybrid Quadrupole-Orbitrap Mass Spectrometer. ATR-IR spectra were collected on a Nicolett 5700 IR using a diamond ATR sampling accessory. Melting point measurements were collected on a Gallenkamp melting point apparatus and are uncorrected. CHN elemental analysis was collected by the Elemental Microanalysis Service, Department of Molecular Sciences, Macquarie University.

Single crystal X-ray data were collected on a Bruker D8 Venture equipped with a IμS 3.0 Microfocus Cu-Kα source (λ = 1.54178 Å) and a PHOTON III detector. Crystals were mounted on MiTeGen mylar loops using Fomblin Y oil and cooled to 100 K using an Oxford cryostream 800. The data was collected and processed using the APEX4 software. The structures were solved using SHELXT and refined using SHELXL within Olex2.[106-109] All non-hydrogen atoms were refined

anisotropically whilst hydrogen atoms were calculated at their ideal positions and refined using a riding model with fixed U_{iso} values.

Magnetic measurements were carried out by Prof. Takayuki Ishida at Tokyo University of Electro Communications, Chofugaoka, Japan. The DC and AC magnetic susceptibilities were measured on a Quantum Design MPMS3 SQUID magnetometer. The susceptibility data were acquired at 500 Oe in a temperature range from 1.8 to 300 K. The magnetisation was recorded at 0 – 7 T and 1.8 K. To avoid a torquing effect, the Gd-containing specimens were fixed with a small amount of eicosane. The magnetic responses were corrected with diamagnetic blank data of a gelatin capsule sample holder and eicosane matrix, measured separately, and further diamagnetic contributions were estimated from Pascal's constants. The AC susceptibility was recorded with frequencies of 1 to 1 kHz, and the temperature dependence was measured on a heating mode.

2.2 Ligand Design

The primary goal of this research was to determine whether secondary interactions could influence the magnetic properties of a series of *3d*/*4f* heterometallic complexes. This would involve the use of intramolecular hydrogen bonding and steric bulk interactions to constrain the M–L–M bond angle. Reducing this bond angle closer to the idealised 90° will promote ferromagnetic exchange, which is predicted to effectively quench QTM, thus enhancing the magnetic properties of any resultant complexes. [18,39]

The synthetic challenge of this research lies in the need to minimise the M–L–M bond angle, which would appear to preclude the use of the typical symmetrical salen/salphen type ligands reported in the literature.[110-113] This is due to the typical inner-outer coordination motif necessitating the hydrogen bonding groups to be located where their interactions would result in an increase in the M–L–M bond angle due to the 'squeezing' of the complex (Figure 2.1).

The first potential solution to this problem identified and pursued, was the development of an asymmetric ligand. This ligand could be designed such that it possesses two distinct 'arms', with one arm containing the *3d* binding pocket, and a second arm containing the *4f* binding pocket. Positioning of the hydrogen bonding groups on the ends of these arms would then result in the 'closing' of the complex thus reducing the M–L–M bond angle (Figure 2.2).

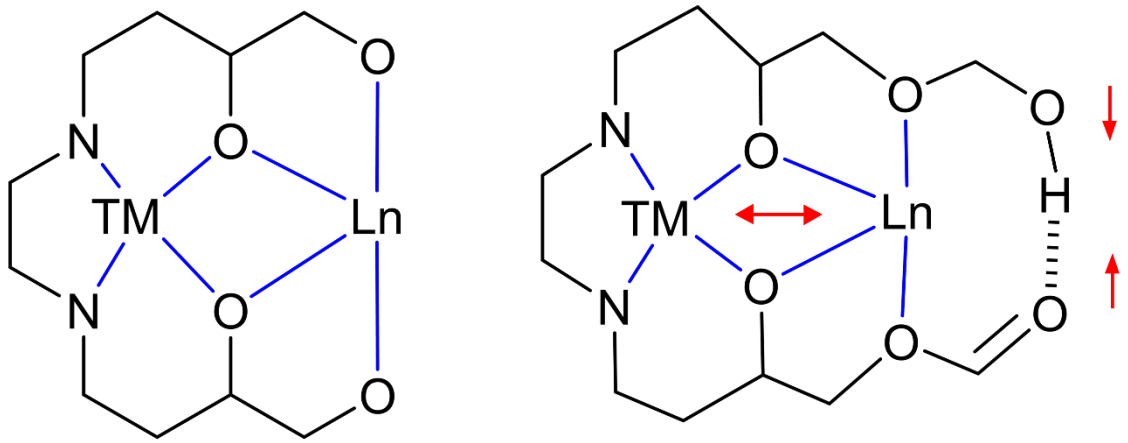

Figure 2.1: Hypothetical schematic showing the potential increase in M-L-M bond angle due to the addition of hydrogen bonding groups for a salen/salphen type ligand.

A second approach utilising heteroleptic complexes was identified as another potential avenue to explore. A major advantage of this approach is that the typical inner/outer coordination motif of salen/salphen type ligands is applicable, as hydrogen bonding interactions between a 'main' ligand and an 'auxiliary' ligand can result in the desired reduction in M–L–M bond angle. This would require careful design of the ligand scaffold as a flexible ligand would allow the metal centres to dictate the binding geometries. Having a rigid ligand will allow the secondary interactions to constrain the metal centres (Figure 2.3). An additional advantage of this approach

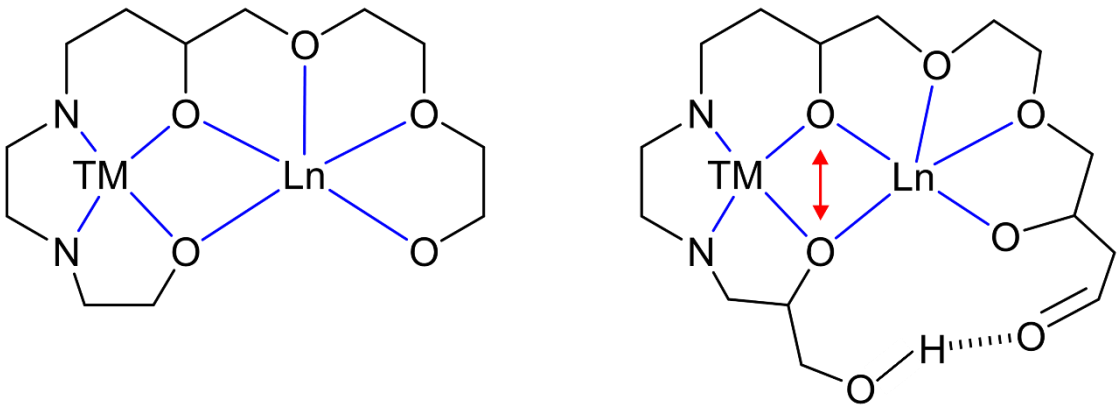

Figure 2.2: Hypothetical schematic showing the potential decrease in bond angle for an asymmetric ligand with the addition of hydrogen bonding groups.

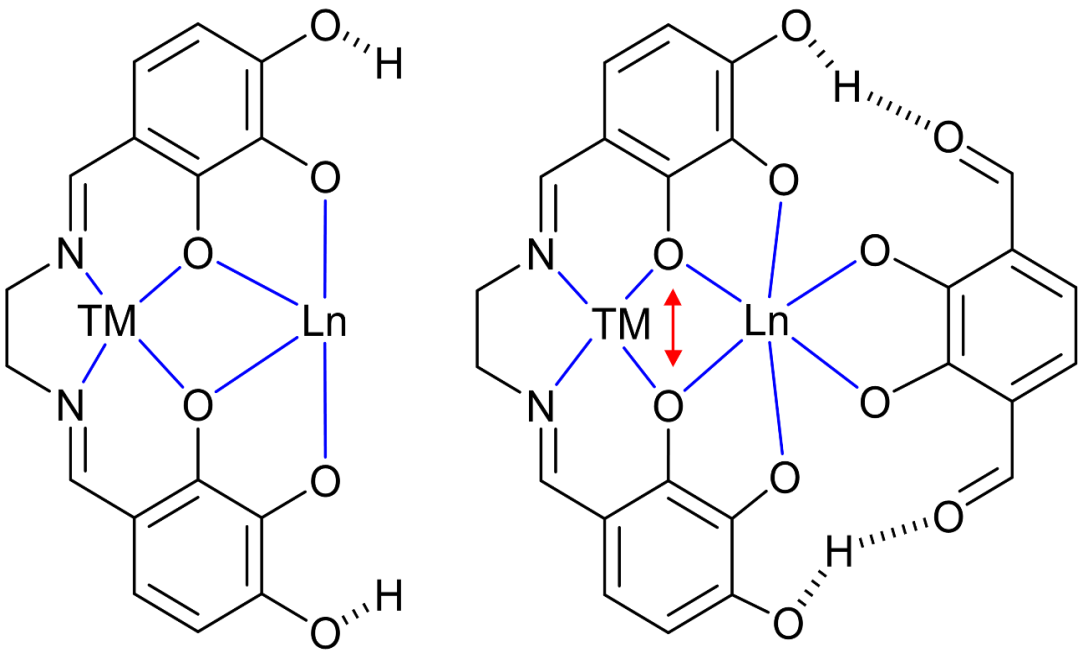

Figure 2.3: Hypothetical schematic showing the potential decrease in M-L-M bond angle through hydrogen bonding of a heteroleptic complex.

is the simpler synthesis required when compared with the asymmetric approach. This has the added benefit of providing a relatively simple means of adding functionality to the ligand systems that can increase the effects of secondary interactions.

2.2.1 Asymmetric Ligand Approach

The design for the asymmetric ligand was split into three subunits, which were synthesised separately before being combined to make the final ligand. The first subunit was based on 4-*tert*-butylphenol as previous work within the Plieger group has shown its suitability as a scaffold for asymmetric functionalisation.[104,114,115] *ortho*-Formylation of the phenol was followed by methyl bromination resulting in a two-armed compound capable of a Schiff base condensation reaction on one arm and a Williamson ether on the other, providing an asymmetric final ligand.

Synthesis of 3-Bromomethyl-5-*tert*-butylsalicylaldehyde Subunit

5-*tert*-Butylsalicylaldehyde (1)

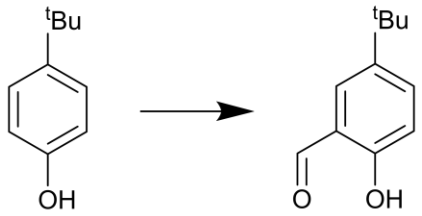

1

Adapted from the procedures of Aldred *et al.* and Woodhouse *et al*.[104,116] Dry magnesium turnings (15.03 g, 0.62 mol) were added to a stirred solution of anhydrous MeOH (60 mL), toluene (140 mL), and 8% magnesium methoxide solution (100 mL) and was refluxed overnight. 4-*tert*-Butylphenol (162.02 g, 1.08 mol) in toluene (110 mL) was added and the reaction mixture refluxed for an additional three hours. Toluene (100 mL) was added followed by fractional distillation of a MeOH/toluene azeotrope under reduced pressure, until the reaction mixture resembled a thick slurry. Additional toluene (100 mL) was added followed by a paraformaldehyde slurry (95.19 g, 3.17 mol) in toluene (200 mL) that was added piecewise over two hours, with volatile by-products being removed by vacuum distillation between aliquots. Toluene (200 mL) was added to the reaction mixture and left to stir overnight at 85 °C under argon, producing a thick yellow mixture. An aqueous solution of 30% H_2SO_4 was added dropwise to the reaction mixture over an hour followed by vigorous stirring for a further three hours, forming two yellow layers. The aqueous layer was extracted with toluene (3 x 150 mL), the combined organic layers were washed with aqueous 10% H_2SO_4 and deionised H_2O (2 x 200 mL), dried over anhydrous $MgSO_4$, and concentrated *in vacuo* producing crude **1** (181.22 g, 1.04 mol) as a brown oil. This oil was found to be of sufficient quality to proceed to the next reaction. A small amount (5.00 g) was further purified by silica gel chromatography eluting with 4:1 *n*-Hex:EtOAc, (R_f = 0.75) yielding pure **1** as a light yellow oil (2.56 g, 0.017 mol, 51.2%). The ^{1}H NMR spectrum agreed with the literature values[116] (500 MHz, $CDCl_3$): δ 10.91 (1H, s, Ar-O**H**), 9.90 (1H, s, C**H**=O), 7.60 (1H, dd, J_1 = 8.8 Hz, J_2 = 2.5 Hz, Ar-**H**), 7.52 (1H, d, J = 2.5 Hz, Ar-**H**), 6.95 (1H, s, Ar-**H**), 1.35 (9H, s, ^{t}Bu) ppm. ESI-MS: *m*/*z* 179.23 [**1**+H]$^+$.

3-Bromomethyl-5-*tert*-butylsalicylaldehyde (2)

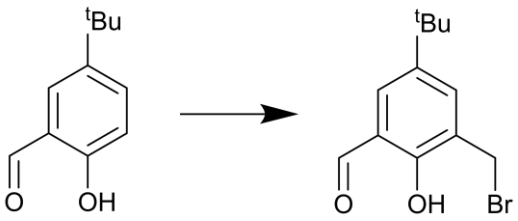

1 **2**

Adapted from the procedure of Wang *et al*.[117] **1** (51.15 g, 0.287 mol, 1 eq.), aqueous HBr (48%, 118 mL, 2,15 mol, 7.5 eq.), and paraformaldehyde (12.92 g, 0.43 mol, 1.5 eq.) were added together and stirred at 0 °C for one hour. Conc. H_2SO_4 (5 mL) was very slowly added dropwise at 0 °C with stirring until a yellow colour persisted, then the mixture was refluxed for 20 hours at 70 °C. After cooling to RT, deionised H_2O (200 mL) was added. The aqueous layer was extracted with DCM (3 x 200 mL) and the combined organic layers dried over anhydrous $MgSO_4$ and concentrated *in vacuo* to produce crude **2** as a brown oil (50.68 g, 0.187 mol, 65.2%). The crude product was recrystallised from hot pentane (10% w/v) yielding pure **2** as yellow block shaped crystals (47.70 g, 0.176 mol, 61.3 %). The ^{1}H NMR spectrum agreed with the literature values[117] (500 MHz, $CDCl_3$): δ 11.32 (1H, s, Ar-OH), 9.89 (1H, s, C**H**=O), 7.64 (1H, d, *J* = 2.2 Hz, Ar-**H**), 7.51 (1H, d, *J* = 2.2 Hz, Ar-**H**), 4.95 (2H, s, C**H**$_2$-Br), 1.34 (9H, s, ^{t}Bu) ppm. ATR-IR: $\overline{\nu}$ = 3026, 2966, 2869, 1652, 1480, 1471, 1458, 1436, 1396, 1380, 1363, 1319, 1291, 1274, 1212, 1136, 1111, 1032, 1003, 927, 891, 877, 824, 766, 742, 717, 653, 585, 519, 476 cm^{-1}. ESI-MS: *m*/*z* 294.72 [**2**+H]$^+$.

Synthesis of 2-((3-(2-Hydroxyethoxy)naphthalen-2-yl)oxy) acetic acid subunit

The second subunit was based on 2,3-dihydroxynaphthalene, each hydroxyl then underwent a separate Williamson ether reaction which added an ethyl alcohol to one and a carboxylic acid functional group to the other. A common difficulty encountered when producing heterometallic *3d*/*4f* complexes is that both *3d* and *4f* are classified as 'hard' acids, meaning they preferentially bind to similar donor atoms. A common way to overcome this issue is by developing binding pockets with rigid size constraints. Additionally, whilst *3d* and *4f* ions are both 'hard' acids, it is well documented that *4f* ions tend to be oxophilic, whilst *3d* ions commonly bind with a large variety of donor atoms. This subunit, with its large binding pocket and plethora of oxygen atoms was intended to provide a binding site for a lanthanide ion.

3-(2-Hydroxyethoxy)naphthalen-2-ol (3)

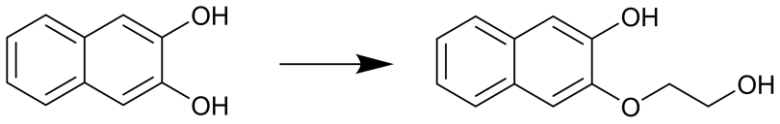

3

Adapted from the procedure of Jain *et al*.[118] K_2CO_3 (31.03 g, 0.22 mol, 7.5 eq.) was added to a solution of 2,3-dihydroxynaphthalene (4.81 g, 0.030 mol, 1 eq.) in acetonitrile (200 mL). 2-Chloroethanol (4.15 g, 3.66 mL, 0.030 mol, 1 eq.) was added dropwise at 70 °C. The resulting solution was stirred at reflux for five hours before cooling to RT and filtering off a purple solid. The solid was suspended in deionised H_2O (200 mL) and aqueous HCl (15%) added dropwise until a yellow colour persisted. This solid was collected by vacuum filtration to afford pure **3** as a yellow powder (3.91 g, 0.019 mol, 63.5%). The ^{1}H NMR spectrum agreed with the literature values[118] (500 MHz, D_2O): δ 7.69 (1H, d, J = 8 Hz, Ar-**H**), 7.58 (1H, d, J = 8 Hz, Ar-**H**), 7.29 (1H, t, 7.9 Hz, Ar-**H**), 7.21 (1H, s, Ar-**H**), 7.20 (1H, d, *J* = 7 Hz, Ar-**H**), 6.93 (1H, s, Ar-**H**), 4.20 (2H, t, *J* = 4.3 Hz, C**H**$_2$-OH), 4.02 (2H, d, *J* = 3.9 Hz, C**H**$_2$-O) ppm. ATR-IR: $\overline{\nu}$ = 3674, 3362, 2989, 2358, 1630, 1604, 1533, 1514, 1489, 1463, 1450, 1437, 1415, 1384, 1364, 1331, 1268, 1249, 1234, 1181, 1175, 1118, 1077, 1039, 951, 932, 910, 891, 871, 856, 751, 740, 618, 481 cm^{-1}. ESI-MS: *m*/*z* 203.51 [**3**-H]$^-$. MP = 163 °C.

2-((3-(2-Hydroxyethoxy)naphthalen-2-yl)oxy)acetic acid (4)

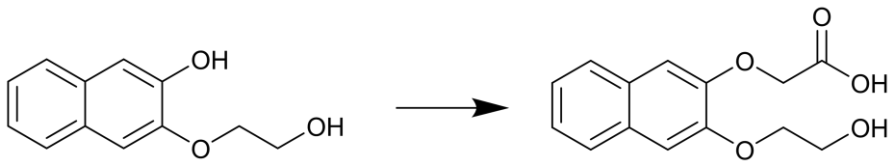

3 **4**

Adapted from the procedure of Sharghi *et al*.[119] To a stirred suspension of **3** (2.12 g, 0.010 mol, 1 eq.) in deionised H_2O (100 mL), 2-chloroacetic acid (4.88 g, 0.052 mol, 5 eq.), and aqueous NaOH (20%, 20 mL, 0.1 mol, 10 eq.) were added. The resulting mixture was refluxed at 110 °C for 24 hours before cooling to RT yielding a dark red solution. Aqueous HCl (15%) was added dropwise to the solution until a ppt formed and the solution turned colourless. The ppt was collected by vacuum filtration to afford pure **4** as a light red powder (2.01 g, 7.66 mmol, 76.7%). The ^{1}H NMR spectrum (500 MHz, DMSO-d_6): δ 13.03 (1H, s, O=C-O**H**), 7.73 (1H, d, J = 7.1 Hz, Ar-**H**), 7.70 (1H, d, 7.1 Hz, Ar-**H**), 7.34 (1H, s, Ar-**H**), 7.31 (2H, t, J = 3.8 Hz, Ar-**H**), 7.19 (1H, s, Ar-**H**), 4.82 (2H, s, O-C**H**$_2$-COOH), 4.12 (2H, t, *J* = 5Hz, C**H**$_2$-OH), 3.81 (2H, d, *J* = 5 Hz, C**H**$_2$-O) ppm. ATR-IR: $\overline{\nu}$ = 3674, 3450, 2989, 2900, 2358, 1733, 1627, 1601, 1511, 1481, 1452, 1435, 1404, 1394, 1383, 1265, 1253, 1215, 1186, 1163, 1119, 1078, 1066, 1045, 931, 879, 855, 756, 620, 479 cm^{-1}. ESI-MS: *m*/*z* 261.16 [**4**-H]$^-$. MP = 155 °C.

Synthesis of (*E*)-3-(((2-Aminophenyl)imino)methylbenzene-1,2-diol subunit

The final subunit was a simple one step Schiff base condensation, where the use of water as a solvent ensured only a single addition of the catechol. The smaller binding pocket combined with the nitrogen donors increases the selectivity of this binding site towards transition metals.

(*E*)-3-(((2-Aminophenyl)imino)methyl)benzene-1,2-diol (5)

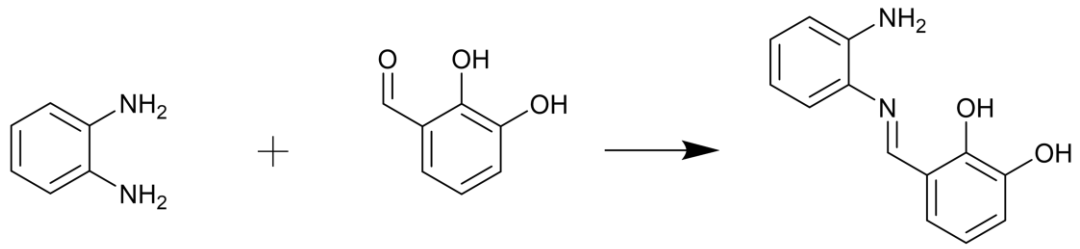

5

Adapted from the procedure of Rao *et al*.[92] A solution of 2,3-dihydroxybenzaldehyde (1.38 g, 0.010 mol, 1 eq.) in deionised H_2O (100 mL) was added dropwise to a solution of 1,2 phenylenediamine (1.08 g, 0.010 mol, 1 eq.) in deionised H_2O with stirring for 30 minutes. The resultant orange ppt was collected via vacuum filtration affording pure **5** as an orange powder (2.26 g, 9.9 mmol, 98%). The ^{1}H NMR spectrum (500 MHz, DMSO-d_6): δ 12.97 (1H, s, Ar-O**H**), 9.17 (1H, s, Ar-O**H**), 8.80 (1H, s, N=C**H**), 7.13 (1H, d, *J* = 7.8 Hz, Ar-**H**), 7.10 (1H, d, *J* = 7.8 Hz, Ar-**H**), 7.01 (1H, t, *J* = 7.4 Hz, Ar-**H**), 6.93 (1H, d, *J* = 7.8 Hz, Ar-**H**), 6.78 (1H, d, *J* = 7.5 Hz, Ar-**H**), 6.77 (1H, t, *J* = 7.6 Hz, Ar-**H**), 6.62 (1H, t, *J* = 7.4 Hz, Ar-**H**), 5.05 (2H, s, N**H**$_2$) ppm. ATR-IR: $\overline{\nu}$ = 3674, 3394, 3314, 2989, 2900, 2606, 2358, 1616, 1571, 1485, 1458, 1394, 1283, 1272, 1242, 1189, 1162, 1154, 1074, 1032, 951, 926, 873, 836, 798, 780, 753, 734, 585, 471 cm^{-1}. ESI-MS: *m*/*z* 229.02 [**5**+H]$^+$. MP = 160 °C.

Synthesis of 2-((3-(2-((5-(*tert*-butyl)-3-(((2-((*E*)-(2,3-Dihydroxybenzylidene) amino)phenyl)imino)methyl)-2-hydroxybenzyl)oxy)ethoxy)naphthalen-2-yl)oxy)acetic acid ligand

Synthesis of the final ligand began with another Williamson ether reaction as the presence of the alkyl bromide would interfere with the required Schiff base condensation. This reaction proved successful with the pure product verified by ^{1}H NMR and ESI-MS analysis. Attempts at performing the final Schiff base condensation necessary proved unsuccessful, with only trace amounts of the desired product detected by ESI-MS. Several months were spent trying various reaction conditions and purification attempts to no avail. This resulted in the research pivoting from a single ligand approach to a ligand / co-ligand approach.

2-((3-(2-((5-(*tert*-Butyl)-3-formyl-2-hydroxybenzyl)oxy)ethoxy)naphthalen-2-yl) oxy)acetic acid (6)

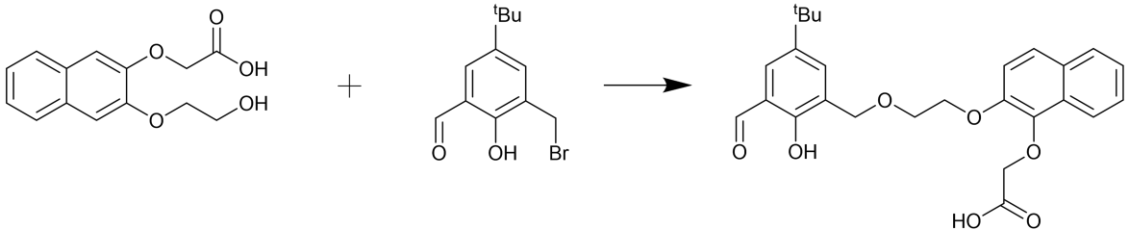

2 **4** **6**

A solution of **2** (2.75 g, 0.010 mol, 1 eq.) in dry THF (150 mL) was added dropwise to a suspension of **4** (2.70 g, 0.010 mol, 1 eq.) and NaH (2.40 g, 0.10 mol, 10 eq.) in dry THF (50 mL), and stirred at RT under argon for 48 hours. The resulting mixture was cooled to 0 °C then deionised H_2O (150 mL) was slowly added affording a light-yellow solution. The THF was removed under reduced pressure, cooled to 0 °C then aqueous HCl (15%) was added dropwise to this solution until a ppt formed and a loss of colour detected. The resultant precipitate was filtered off affording crude **6** as a dark orange solid (3.10 g, 6.85 mmol, 67%). The crude product was purified by silica gel chromatography eluting with 4:1 EtOAc:*n*-hex affording pure **6** as a light-yellow product (1.90 g, 4.20 mmol, 42%). The ^{1}H NMR spectrum (500 MHz, DMSO-d_6): δ 13.02 (1H, s, O=C-O**H**), 10.89 (1H, s, Ar-O**H**), 10.06 (1H, s, O=C**H**), 7.70-7.73 (4H, m, Ar-**H**), 7.37 (1H, s, Ar-**H**), 7.31 (2H, t, *J* = 3.8 Hz, Ar-**H**), 7.20 (1H, s, Ar-**H**), 4.80 (2H, s, O-C**H**$_2$-COOH), 4.67 (2H, s, O-C**H**$_2$-Ar), 4.30 (2H, t, *J* = 4.8 Hz, CH_2-O-C**H**$_2$), 3.92 (2H, d, *J* = 4.5 Hz, C**H**$_2$-O-Ar) ppm. ATR-IR: $\overline{\nu}$ = 3675, 2989, 2960, 2922, 1602, 1508, 1483, 1461, 1404, 1394, 1363, 1325, 1254, 1168, 1118, 1066, 1057, 850, 744, 619, cm^{-1}. ESI-MS: *m*/*z* 475.15 [**6**+Na]$^{+}$. MP = 135 °C.

2-((3-(2-((5-(*tert*-Butyl)-3-(((2-((*E*)-(2,3-dihydroxybenzylidene)amino)phenyl)imino)methyl)-2-hydroxybenzyl)oxy)ethoxy)naphthalen-2-yl)oxy)acetic acid (7)

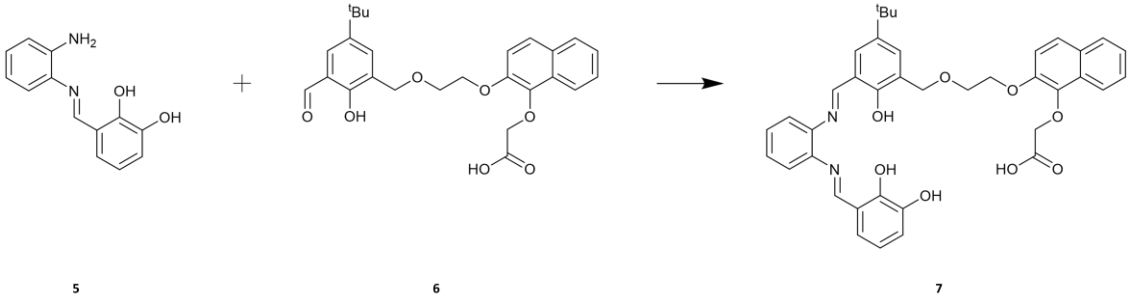

5 6 7

To a stirred solution of **5** (1.51 g, 6.62 mmol, 1.2 eq.) in anhydrous THF (20 mL) was added a solution of **6** (2.47 g, 5.46 mmol, 1.2 eq.) in anhydrous THF (60 mL). The reaction mixture was refluxed for five hours, cooled to RT, and concentrated *in vacuo*. THF (3 mL) and Et_2O (150 mL) were then added to the reaction mixture, and the resulting ppt collected by vacuum filtration, washed with Et_2O affording a bright red powder (2.02 g, 3.05 mmol, 46%). Presence of the desired product was detected by ESI Mass Spectrometry however later attempts of purification were ineffective. ESI-MS: *m/z* 685.14 [**7**+Na]$^+$.

2.2.2 Heteroleptic Approach

The heteroleptic approach was devised to provide a simpler synthetic route to achieve the desired ligand functionality at the cost of providing a potentially more challenging environment for complexation. This approach consists of a primary ligand and an auxiliary ligand. The primary ligand would bind to the metal centres whilst the auxiliary ligand would possess functional groups capable of providing or enhancing the secondary interactions of any synthesised complexes. The first attempt of this approach utilised compounds and syntheses developed during research into the initial ligand design. The primary ligand underwent Schiff base condensation with a more standard procedure to ensure double addition of the diphenol. The auxiliary ligand underwent Williamson ether synthesis adding two carboxylic acid functional groups.

3,3'-[1,2-Phenylenebis(nitrilomethylidyne)]bis[1,2-benzenediol] (8)

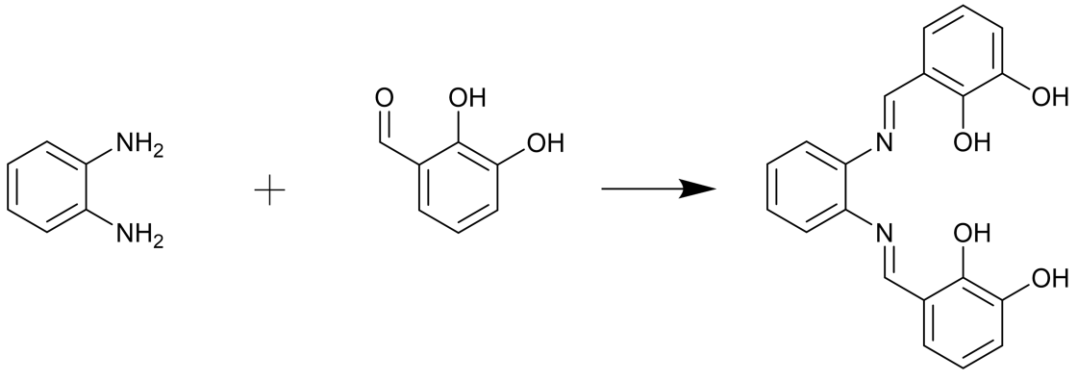

8

Adapted from the procedure of Reyes-Guitierrez *et al*.[120] A solution of 2,3-dihydroxybenzaldehyde (0.55 g, 3.98 mmol, 2 eq.) in anhydrous MeOH (5 ml) was added dropwise to a stirred solution of 1,2 phenylenediamine (0.23 g, 2.13 mmol, 1 eq.) in anhydrous MeOH (5 mL). The resulting mixture was refluxed at 80 °C for four hours, cooled to room temperature and concentrated *in vacuo*. To the resulting solid was added MeOH (5 mL) and Et_2O (100 mL) then sonicated for one minute. The ppt was collected by vacuum filtration, washed with Et_2O (60 mL) then air dried, affording **8** as a bright orange solid (0.63 g, 1.81 mmol, 91%). The ^1H NMR spectrum agreed with the literature values[120] (500 MHz, DMSO-d_6): δ 12.90 (2H, s, Ar-O**H**), 9.26 (2H, s, Ar-O**H**), 8.88 (2H, s, N=C-**H**), 7.41 (4H, m, Ar-**H**), 7.11 (2H, d, Ar-**H**), 6.94(2H, d, *J* = 7.6 Hz, Ar-**H**), 6.78 (2H, t, *J* = 7.6 Hz, Ar-**H**) ppm. ATR-IR: $\overline{\nu}$ = 3464, 3052, 2988, 1623, 1612,

1463, 1364, 1273, 1206, 1194, 1177, 1102, 1075, 1029, 980, 963, 879, 863, 844, 828, 771, 732, 712, 591, 574, 561, 519 cm^{-1}. ESI-MS: *m/z* 349.30 [**8**+H]$^+$. MP = 187 °C.

2,2'-(Naphthalene-2,3-diylbis(oxy))diacetic acid co-ligand (9)

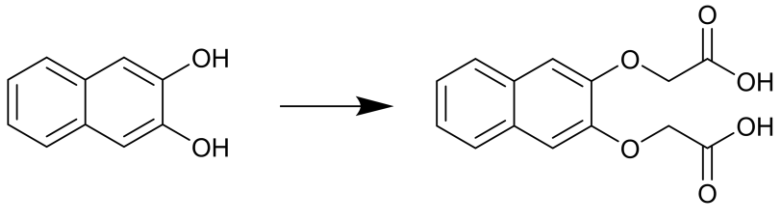

9

Adapted from the procedure of Sharghi *et al*.[119] To a stirred mixture of 2,3-dihydroxynaphthalene (5.63 g, 0.035 mol, 1 eq.) and 2-chloroacetic acid (13.55 g, 0.143 mol, 4 eq.) in deionised H_2O (50 mL) at 90 °C was added a solution of aqueous NaOH (34.20 g, 100 mL, 0.855 mol, 24 eq.). The reaction mixture was heated at 90 °C for two hours before cooling to 0 °C in an ice bath. Aqueous HCl (20%) was added dropwise to the reaction mixture until a ppt formed. The ppt was collected by vacuum filtration and washed with cold water to afford **9** as a pale brown solid (6.18 g, 0.022 mol, 63%). The ^{1}H NMR spectrum agreed with the literature values[119] (500 MHz, DMSO-d_6): δ 7.63 (2H, d, J = 8 Hz, Ar-**H**), 7.30 (2H, t, *J* = 7.9 Hz, Ar-**H**), 7.22 (2H, s, Ar-**H**), 4.50 (2H, s, COO**H**) 5.77 (4H, s, O-C**H**$_2$) ppm. ATR-IR: $\overline{\nu}$ = 3675, 3609, 3512, 3287, 2989, 2900, 2358, 2342, 1617, 1601, 1581, 1550, 1497, 1443, 1384, 1325, 1259, 1188, 1172, 1089, 1066, 1028, 1005, 870, 784, 755, 712, 631, 579, 538 cm^{-1}. ESI-MS: *m/z* 275.09 [**9**-H]$^-$. MP = 334 °C.

o-Phenylenediamine co-ligand complexation attempts

A solution of $CuCl_2$ (2 eq.) in MeOH (5 mL) was added to a stirred solution of H_6**L1** (2 eq.) in MeOH (5 mL) and heated to 50 °C for 30 minutes. A solution of $LnCl_3.6H_2O$ (1 eq.) in MeOH (5 mL) was added followed by addition of *o*-Phenylenediamine (4 eq.) then stirred for a further 30 minutes at 50 °C before filtering. Vapour diffusion of Et_2O into the filtrate over three weeks afforded crystals suitable for X-ray diffraction.

o-Phenylenediamine was one of many species utilised as a potential auxiliary ligand, however it was the only one that an X-ray crystal structure was obtained for. This reaction did not yield the desired complex, instead two molecules of *o*-phenylenediamine reacted with acetone to form 2-dimethyl-1,2'-imidazo[4,5-*b*]phenazine through a two-step reaction (Scheme 1). The first step involved the condensation of two molecules of *o*-phenylenediamine in the presence of $CuCl_2$ to form 2,3-diaminophenazine.[121] 2,3-diaminophenazine then reacted with acetone in the presence of acid to form dimethyl-1,2'-imidazo[4,5-*b*]phenazine.[122]

The lack of successful complexations utilising the heteroleptic approach resulted in the focus on anion metathesis covered in Chapter 4.

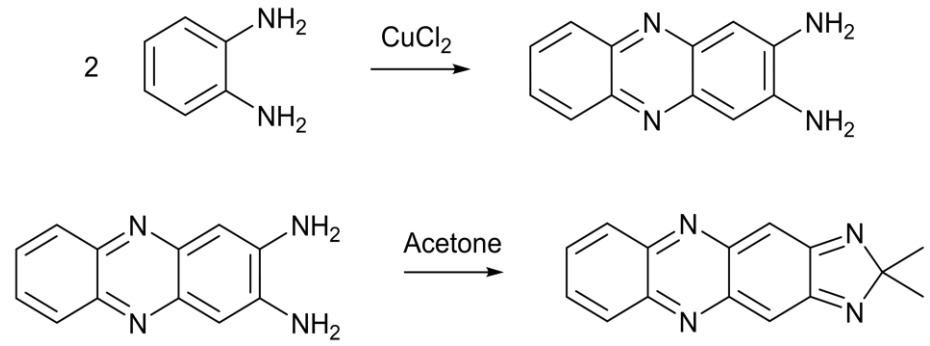

Scheme 1: Proposed reaction scheme for the synthesis of 2-dimethyl-1,2'-imidazo[4,5-*b*]phenazine.

2.2.3 Synthesis of H_6**L1**

A second primary ligand, H_6**L1**, was synthesised concurrently with the first, this possessed two additional hydroxy groups, enriching the second coordination sphere with potential H-bond donors. H_6**L1** was synthesised through the formylation of 2,3,4-trihydroxybenzaldehyde followed by a Schiff base condensation with *o*-phenylenediamine. Complexations attempts of H_6**L1** in the presence of the auxiliary ligand **(9)** produced trinuclear complexes with an absence of **(9)**. When coordinating, the ligand is in the form H_4**L1**$^{2-}$ with a transition metal ion bound to the two imine nitrogen atoms and two bridging phenolate oxygen atoms which are also bound to a central lanthanide ion. The lanthanide ion is also coordinated to two phenol oxygens. A second H_4**L1**$^{2-}$ ligand and transition metal subunit is also bound to the lanthanide ion, producing a complex with the general form of H_4**L1**$_2$:TM_2:Ln1 (Figure 2.4).

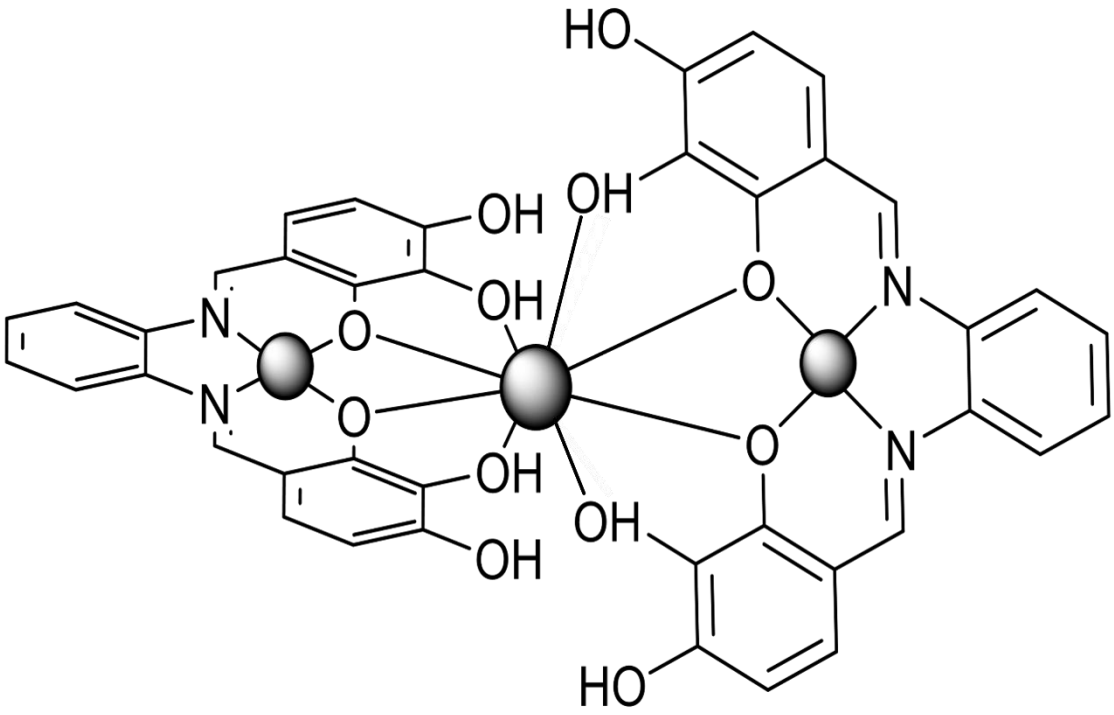

Figure 2.4: Diagram showing the coordination mode of a typical complex synthesised utilising H_6**L1.**

2,3,4-Trihydroxybenzaldehyde (10)

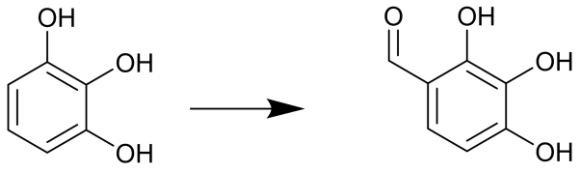

10

Adapted from the procedure of Zelazkova *et al*.[123] Anhydrous $AlCl_3$ (21.15 g, 0.158 mol, 2 eq.) was dissolved in EtOAc (330 mL) under argon. After cooling of the reaction mixture to 0 °C, pyrogallol (10.01 g, 0.079 mol, 1 eq.) and $HC(OEt)_3$ (39.6 mL, 0.238 mol, 3 eq.) were added then stirred for 30 minutes at 0 °C resulting in a bright red solution. Pre-cooled aqueous HCl (10%, 100 mL) was added to the reaction mixture. The aqueous layer was separated then washed with Et_2O (3 x 120 mL), the combined organic layers were washed with brine (5 x 100 mL), dried over anhydrous $MgSO_4$, filtered, and concentrated *in vacuo*, affording **10** as light beige crystals (8.03 g, 0.052 mol, 66%). The ^{1}H NMR spectrum agreed with the literature values[123] (500 MHz, $CDCl_3$): δ 11.39 (1H, s, Ar-O**H**), 9.71 (1H, s, O=C**H**), 7.10 (1H, d, *J* = 8.6 Hz, Ar-**H**), 6.63 (1H, d, *J* = 8.6 Hz, Ar-**H**), 6.21 (1H, s, Ar-O**H**), 5.78 (1H, s, Ar-O**H**) ppm. ATR-IR: $\overline{\nu}$ = 3337, 3110, 1643, 1616, 1520, 1503, 1450, 1395, 1279, 1242, 1221, 1198, 1163, 1085, 982, 798, 790, 721, 687, 667, 638, 633, 561 cm^{-1}. ESI-MS: *m*/*z* 155.02 [**10**+H]$^+$. MP = 152 °C.

N,N'-bis-2,3,4-trihydroxybenzylidene-1,2-phenylendiamine (11)

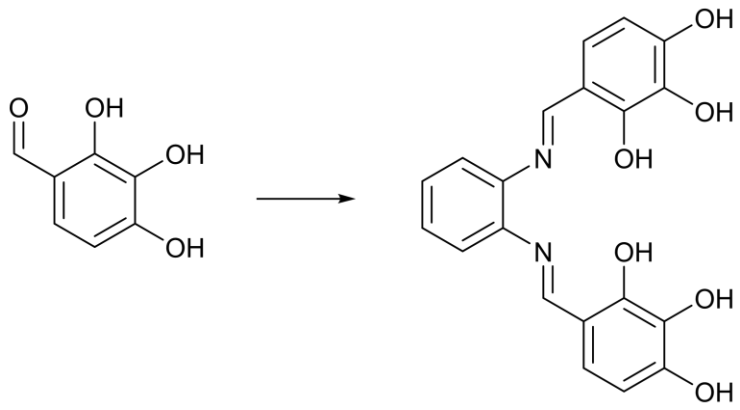

A solution of **10** (0.62 g, 4.02 mmol, 2 eq.) in anhydrous MeOH (5 ml) was added dropwise to a stirred solution of 1,2-phenylenediamine (0.22 g, 2.03 mmol, 1 eq.) in anhydrous MeOH (5 mL). The resulting mixture was refluxed at 70 °C for four hours, cooled to room temperature, and concentrated *in vacuo*. To the resulting solid was added MeOH (3 mL) and Et_2O (100 mL) then sonicated for one minute. The ppt was collected by vacuum filtration, washed with Et_2O (60 mL) affording **11** as a bright orange solid (0.67 g, 1.76 mmol, 88%). The ^{1}H NMR spectrum agreed with the literature values[120] (500 MHz, DMSO-d_6): δ 13.29 (2H, bs, Ar-O**H**), 9.73 (2H, bs, Ar-O**H**), 8.73 (2H, s, N=C-**H**), 8.55 (2H, bs, Ar-O**H**)), 7.32-7.39 (4H, m, Ar-**H**) 6.98 (2H, d, *J* = 8.6 Hz, Ar-**H**), 6.42 (2H, d, *J* = 8.5 Hz, Ar-**H**) ppm. ATR-IR: $\overline{\nu}$ = 3466, 3383, 2989, 1609, 1517, 1497, 1456, 1362, 1288, 1260, 1225, 1194, 1157, 1072, 981, 925, 872, 830, 806, 737, 608, 551, 523 cm^{-1}. ESI-MS: *m*/*z* 380.94 [**11**+H]$^+$. MP = 219 °C.

2.2.4 Synthesis of H_6L2

Following on from the successful complexation of H_6**L1**, a second ligand modified to help elucidate the impact that steric effects would have on any synthesised complexes was designed and synthesised. H_6**L2** was synthesised through two reactions, the first being a Suzuki-coupling reaction to add the sterically bulky substituents followed by a Schiff base condensation with the previously synthesised **(10)**. Stability tests determined that H_6**L2** is significantly more stable than H_6**L1** lasting five months exposed to air and light before showing signs of decomposition compared to two weeks for H_6**L1**.

[1,1′:2′,1″-Terphenyl]-4′,5′-diamine (12)

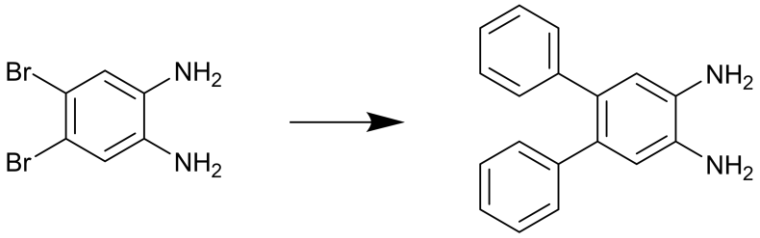

12

Adapted from the procedure of Sakai *et al.*[124] To a stirred mixture of 4,5-dibromo-1,2-phenylenediamine (0.53 g, 2.00 mmol, 1 eq.), phenylboronic acid (0.61 g, 5.00 mmol, 2.5 eq.), and tetrakis(triphenylphosphine)palladium(0) (0.12 g, 0.10 mmol, 0.05 eq.) in degassed toluene (50 mL) was added a degassed potassium carbonate aqueous solution (2.0 M, 15 mL) under an argon atmosphere. The resulting mixture was stirred at 85 °C for 24 hours then quenched with water (100 mL). The aqueous layer was separated then extracted with EtOAc (3 x 100 mL), the combined organic layers were then washed with brine (3 x 100 mL), dried over anhydrous $MgSO_4$, and concentrated *in vacuo* affording crude **12** as a dark green solid. The crude product was purified by silica gel chromatography eluting with 4:1 *n*-hex:EtOAc affording pure **12** as a white product (0.47 g, 1.81 mmol, 91%). The ^{1}H NMR spectrum agreed with the literature values (500 MHz, $CDCl_3$):[124] δ 7.09-7.19 (10H, m, Ar-**H**), 6.79 (2H, s, Ar-**H**), 3.17 (4H, bs, N-$\mathbf{H}_2$) ppm. ESI-MS: *m*/*z* 261.19 [**12**+H]$^+$.

4-[(1*E*)-((5'-[(1*E*)-(2,3,4-Trihydroxyphenyl)methylideneamino][1,1':2',1''-terphenyl]-4'-yl)imino)methyl]benzene-1,2,3-triol (13)

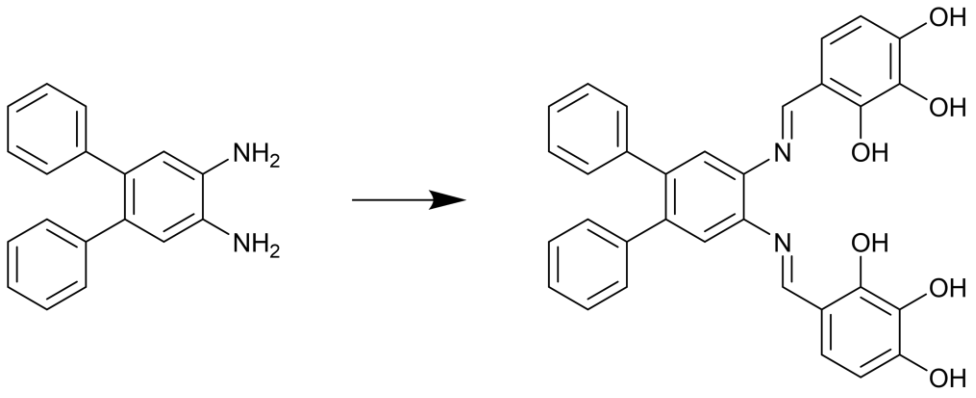

12 **13**

A solution of **10** (0.77 g, 5.00 mmol, 2 eq.) in anhydrous MeOH (10 ml) was added dropwise to a stirred solution of **12** (0.65 2.50 mmol, 1 eq.) in anhydrous MeOH (10 mL). The resulting mixture was refluxed at 70 °C for six hours, forming an orange ppt which was collected by vacuum filtration affording pure **13** as red powder (0.95 g, 1.78 mmol, 71%). ^{1}H NMR (500 MHz, DMSO-d_6): δ 13.42 (2H, bs, Ar-O**H**), 9.72 (2H, bs, Ar-O**H**), 8.89 (2H, s, N=C-**H**), 8.55 (2H, bs, Ar-O**H**)), 7.41 (2H, *s,* Ar-**H**), 7.19-7.28 (10H, m, Ar-**H**), 6.98 (2H, d, *J* = 8.6 Hz, Ar-**H**) 6.41 (2H, d, *J* = 8.5 Hz, Ar-**H**) ppm. ^{13}C NMR (126 MHz, DMSO-d_6) δ 164.5, 152.4, 151.0, 141.4, 140.8, 139.0, 132.8, 130.8, 128.5, 127.3, 124.8, 122.1, 113.2, 108.3 ppm. ATR-IR: $\overline{\nu}$ = 3513, 3336, 3057, 1639, 1616, 1586, 1558, 1520, 1501, 1460, 1404, 1363, 1339, 1259, 1200, 1167, 1079, 1026, 978, 885, 866, 812, 789, 769, 741, 699, 500, 449 cm^{-1}. ESI-MS: *m*/*z* 533.07 [**13**+H]$^{+}$. MP = 278 °C.

Chapter 3

Ni_2Ln Complexes

This chapter explores the synthesis and characterisation of a series of trinuclear heterometallic $Ni^{II}_2Ln^{III}$ complexes, where Ln = Dy^{III}, Ho^{III}, Er^{III}, or Tb^{III}. Single crystal X-ray diffraction experiments showed the expected [(H_4**L1**)$_2Ni^{II}_2Ln^{III}$] structure was present in all four complexes. The Ni^{II} centres adopt a square planar geometry affording a diamagnetic metal centre with minimal opportunities to directly modulate the secondary interactions. This series acts as a reference to highlight how secondary interactions can alter the structural properties of the core trinuclear moiety.

3.1 Results and Discussion

The complexes **C1** – **C4** were synthesised by the reaction of a methanolic solution of H_6**L1**, $Ni(BF_4)_2{\cdot}6H_2O$, and $LnCl_3{\cdot}6H_2O$ (Ln = Dy^{III}, Ho^{III}, Er^{III}, or Tb^{III}) in a 2:2:1 molar ratio. For all complexes, the bright red solution of the ligand darkened to a deep red upon successful complexation. Crystalline samples of the complexes were obtained through the vapour diffusion of diethyl ether into the reaction solution over a period of two to eight weeks. Isolated complexes were characterised by SCXRD, ATR-IR, ESI-MS, and CHN microanalysis.

3.1.1 Crystal Structure

Complexes **C1** – **C4**, were found to be trinuclear, crystallising either in the triclinic space group $P\bar{1}$ (**C1** – **C3**) or the monoclinic space group $C2/c$ (**C4**). The Ln^{III} centre for complexes **C1** – **C3** are nine-coordinate, with eight sites being bound to the outer coordination pocket of two H_4**L1**$^{2-}$ molecules. The donor groups consist of two phenolate and two hydroxy groups per ligand. The final site is occupied by a bound methanol molecule (Figure 3.1). The inner coordination pocket of the H_4**L1**$^{2-}$ molecules are occupied by a four-coordinate Ni^{II} atom that adopts a square planar geometry. The Ni^{II} centres are diamagnetic, so any magnetic properties shown by the complexes must arise from the lanthanide centre. Complex **C4** shares a similar coordination environment to complexes **C1** – **C3** except that now a chloride ion has replaced the previously bound methanol molecule (Figure 3.2). The larger Tb^{III} ion allows the bulkier chlorido ligand to occupy

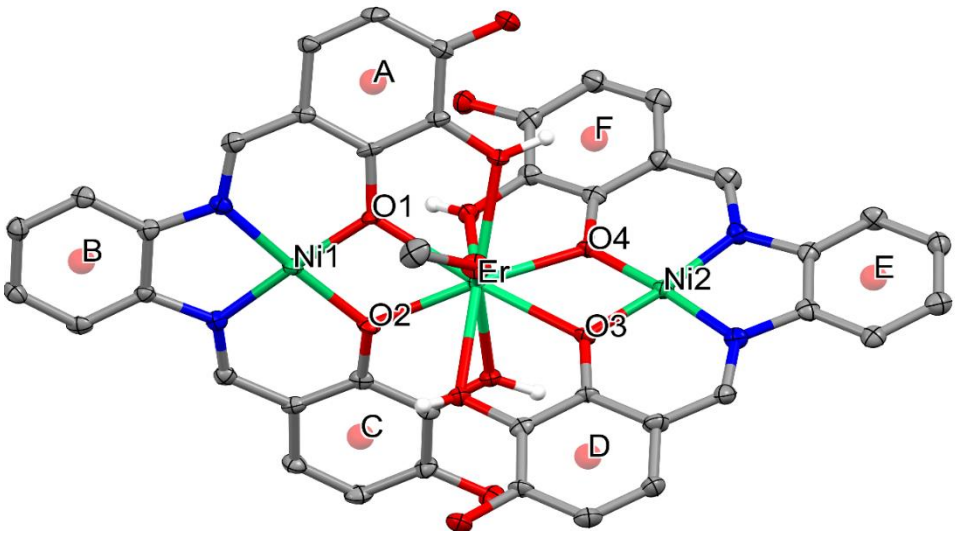

Figure 3.1: X-ray structure of **C3**, non-coordinated molecules and hydrogen atoms have been omitted for clarity. Thermal ellipsoids shown at the 40% probability level. Colour code: C, N, O, Ni, and Er are grey, blue, red, lime, and green, respectively. Atom labels for the selected bond lengths and angles reported in Table 3.1 are provided and are consistent for complexes **C1** – **C4**.

the ninth coordination site. Selected bond lengths and angles for complexes **C1** – **C4** are found in Table 3.1. The asymmetric unit of complexes **C1** – **C3** consist of the $[(H_4\mathbf{L1})_2Ni_2LnMeOH]^{3+}$ unit and three non-coordinated MeOH molecules and three chloride ions.

To ensure the charge neutrality of the complexes, the two outermost binding phenols of each $H_4\mathbf{L1}^{2-}$ ligand remain protonated (HO5 – HO8). The asymmetric unit of complex **C4** consists of half of the $[(H_4\mathbf{L1})_2Ni_2TbCl]^{2+}$ unit, two methanol molecules and one chloride ion. The Ni–Ln

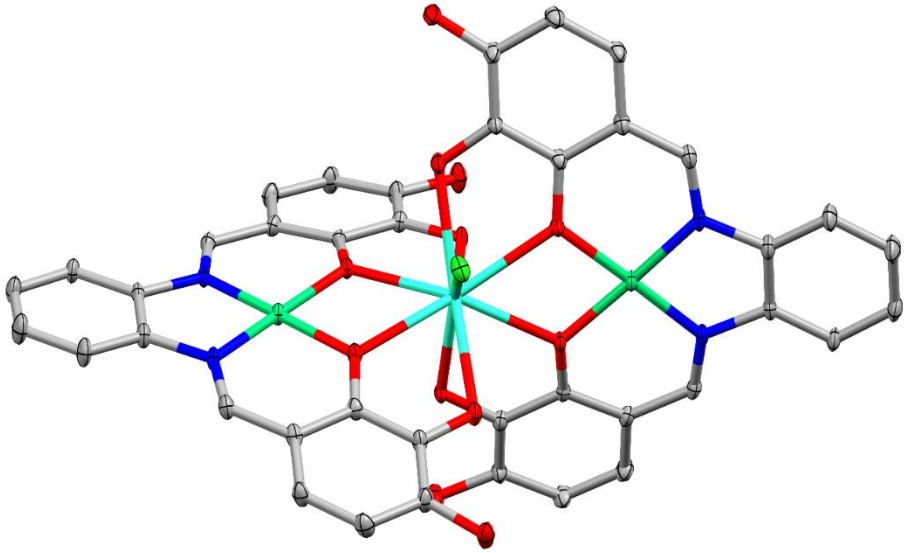

Figure 3.2: X-ray structure of **C4**, non-coordinated molecules and hydrogen atoms have been omitted for clarity. Thermal ellipsoids shown at the 40% probability level. Colour code: C, N, O, Ni, Cl, and Tb are grey, blue, red, lime, green, and cyan, respectively.

Table 3.1. Selected structural parameters for complexes **C1** – **C4**

	C1	**C2**	**C3**	**C4**
Ni1–Ln (Å)	3.401(2)	3.395(2)	3.390(1)	3.407(1)
Ni2–Ln (Å)	3.410(3)	3.400(2)	3.390(1)	3.407(1)
Ni1–O1–Ln (°)	108.7(4)	108.1(3)	108.6(2)	108.2(2)
Ni1–O2–Ln (°)	108.8(5)	109.0(3)	109.2(2)	108.3(2)
Ni2–O3–Ln (°)	108.0(4)	107.6(3)	107.4(2)	108.2(2)
Ni2–O4–Ln (°)	108.8(4)	108.9(3)	109.5(2)	108.3(2)
Ni–O Average (°)	108.6(4)	108.4(3)	108.7(2)	108.3(2)
O5–Ln–O6 (°)	149.4(3)	148.7(2)	149.3(2)	141.3(1)
O7–Ln–O8 (°)	149.9(3)	150.1(2)	149.5(2)	141.3(1)

distances and the Ni–O–Ln bond angles would dictate the strength and type of magnetic superexchange between the metal centres, however the Ni^{II} ions have adopted a low spin square planar geometry and as such are diamagnetic. The Ni–Ln distance decreases with decreasing lanthanide size, which in the absence of secondary interactions, is to be expected. The angle between the two outermost binding phenols of H_4**L1**$^{2-}$ and the lanthanide ion (O5–Ln–O6 and O7–Ln–O8) represents the distortion of the ligand, with an angle of 180° indicating no distortion. Complexes **C1** – **C3** all have very similar O–Ln–O angles, averaging between 149 – 150° whilst **C4** has an angle of 141.3°. This difference is due to the increased bulk of the chloride ion causing greater distortion to the lanthanide's coordination environment.

ESI-MS analysis showed almost identical fragmentation patterns for all four complexes, with a set of peaks between 1030 – 1040 *m/z* which represents the $[(H_3$**L1**$)_2Ni_2Ln]^+$ unit. A second, higher intensity set of peaks exists between 515 – 525 *m/z* which corresponds to the $[(H_3$**L1**$)(H_4$**L1**$)Ni_2Ln]^{2+}$ unit. The bound MeOH (**C1** – **C3**) or chloride ion (**C4**) dissociates when running the ESI-MS experiment. This is likely due to the experiment being run in a positive mode, which results in the protonation of these species, causing their dissociation.

3.1.2 Intermolecular Interactions

Each complex of **C1** – **C3** displays three intermolecular hydrogen bonding interactions between complexes through a chloride ion (Figure 3.3). All hydrogen bond lengths mentioned in this thesis are defined as the distance between the hydrogen and the acceptor atom. Each of these three chloride ions are hydrogen bonded to three complex units, with analogous hydrogen bonds having very similar distances: H(**a**) 2.287 (3) – 2.310 (2), H(**b**) 2.178 (2) – 2.212 (2), and H(**c**) 2.271 (2) – 2.294 (3) (Table 3.2).

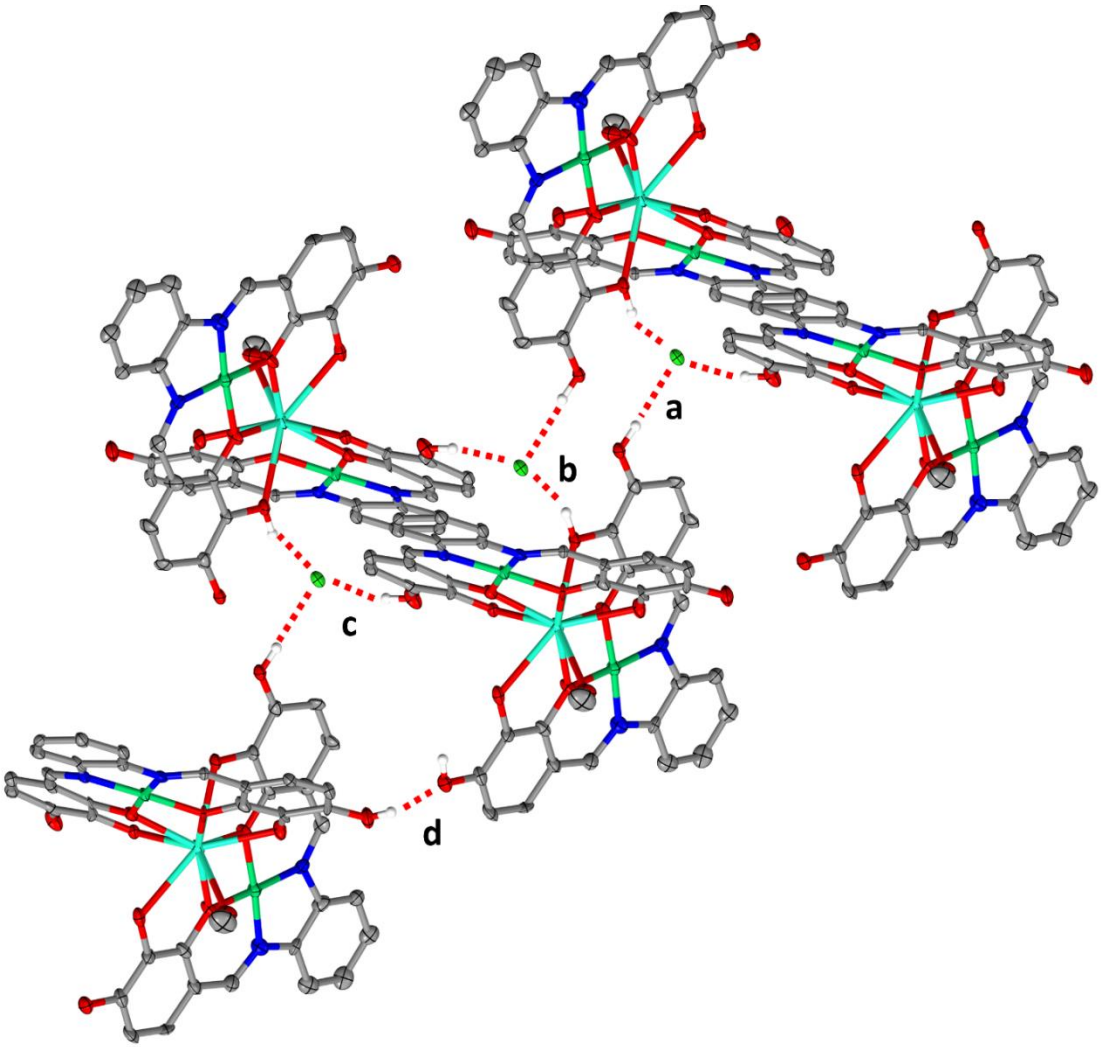

Figure 3.3: X-ray structure of **C1** displaying the intermolecular hydrogen bonding interactions present in complexes **C1** and **C3**. Non-interacting hydrogens and solvent species have been omitted for clarity. Colour code: C, N, O, Ni, Cl, and Dy are grey, blue, red, lime, green, and light blue, respectively.

Complexes **C1** and **C3** also contain a single direct hydrogen bond between nearby complex units involving a non-binding phenol group from each complex (Figure 3.3, **a**). Complex **C2** does not contain this interaction since the relevant hydrogen is instead hydrogen bonded to a nearby methanol molecule. Complex **C4** does not contain any intermolecular hydrogen bonding, with only interactions with nearby species present (Figure 3.4).

Table 3.2. Selected intermolecular hydrogen bonding interactions for complexes **C1** – **C3** (Å)

	C1	**C2**	**C3**
a	2.287(3)	2.290(2)	2.310(2)
b	2.18(2)	2.212(2)	2.178(2)
c	2.294(3)	2.271(2)	2.271(2)
d	2.030(1)	-	2.170(5)

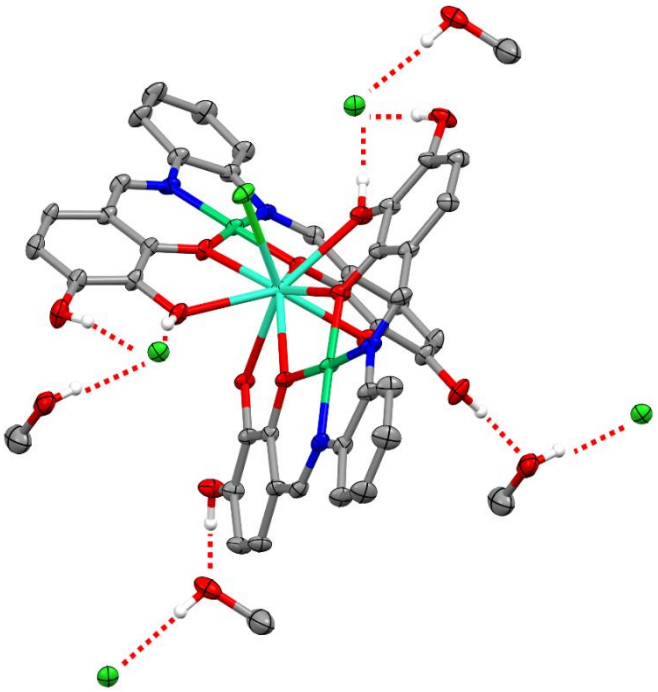

Figure 3.4: X-ray structure of **C4** displaying the hydrogen bonding interactions. Non interacting hydrogens and solvent molecules have been omitted for clarity. Colour code: C, N, O, Ni, Cl, and Tb are grey, blue, red, lime, green, and cyan, respectively.

Complexes **C1** – **C3** each possess π-π stacking interactions with five separate complexes. Three complexes are linked by double π-π stacking interactions and two complexes are linked by single π-π stacking interactions, giving a total of eight π-π stacking interactions (Figure 3.5). These

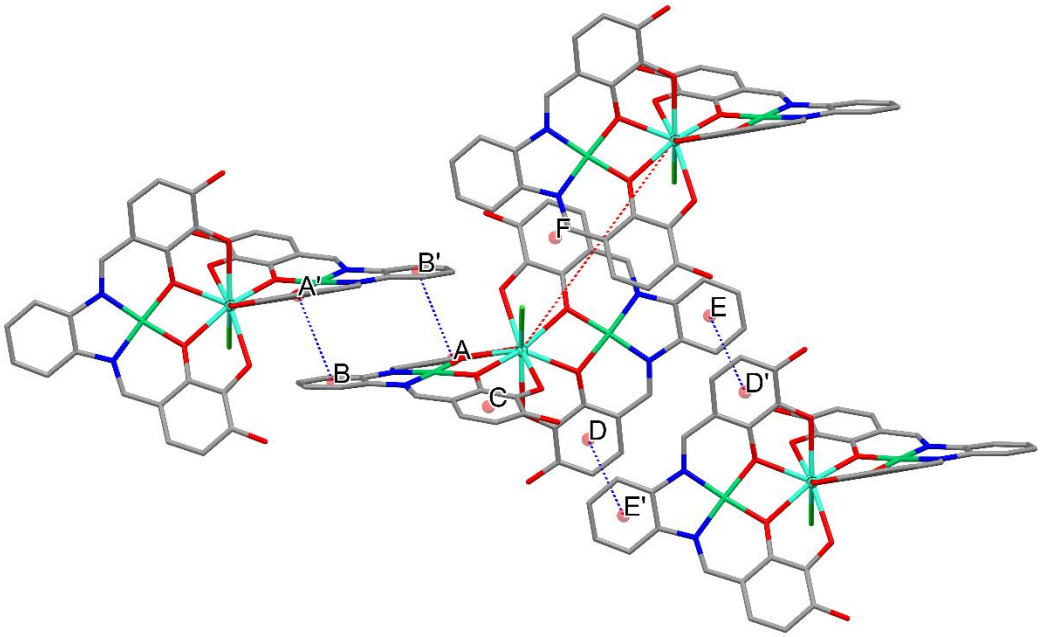

Figure 3.5: X-ray structure of **C4** showing the smallest complete packing unit. Blue dashed lines represent π–π stacking interactions, red dashed line represents the smallest Ln–Ln distance. Hydrogens and solvent molecules have been omitted for clarity.

interactions result in the formation of a 3D supramolecular architecture. The shortest Ln–Ln distance occurs between complexes that do not directly share π-π stacking interactions (Figure 3.6). Instead, this distance is between complexes that pack into the space where the species bound to the lanthanide ion is located (10.341, 10.286, and 10.257 Å for **C1**, **C2**, and **C3** respectively). The complex unit of **C4** possesses double π-π stacking interactions with two complexes resulting in a total of four π-π stacking interactions per complex (Figure 3.5). This stacking results in the formation of 1D chains, which then pack into a 3D structure such that the shortest Ln–Ln distance, 9.915 Å, is between chains (Figure 3.7). The difference in supramolecular architecture between complexes **C1** – **C3** and **C4** could arise from the differing number of non-coordinated chloride ions. As shown by the intermolecular hydrogen bonding interactions for complexes **C1** – **C3**, the non-coordinated chlorides act as a central templating anion, organising the self-assembly of the 3D crystal structure. Complex **C4** has one fewer chloride ion free to act as this templating anion, resulting in the formation of the 1D chains. Furthermore, the linear geometry of these chains, and the absence of a third anion allows for a much tighter packing of the overall crystal lattice, when compared with complexes **C1** – **C3**.

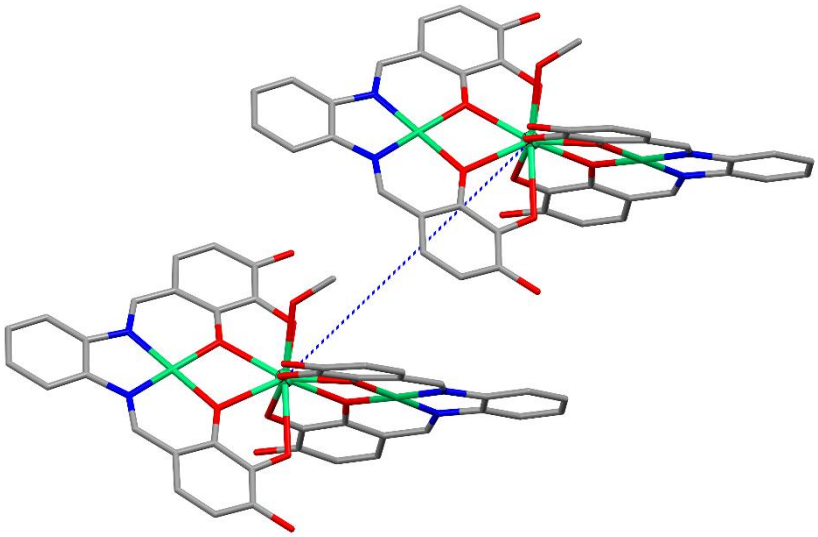

Figure 3.6: X-ray structure of **C3** showing the shortest Ln–Ln distance for complexes **C1** – **C3**, dashed blue line represent the smallest Ln–Ln distance. Hydrogens and solvent molecules have been omitted for clarity; thermal ellipsoids shown at the 70% probability level.

3.2 Conclusions

Four new trinuclear heterometallic $Ni^{II}_2Ln^{III}$ complexes have been synthesised and characterised. X-ray structural analysis revealed complexes **C1** – **C3** to be isostructural, forming a 3D supramolecular structure with extensive hydrogen bonding and π–π stacking interactions.

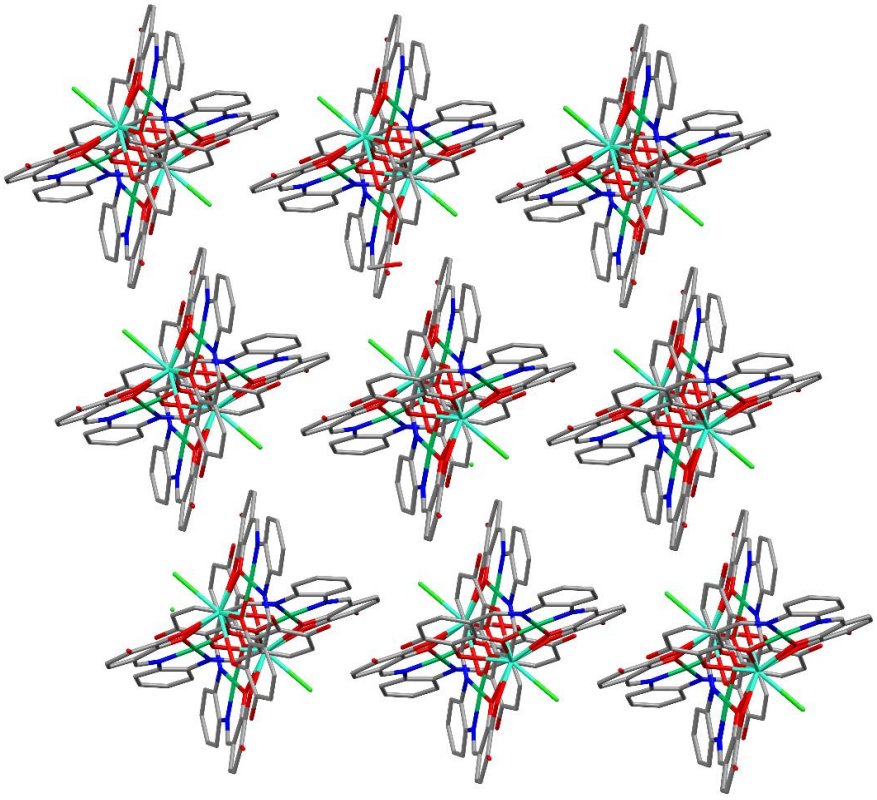

Figure 3.7: X-ray structure of **C4** showing the supramolecular packing as viewed down the chains. Hydrogen atoms and solvent molecules have been omitted for clarity.

Complex **C4** formed 1D chain structures, which packed into a 3D structure. The difference in supramolecular architecture was found to be due to the templating effect of the chloride ions within the crystal lattice, of which three are found per unit complex for **C1** – **C3** and only two for **C4**. The shortest Ln–Ln distance correlates to the size of the lanthanide ion, with the smallest ions possessing the shortest Ln–Ln distance, except for **C4** being abnormally short due to the different crystal packing mentioned above. Magnetic measurements were not performed on this series, though similar systems reported in the literature show that diamagnetic $Ni^{II}Ln$ systems essentially act as lanthanide SIMs.[102,125-127] The square planar geometry of the Ni^{II} ions precludes the direct modulation of secondary interactions due to the lack of an apically bound species capable of performing these secondary interactions. Thus, this work provides an essential reference point for investigating the impact that modulation of secondary interactions has on the structural and magnetic properties of other complex series that will be covered in future chapters.

Complex Preparation

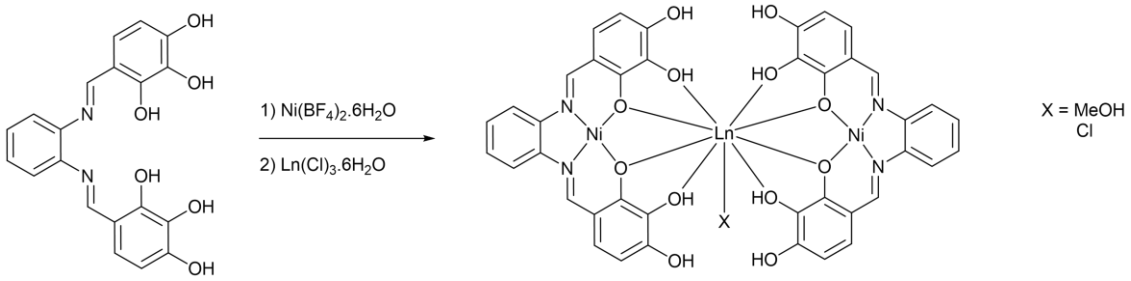

Figure 3.8: Schematic showing the complexation reaction undertaken by complexes **C1** – **C4**.

Complexes **C1** – **C4** were obtained by the addition of $Ni(BF_4)_2{\cdot}6H_2O$ (0.0340 g, 0.1 mmol, 2eq.) in MeOH (2.5 mL) to a solution of H_6**L1** (0.0380 g, 0.1 mmol, 2eq.) at 50 °C in MeOH (5 mL) resulting in a deep red solution. A solution of $LnCl_3{\cdot}6H_2O$ (0.05 mmol, 1eq.) in MeOH (2.5 mL) (Ln = Dy, Ho, Er or Tb) was added and stirred at 50 °C for 30 minutes before being cooled to RT. Vapour diffusion of Et_2O into the reaction mixture yielded the complexes **C1** – **C4**.

C1 $[(H_4\mathbf{L1})_2Ni_2Dy(MeOH)](MeOH)_4Cl_3$: Red needle shaped crystals were obtained after 3 weeks. Yield 17% based on $DyCl_3{\cdot}6H_2O$. ATR-IR $\bar{\nu}$: 3147, 1624, 1603, 1560, 1555, 1502, 1459, 1294, 1233, 1203, 1096, 1027, 741 cm^{-1}. Elemental analysis calculated (%) for $C_{40}H_{28}N_4O_{12}Ni_2Dy{\cdot}Cl_3(MeOH)_3$: C 41.58, H 3.49, N 4.41; found C 41.82, H 3.38, N 4.69. ESI-MS *m/z* 1033.79 $[(H_3\mathbf{L1})_2Ni_2Dy]^+$, 517.63 $[(H_3\mathbf{L1})(H_4\mathbf{L1})Ni_2Dy]^{2+}$.

C2 $[(H_4\mathbf{L1})_2Ni_2HoMeOH](MeOH)$: Red needle shaped crystals were obtained after 2 weeks. Yield 13% based on $HoCl_3{\cdot}6H_2O$. ATR-IR $\bar{\nu}$: 3535, 3147, 2834, 1601, 1567, 1557, 1504, 1456, 1430, 1382, 1323, 1296, 1233, 1202, 1096, 1026, 896, 810, 751, 694, 631, 609, 548, 520, 489 cm^{-1}. Elemental analysis calculated (%) for $C_{40}H_{28}N_4O_{12}Ni_2Ho{\cdot}Cl_3(MeOH)_3$: C 41.50, H 3.48, N 4.40; found C 41.79, H 3.43, N 4.68. ESI-MS *m/z* 1036.92 $[(H_3\mathbf{L1})_2Ni_2Ho]^+$, 518.63 $[(H_3\mathbf{L1})(H_4\mathbf{L1})Ni_2Ho]^{2+}$.

C3 $[(H_4\mathbf{L1})_2Ni_2ErMeOH](MeOH)$: Red needle shaped crystals were obtained after 5 weeks. Yield 24% based on $ErCl_3{\cdot}6H_2O$. ATR-IR $\bar{\nu}$: 3189, 2357, 1618, 1603, 1553, 1504, 1445, 1381, 1281, 1231, 1204, 1171, 1090, 1017, 778, 743, 629, 548 cm^{-1}. Elemental analysis calculated (%) for $C_{40}H_{28}N_4O_{12}Ni_2Er{\cdot}Cl_3(MeOH)_3$: C 41.42, H 3.48, N 4.39; found C 41.69, H 3.55, N 4.73. ESI-MS *m/z* 1037.89 $[(H_3\mathbf{L1})_2Ni_2Er]^+$, 519.56 $[(H_3\mathbf{L1})(H_4\mathbf{L1})Ni_2Er]^{2+}$.

C4 $[(H_4\mathbf{L1})_2Ni_2TbCl](MeOH)_4Cl_2$: Red needle shaped crystals were obtained after 8 weeks. Yield 6% based on $TbCl_3{\cdot}6H_2O$. ATR-IR $\bar{\nu}$: 3507, 3275, 1617, 1551, 1504, 1443, 1381, 1331, 1278, 1254, 1198, 1172, 1160, 1088, 1016, 1005, 893, 777, 746, 628, 597, 548, 437 cm^{-1}. Elemental analysis

calculated (%) for $C_{40}H_{28}N_4O_{12}Ni_2Tb{\cdot}Cl_3(MeOH)_3$: C 41.73, H 3.42, N 4.42; found C 41.94, H 3.49, N 4.73. ESI-MS *m*/*z* 1030.89 $[(H_3\mathbf{L1})_2Ni_2Tb]^+$, 515.63 $[(H_3\mathbf{L1})(H_4\mathbf{L1})\ Ni_2Tb]^{2+}$.

Chapter 4

CuLn Complexes

This chapter explores the synthesis and characterisation of heterometallic $Cu^{II}Ln^{III}$ complexes. Two series of $Cu^{II}_2Ln^{III}$ complexes have been synthesised, where Ln = Y^{III}, Gd^{III}, Er^{III}, and Tb^{III}, with the series differing depending on whether the counterion is bromide or chloride. An additional two complexes with Ln = Dy^{III}, or Ho^{III} have been synthesised with the bromide counterion. X-ray analysis revealed that all ten complexes crystallised with the expected [(H_4**L1**)$_2Cu^{II}_2Ln^{III}$] structure, with each Cu^{II} centre adopting a square-pyramidal geometry. The additional apically bound species, compared to the work covered in Chapter 3, provides a way to modulate the secondary interactions of the species. Complexes **C6** – **C9** and **C12** – **C15** were produced in sufficient quantities to undergo magnetic characterisation. Additionally, a unique tetranuclear **L1**$_3Cu^{II}_3La^{III}$ complex has been isolated and shows how the lanthanide size can affect the nuclearity of resultant complexes.

4.1 La Complex

The tetranuclear complex **C5** was synthesised by the reaction of an MeOH solution of H_6**L1**, $Cu(BF_4)_2{\cdot}6H_2O$, and $LaCl_3{\cdot}7H_2O$ in a 2:2:1 molar ratio. Vapour diffusion of Et_2O into this solution over a period of five weeks resulted in the formation of red plate like crystals. Due to a lack of material, only X-ray analysis of the resulting material was accomplished.

Complex **C5** crystallised in the triclinic space group $P\bar{1}$ with the asymmetric unit containing the central [(H_4**L1**)$_2H_2$**L1**$LaCu_3Cl_2$]$^-$ unit as well as five non-coordinated MeOH molecules and one non-coordinated sodium ion (Figure 4.1). This non-coordinated cation was assumed to be sodium, likely from the glass vials used in complexation, to ensure the charge balance of the overall system and to match the electron density of the species located there. The Cu1 and Cu2 ions are five-coordinate adopting a square pyramidal geometry, with the equatorial sites being occupied by the inner binding pocket of an **L1** ligand, and the axial site being occupied by a chloride anion. The Cu3 ion is four-coordinate with all four sites being occupied by the inner coordination pocket of an **L1** ligand. The central La^{III} ion is ten-coordinate, with eight sites being occupied by the full O_4 outer coordination pocket of two **L1** ligands, while the remaining two sites are occupied by half of the outer coordination pocket of the remaining **L1** ligand. The Cu–

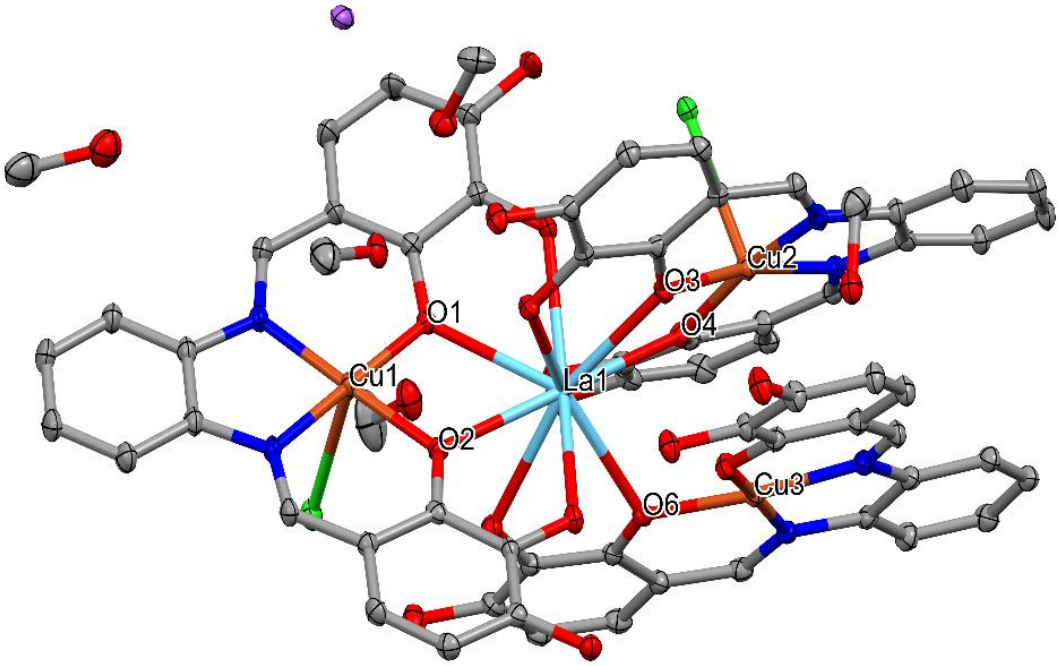

Figure 4.1: X-ray structure of the asymmetric unit of **C5**, hydrogen atoms have been omitted for clarity. Thermal ellipsoids shown at the 30% probability level. Colour code: C, N, O, Cu, La, Na, and Cl are grey, blue, red, orange, sky blue, purple, and green respectively.

O–La angles range from 107.9(1)° for Cu3–O6–La1 to 109.1(1)° for Cu1–O1–La1, whilst the Cu–La distances range from 3.6773 (6) Å for Cu1–La1 to 3.6920 (6) Å for Cu3–La1. The significantly larger Cu–O–La angle for the fully-coordinated ligands suggests that full coordination forces this angle to be larger.

Complex **C5** contains a total of four intramolecular hydrogen bonds (Figure 4.2). Each of the apically bound chloride anions act as a hydrogen bond acceptor for two phenolic hydrogens from an adjacent ligand (Cl1 · · · HO12 = 2.25 (2) Å, Cl1 · · · HO18 = 2.249 (1) Å, Cl2 · · · HO7 = 2.36 (5) Å, and Cl2 · · · HO13 = 2.2422 (9) Å). The apically bound chloride ions participates in two intramolecular hydrogen bonding interactions, which is unique with regards to the work reported in this thesis and is due to three **L1** units being bound to the central La^{III} ion forcing the hydrogen bonding groups closer together.

Complex **C5** has a total of six significant intermolecular interactions with adjacent complex units (Figure 4.3). A pair of π–π stacking interactions exists between the rings A · · · B' and B · · · A' (3.685 Å) of an adjacent complex. A pair of hydrogen bonding interactions occurs between the phenolic hydrogen HO17 through the intermediary MeOH molecule O22 and the apically bound

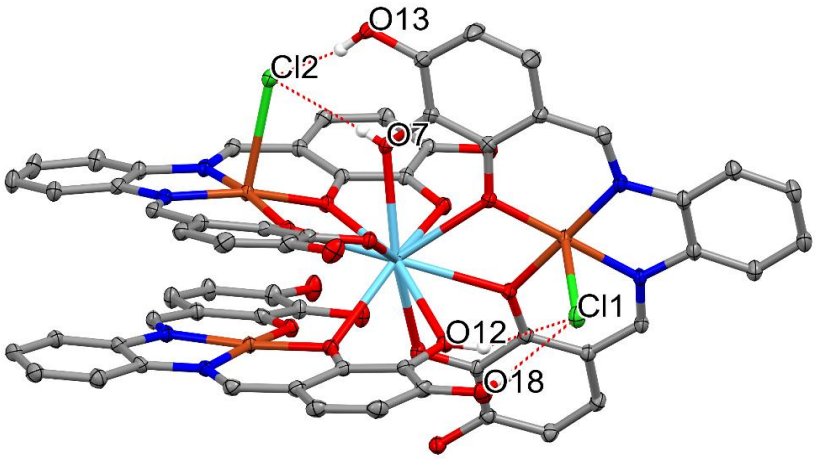

Figure 4.2: X-ray structure of **C5** showing the intramolecular hydrogen bonding interactions. Red dashed lines represent hydrogen bonding, non-interacting hydrogens and non-coordinated species have been omitted for clarity thermal ellipsoids shown at the 30% probability level. Colour code: C, N, O, Cu, La, and Cl are grey, blue, red, orange, sky blue, and green respectively.

chloride anion Cl1 (HO17 · · · O22, HO22 · · · Cl1). The final pair of hydrogen bonds occurs between the phenolic hydrogen HO14 through the intermediary MeOH molecule O21 and the phenolic oxygen O15 (HO14 · · · O21, HO21 · · · O15). This gives a total of four separate complexes that each **C5** complex has intermolecular interactions with.

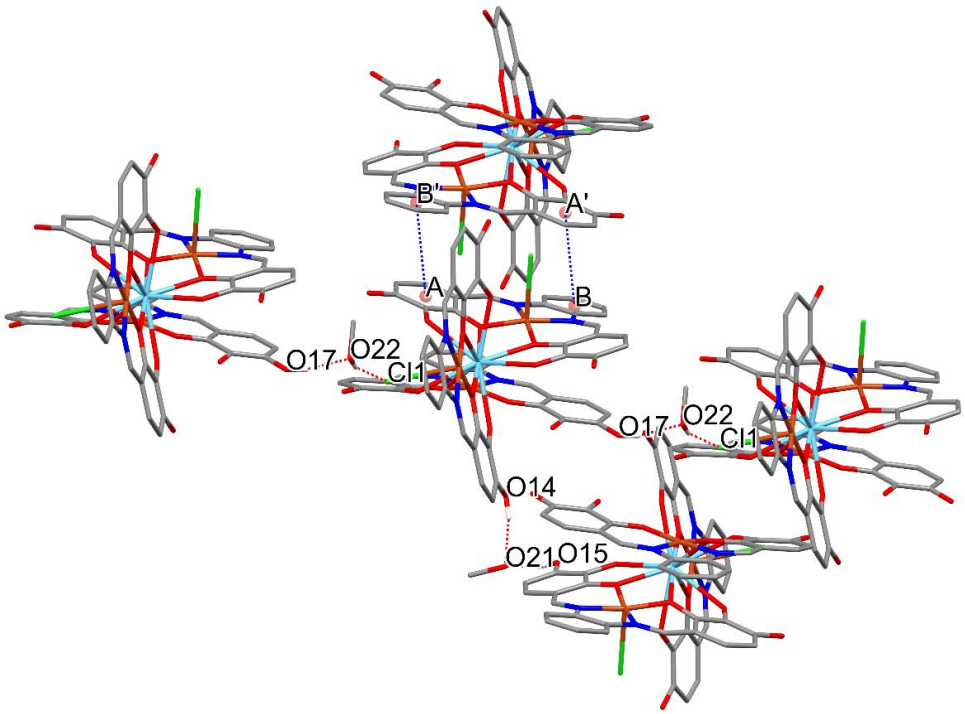

Figure 4.3: X-ray structure of **C5** showing the intermolecular interactions. Red dashed lines represent hydrogen bonding, blue dashed lines represent π–π stacking interactions. Non-interacting hydrogens and non-coordinated species have been omitted for clarity. Colour code: C, N, O, Cu, La, and Cl are grey, blue, red, orange, sky blue, and green respectively.

The La^{III} ion is significantly larger than the other lanthanide ions reported in this thesis.[128] It is this larger size that allows for the formation of the tetranuclear complex compared to the trinuclear complexes covered in this thesis.

4.2 Cu_2Ln Series

The complexes **C6** – **C15** were synthesised by the reaction of a methanolic solution of H_6**L1**, $Cu(BF_4)_2{\cdot}6H_2O$, and $Ln(NO_3)_3{\cdot}6H_2O$ (Ln = Y^{III} or Gd^{III}) or $LnCl_3{\cdot}6H_2O$ (Ln = Er^{III}, Tb^{III}, Dy^{III}, or Ho^{III}) in a 2:2:1 molar ratio. The bromide containing complexes had an additional synthetic step where an excess of TBABr (10 eq.) was added. For all complexes, the bright red solution of the ligand darkened to a dark red upon successful complexation. Crystalline samples of the complexes were obtained through the vapour diffusion of diethyl ether into the reaction solution over a period of four to ten weeks. Isolated complexes were characterised by SCXRD, ATR-IR, ESI-MS, and CHN microanalysis.

4.2.1 Crystal Structure

The bromide containing complexes **C6** – **C9** crystallised in the monoclinic space group $P2_1/n$ and are isostructural except for complex **C6** containing a 0.2 occupancy nitrate anion sharing the same space as a 0.8 occupancy chloride anion. The Ln^{III} centre for these four complexes are nine-coordinate, with eight sites being bound to two H_4**L1**$^{2-}$ molecules through two phenolate and two hydroxy groups per ligand with the final site occupied by a bound MeOH molecule. Each Cu^{II} centre is five-coordinate with the four equatorial binding sites occupied by two imine and two phenolate groups of H_4**L1**$^{2-}$. The final site is occupied by either one bromide anion (Cu1) or one MeOH group (Cu2) anion, affording a square-pyramidal geometry (Figure 4.4). Similar to the nickel series, to ensure the charge neutrality of the complexes, the two outermost binding phenols of each H_4**L1**$^{2-}$ ligand remain protonated (HO5 – HO8). The asymmetric units of complexes **C6** – **C9** contain the [H_4**L1**$_2Cu_2$LnBr$(MeOH)_2$] unit as well as an additional four non-coordinated MeOH molecules, two bromide anions, and a single Et_2O molecule (Figure 4.5). Complexes **C10** and **C11** are similar to complexes **C6** – **C9** however there are three fewer MeOH molecules. Two water molecules are in place of the MeOH molecule, including the molecule bound to the lanthanide.

Of the chloride containing complexes, **C12** crystallised in the monoclinic space group $P2_1/n$, **C13** in $C2/c$, and **C14** and **C15** in $I2/a$. The space group $I2/a$ can be converted to $C2/c$, with an appropriate cell choice, thus giving the cell parameters quite close to those of **C13**. The Ln^{III}

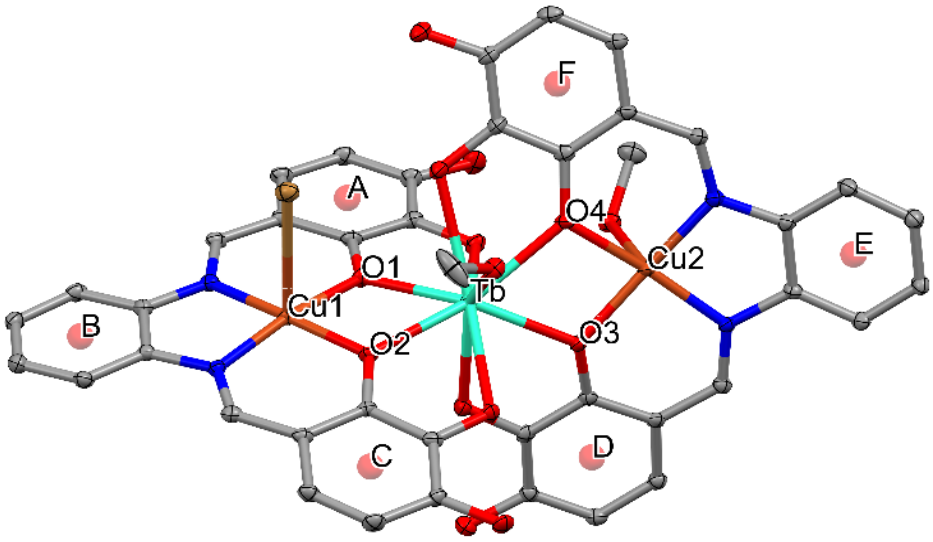

Figure 4.4: X-ray crystal structure of **C9**. Non-coordinated species and hydrogen atoms have been omitted for clarity. Thermal ellipsoids shown at the 40% probability level. Colour code: C, N, O, Cu, Tb, Br are grey, blue, red, orange, cyan, and gold respectively.

centre for complexes **C12** and **C15** are nine-coordinate, with eight sites being bound to two H_4**L1**$^{2-}$ molecules through two phenolate and two hydroxy groups per ligand. The final site is occupied by a bound MeOH molecule. The Ln^{III} centre for complexes **C13** and **C14** are eight-coordinate with all eight sites being occupied by two H_4**L1**$^{2-}$ molecules. Each Cu^{II} centre is five-coordinate with the four equatorial binding sites occupied by two imine and two phenolate groups of H_4**L1**. The final site is occupied by a chorine anion giving an overall square-pyramidal geometry. The asymmetric unit of complex **C12** is the same as complexes **C6** – **C9** except with the bromide ions being replaced with 0.5:0.5 occupancy chloride : nitrate ions. This is due to

incomplete replacement of the nitrate anions within the crystal that the X-ray data was collected from. The asymmetric unit of complexes **C13** – **C15** each contains a $[H_4\mathbf{L1}CuLn_{0.5}Cl]^{0.5}$ unit which represents half of the overall architecture with **C13** containing one well defined MeOH molecule, a half-occupied chloride ion, seven further MeOH molecules and a Et_2O molecule are poorly defined. Complex **C14** contains a half-occupied chloride ion spread across two sites, as well as six MeOH and one Et_2O molecule which are poorly defined. Whilst complex **C15** contains one water molecule, one and a half methanol molecules, one chloride ion and a further four poorly defined MeOH molecules.

Within the complexes, the Cu–Ln distance and the Cu–O–Ln bond angles are of particular interest as these relate to potential magnetic exchange between the metal centres (Figure 4.4).[38]

Table 4.1. Selected structural parameters for complexes **C6** – **C15**

	Cu1–Ln (Å)	Cu2–Ln (Å)	Cu1–O1–Ln (°)	Cu1–O2–Ln (°)	Cu2–O1–Ln (°)	Cu2–O2–Ln (°)	Ave. Cu–O–Ln (°)
C6	3.397(1)	3.411(1)	108.2(2)	106.2(2)	108.0(2)	107.3(2)	107.4(2)
C7	3.421(1)	3.435(1)	108.2(2)	106.2(2)	107.4(2)	107.4(2)	107.3(2)
C8	3.379(1)	3.392(1)	105.8(2)	108.2(3)	107.7(2)	106.8(3)	107.1(3)
C9	3.405(1)	3.421(1)	107.8(2)	105.9(2)	107.8(2)	106.9(2)	107.1(2)
C10	3.407(1)	3.400(1)	106.7(2)	108.0(2)	107.1(2)	106.8(2)	107.2(2)
C11	3.394(2)	3.390(2)	106.1(3)	108.0(3)	107.2(3)	107.4(3)	107.2(3)
C12	3.363(2)	3.360(2)	105.3(3)	107.2(3)	106.0(3)	106.2(3)	106.2(3)
C13	3.320(2)	3.320(2)	106.9(4)	106.7(4)	106.9(4)	106.7(4)	106.8(4)
C14	3.342(1)	3.342(1)	106.6(2)	106.0(2)	106.6(2)	106.0(2)	106.3(2)
C15	3.390(3)	3.390(3)	108.4(5)	106.8(5)	108.4(5)	106.8(5)	107.6(5)

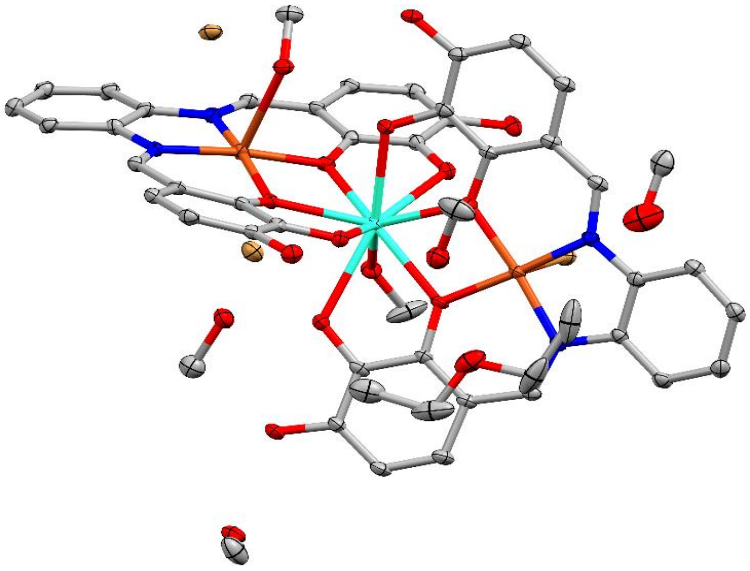

Figure 4.5: X-ray crystal structure of the asymmetric unit of **C9**. Thermal ellipsoids are shown at the 30% probability level. Colour code: C, N, O, Cu, Tb, and Br are grey, blue, red, orange, cyan, and gold, respectively. Hydrogen atoms have been omitted for clarity.

The bromide containing **C6** – **C11** tended to have larger Cu–Ln distances and angles than the chloride containing complexes **C12** – **C15** (Table 4.1). Comparison between the bromide series and the nickel series reported in Chapter 3 shows a similar trend of the size of the lanthanide determining the TM–Ln distance. Notably however, the TM–O–Ln angle is larger for the nickel series (108.3(2) – 108.7(2)°) compared to the bromide series (107.1(3) – 107.4(2)°), despite the Cu^{II} ion being larger than the Ni^{II} ion.[129] Further, the chloride series has on average an even smaller TM–O–Ln angle ranging from 106.2(3) – 107.6(5)°, these results can be explained by the intramolecular hydrogen bonding interactions present in the copper series.

Table 4.2. Intramolecular hydrogen bonding interactions for the complexes **C6** – **C15** (Å)

	C6	**C7**	**C8**	**C9**	**C10**	**C11**
Br-OH	2.53(3)	2.59(3)	2.53(4)	2.52(3)	2.399(1)	2.44(4)
MeOH-OH	1.86(3)	2.13(7)	1.84(4)	1.85(3)	2.00(7)	1.83(4)
	C12	**C13**	**C14**	**C15**		
Cl-OH	2.934(6)	2.28(7)	2.291(1)	2.31(7)		

4.2.2 Intermolecular Interactions

Complexes **C6** – **C15** displayed intramolecular hydrogen bonding between the species bound at the apical site of the copper ions and the nearest phenolic hydrogen. The bromide hydrogen bonding interactions range from a distance of 2.399(1) – 2.59(3) Å, the MeOH from 1.83(4) – 2.13(7) Å, and chloride from 2.14(3) – 2.934(6) Å, with no apparent correlation to lanthanide size (Table 4.2). The size of these interactions correlates to the comparative electronegativities of the donor species, with bromide being the least electronegative, thus having the longest hydrogen bonds, whilst oxygen is the most electronegative. The presence of these intramolecular hydrogen bonds is likely what causes the decrease in TM–O–Ln angle. The nickel series has no intramolecular hydrogen bonds and the largest TM–O–Ln angle, whilst the chloride series has the strongest intramolecular hydrogen bonds and the smallest TM–O–Ln angle.

The bromide containing series (**C6** – **C11**) all possess an identical array of π-π stacking interactions, with five of the six aromatic rings involved in π-π stacking. Two pairs of two π-π stacking interactions form a chain of linked complexes where they oscillate between two conformations (Figure 4.6). Each complex also possesses a single π-π stacking interaction with a complex in a neighbouring chain that is inverted relative to it. This network of interactions results in a zig-zag type of supramolecular sheet where every second complex in an individual chain has a single π-π interaction 'above', with the rest having a π-π stacking interaction with the chain 'left' of it (Figure 4.7). These sheets then layer themselves within the gaps in the zig-zag lattice such that the intersheet Ln–Ln distance is shorter than either of the inter/intra-chain distances (Figure 4.8). Three distinct intermolecular hydrogen bonding interactions are observed, two interchain and the other between complex sheets. The inter-sheet interaction occurs between the bromide ion bound to the apical position of the copper ion and a phenolic hydrogen of a neighbouring complex (Figure 4.9, a). This interaction helps explain the relatively close inter-sheet distance. The first interchain interaction occurs between the MeOH group bound to the apical position of the copper ion, to a non-coordinated bromide ion which in turn is hydrogen bonded to a non-coordinating phenol of a separate complex (Figure 4.9, b). The final interaction is between the MeOH group bound to the lanthanide, through a non-coordinated bromide ion to a non-binding phenol of a separate complex (Figure 4.9, c).

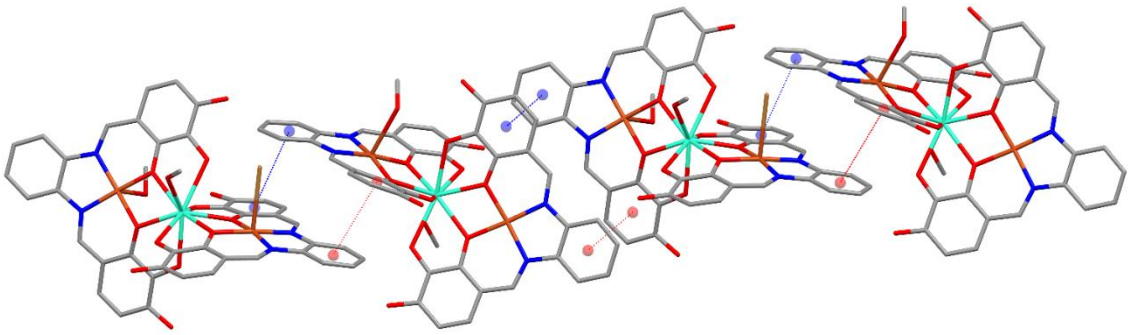

Figure 4.6: X-ray crystal structure of complex **C9** showing the intrachain π-π stacking interactions present in complexes **C6** – **C11**. The coloured dashed lines represent identical interactions. Solvent molecules and hydrogen atoms have been omitted for clarity.

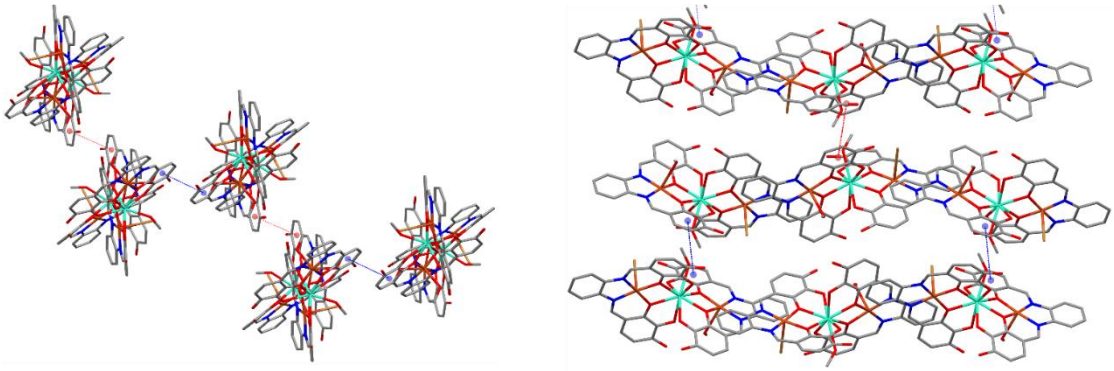

Figure 4.7: X-ray crystal structure showing the single π-π stacking interactions viewing from down the chain (left) and at the chain (right). Solvent molecules and hydrogen atoms have been omitted for clarity.

Due to the presence of the nitrate ions, complex **C12** has its own unique set of π-π stacking interactions, with one pair of two π-π stacking interactions between complexes and an additional single π-π stacking interaction for a total of three π-π stacking interactions. This forms

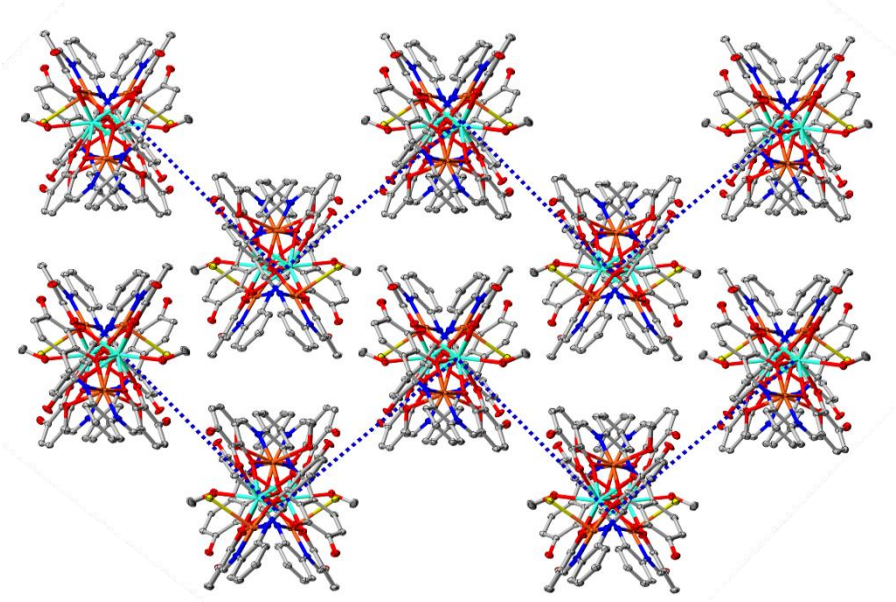

Figure 4.8: X-ray crystal structure showing the intersheet packing of complexes **C6** – **C11** viewed along the chains. Blue dashed lines indicate interchain π-π stacking. Solvent molecules and hydrogen atoms have been omitted for clarity.

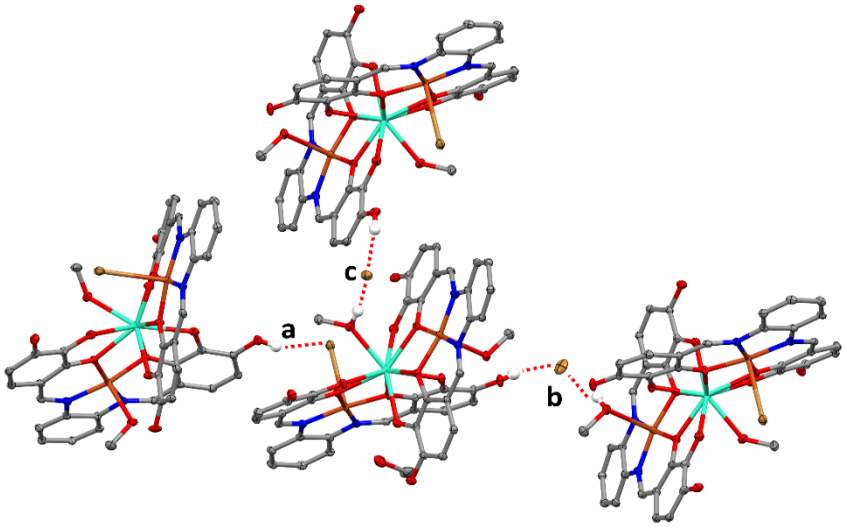

Figure 4.9: X-ray crystal structure showing the intermolecular hydrogen bonding interactions present in complexes **C6** – **C11**. Non interacting hydrogens and solvent species have been omitted for clarity.

a 1D chain with Ln–Ln distances far larger than for the rest of the chloride series, **C13** – **C15**. The chloride containing series (**C13** – **C15**) has an even more extensive π-π stacking network with each of the six aromatic rings involved in π-π stacking. The intrachain π-π stacking interactions are identical to those found in the bromide series, with two pairs of two π-π stacking interactions linking neighbouring complexes (Figure 4.6). The remaining two rings each have a single π-π stacking with a complex in a separate chain (Figure 4.10). This results in a supramolecular 3D

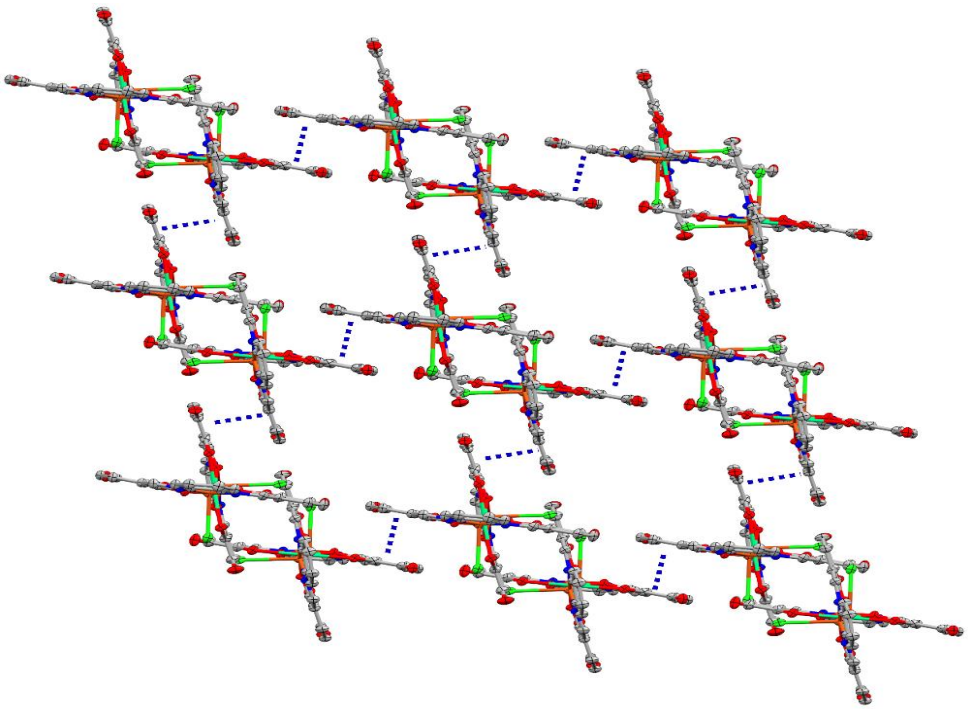

Figure 4.10: X-ray crystal structure showing the crystal packing for complexes **C13** – **C15** viewed along the chains. Blue dashed lines indicate interchain π-π stacking. Solvent molecules and hydrogen atoms have been omitted for clarity.

lattice with individual complexes packed much closer than the bromide analogues. Lists of the relevant Ln–Ln distances and π-π stacking distances and angles are found in tables 4.3 and 4.4 respectively.

Table 4.3. Selected Ln-Ln distances for complexes **C6** – **C15**

	Intersheet Ln–Ln (Å)	Interchain Ln–Ln (Å)	Intrachain Ln–Ln (Å)
C6	10.472	11.163	11.554
C7	10.520	11.125	11.507
C8	10.290	10.953	11.471
C9	10.221	10.874	11.474
C10	10.290	10.953	11.471
C11	10.221	10.874	11.474
C12	-	10.787	12.462
C13	-	8.792	11.837
C14	-	8.977	11.854
C15	-	9.909	11.893

Table 4.4. List of π-π stacking interactions with centroid–centroid distances and angles for complexes **C6** – **C15**

	A	B	C	D	E	F
C6 Distance (Å)	3.702	3.793	-	3.793	3.702	4.028
Angle (°)	0.55	4.40	-	4.03	0.17	10.45
C7 Distance (Å)	3.686	3.757	-	3.757	3.686	4.033
Angle (°)	0.71	2.80	-	4.11	0.55	11.94
C8 Distance (Å)	-	3.770	3.696	3.989	3.696	3.770
Angle (°)	-	4.21	0.44	16.03	0.27	3.85
C9 Distance (Å)	3.685	3.763	-	3.763	3.685	4.021
Angle (°)	0.51	3.69	-	4.88	0.31	16.51
C10 Distance (Å)	-	3.675	3.593	3.675	3.593	3.835
Angle (°)	-	1.53	2.83	5.69	1.99	0.35
C11 Distance (Å)	-	3.676	3.590	3.788	3.590	3.676
Angle (°)	-	2.08	1.86	9.46	1.66	4.74
C12 Distance (Å)	-	3.766	3.766	3.600	-	-
Angle (°)		0.58	0.54	0.07		
C13 Distance (Å)	3.901	3.901	3.461	3.901	3.901	3.461
Angle (°)	2.69	1.39	3.31	2.69	1.39	3.31
C14 Distance (Å)	3.526	3.865	3.865	3.526	3.865	3.865
Angle (°)	5.14	1.11	4.58	5.14	1.11	4.58
C15 Distance (Å)	4.102	3.666	3.666	4.102	3.666	3.666
Angle (°)	0.83	9.09	6.98	0.83	9.09	6.98

4.2.3 Magnetic Analysis

DC magnetic susceptibility and magnetisation measurements were initially performed on the diamagnetic yttrium containing complexes **C6** (Br) and **C12** (Cl) to assess the Cu–Cu interactions. The $\chi_m T$ products reached a maximum of 0.84 and 0.81 cm^3 K mol^{-1} at 300 K (Figure 4.11 and Table 4.5), indicative of two isolated S = ½ spins with g = 2.08 and 2.12, for complexes **C6** and **C12**, respectively, which agrees with the expected value of ca. 2.1. There was virtually no change in the $\chi_m T$ plot indicating a lack of any exchange interactions between the Cu^{II} centres. The magnetisation values for both complexes were nearly identical, 2.14 and 2.13 $N_A\mu_B$ at 7 T for complexes **C6** and **C12**, respectively, exceeding the theoretical saturation magnetisation of 2.0 $N_A\mu_B$. The $\chi_m T$ product for the gadolinium containing complexes **C7** (Br) and **C13** (Cl) reached a maximum of 8.37 and 7.83 cm^3 K mol^{-1} at 300 K which are close to the theoretical spin-only value of 8.63 cm^3 K mol^{-1}. They also showed a sharp increase in the $\chi_m T$ plot when cooled below ca. 60 K reaching a peak at ca. 5 K of 11.8 and 11.0 cm^3 K mol^{-1} for complexes **C7** and **C13**, respectively. Furthermore, the monotonic increase in $\chi_m T$ values upon cooling is also indicative of the presence of ferromagnetic exchange interactions.

The exchange model is $\mathcal{H} = -2J\left(\hat{S}_{\mathrm{Cu1}} \cdot \hat{S}_{\mathrm{Gd}} + \hat{S}_{\mathrm{Gd}} \cdot \hat{S}_{\mathrm{Cu2}}\right)$, and the following van Vleck equation was given.

$$\chi_m T = \frac{N_A \mu_B g^2}{3 k_B T} \times \frac{165 + 84\exp\left(-\frac{9J}{k_B T}\right) + 35\exp\left(-\frac{16J}{k_B T}\right) + 84\exp\left(-\frac{7J}{k_B T}\right)}{5 + 4\exp\left(-\frac{9J}{k_B T}\right) + 3\exp\left(-\frac{16J}{k_B T}\right) + 4\exp\left(-\frac{7J}{k_B T}\right)} \times a$$

Here, 2J implies the exchange coupling constant, and the purity factor is confined to a. The parameters were optimised as $2J/k_B$ = 12.18(12) and 11.6(2) K and a = 0.9428(7) and 0.8940(12) for **C7** and **C13**, respectively. The curves calculated form the van Vleck equation matched the experimental data (Figure 4.11 top). The magnetisation measurements for complexes **C7** and **C13** reached a maximum of 8.95 and 9.06 $N_A\mu_B$ at 7 T, respectively, which is in agreement with the theoretical saturation magnetisation. A slight anomaly was recorded in the AC magnetic susceptibility measurements for complex **C7** at an applied 2000 Oe DC field below ca. 5 K (Figure 4.12).

Table 4.5. DC magnetic susceptibility and magnetisation data for complexes **C6** – **C15**				
	$\chi_m T$ cm^3 K mol^{-1} (exp. at 300 K)	$\chi_m T$ (calc.)	$M/N_A\mu_B$ (exp. at 7 T)	M (calc.)
C6	0.84	0.75	2.14	2
C7	8.37	8.63	8.95	9
C8	11.77	12.30	6.80	11.2
C9	14.13	12.64	7.12	11.2
C12	0.81	0.75	2.13	2
C13	7.83	8.63	9.06	9
C14	12.23	12.30	7.11	11.2
C15	12.81	12.64	6.94	11.2

The $\chi_m T$ product for the erbium containing complexes **C8** and **C14** (Figure 4.13, top) reached a maximum of 11.77 and 12.20 cm^3 K mol^{-1} at 300 K respectively, which nears the theoretical value of 12.30 cm^3 K mol^{-1}. The $\chi_m T$ plot for **C8** and **C14** shows a monotonic decrease upon cooling to ca. 5 K indicative of weak antiferromagnetic coupling and/or crystal field splitting of the Er^{III} ion.[130] Below this temperature the $\chi_m T$ value for **C8** sharply increases indicating Er–Cu ferromagnetic exchange coupling. On the other hand, the $\chi_m T$ plot for **C14** shows a monotonic decrease upon cooling, indicating that any possible Er–Cu ferromagnetic exchange coupling

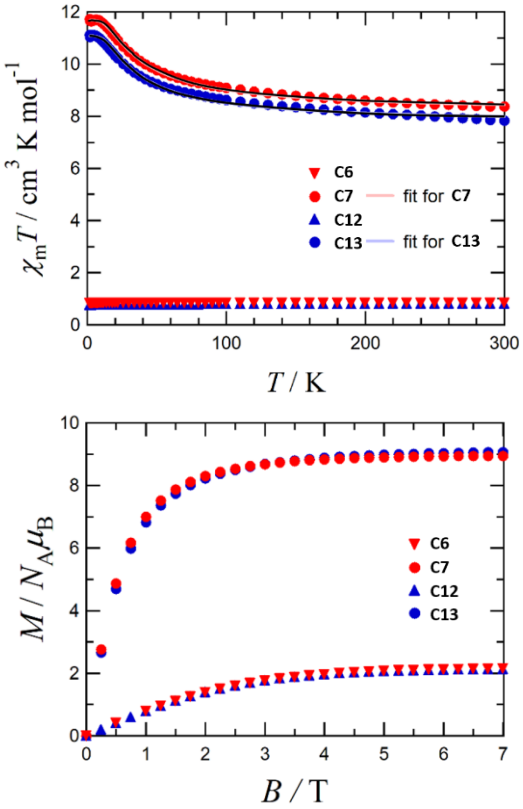

Figure 4.11: Superpositions of the $\chi_m T$ – T (500 Oe, top) and M – H (1.8 K, bottom) curves for complexes **C6**, **C7**, **C12**, and **C13**. A solid line indicates the best fit calculated from the van Vleck equation (see the main text).

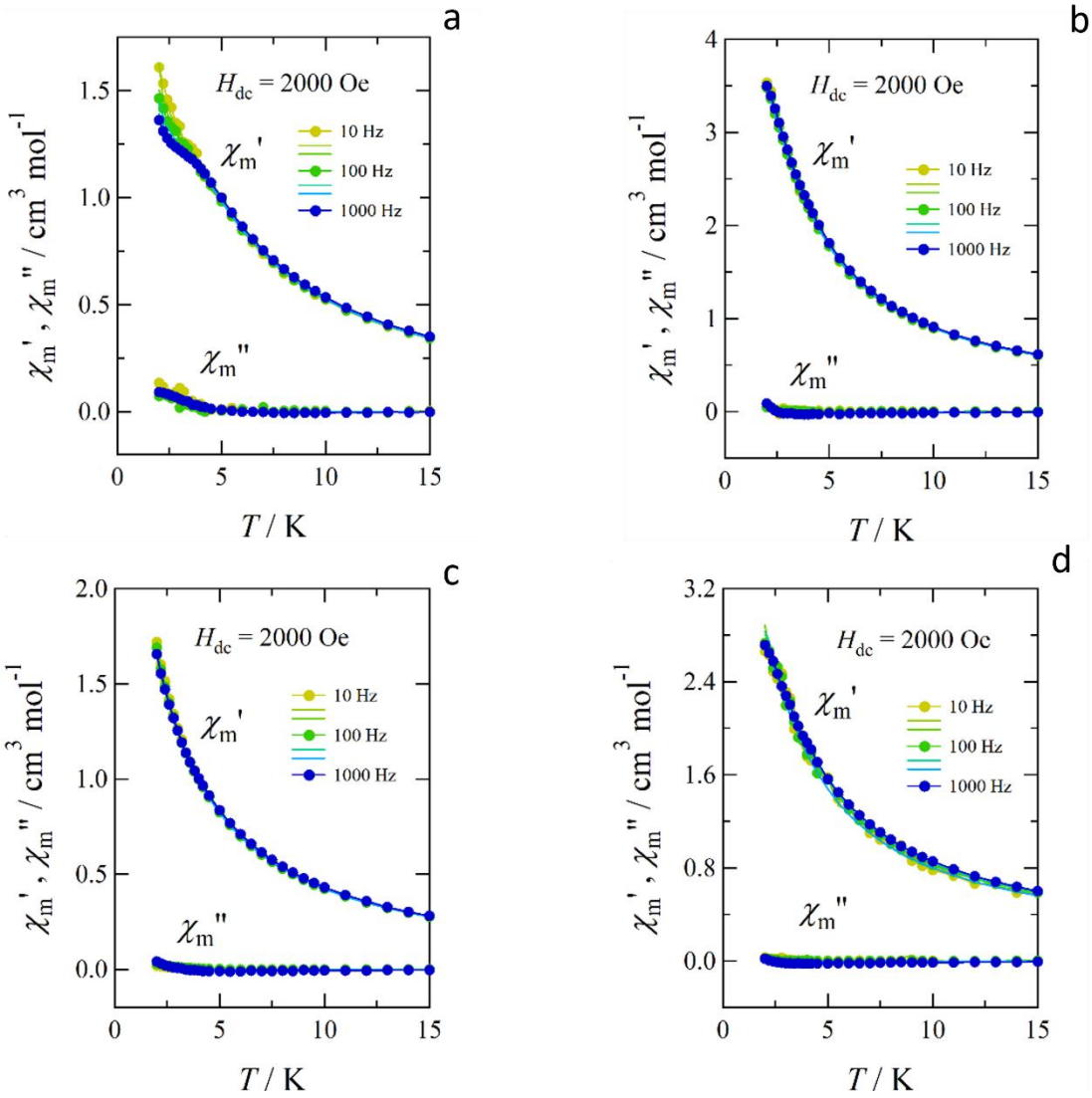

Figure 4.12: In-phase (χ') and out-of-phase (χ'') AC magnetic susceptibilities as a function of temperature with a DC bias field (2000 Oe) for (a) **C7**, (b) **C8**, (c) **C13**, and (d) **C14**.

would be negligible. The magnetisation values at 7 T were 6.80 and 7.11 $N_A\mu_B$ for **C8** and **C14**, respectively, which are ca. 61% and 63% the theoretical spin only value of 11.2 $N_A\mu_B$. The lower than expected magnetisation value can be likely due to the magnetic anisotropy of the erbium ion.

The bromide containing terbium complex **C9** has an experimental χ_mT value of 14.13 cm^3 K mol^{-1} at 300 K which is greater than the theoretical value of 12.64 cm^3 K mol^{-1}. The chloride containing terbium complex **C15** has an experimental χ_mT value of 12.81 cm^3 K mol^{-1} at 300 K which is in good agreement of the theoretical value. The χ_mT values of both **C9** and **C15** monotonically increase upon cooling until ca. 40 K where a sharp increase is observed which is indicative of ferromagnetic exchange coupling (Figure 4.13, top). A decrease in the χ_mT value is observed below ca. 10 K which is attributed to the crystal-field splitting of the terbium ions. The

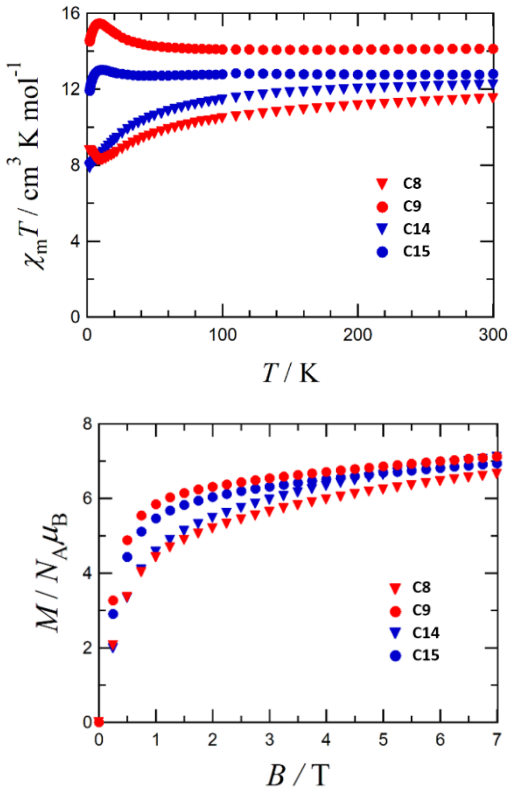

Figure 4.13: Superpositions of the $\chi_m T$ – T (500 Oe, top) and M – H (1.8 K, bottom) curves for complexes **C8**, **C9**, **C14**, and **C15**.

magnetisation value at 7 T was 7.12 and 6.94 $N_A\mu_B$ for complexes **C9** and **C15**, respectively, which are ca. 64% and 62% the theoretical spin only value of 11.2 $N_A\mu_B$, which again is likely due to the magnetic anisotropy of the terbium ion.

AC susceptibility measurements were performed for all of Gd, Er and Tb derivatives (Figure 4.12, Figure 4.14, and Figure 4.15). Complexes **C9** (Br) and **C15** (Cl) exhibited features typical of SMMs such as an onset of out-of-phase AC susceptibility without any bias DC field (Figure 4.14, left and Figure 4.15, left). The frequency-dependence was much clearer under an applied 1000 or 2000 Oe DC field at temperatures below ca. 5 K (Figure 4.14, right and Figure 4.15, right). This is indicative of the blocking of magnetisation due to an anisotropy barrier. The shift of the maximum in the $\chi_m''T$ product was observed upon application of a 1000 Oe DC field, which is

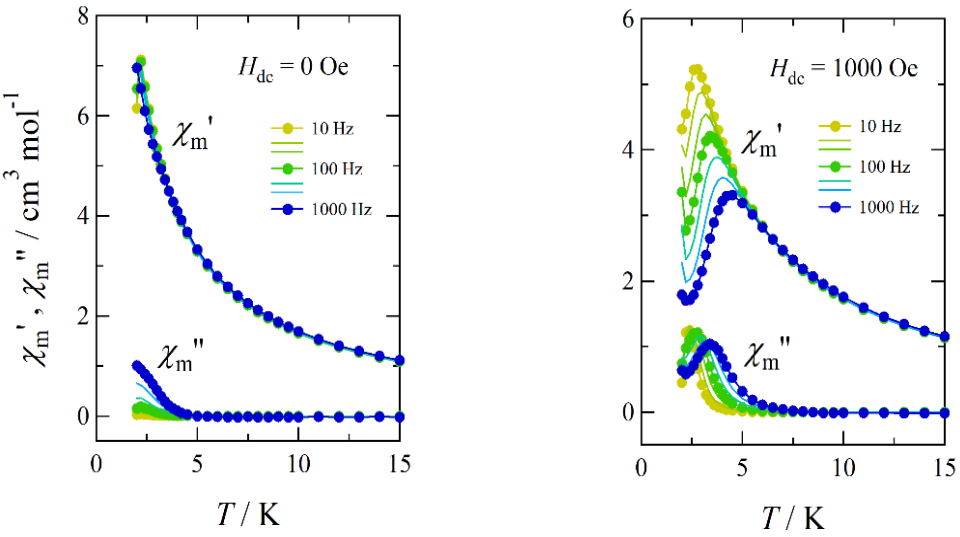

Figure 4.14: In-phase (χ') and out-of-phase (χ") AC magnetic susceptibilities as a function of temperature and DC bias field (0 Oe, left, and 1000 Oe, right) for **C9.**

indicative of suppression of QTM. QTM is common in terbium complexes due to the non-Kramers nature of the terbium ion.[131] The effective barrier, U_{eff}, for **C9** and **C15** was calculated for the zero-DC field data using a modified Arrhenius plot[33] (Figure 4.16, a and b). These values are 17.8(6) and 16.0(9) K with pre-exponential factors (τ_0) of 3.0(5) x 10^{-8} and 4.1(11) x 10^{-8} s for **C9** and **C15**, respectively. Additionally, according to the Arrhenius analysis (Figure 4.16, c and d), the U_{eff} values measured at applied fields of 1000 Oe for **C9** and 2000 Oe for **C15** are 32.3(12) and 30.2(13) K with the t_0 values of 1.1(5) x 10^{-8} and 4.0(17) x 10^{-8} s, respectively. Based on the

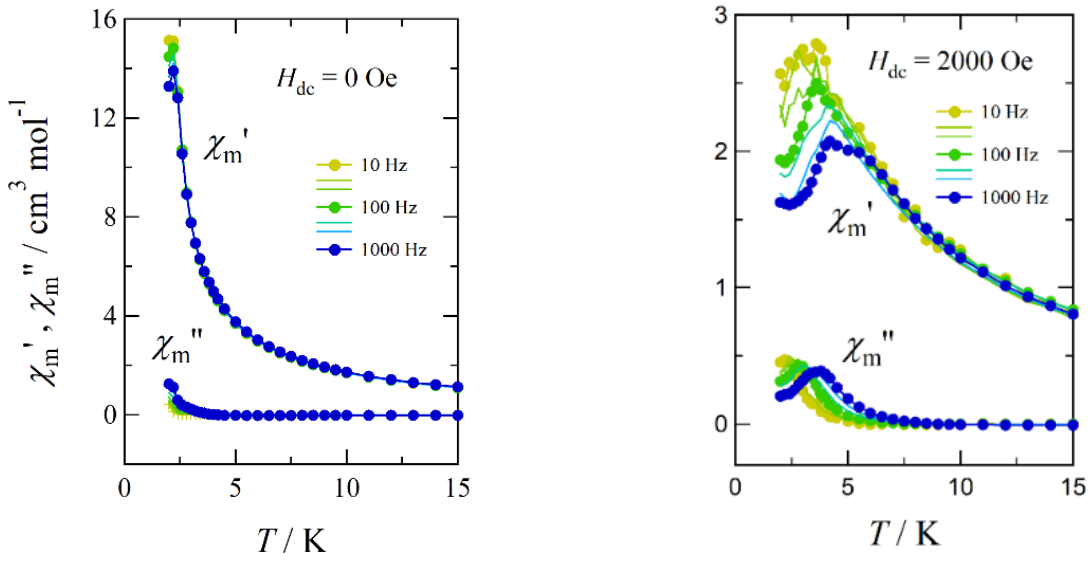

Figure 4.15: In-phase (χ') and out-of-phase (χ") AC magnetic susceptibilities as a function of temperature and DC bias field (0 Oe, left; 1000 Oe, centre; 2000 Oe, right) for **C15**.

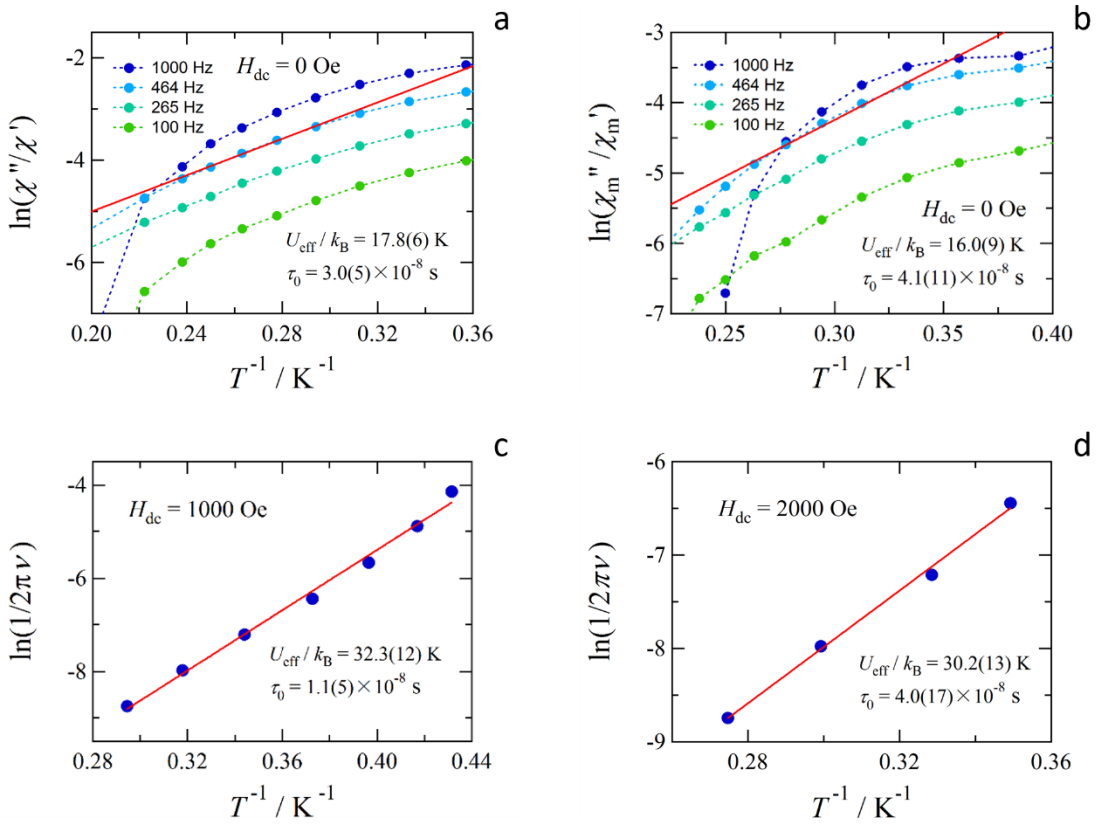

Figure 4.16: Modified Arrhenius plot of complexes **C9** (a and c) and **C15** (b and d), measured at zero bias field (a and b) 1000 Oe bias field (c), and 2000 Oe bias field (d).

AC susceptibility data for **C9** in a 1000 Oe applied field, a Cole-Cole plot [34] can be drawn to show the relationship between in-phase (χ') and out-of-phase (χ'') data (Figure 4.17). The best fit semi-circular lines were given for 3.0 – 3.6 K. The obtained distribution index α, which is related to the distribution of relaxation times, is in the range 0.28 – 0.37, inversely proportional to temperature (Table C1). The relatively low values of α, indicate the presence of a single

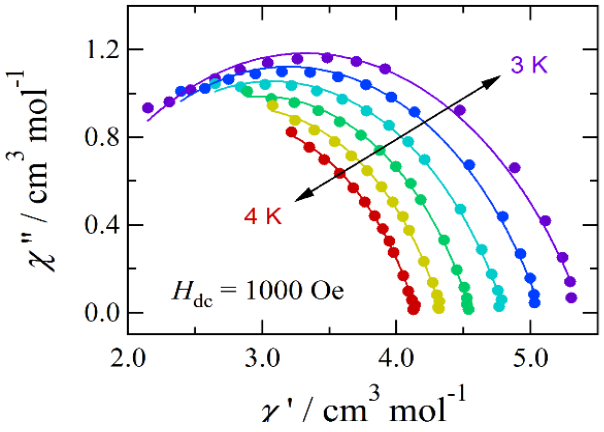

Figure 4.17: Cole-Cole plot for **C9**, acquired in a bias field 1000 Oe. The solid lines imply the best fit to the generalised Debye model.

relaxation mechanism possessing a broad range of relaxation times. A Cole-Cole plot for complex **C15** could not be drawn as the data was too scattered.

4.3 Literature Comparison

A greater understanding of the DC magnetic behaviour can be found by comparing to the research performed by Salmon *et al*. who investigated the nature of the exchange interactions present in a series of trinuclear Cu_2X complexes (X = U^{IV} or Th^{IV}).[132] Utilising a variety of 2,3-dihydroxy benzaldehyde based Schiff base ligands similar to H_6**L1** utilised throughout this thesis, they found that complexes with larger Cu-X distances showed antiferromagnetic exchange between the Cu-X centres as well as antiferromagnetic exchange between the two copper centres. However, smaller Cu-X distances yielded ferromagnetic exchange between the Cu-X centres as well as no interaction between copper centres. As the Cu-Ln distances of the complexes presented in this thesis are smaller than the Cu-X distances presented in Salmon's research, the lack of Cu-Cu exchange interactions as well as the ferromagnetic exchange found in the Cu-Gd complexes **C7** and **C13** are to be expected.

Several examples of Cu_2Ln complexes adopting similar coordination motifs to the work presented in this chapter are found in the literature.[133-135] Research performed by Chen *et al*. utilised ligands that possess two hydroxy and two methoxy groups capable of binding to a central dysprosium ion (Figure 4.18, a/b).[133] These produced zero-field SMMs with U_{eff} = 17.16 and 39.06 K for ligands a and b respectively, a third ligand with an identical amine backbone to that

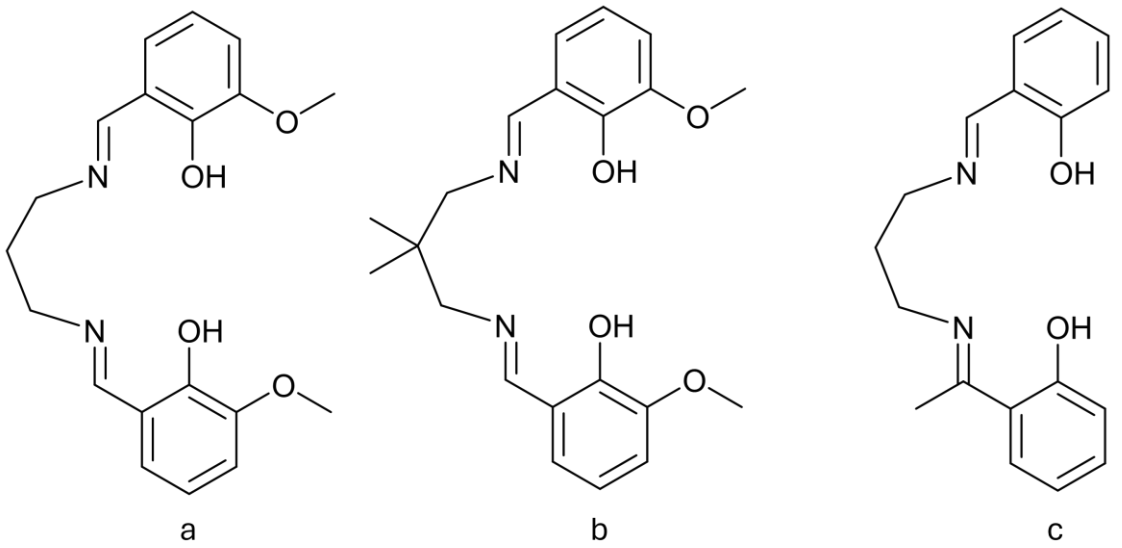

Figure 4.18: Ligands utilised by Chen *et al.* (a and b) and Mahapatra *et al*. (c) which produced complexes displaying SMM behaviour.

present in H_6**L1** failed to show any zero-field SMM behaviour, possibly due to the 'sandwich' coordination motif it adopted . Chen's analysis of the magnetic behaviour showed that the alignment of the easy axis of magnetisation with the Cu-Dy-Cu plane determined the strength of the energy barrier. However, this could also be due to the difference in superstructure, with b forming discrete trinuclear complexes whilst a formed one-dimensional chains connected through chlorido ligands axially bound to the copper centres. The higher U_{eff} value obtained for b (39.06 K) compared to complexes **C9** and **C15** (17.8 and 16.0 K respectively) from this chapter, is likely due to the alignment of the easy axis of magnetisation.

Mahapatra *et al*. utilised a ligand containing two hydroxy groups capable of binding to a lanthanide ion to produce two SMM's, one with dysprosium and the other with terbium (Figure 4.18, c).[134] This lower coordination, compared to ligands used in this thesis, enabled the central lanthanide ion to bind to two ligand units as well as three nitrate ions. This produced SMMs with U_{eff} = 36 and 26 K for the terbium and dysprosium analogues respectively. The higher energy barrier for the complexes produced by Mahapatra *et al*. compared to complexes **C9** and **C15** is possibly due to bound nitrate ions providing a stronger axial coordination environment. This would enhance the intrinsic anisotropy of the lanthanide ions leading to the higher energy barriers.

4.4 Conclusions

Ten new trinuclear $[(H_4\mathbf{L1})_2Cu^{II}_2Ln^{III}]$ complexes and one tetranuclear $[(H_4\mathbf{L1})_2H_2\mathbf{L1}LaCu_3]$ have been successfully synthesised. The tetranuclear complex **C5** established an upper limit on the size of the lanthanide able to be used for further development of the trinuclear complex series. The trinuclear complexes **C6** – **C15** fall into one of two series depending on the type of anion present, chloride, or bromide. X-ray analysis revealed that the Cu–Ln bond distances decreased with the decreasing size of the lanthanide as well as the smaller size of the anion. Further analysis showed that the intramolecular hydrogen bonding interactions do not significantly alter the Cu–Ln distance, with the hydrogen bonding distances increasing from MeOH < Cl < Br, whilst the Cu–Ln distance increases from Cl < Br < MeOH. Analysis of the supramolecular structures revealed that the bromide containing complexes, **C6** – **C11**, formed 2D sheets whilst the chloride containing complexes, **C12** – **C15**, formed a 3D network. This, combined with the smaller size of the chloride ion results in a decrease in the smallest inter-complex Ln–Ln distance.

Compared with the nickel series, **C1** – **C4**, presented in Chapter 3, the copper containing complexes tend to have fewer intermolecular secondary interactions and less dense crystal

packing. This is due to the five-coordinate copper centres having two more species directly bound to the complex compared to the four-coordinate nickel complexes. This added bulk prevents the extensive π-π stacking networks found in the nickel series being replicated in the copper series.

DC magnetic susceptibility measurements of the yttrium containing complexes, **C6** and **C12**, revealed no magnetic interaction between the two copper centres suggesting that all magnetic activity is either entirely due to the lanthanide ion or copper–lanthanide coupling. Further magnetic analysis revealed that the erbium containing complexes **C8** and **C14**, exhibited weak antiferromagnetic coupling between the copper and erbium ions and/or crystal field splitting of the erbium ion. Below ca. 10 K, the bromide containing complex **C8** showed possible ferromagnetic exchange coupling whilst the chloride containing complex **C14** did not. The gadolinium and terbium containing complexes (**C7**, **C13** and **C9**, **C15** respectively) both exhibited ferromagnetic coupling with a sharp uptick in susceptibility below ca. 50 K. AC magnetic susceptibility measurements revealed that complexes **C9** and **C15** exhibited zero-field SMM behaviour with U_{eff} of 17.8(6) and 16.0(9) K respectively. Presence of QTM was identified by the shift in the χ_m" maximum in the presence of an applied 1000 or 2000 Oe DC field. A Cole-Cole plot was able to be drawn for the bromide containing complex **C9** suggesting the presence of a single relaxation mechanism. Overall, this chapter suggests that the steric effects of the bulkier bromide ion works to physically isolate the magnetic centres of the complexes, enhancing the resultant magnetic properties.

Complex Preparation

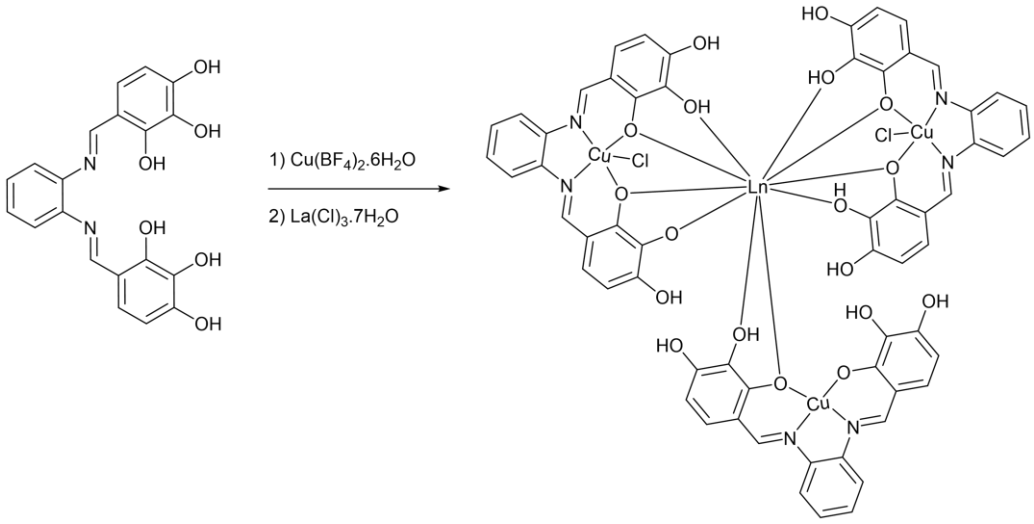

Figure 4.19: Schematic showing the complexation reaction undertaken by complex **C5**.

C5 $[(H_4\mathbf{L1})_2(H_2\mathbf{L1})LaCl_2](MeOH)_5Na$: Was obtained by the addition of $Cu(BF_4)_2{\cdot}6H_2O$ (0.0345 g, 0.1 mmol, 2eq.) in MeOH (7.5 mL) to a solution of $H_6\mathbf{L1}$ (0.0380 g, 0.1 mmol, 2eq.) at 50 °C in MeOH (5 mL) resulting in a light red solution. A solution of $LaCl_3{\cdot}7H_2O$ (0.0186 g, 0.05 mmol, 1eq.) in MeOH (7.5 mL) was added and the reaction mixture was stirred at 50 °C for 30 minutes before being cooled to RT. Vapour diffusion of Et_2O into the reaction mixture yielded red plate shaped crystals after 5 weeks. Yield 6% based on $LaCl_3{\cdot}7H_2O$. ESI-MS *m/z* 1020.40 $[(H_3\mathbf{L1})_2Cu_2La]^+$, 510.75 $[(H_3\mathbf{L1})(H_4\mathbf{L1})Cu_2La]^{2+}$.

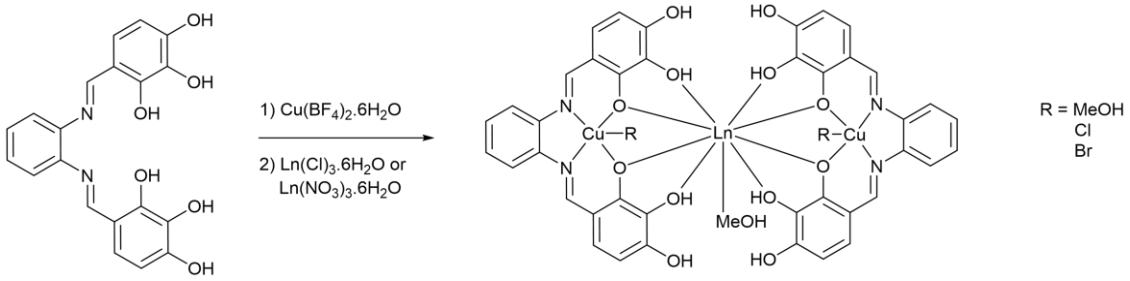

Figure 4.20: Schematic showing the complexation reaction undertaken by complexes **C6** – **C15**.

Complexes **C6** – **C15** were obtained by the addition of $Cu(BF_4)_2{\cdot}6H_2O$ (0.0345 g, 0.1 mmol, 2eq.) in MeOH (5 mL) to a solution of $H_6\mathbf{L1}$ (0.0380 g, 0.1 mmol, 2eq.) at 50 °C in MeOH (5 mL) resulting in a dark red solution. A solution of $Ln{\cdot}6H_2O$ (0.05 mmol, 1eq.) in MeOH (5 mL) (Ln = $Y(NO_3)_3$, $Gd(NO_3)_3$, $DyCl_3$, $HoCl_3$, $ErCl_3$ or $TbCl_3$) was added and the reaction mixture was stirred at 50 °C for 30 minutes. Addition of TBAX (1 mmol, 10eq.) in MeOH (5 mL) followed with stirring

at RT for a further 30 minutes (X = Br for complexes **C6** – **C11** or Cl for complexes **C12** – **C15**). Vapour diffusion of Et_2O into the reaction mixture yielded the complexes **C6** – **C15**.

C6 $[(H_4\mathbf{L1})_2Cu_2Y(MeOH)_2Br](MeOH)_4Br_{1.8}Et_2O(NO_3)_{0.2}$: Red needle shaped crystals were obtained after 4 weeks. Yield 22% based on $Y(NO_3)_3{\cdot}6H_2O$. ATR-IR $\bar{\nu}$: 3140, 1602, 1581, 1558, 1498, 1463, 1384, 1344, 1281, 1187, 1087, 1005, 871, 794, 751, 722, 630, 597, 539 cm^{-1}. Elemental analysis calculated (%) for $C_{40}H_{28}N_4O_{12}Cu_2Y{\cdot}Br_3(MeOH)_6Et_2O$: C 40.61, H 4.23, N 3.79; found C 38.69, H 4.07, N 3.69. ESI-MS *m/z* 970.81 $[(H_3\mathbf{L1})_2Cu_2Y]^+$, 485.59 $[(H_3\mathbf{L1})(H_4\mathbf{L1})Cu_2Y]^{2+}$.

C7 $[(H_4\mathbf{L1})_2Cu_2Gd(MeOH)_2Br](MeOH)_4Br_{1.6}Et_2O(NO_3)_{0.4}$: Red needle shaped crystals were obtained after 4 weeks. Yield 38% based on $Gd(NO_3)_3{\cdot}6H_2O$. ATR-IR $\bar{\nu}$: 3131, 1626, 1602, 1557, 1553, 1538, 1495, 1456, 1436, 1386, 1279, 1185, 1086, 1001, 871, 793, 751, 720, 655, 593, 539 cm^{-1}. Elemental analysis calculated (%) for $C_{40}H_{28}N_4O_{12}Cu_2Gd{\cdot}Br_3(MeOH)_6Et_2O$: C 38.82, H 4.04, N 3.62; found C 38.56, H 4.18, N 3.55. ESI-MS *m/z* 1037.95 $[(H_3\mathbf{L1})_2Cu_2Gd]^+$, 520.16 $[(H_3\mathbf{L1})(H_4\mathbf{L1})Cu_2Gd]^{2+}$.

C8 $[(H_4\mathbf{L1})_2Cu_2Er(MeOH)_2Br](MeOH)_{3.8}Br_2Et_2O$: Red needle shaped crystals were obtained after 4 weeks. Yield 44% based on $ErCl_3{\cdot}6H_2O$. ATR-IR $\bar{\nu}$: 3168, 1623, 1600, 1557, 1498, 1456, 1382, 1338, 1280, 1196, 1091, 1012, 798, 754, 723 cm^{-1}. Elemental analysis calculated (%) for $C_{40}H_{28}N_4O_{12}Cu_2Er{\cdot}Br_3(MeOH)_6Et_2O$: C 38.57, H 4.01, N 3.60; found C 38.53, H 4.24, N 3.57. ESI-MS *m/z* 1048.04 $[(H_3\mathbf{L1})_2Cu_2Er]^+$, 524.66 $[(H_3\mathbf{L1})(H_4\mathbf{L1})Cu_2Er]^{2+}$.

C9 $[(H_4\mathbf{L1})_2Cu_2Tb(MeOH)_2Br](MeOH)_4Br_2Et_2O$: Red needle shaped crystals were obtained after 6 weeks. Yield 31% based on $TbCl_3{\cdot}6H_2O$. ATR-IR $\bar{\nu}$: 3111, 1626, 1602, 1557, 1495, 1455, 1386, 1280, 1187, 1002, 794, 751, 720 cm^{-1}. Elemental analysis calculated (%) for $C_{40}H_{28}N_4O_{12}Cu_2Tb{\cdot}Br_3(MeOH)_6Et_2O$: C 38.78, H 4.04, N 3.62; found C 38.68, H 4.18, N 3.57. ESI-MS *m/z* 1040.98 $[(H_3\mathbf{L1})_2Cu_2Tb]^+$, 520.72 $[(H_3\mathbf{L1})(H_4\mathbf{L1})Cu_2Tb]^{2+}$.

C10 $[(H_4\mathbf{L1})_2Cu_2Dy(MeOH)H_2OBr](MeOH)_2(H_2O)Br_2Et_2O$: Red block shaped crystals were obtained after 3 weeks. Yield 19% based on $DyCl_3{\cdot}6H_2O$. ATR-IR $\bar{\nu}$: 3111, 1627, 1602, 1557, 1498, 1461, 1386, 1282, 1188, 1090, 1004, 795, 752, 721, 658 cm^{-1}. ESI-MS *m/z* 1044.04 $[(H_3\mathbf{L1})_2Cu_2Dy]^+$, 522.22 $[(H_3\mathbf{L1})(H_4\mathbf{L1})Cu_2Dy]^{2+}$.

C11 $[(H_4\mathbf{L1})_2Cu_2Ho(MeOH)H_2OBr](MeOH)_2(H_2O)Br_2Et_2O$: Red plate shaped crystals were obtained after 3 weeks. Yield 28% based on $HoCl_3{\cdot}6H_2O$. ATR-IR $\bar{\nu}$: 3167, 1625, 1602, 1560, 1497, 1460, 1385, 1281, 1187, 1089, 1004, 872, 795, 752, 722, 658, 598, 540 cm^{-1}. ESI-MS *m/z* 1047.07 $[(H_3\mathbf{L1})_2Cu_2Ho]^+$, 523.75 $[(H_3\mathbf{L1})(H_4\mathbf{L1})Cu_2Ho]^{2+}$.

C12 $[(H_4\mathbf{L1})_2Cu_2Y(MeOH)_2(NO_3)_{0.5}Cl_{0.5}](MeOH)_3ClEt_2O(NO_3)$: Red needle shaped crystals were obtained after 7 weeks. Yield 14% based on $Y(NO_3)_3{\cdot}6H_2O$. ATR-IR $\bar{\nu}$: 3131, 1629, 1603, 1582, 1560, 1498, 1462, 1388, 1345, 1282, 1231, 1190, 1093, 1005, 872, 795, 753, 722, 658, 540, 485 cm^{-1}. Elemental analysis calculated (%) for $C_{40}H_{28}N_4O_{12}Cu_2Y{\cdot}Cl_3(MeOH)_5Et_2O$: C 42.26, H 4.19, N 4.16; found C 44.64, H 4.65, N 4.16. ESI-MS *m/z* 970.83 $[(H_3\mathbf{L1})_2Cu_2Y]^+$, 485.55 $[(H_3\mathbf{L1})(H_4\mathbf{L1})Cu_2Y]^{2+}$.

C13 $[(H_4\mathbf{L1})_2Cu_2GdCl_2](MeOH)_9ClEt_2O$: Red needle shaped crystals were obtained after 8 weeks. Yield 18% based on $Gd(NO_3)_3{\cdot}6H_2O$. ATR-IR $\bar{\nu}$: 2989, 1600, 1553, 1489, 1456, 1386, 1338, 1280, 1187, 1087, 1010, 752, 720 cm^{-1}. Elemental analysis calculated (%) for $C_{40}H_{28}N_4O_{12}Cu_2Gd{\cdot}Cl_3(MeOH)_6Et_2O$: C 42.48, H 4.42, N 3.96; found C 42.16, H 4.38, N 4.02. ESI-MS *m/z* 1039.95 $[(H_3\mathbf{L1})_2Cu_2Gd]^+$, 520.16 $[(H_3\mathbf{L1})(H_4\mathbf{L1})Cu_2Gd]^{2+}$.

C14 $[(H_4\mathbf{L1})_2Cu_2ErCl_2](MeOH)_6ClEt_2O$: Red plate shaped crystals were obtained after 10 weeks. Yield 16% based on $ErCl_3{\cdot}6H_2O$. ATR-IR $\bar{\nu}$: 3164, 1628, 1604, 1562, 1499, 1461, 1387, 1346, 1283, 1232, 1190, 1093, 1006, 873, 795, 753, 723, 660, 598, 540, 485 cm^{-1}. Elemental analysis calculated (%) for $C_{40}H_{28}N_4O_{12}Cu_2Er{\cdot}Cl_3(MeOH)_6Et_2O$: C 41.18, H 4.39, N 3.94; found C 42.19, H 4.37, N 3.84. ESI-MS *m/z* 1047.95 $[(H_3\mathbf{L1})_2Cu_2Er]^+$, 524.66 $[(H_3\mathbf{L1})(H_4\mathbf{L1})Cu_2Er]^{2+}$.

C15 $[(H_4\mathbf{L1})_2Cu_2TbH_2OCl_2](H_2O)_2(MeOH)_7Cl$: Red plate shaped crystals were obtained after 10 weeks. Yield 27% based on $TbCl_3{\cdot}6H_2O$. ATR-IR $\bar{\nu}$: 3098, 1627, 1603, 1559, 1498, 1460, 1387, 1345, 1283, 1230, 1189, 1086, 1006, 872, 794, 722, 657, 595, 539, 503, 484 cm^{-1}. Elemental analysis calculated (%) for $C_{40}H_{28}N_4O_{12}Cu_2Tb{\cdot}Cl_3(MeOH)_6Et_2O$: C 42.43, H 4.42, N 3.96; found C 42.63, H 4.18, N 3.90. ESI-MS *m/z* 1040.95 $[(H_3\mathbf{L1})_2Cu_2Tb]^+$, 520.72 $[(H_3\mathbf{L1})(H_4\mathbf{L1})Cu_2Tb]^{2+}$.

Chapter 5

Alternative Research Avenues

Throughout the course of this research multiple research pathways were explored, with the series covered in Chapters 3 and 4 encompassing the bulk of this thesis's focus. This chapter focuses on the work that doesn't fit into the themes of previous chapters but was still important to the completion of this research. This includes our research into a potential six-coordinate TM centre, which would allow us to modulate a greater number of secondary interactions. It also includes our research into a nitrate series of complexes, analogous to the work presented in Chapter 4, which will explore the secondary interactions present with non-halide anions. Finally, this chapter also covers all our research on the sterically bulkier H_6**L2** ligand, to investigate the effects that sterics have on the crystal packing of the resultant complexes.

5.1 Other TM Attempts

The successful synthesis of the nickel and copper series of complexes with H_6**L1** led to attempts to synthesise a series of complexes targeting a six-coordinate transition metal centre. Ions included in these attempts were: Fe^{II}, Fe^{III}, Co^{II}, Zn^{II}, Mn^{II} and Mn^{III}. Of these only the reaction between $MnCl_2$ and H_6**L1** produced an X-ray quality crystal. The compound crystallised in the monoclinic space group *C*2/*c* with the asymmetric unit containing a 3-(1*H*-benzimidazol-2-yl)-1,2,3-benzenetriol molecule, a chloride ion and a MeOH molecule (Figure 5.1).

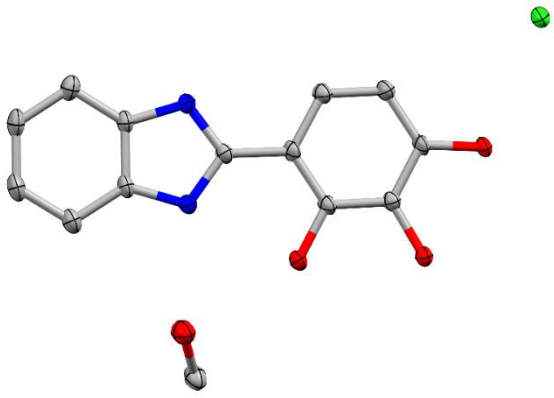

Figure 5.1 X-ray structure of the asymmetric unit of 3-(1*H*-benzimidazol-2-yl)-1,2,3-benzenetriol, hydrogen atoms have been omitted for clarity. Thermal ellipsoids shown at the 30% probability level. Colour code: C, N, O, and Cl are grey, blue, red, and green respectively.

The formation of 3-(1*H*-benzimidazol-2-yl)-1,2,3-benzenetriol was proposed to be a two-step reaction (Scheme 2). First, H_6**L1** undergoes hydrolysis to give the precursors *o*-phenylenediamine, and 2,3,4-trihydroxybenzaldehyde. $MnCl_2$ then catalyses the condensation of these substrates into 3-(1*H*-benzimidazol-2-yl)-1,2,3-benzenetriol. The synthesis of benzimidazoles from a benzaldehyde and *o*-phenylenediamine utilising a manganese catalyst is common throughout the literature, which caused us to abandon further attempts to complex manganese salts with H_6**L1**.[136-138]

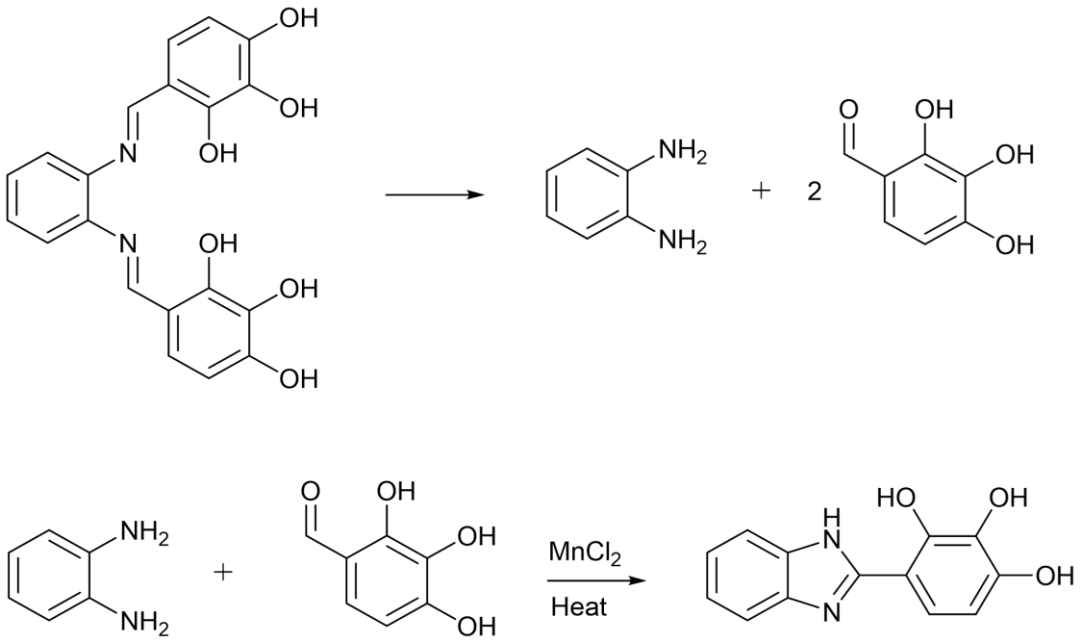

Scheme 2: Proposed reaction scheme for the synthesis of 3-(1*H*-benzimidazol-2-yl)-1,2,3-benzenetriol.

5.2 Nitrate Complexes

A series of complexations between H_6**L1**, a transition metal ion, and a lanthanide ion, in the presence of the nitrate anion, was amongst the first to be attempted. This is owing to the capacity of the nitrate ion to perform hydrogen bonding interactions. The complexes **C16** – **C19** were synthesised by the reaction of a methanolic solution of H_6**L1**, $TM(BF_4)_2{\cdot}6H_2O$, and $Ln(NO_3)_3{\cdot}6H_2O$ (TM = Ni^{II} or Cu^{II}, Ln = Dy^{III}, Gd^{III}, or Y^{III}) in a 2:2:1 molar ratio. Crystalline samples of the complexes were obtained through the vapour diffusion of diethyl ether into the reaction solution over a period of ten to twenty weeks. Complexes **C17** – **C19** had an additional step where 10 eq. of TBAX (X = Cl or Br) was added following addition of the lanthanide species.

5.2.1 Binuclear Complex

The first complex successfully synthesised in this series was the binuclear complex **C16**, which was synthesised by the reaction between H_6**L1** (2 eq.) in MeOH (5 mL) with $Ni(BF_4)_2$ (2 eq.) in MeOH (5 mL) and $Dy(NO_3)_3{\cdot}6H_2O$ (1 eq.) in MeOH (5 mL). **C16** crystallised in the monoclinic space group *P*2/*n*. The Dy^{III} centre of this complex is ten-coordinate with four sites being bound to the outer coordination pocket of a H_4**L1**$^{2-}$ molecule. The remaining six sites are occupied by three κ_2–NO_3 anions. This inner coordination pocket of H_4**L1**$^{2-}$ is occupied by a four coordinate Mg^{II} ion that adopts a square planar geometry. The asymmetric unit of **C16** contains half of the complex structure, with the full complex consisting of an [H_4**L1**$MgDy(NO_3)_3$] unit and two MeOH molecules, which hydrogen bond to the outermost binding phenol group (Figure 5.2).

Each complex unit is involved in two identical π–π stacking interactions (3.489 Å, 6.39°) which form 1D chains, which are further strengthened by the presence of a pair of hydrogen bonds (1.929(9) Å) between the non-coordinating phenol of H_4**L1**$^{2-}$ and a bound nitrate ion of an adjacent complex (Figure 5.3). These chains then assemble into sheets which stack together much like sheets of paper to from the complete crystal structure (Figure 5.4).

Attempts to develop a binuclear series analogous to the trinuclear series covered in Chapters 3 and 4 were unsuccessful due to difficulties in crystallisation. Additionally, the lack of secondary interactions in comparison to the trinuclear complexes and the abundance of similar binuclear complexes in the literature, led to us focusing our research efforts on the more promising trinuclear series.[139-141]

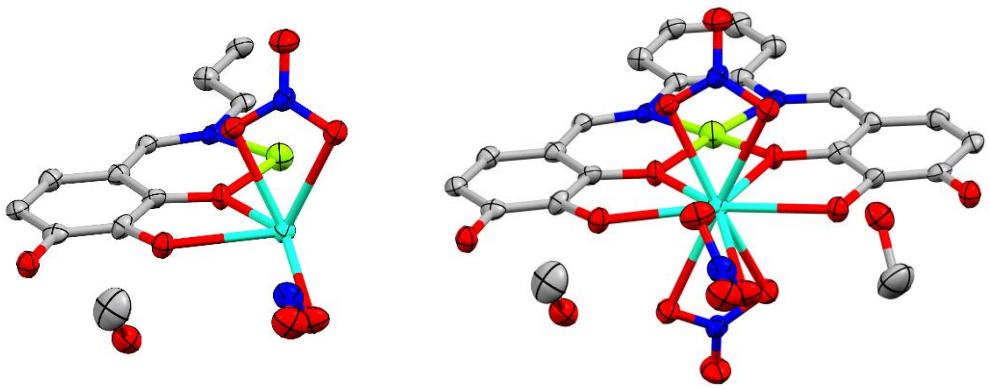

Figure 5.2: X-ray structure of the asymmetric unit (left) and full complex (right) of **C16**. Hydrogen atoms have been omitted for clarity; thermal ellipsoids shown at the 30% probability level. Colour code: C, N, O, Mg, and Dy are grey, blue, red, lime, and cyan, respectively.

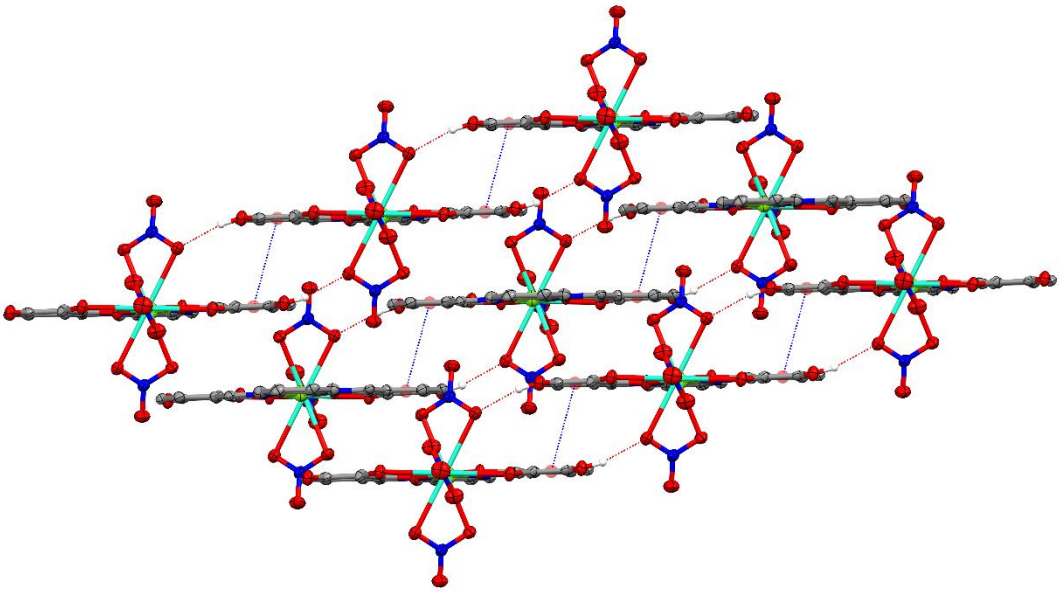

Figure 5.3: X-ray structure showing the supramolecular packing of **C16**. Red dashed lines represent hydrogen bonding interactions, blue dashed lines represents π–π stacking interactions. Non-coordinating solvent molecules and hydrogen atoms have been omitted for clarity. Thermal ellipsoids shown at the 30% probability level. Colour code: C, N, O, Mg, and Dy are grey, blue, red, lime, and cyan, respectively.

5.2.2 Trinuclear Complexes

A small series of three trinuclear nitrate containing complexes **C17** – **C19** were successfully synthesised, all of which crystallised in the monoclinic space group $P2_1/n$. Each Ln^{III} centre is nine-coordinate with eight binding sites occupied by the outer binding pocket of two H_4**L1**$^{2-}$

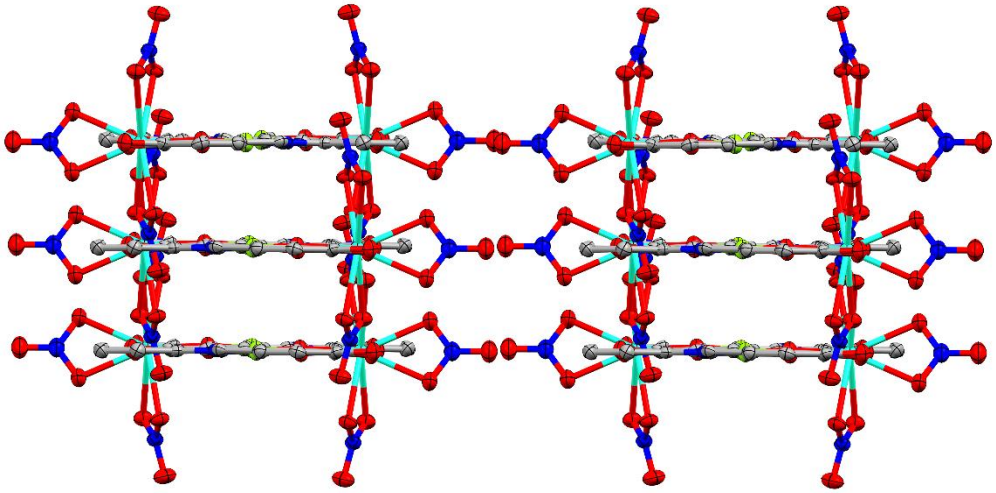

Figure 5.4: X-ray structure showing the supramolecular packing of **C16**. Red dashed lines represent hydrogen bonding interactions, blue dashed lines represents π–π stacking interactions. Non-coordinating solvent molecules and hydrogen atoms have been omitted for clarity. Thermal ellipsoids shown at the 30% probability level. Colour code: C, N, O, Mg, and Dy are grey, blue, red, lime, and cyan, respectively.

ligands and the final site being occupied by either a MeOH (**C17** and **C19**) or H_2O (**C18**) molecule. The two Cu^{II} ions in complex **C17** adopt five-coordinate square pyramidal geometries, with the equatorial sites occupied by the inner coordination pocket of H_4**L1**$^{2-}$ and the axial site occupied by a bromide ion or MeOH molecule The asymmetric unit of **C17** contains the central $[(H_4\mathbf{L1})_2GdCu_2Br(MeOH)_2]^{2+}$ unit as well as four non-coordinating MeOH molecules, a Et_2O molecule, a bromide anion, and a third anion that is split between a 0.6 occupancy bromide and a 0.4 occupancy nitrate anion (Figure 5.5). The Cu^{II} ions for complex **C18** adopt five-coordinate square pyramidal geometries, with the equatorial sites occupied by the inner coordination pocket of H_4**L1**$^{2-}$ and the axial site occupied by a nitrate ion. The asymmetric unit of **C18** contains the central $[(H_4\mathbf{L1})_2GdCu_2(NO_3)_2(H_2O)]$ unit as well as two non-coordinated H_2O molecules and a nitrate anion (Figure 5.6). Complex **C19** also possesses two Cu^{II} ions that are five coordinate, adopting a square pyramidal geometry. The equatorial sites are again occupied by the inner coordination pocket of H_4**L1**$^{2-}$ whilst the axial sites are occupied by nitrate anions. The asymmetric unit of **C19** contains the central $[(H_4\mathbf{L1})_2YCu_2(NO_3)_2(MeOH)]$ unit as well as three non-coordinated MeOH molecules, a nitrate anion, and a Et_2O molecule (Figure 5.7).

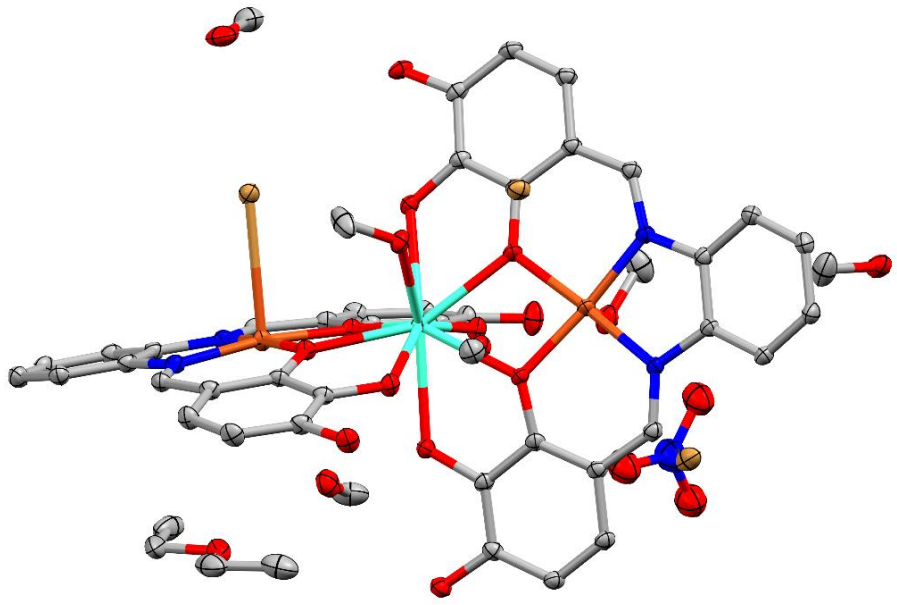

Figure 5.5: X-ray structure of the asymmetric unit of **C17**. Hydrogen atoms have been omitted for clarity; thermal ellipsoids shown at the 30% probability level. Colour code: C, N, O, Cu, Br, and Gd are grey, blue, red, orange, gold, and cyan, respectively.

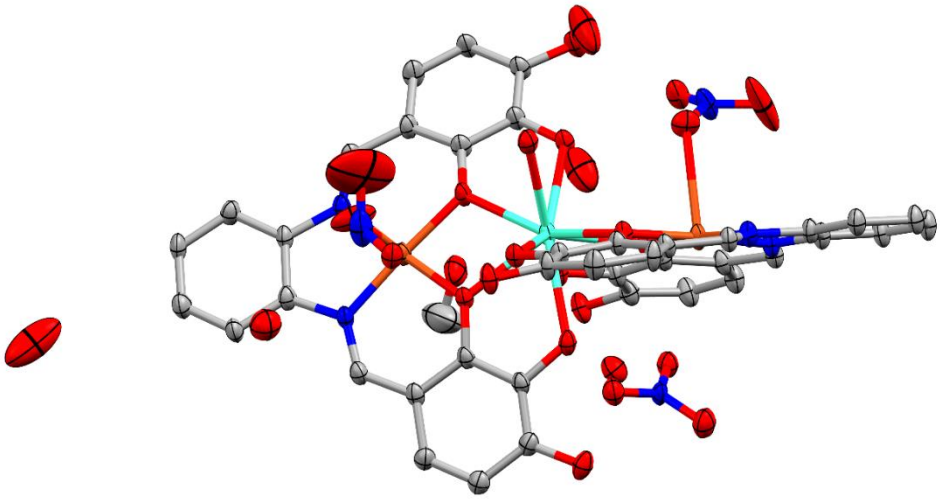

Figure 5.7: X-ray structure of the asymmetric unit of **C18**. Hydrogen atoms have been omitted for clarity; thermal ellipsoids shown at the 15% probability level. Colour code: C, N, O, Cu, and Gd are grey, blue, red, orange, and cyan, respectively.

Complex C17 shares an analogous supramolecular environment as the complexes from the bromine series covered in Chapter 4, with a total of five π–π stacking interactions. This similarity is due to the 0.4:2.6 anion ratio of nitrate:bromide resulting in the bromine anions dictating the overall packing of the complex. This also means that C17 possesses the same intramolecular hydrogen bonds as present in the bromine series, C6 – C11, with one between the axially

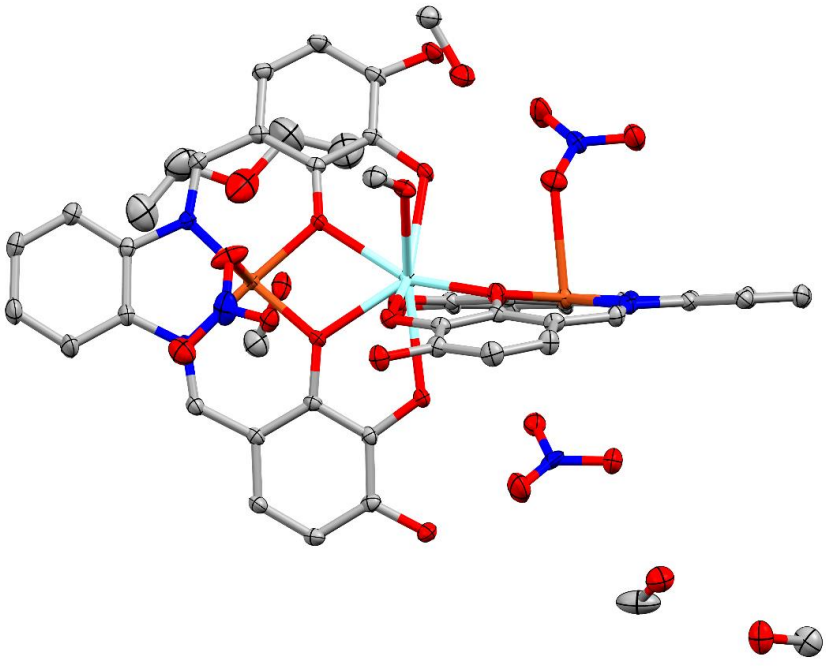

Figure 5.6: X-ray structure of the asymmetric unit of **C19**. Hydrogen atoms have been omitted for clarity; thermal ellipsoids shown at the 30% probability level. Colour code: C, N, O, Cu, and Y are grey, blue, red, orange, and light blue, respectively.

coordinated MeOH molecule and an outermost binding phenol (1.882(3) Å) and the other between the coordinated bromine and an outermost binding phenol (2.5060(4) Å). Complexes **C18** and **C19** only have the nitrate anion present, and so they adopt a unique supramolecular arrangement. **C18** has π–π stacking interactions with four different complexes, three single and one double for a total of five interactions. **C19** has π–π stacking interactions with two complexes, one double and one single for a total of three interactions (Figure 5.8). The overall crystal packing is similar for both **C18** and **C19** with the only significant difference being the number of π–π stacking interactions (Table 5.1). This difference is due to the individual complexes on average being spatially further apart for **C19** causing the centroid–centroid distance to fall outside the typical range for strong π–π stacking.[142] Complexes **C18** and **C19** also possess intramolecular hydrogen bonds between the axially bound nitrate anions and the outermost binding phenols, with distances of 1.944(4) and 2.006(2) Å for **C18** and 1.918(4) and 1.951(4) Å for **C19**.

A crucial factor in the synthesis of the nitrate complexes is the time between the complexation reaction and X-ray collection. Complexes **C17** – **C19** were all synthesised following the same synthetic procedure as was used for the series of complexes presented in Chapter 4, however the X-ray data collection occurred much later for the nitrate containing complexes, less than eight weeks for the Chapter 4 work and up to 19 weeks for the nitrate complexes. This leads us to believe that the nitrate containing complexes can be obtained after initially forming a complex

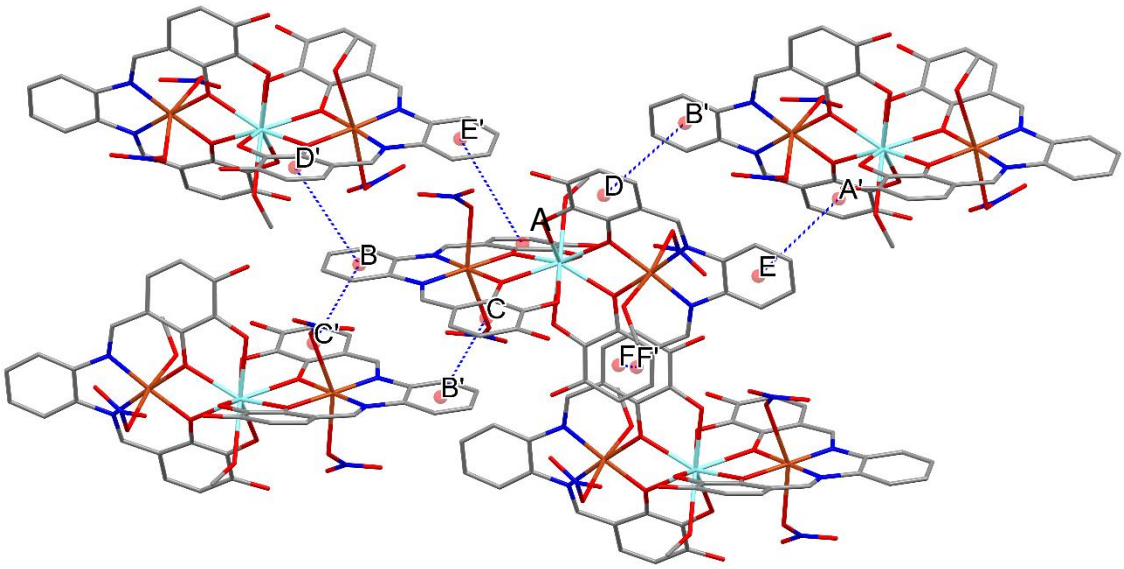

Figure 5.8: X-ray structure of **C19**, showing the crystal packing and π–π stacking interactions. Hydrogen atoms have been omitted for clarity. Colour code: C, N, O, Cu, and Y are grey, blue, red, orange, and light blue, respectively.

with a halide. The presence of a small amount of nitrate anion in the crystal structure of **C17**, which was obtained ten weeks after initial complexation agrees with this conclusion. The reason for this is either due to the halide complex being a kinetic product, whilst the nitrate complex is a thermodynamic product, or that the nitrate complex is more soluble thus requiring a longer time to crystallise.

Table 5.1: List of π-π stacking interactions with centroid–centroid distances and angles for complexes **C17 – C19**

	C16 Distance (Å) Angle (°)	**C17** Distance (Å) Angle (°)	**C18** Distance (Å) Angle (°)
A – E'	3.671 0.46	- -	- -
B – D'	3.749 2.65	3.877 2.99	- -
B – C'	- -	3.505 12.36	3.842 1.27
C – B'	- -	3.505 13.39	3.842 1.52
D – B'	3.749 4.08	3.877 1.81	- -
E – A'	3.671 0.92	- -	- -
F – F'	4.043 7.15	3.528 1.89	3.589 1.01

5.3 L2 Complexes

An attempt at replicating the successful complexation series reported in Chapters 3 and 4 was undertaken utilising the bulkier ligand H_6**L2** (Figure 5.9). The purpose of this was to investigate the effects that steric hindrance has on the structural and magnetic properties of the system. Unfortunately, crystallisation attempts were met with limited success, with a total of three complexes successfully crystallised. One mononuclear and two trinuclear complexes (**C20** – **C22**) involving H_6**L2** were successfully isolated and characterised by X-ray diffraction.

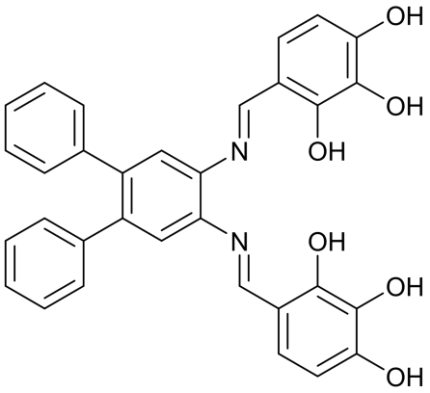

Figure 5.9: Chemical structure of the ligand H_6**L2** reported in this thesis.

5.3.1 Mononuclear Complex

The mononuclear complex **C20** crystallised in the triclinic space group $P\bar{1}$ with the asymmetric unit containing H_4**L2**$^{2-}$, a bound Cu^{II} ion, and a single MeOH molecule (Figure 5.10, left). The Cu^{II} ion is square planar, occupying the inner coordination pocket of H_4**L2**$^{2-}$. The MeOH molecule occupies the outer coordination pocket, forming hydrogen bonding interactions with all four phenolic oxygens in this pocket (O1 · · · HO7 = 2.054(2) Å, O2 · · · HO7 = 2.163(2) Å, HO3 · · · O7 = 2.031(2) Å, and HO4 · · · O7 = 2.146(2) Å). Each complex forms two hydrogen bonding interactions (O3 · · · HO5 and HO5 · · · O3, 2.050(2) Å) with a neighbouring complex (Figure 5.10, right). Complex **C20** has zero π–π interactions due to the bulky 'tails' of the ligands forcing the complexes to pack so that the centroid of the ring is located vertically above a nitrogen atom of an adjacent ligand, which agrees with our prediction that the addition of the bulky tails helps disrupt the packing of the complexes (Figure 5.11).

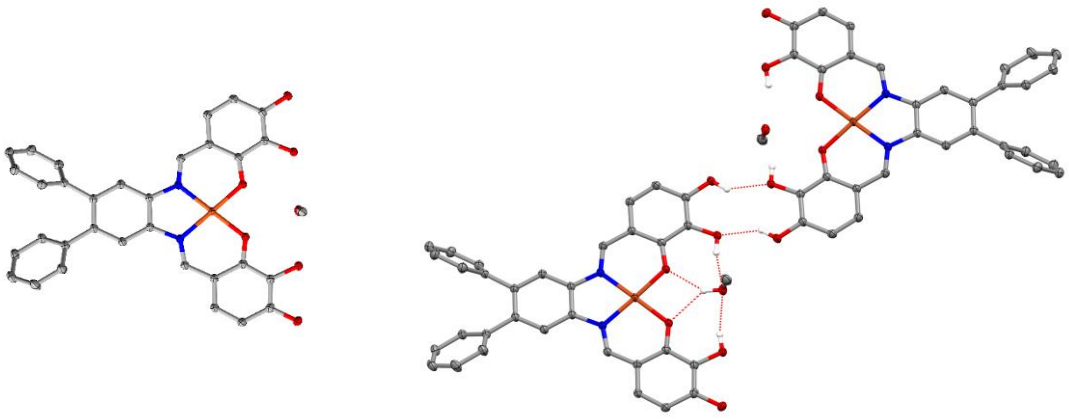

Figure 5.10: X-ray structure of the asymmetric unit of **C20** (left) and the hydrogen bonded dimer (right). Non-interacting hydrogen atoms have been omitted for clarity; thermal ellipsoids shown at the 30% probability level. Colour code: C, N, O, and Cu, are grey, blue, red, and orange, respectively.

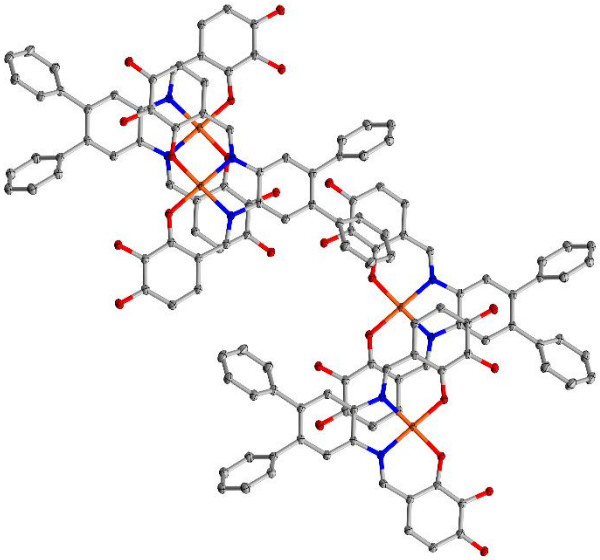

Figure 5.11: X-ray structure of **C20**, showing the intermolecular packing. Hydrogen atoms and solvent molecules have been omitted for clarity; thermal ellipsoids shown at the 30% probability level. Colour code: C, N, O, and Cu, are grey, blue, red, and orange, respectively.

5.3.2 Trinuclear Complexes

The trinuclear complexes **C21** and **C22** were synthesised by the reaction of a methanolic solution of H_6**L2**, $TM(BF_4)_2{\cdot}6H_2O$ (Cu^{II} or Ni^{II}), and $Y(NO_3)_3{\cdot}6H_2O$ in a 2:2:1 molar ratio. This was followed by the addition of excess TBAI (10 eq.). flame atomic absorption spectroscopy revealed a calcium impurity in the TBAI, which is the source of the calcium ion found in **C22.** Complexes **C21** and **C22** crystallised in the monoclinic space group *C*2/*c* and the triclinic space group $P\bar{1}$, respectively. The asymmetric unit of **C21** consists of a half of the complex unit $[(H_4\mathbf{L2})_2Cu_2YI]$ with two non-coordinated chloride ions (Figure 5.12, top). The central Y^{III} ion is octa-coordinate, occupying the outer coordination pocket of two $H_4\mathbf{L2}^{2-}$ ligands. The two Cu^{II} ions occupy the inner coordination pocket of an $H_4\mathbf{L2}^{2-}$ ligand, with one adopting a square planar geometry, whilst the other adopts a square pyramidal geometry with the axial site occupied by a single iodide ion displaced over two locations (Figure 5.12, bottom). The asymmetric unit of **C22** consists of the central $[(H_4\mathbf{L2})_2Ni_2Ca]$ unit alongside two non-coordinated chlorine anions and two MeOH molecules (Figure 5.13). A Ca^{II} ion occupies the outer coordination pocket of the two $H_4\mathbf{L2}^{2-}$ ligands and is eight-coordinate. Both Ni^{II} centres occupy the inner coordination pocket of a $H_4\mathbf{L2}^{2-}$ ligand and adopt a square planar geometry.

Complex **C21** has two single π–π stacking interactions (3.452 Å) with two separate complexes, one through ring 'a' and the other through ring 'c' (Figure 5.14). These π–π stacking interactions form a 1D chain of interconnected complexes. These chains are connected by a pair of hydrogen

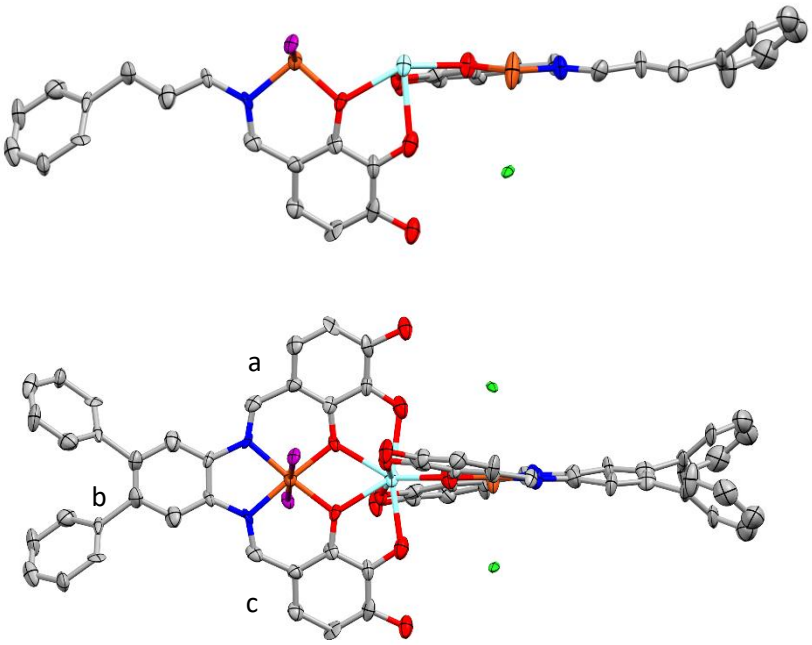

Figure 5.12: X-ray structure of the asymmetric unit (top) and full complex (bottom) of **C21**. Hydrogen atoms have been omitted for clarity; thermal ellipsoids shown at the 15% probability level. Colour code: C, N, O, Cu, Cl, I, and Y are grey, blue, red, orange, green, violet, and light blue, respectively.

bonds between a bound iodide anion and the outermost phenol of an adjacent complex (2.40(2) Å), forming a 2D sheet. These sheets then stack along the bulky tails forming a 3D crystal structure (Figure 5.15). A pair of intramolecular hydrogen bonding interactions is present between the bound half occupancy iodine anion and the outermost coordinating phenol (2.542(2) Å). Complex **C22** has no π–π stacking interactions, instead the individual complexes assemble into 2D sheets along the bulky tails (Figure 5.16). The sheets then symmetrically stack with the chloride anions filling the gaps between sheets.

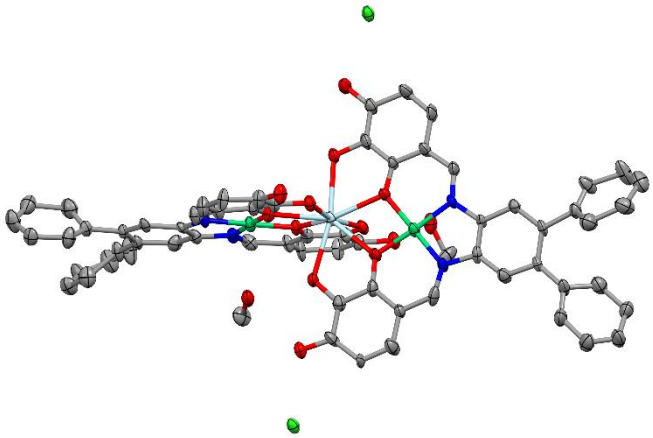

Figure 5.13: X-ray structure of the asymmetric unit of **C22**. Hydrogen atoms have been omitted for clarity; thermal ellipsoids shown at the 15% probability level. Colour code: C, N, O, Ni, Ca, and Cl, are grey, blue, red, lime, light blue, and green, respectively.

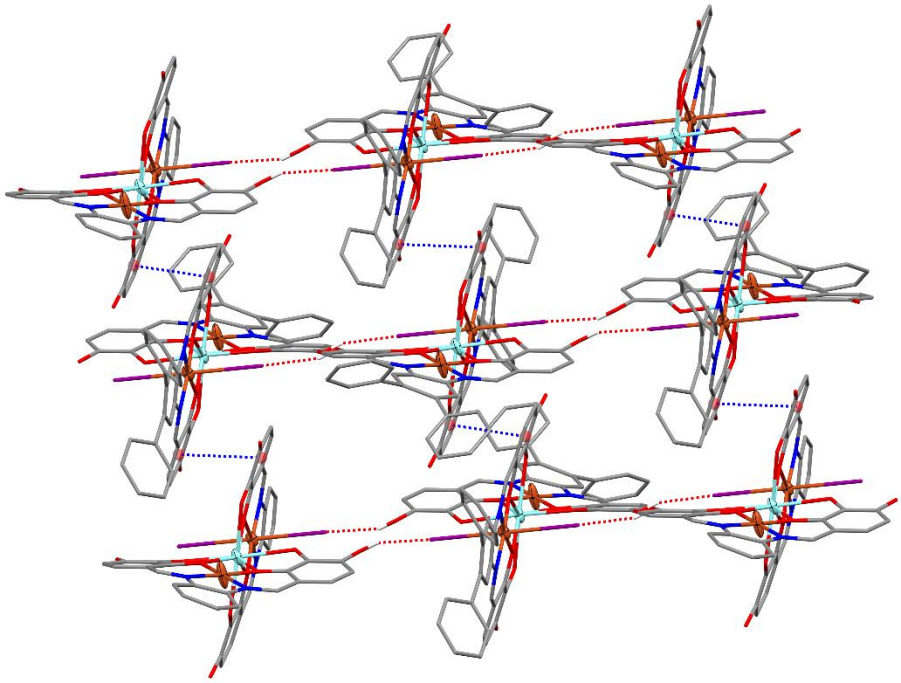

Figure 5.14: X-ray structure of **C21** showing the intermolecular interactions. Blue dashed lines represent π–π stacking, red dashed lines represent hydrogen bonding. Hydrogen atoms and solvent molecules have been omitted for clarity. Thermal ellipsoids shown at the 30% probability level. Colour code: C, N, O, Cu, Cl, I, and Y are grey, blue, red, orange, green, violet, and light blue, respectively.

The complexes with the bulkier ligand H_6**L2** have far fewer intermolecular interactions, namely π–π stacking interactions, compared to the H_6**L1** complexes reported in Chapters 3 and 4. Instead, the phenyl tails determine the overall crystal packing of these complexes. This is due to the phenyl tail's ability to freely rotate, providing a thermodynamic resistance to packing

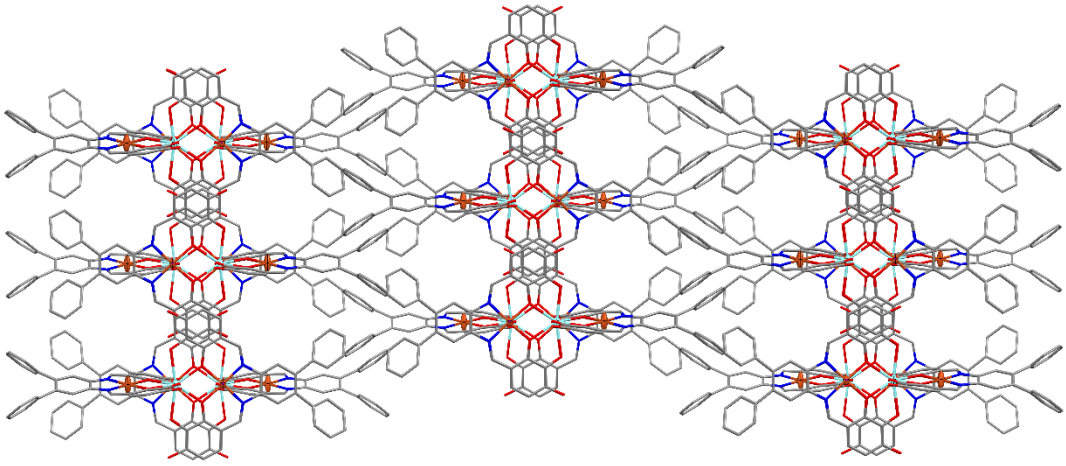

Figure 5.15: X-ray structure of **C21** showing the π–π stacking interactions. Blue dashed lines represent π–π stacking interactions. Hydrogen atoms and solvent molecules have been omitted for clarity. Thermal ellipsoids shown at the 30% probability level. Colour code: C, N, O, Cu, Cl, I, and Dy are grey, blue, red, orange, green, violet, and light blue, respectively.

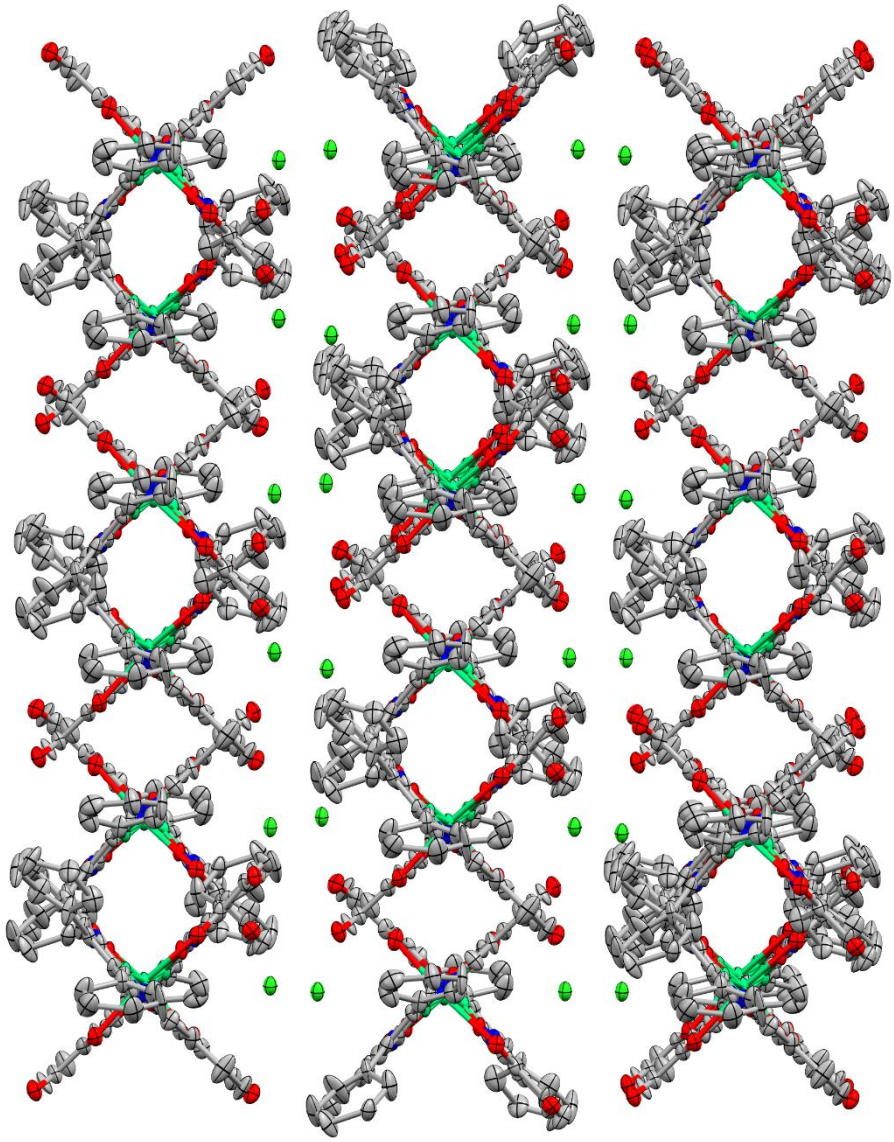

Figure 5.16: X-ray structure of **C22** showing the crystal packing. Hydrogen atoms have been omitted for clarity; thermal ellipsoids shown at the 15% probability level. Colour code: C, N, O, Ni and Cl, are grey, blue, red, lime, and green, respectively.

necessary for π–π stacking interactions. Chapter 4 showed that the species with fewer intermolecular interactions possessed superior magnetic properties thus, magnetic analysis of complexes with H_6**L2** would potentially have interesting magnetic properties.

5.4 Conclusions

The reaction between H_6**L1**, $Cu(BF_4)_2{\cdot}H_2O$, and $Ln(NO_3)_3{\cdot}6H_2O$ (Ln = Dy, Gd, Y) in the presence of varying amounts of a halide anion can produce trinuclear nitrate containing complexes depending on the time between synthesis and crystallisation. In the absence of a halide anion,

a dinuclear species is obtained where the central lanthanide ion occupies the outer binding pocket of H_4**L1** with the remaining sites occupied by three nitrate anions (**C16**). In the presence of an excess amount of a halide anion, collecting the X-ray data within ten weeks of complexation yielded trinuclear complexes with less than one nitrate anion per complex unit (**C17**). Collecting X-ray data after 18-20 weeks of complexation yielded trinuclear complexes with three nitrate anions per unit complex (**C18** and **C19**). From this we concluded that the trinuclear nitrate containing complexes can be synthesised by first going through a halide containing intermediate. Then allowing crystallisation to occur for upwards of 18 weeks will result in a species with only the nitrate anion present. This is either due to thermodynamics of the reaction or the relative solubilities of the resulting complexes. Three complexes were obtained utilising the bulkier ligand H_6**L2**. A mononuclear complex, with strong inter-complex hydrogen bonding (**C20**), and two trinuclear complexes with either two (**C21**) or zero (**C22**) π–π stacking interactions. The overall crystal packing of these complexes is dominated by the bulky 'tails' present on the ligand H_6**L2**. The work presented in Chapter 4 demonstrated that species with fewer intermolecular secondary interactions had superior magnetic properties (the bromine series outperformed the chlorine series). Thus, the magnetic properties of complexes synthesised utilising the bulkier ligand H_6**L2**, which display even fewer significant secondary interactions, would be a valuable avenue to explore.

Complex Preparation

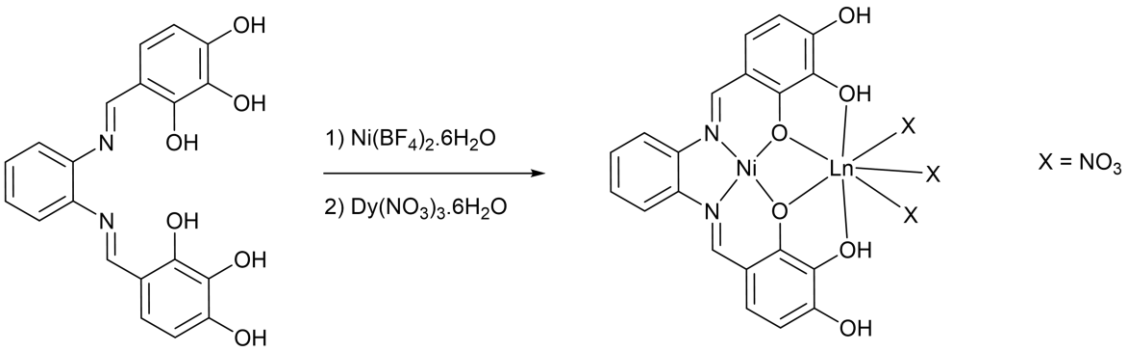

Figure 5.17: Schematic showing the complexation reaction undertaken by complex **C16**.

C16 To a stirred solution of H_6**L1** (0.0380 g, 0.1 mmol, 2 eq.) in MeOH (10 mL) was added a solution of $Ni(BF_4)_2{\cdot}6H_2O$ (0.0340 g, 0.1 mmol, 2 eq.) in MeOH (5 mL) followed by a solution of $Dy(NO_3)_3{\cdot}6H_2O$ (0.0228 g, 0.05 mmol 1 eq.) in MeOH (5 mL). The reaction mixture was stirred at 50 °C for 20 minutes. Vapour diffusion of Et_2O into the reaction solution resulted in isolation of the complex $[H_4$**L1**$MgDy(NO_3)_3](MeOH)_2$ which was obtained as red block shaped crystals after 2 weeks. Yield 17% based on $Dy(NO_3)_3{\cdot}6H_2O$.

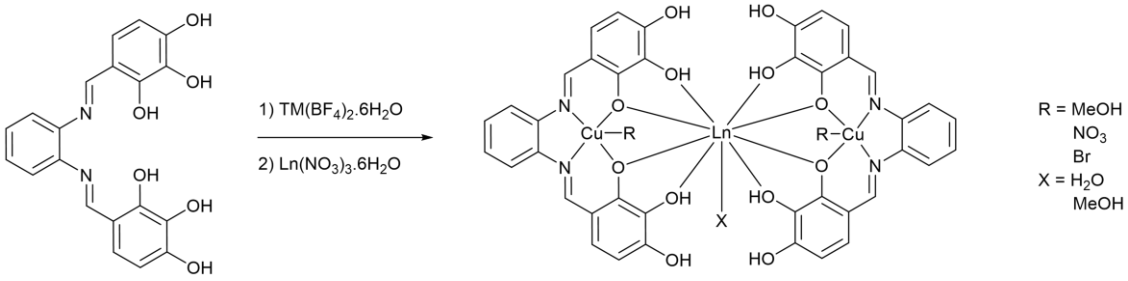

Figure 5.18: Schematic showing the complexation reaction undertaken by complexes **C17** – **C19**.

Complexes **C17** – **C19** were obtained by the addition of $Cu(BF_4)_2{\cdot}6H_2O$ (0.0345 g, 0.1 mmol, 2 eq.) in MeOH (5 mL) to a stirred solution of H_6**L1** (0.0380 g, 0.1 mmol, 2 eq.) in MeOH (10 mL) followed by a solution of $Ln(NO_3)_3{\cdot}6H_2O$ (0.0226 g, 0.05 mmol, 1 eq.) in MeOH (5 mL) (Ln = Gd or Y). The reaction mixture was stirred at 50 °C for 20 minutes followed by the addition of an excess amount of TBABr (0.3224 g, 1 mmol, 10 eq.) and stirred for a further 30 minutes at RT. Vapour diffusion of Et_2O into the reaction solution yielded the complexes **C17** – **C19**.

C17 $[(H_4$**L1**$)_2Cu_2GdBr(MeOH)]Br_{1.6}(NO_3)_{0.4}(MeOH)_4Et_2O$: Red plate shaped crystals were obtained after 10 weeks. Yield 13% based on $Gd(NO_3)_3{\cdot}6H_2O$.

C18 $[(H_4$**L1**$)_2Ni_2Gd(H_2O)(NO_3)_2](H_2O)_4(MeOH)_2NO_3$: Red needle shaped crystals were obtained after 18 weeks. Yield 14% based on $Gd(NO_3)_3{\cdot}6H_2O$.

C19 $[(H_4\mathbf{L1})_2Cu_2Y(NO_3)_2(MeOH)_2](MeOH)_3NO_3Et_2O$: Red needle shaped crystals were obtained after 19 weeks. Yield 12% based on $Y(NO_3)_3{\cdot}6H_2O$.

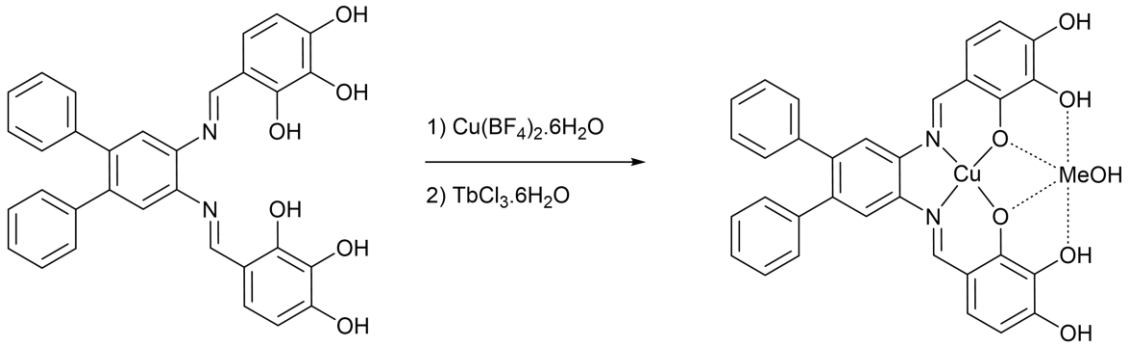

Figure 5.19: Schematic showing the complexation reaction undertaken by complex **C20**.

C20 To a solution of $H_6\mathbf{L2}$ (0.0533 g, 0.1 mmol, 2 eq.) in MeOH (10 mL) was added a solution of $Cu(BF_4)_2{\cdot}6H_2O$ (0.0345 g, 0.1 mmol, 2 eq.) in MeOH (5 mL) followed by a solution of $TbCl_3{\cdot}6H_2O$ (0.0187g, 0.05 mmol, 1 eq.) in MeOH (5 mL). The reaction mixture was stirred at 50 °C for 20 minutes. Vapour diffusion of Et_2O into the reaction solution resulted in isolation of the complex $[H_4\mathbf{L2}Cu(MeOH)]$ which was obtained as dark red block shaped crystals after 4 weeks. Yield 4% based on $Cu(BF_4)_2{\cdot}6H_2O$.

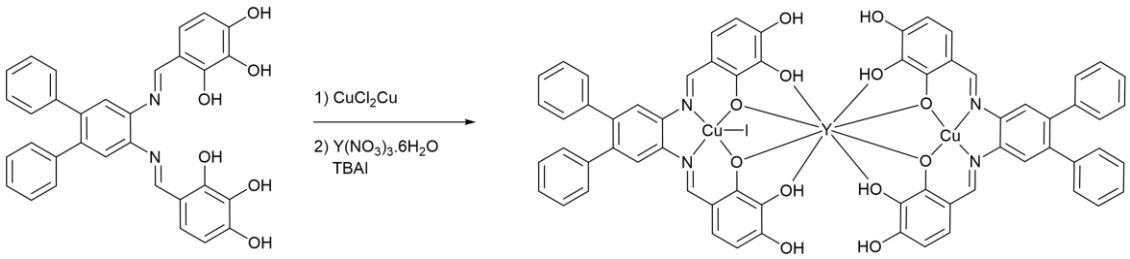

Figure 5.20: Schematic showing the complexation reaction undertaken by complex **C21**.

C21 To a solution of $H_6\mathbf{L2}$ (0.0533 g, 0.1 mmol, 2 eq.) in MeOH (10 mL) was added a solution of $CuCl_2$ (0.0067 g, 0.1 mmol, 2 eq.) in MeOH (5 mL) followed by a solution of $Y(NO_3)_3{\cdot}6H_2O$ (0.0192 g, 0.05 mmol, 1 eq.) in MeOH (5 mL). The reaction mixture was stirred at 50 °C for 20 minutes followed by the addition of excess TBAI (0.3672 g, 1 mmol, 10 eq.) and stirred for a further 30 minutes at RT. Vapour diffusion of Et_2O into the reaction solution resulted in isolation of the complex $[(H_4\mathbf{L2})_2Cu_2YCl]_2(Cl)(I)$ which was obtained as dark red plate shaped crystals after 5 weeks. Yield 4% based on $Y(NO_3)_3{\cdot}6H_2O$.

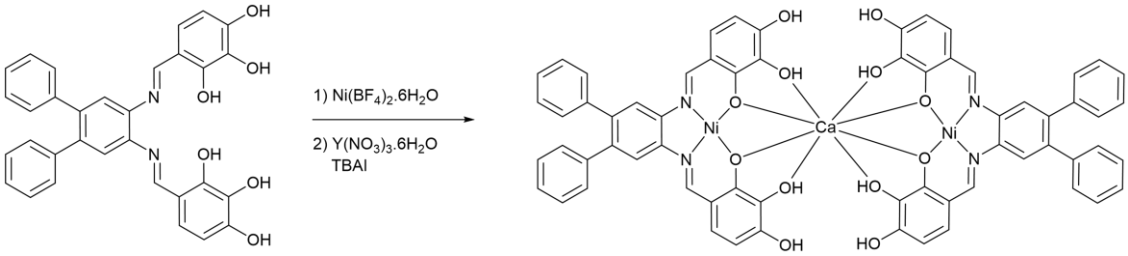

Figure 5.21: Schematic showing the complexation reaction undertaken by complex **C22**.

C22 To a solution of H_6**L2** (0.0533 g, 0.1 mmol, 2 eq.) in MeOH (10 mL) was added a solution of $Ni(BF_4)_2{\cdot}6H_2O$ (0.0340 g, 0.1 mmol, 2 eq.) in MeOH (5 mL) followed by a solution of $Y(NO_3)_3{\cdot}6H_2O$ (0.0192 g, 0.05 mmol, 1 eq.) in MeOH (5 mL). The reaction mixture was stirred at 50 °C for 20 minutes followed by the addition of excess TBAI (0.3672 g, 1 mmol, 10 eq.) and stirred for a further 30 minutes at RT. Vapour diffusion of Et_2O into the reaction solution resulted in isolation of the complex $[(H_4\mathbf{L2})_2Ni_2Ca](MeOH)_2Cl_2$ which was obtained as dark red needle shaped crystals after 4 weeks. Yield 3% based on $Ni(BF_4)_2{\cdot}6H_2O$.

Chapter 6

Conclusions and Future Work

The primary focus of this research was to elucidate the influence of secondary interactions on the structural and magnetic properties of heterometallic complexes. This was divided into two types of secondary interactions and approaches: attractive and repulsive. The attractive approach utilised interactions such as hydrogen bonding to constrain the complex systems, reducing the M–L–M bond angles. Reducing this angle closer to 90° promotes ferromagnetic exchange, which can quench QTM. The repulsive approach primarily utilised the steric effect to isolate the complex systems, potentially removing the avenues for the relaxation of magnetisation.

Two 2,3,4-trihydroxybenzaldehyde based Schiff base ligands, H_6**L1** (N,N'-bis-2,3,4-trihydroxybenzylidene-1,2-phenylendiamine) and H_6**L2** (4-[(1*E*)-((5'-[(1*E*)-(2,3,4-trihydroxyphenyl)methylideneamino][1,1':2',1''-terphenyl]-4'-yl)imino)methyl]benzene-1,2,3-triol), were developed to test these two approaches. Additionally, these ligands were able to form heterometallic trinuclear complexes, which provides a greater amount of possible secondary interactions compared to a binuclear species. Ligand H_6**L1** formed the basis of Chapters 3, 4, and half of Chapter 5. This ligand was synthesised in two steps and provided a great way to explore intramolecular hydrogen bonding interactions. Four of the six phenol groups present on H_6**L1** can form hydrogen bonds when following the typical coordination motif, making H_6**L1** an ideal ligand for investigating the attractive approach. The second ligand H_6**L2** required an additional synthetic step, adding significant steric bulk in the form of two phenyl tails. The effects of these bulky substituents was described in Chapter 5, where the complexes formed with H_6**L2** have fewer secondary interactions than the H_6**L1** analogues. Chapter 2 also include the research done on the heteroleptic approach with the formation of a benzimidazole being the sole result from this approach. This led to us focusing our efforts focus on investigating the effects that anions have on secondary interactions. The heteroleptic approach still show promise, as the proper selection of auxiliary ligand could provide significantly stronger secondary interactions in comparison to the halides covered in this thesis. An auxiliary ligand containing multiple hydrogen bonding groups along with a bulky ‘tail’ would work to explore both attractive and repulsive approaches (Figure 6.1).

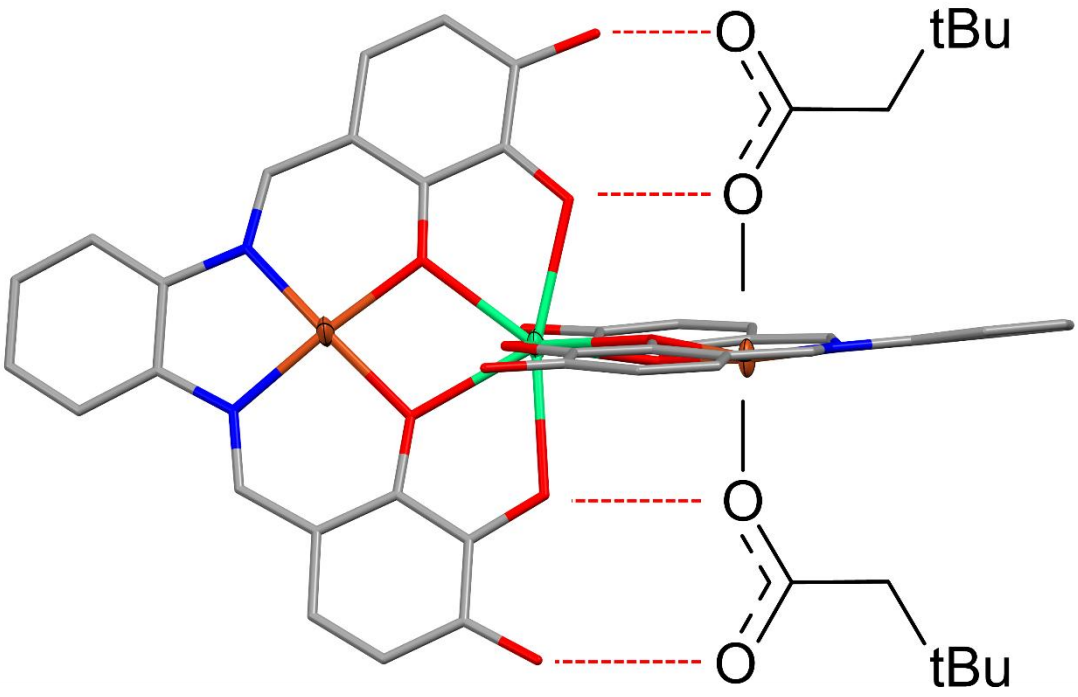

Figure 6.1: Diagram depicting potential intramolecular hydrogen bonding interactions with a six-coordinate TM centre.

Chapter 3 focused on the development of a series of trinuclear Ni^{II}–Ln complexes utilising the ligand H_6**L1** as a control series for comparing the effects of the different secondary interactions. The Ni^{II} centres adopt a four-coordinate square planar geometry which prevents any intramolecular hydrogen bonding from occurring. This resulted in the Ni^{II}–Ln distance being entirely determined by lanthanide size, whilst the Ni–O–Ln bond angles were essentially the same. The absence of species bound to the axial position of the Ni^{II} centre resulted in the nickel series of complexes containing the largest number of intermolecular secondary interactions of all the work covered in this thesis, with a total of eight π–π stacking interactions and 3-4 intermolecular hydrogen bonding interactions present in complexes **C1** – **C3** (Table C4). **C4** is the exception to this, as the central Tb^{III} ion has a chloride anion bound to it, so that anion is not free to template the supramolecular architecture as it is for **C1** – **C3**.

Chapter 4 further expanded on the work done with H_6**L1** into two series of Cu^{II} based trinuclear complexes. These series differed by the halide ion present, with either the chloride or bromide ions being present in the complex unit. X-ray structural analysis revealed that the determining factor for the Cu–Ln distance was lanthanide size, with no evident dependency on the apically bound species. This suggests that intramolecular hydrogen bonding does not have a direct effect on the coordination geometry of the overall complex. The halide present did have a significant effect on the overall supramolecular structure of the corresponding complexes. The bromide

containing complexes had a total of five π–π stacking interactions as well as three intermolecular hydrogen bonding interactions. The overall supramolecular structure of the bromide series consists of chains of complex units strongly linked by π–π stacking which then further expand into 2D sheets through an additional π–π stacking interaction between chains. The chloride containing complexes have a total of six π–π stacking interactions, forming chains analogous to the bromide series. The two series supramolecular structures then differ with the chloride series having each complex unit possess π–π stacking interactions with two adjacent chains forming a 3d interconnected structure. This difference in supramolecular architecture is a result of the relative sizes of the halides present, with the bulkier bromide anion causing a greater separation between complex units, and a less tightly packed supramolecular architecture then the chloride counterparts.

Magnetic measurements performed on complexes in Chapter 4 showed that the erbium containing complexes exhibited weak antiferromagnetic coupling between the copper and erbium ions and/or crystal field splitting of the erbium ion. The gadolinium and terbium containing complexes exhibited ferromagnetic coupling between the copper and lanthanide ions. The terbium containing complexes both exhibited zero-field SMM behaviour, with a barrier height U_{eff} of 17.8(6) and 16.0(9) K for the bromide and chloride analogues, respectively. It is proposed that the steric effects of the bulkier bromide anion aids in isolating the magnetic centres of the complexes, enhancing the resultant magnetic properties. Additionally, the bromide ion has a lower charge density than the chloride ion, resulting in weaker interactions between the metal ions and the hydrogen bonding units. This combined with the intramolecular hydrogen bonding having little effect on the coordination geometry of complexes presented in this thesis, implies that the repulsive secondary interactions are more influential. Further expansion of this series to include the iodide anion was met with limited success but provides an exciting opportunity for future research. The iodide anion is larger than the bromide anion, so is expected to further sterically isolate the magnetic centres. If this follows the trend we've observed in Chapter 4, this would lead to an increase in the energy barrier U_{eff}. Additionally, a tetranuclear $La^{III}Cu^{II}_3$**L1**$_3$ complex was synthesised which revealed the effect that lanthanide size has on the nuclearity of the complexes. Further exploration could yield a tetranuclear series of complexes which would provide a comparison to the trinuclear series covered in this thesis.

The research presented in Chapter 5 focuses on the bulkier ligand, H_6**L2**, attempts at complexations with six-coordinate TM ions, as well as the partial completion of a nitrate series of complexes utilising H_6**L1**. X-ray analysis of the supramolecular structures of the H_6**L2** complexes showed far fewer intermolecular secondary interactions than the H_6**L1** analogues,

with the bulky phenyl substituents directing the overall crystal packing. The expansion of the series involving H_6**L2** is a very promising avenue for future work, as the trinuclear complexes synthesised with H_6**L2** share an analogous coordination environment to those synthesised with H_6**L1**. Thus, the increased isolation of the magnetic centres caused by the bulky substituents would be expected to enhance the resultant magnetic properties of these complexes.

A series of trinuclear complexes utilising the nitrate anion was initially believed to be unobtainable due to the observation that all attempts instead led to the isolation and subsequent small molecule X-ray confirmation of the binuclear complex **C15**. This led us to believe that the nitrate anion successfully competed for the vacant coordination sites on the lanthanide ion, excluding a second unit of H_6**L1**, preventing it from binding and subsequently forming the trinuclear complex. Later complexations revealed that the trinuclear series is possible if the complex first goes through an intermediary halide metathesis, before being left long enough (≈ 20 weeks) for nitrate metathesis to occur yielding the trinuclear nitrate complexes. Unfortunately, due to the long time for complexation and how late in the research this method was discovered, only two trinuclear nitrate complexes have been obtained. Future research should be directed to the expansion of the nitrate series, now that a method for obtaining the trinuclear complexes has been developed.

Attempts to synthesise complexes with a six-coordinate TM ion led to the hydrolysis of H_6**L1** by a $MnCl_2$ catalysed reaction. This caused us to focus our efforts on the four-coordinate Ni^{II} series and the five-coordinate Cu^{II} series. However, utilising a six-coordinate TM ion remains an attractive avenue to explore, as this would allow two anions/auxiliary ligands to coordinate to the metal centre. Following the same coordination motif as the complexes presented in this thesis would provide this potential new series a larger array of secondary interactions (Figure 6.1).

Overall, this thesis has demonstrated that careful consideration of secondary interactions is vital for the design of future SMMs.

Appendix A

Assorted Organic Spectra

Figures Figure A.1: ^{1HNMR} spectrum of **1. Error! Reference source not found.** show the ^{1}HNMR, ^{13}CNMR, and ATR-FTIR of compounds **1**-**13** reported in this thesis.

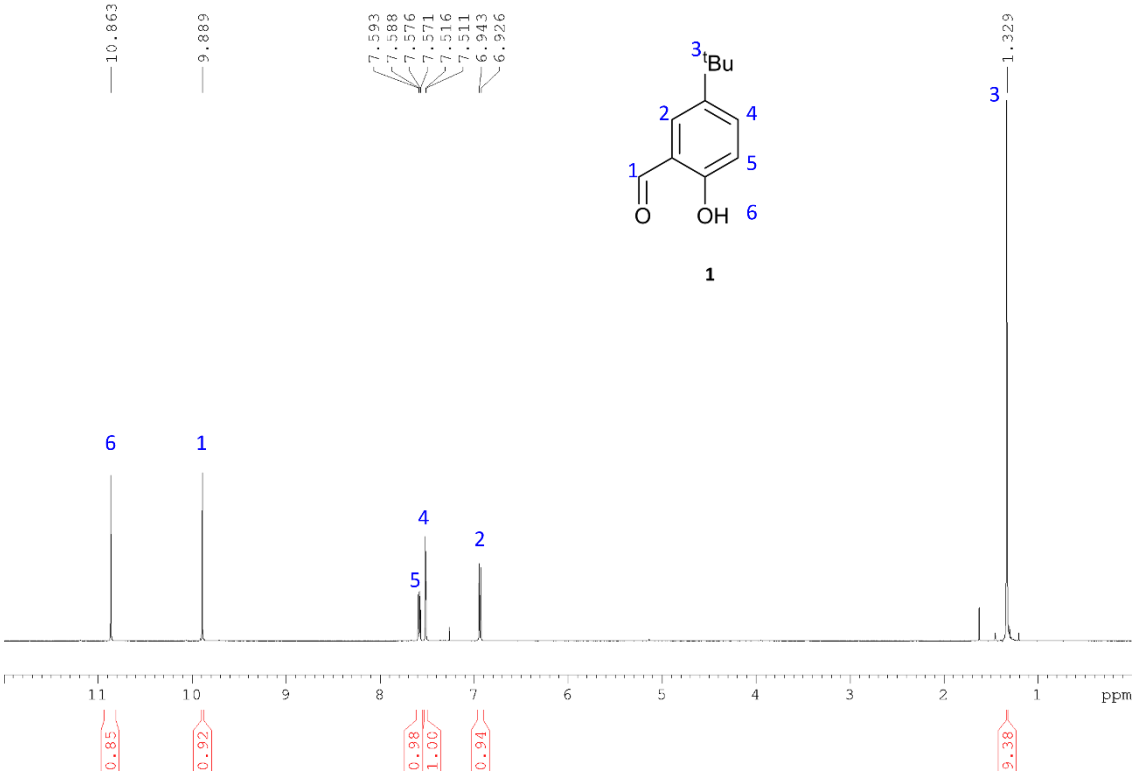

Figure A.1: ^{1}HNMR spectrum of **1**.

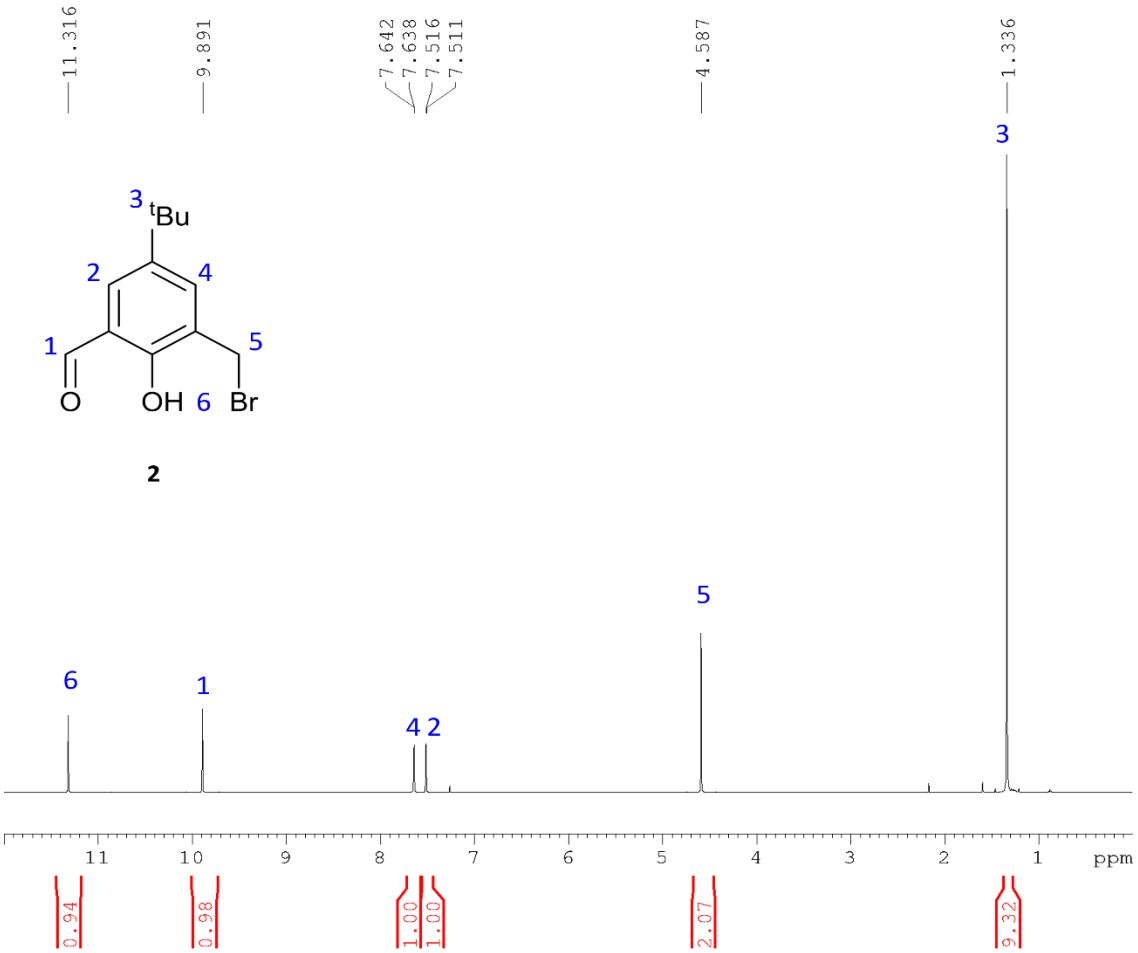

Figure A.2: ^{1}HNMR spectrum of **2**.

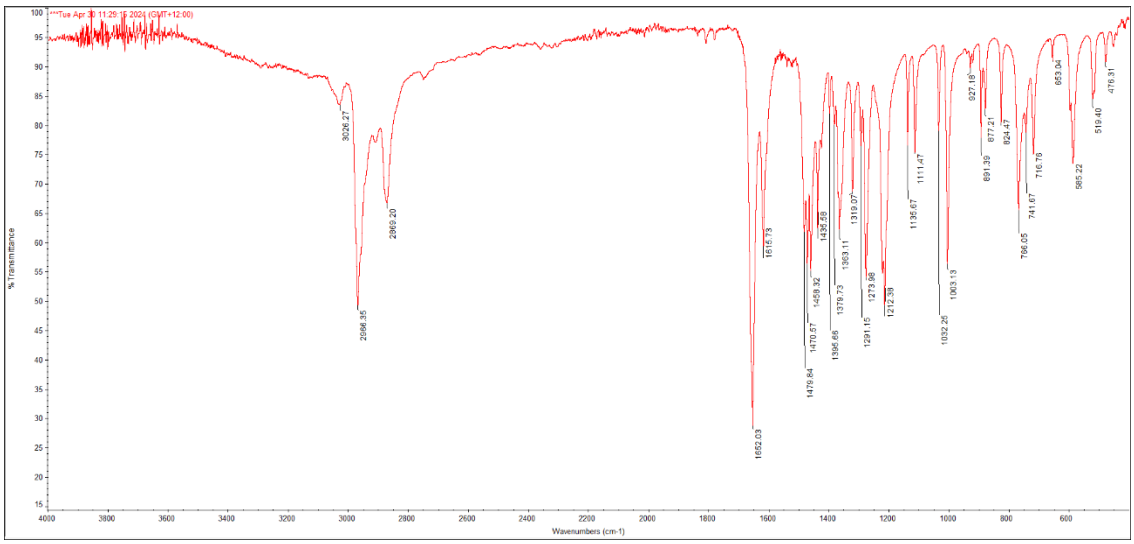

Figure A.3: ATR-FTIR spectrum of **2**.

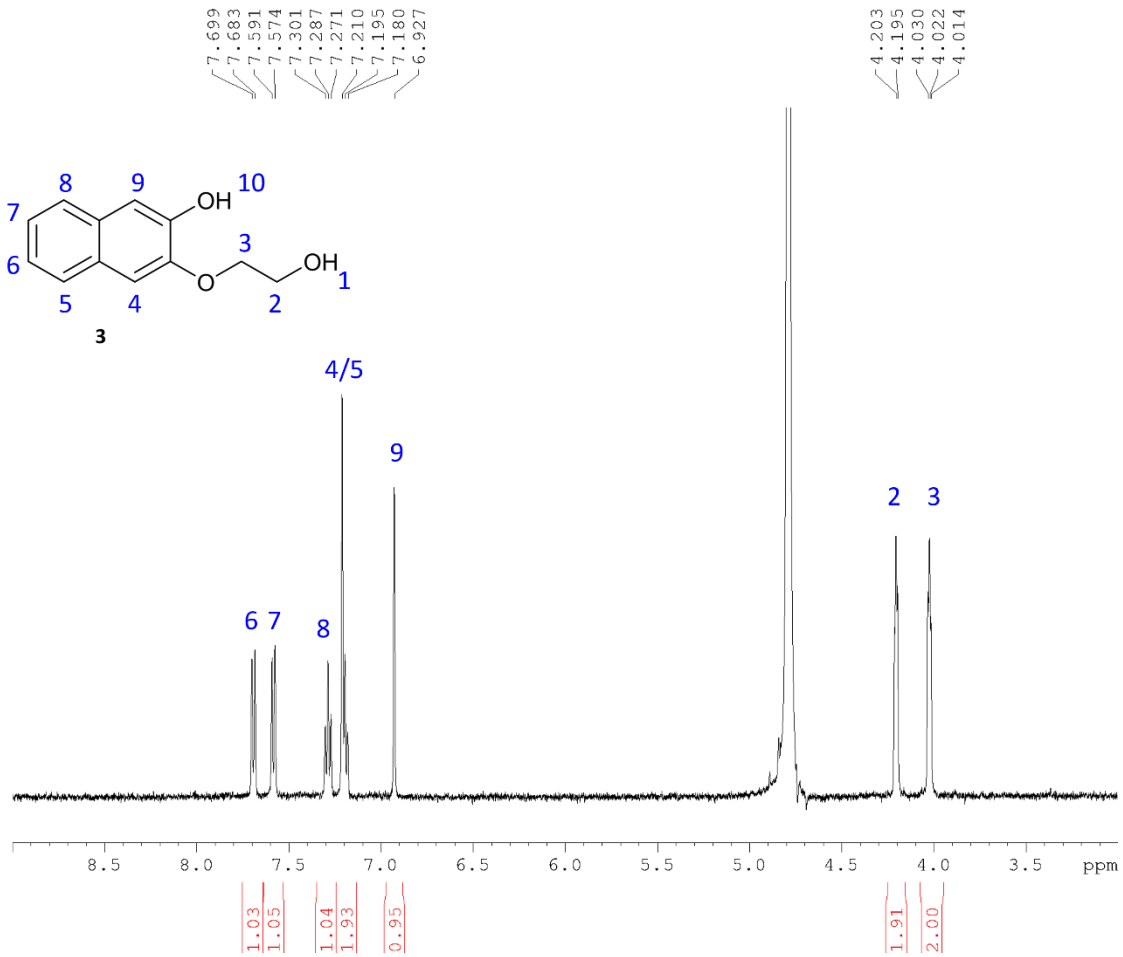

Figure A.4: ^{1}HNMR spectrum of **3**.

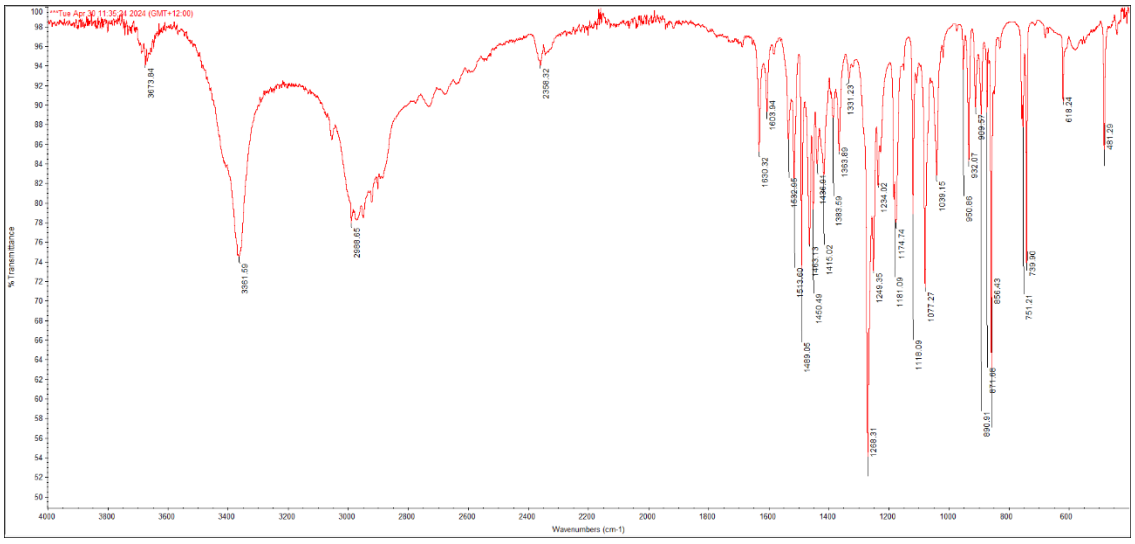

Figure A.5: ATR-FTIR spectrum of **3**.

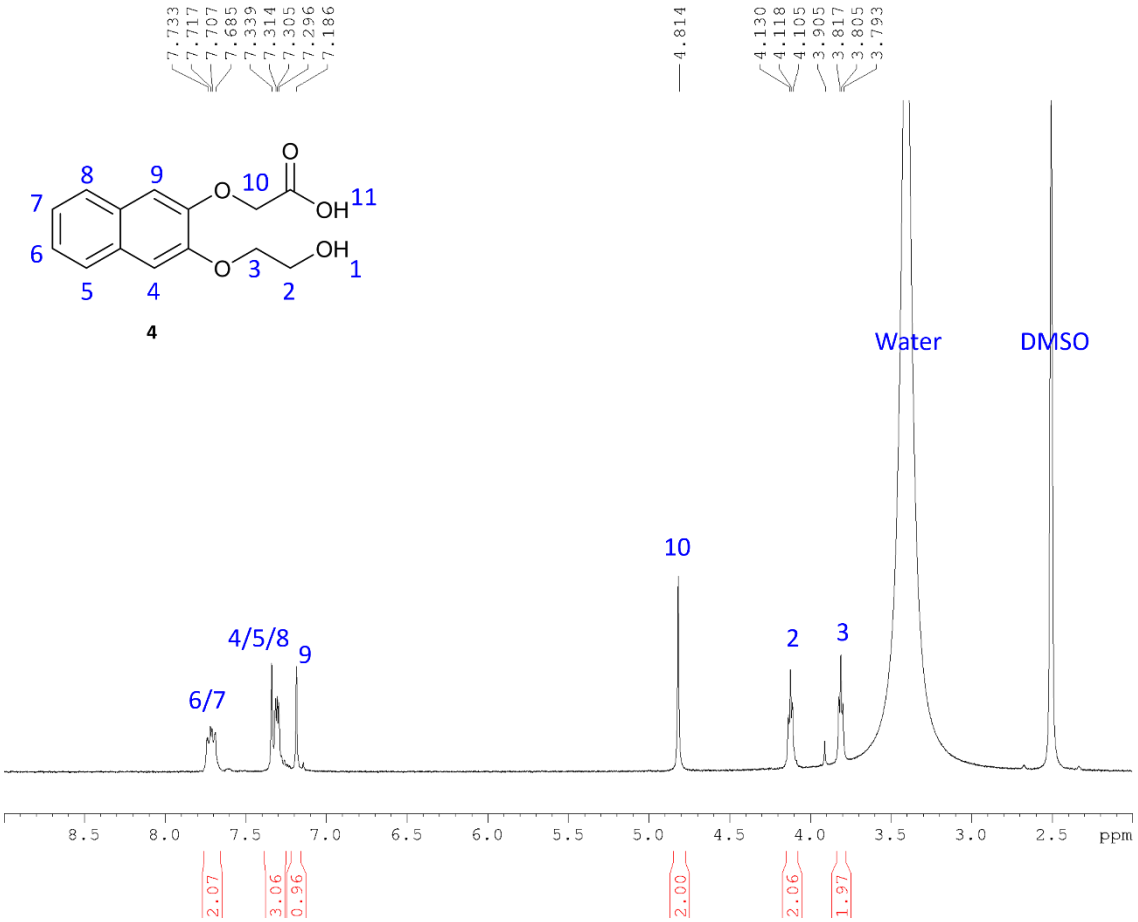

Figure A.6: ^{1}HNMR spectrum of **4**.

Figure A.7: ATR-FTIR spectrum of **4**.

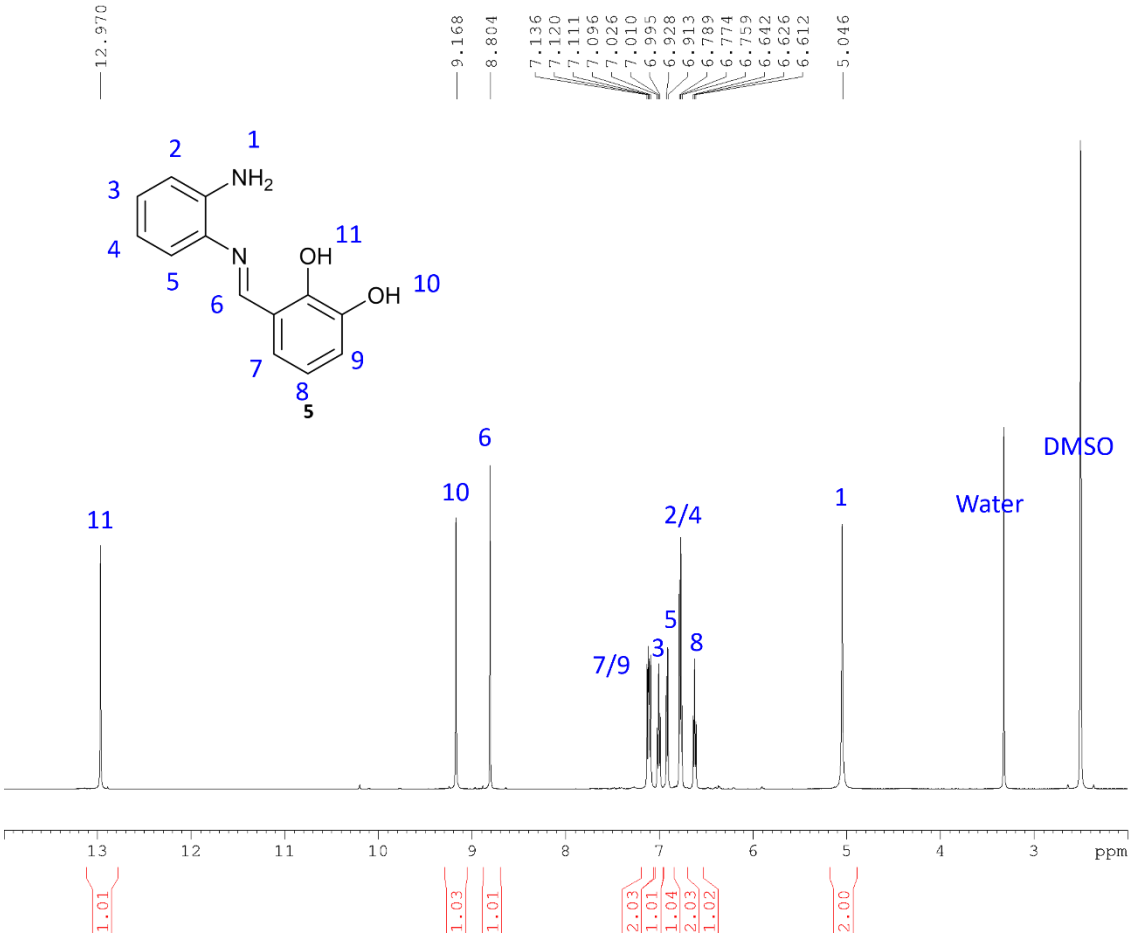

Figure A.8: ^{1}HNMR spectrum of **5**.

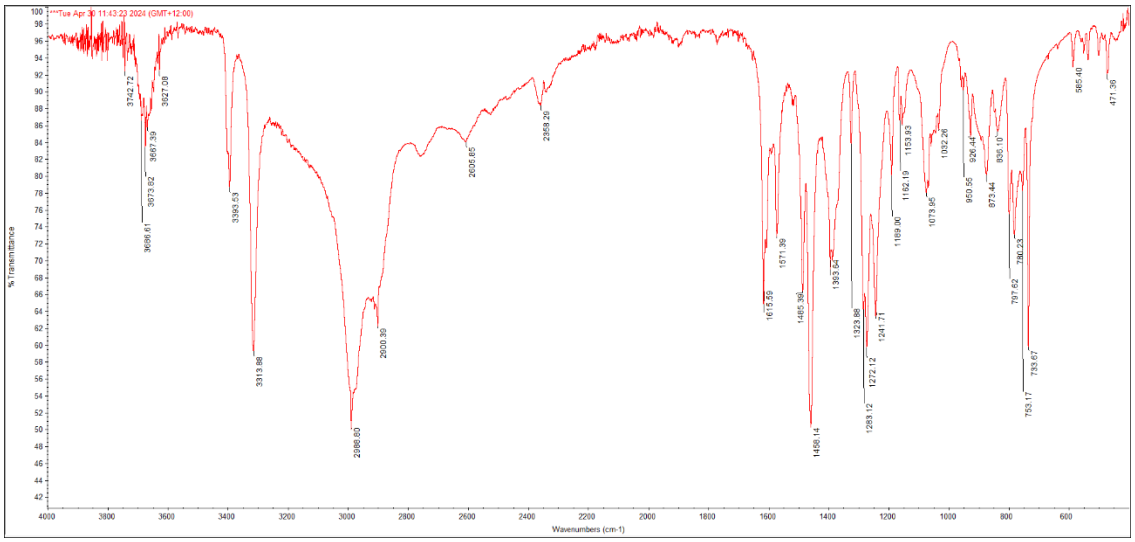

Figure A.9: ATR-FTIR spectrum of **5**.

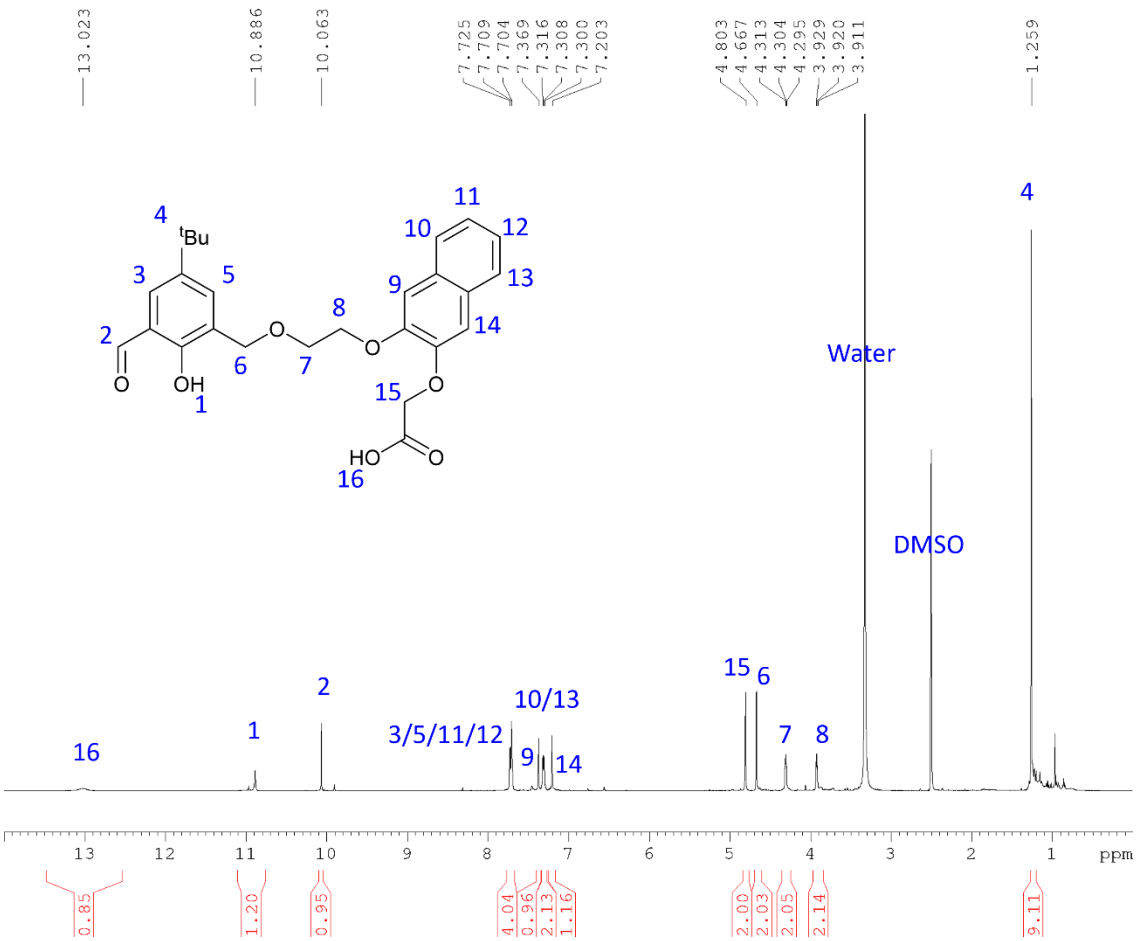

Figure A.10: ^{1}HNMR spectrum of **6**.

Figure A.11: ATR-FTIR spectrum of **6**.

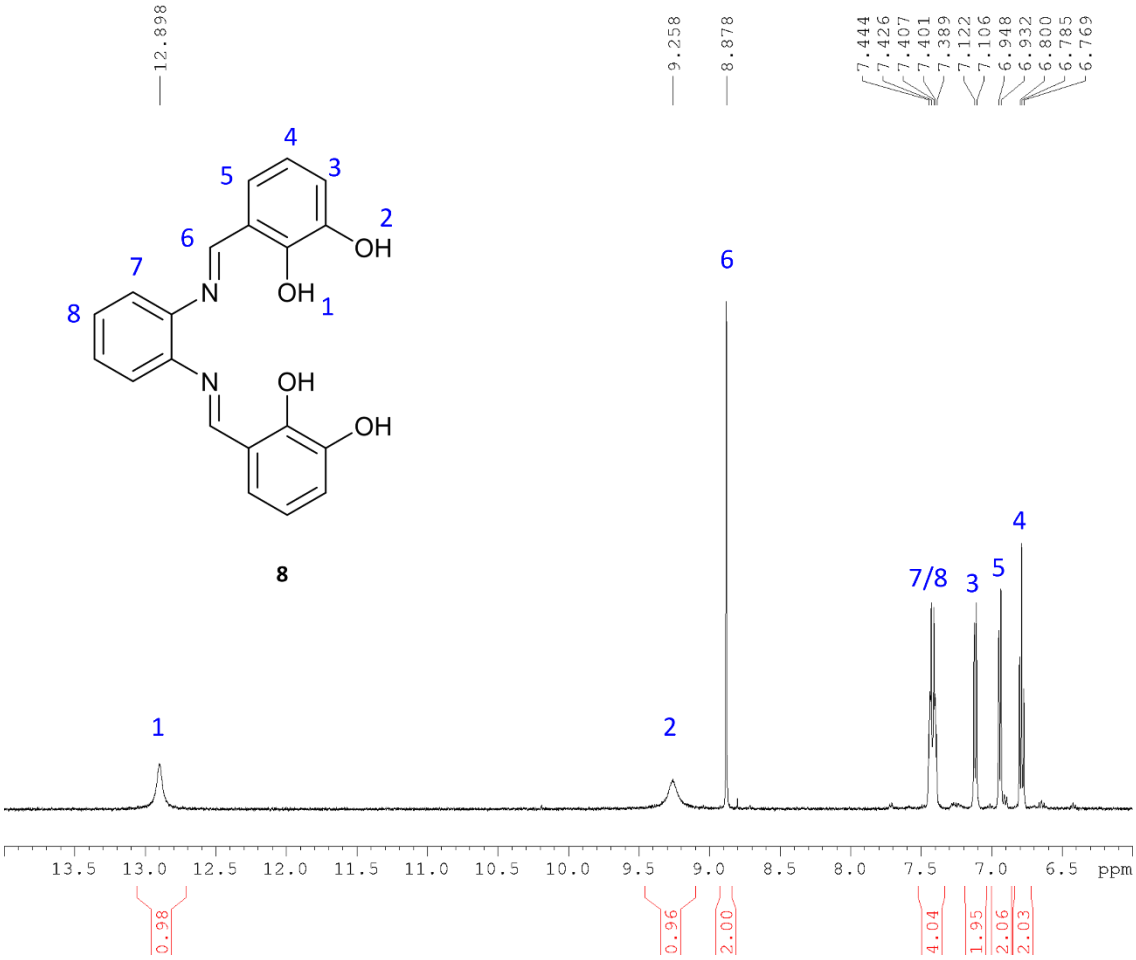

8

Figure A.12: ^{1}HNMR spectrum of **8**.

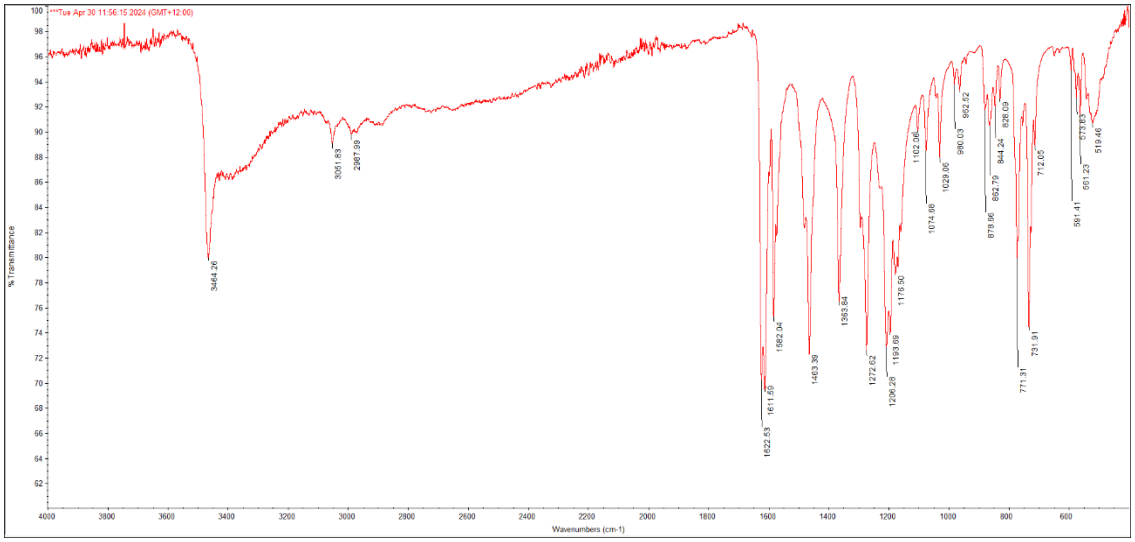

Figure A.13: ATR-FTIR spectrum of **8**.

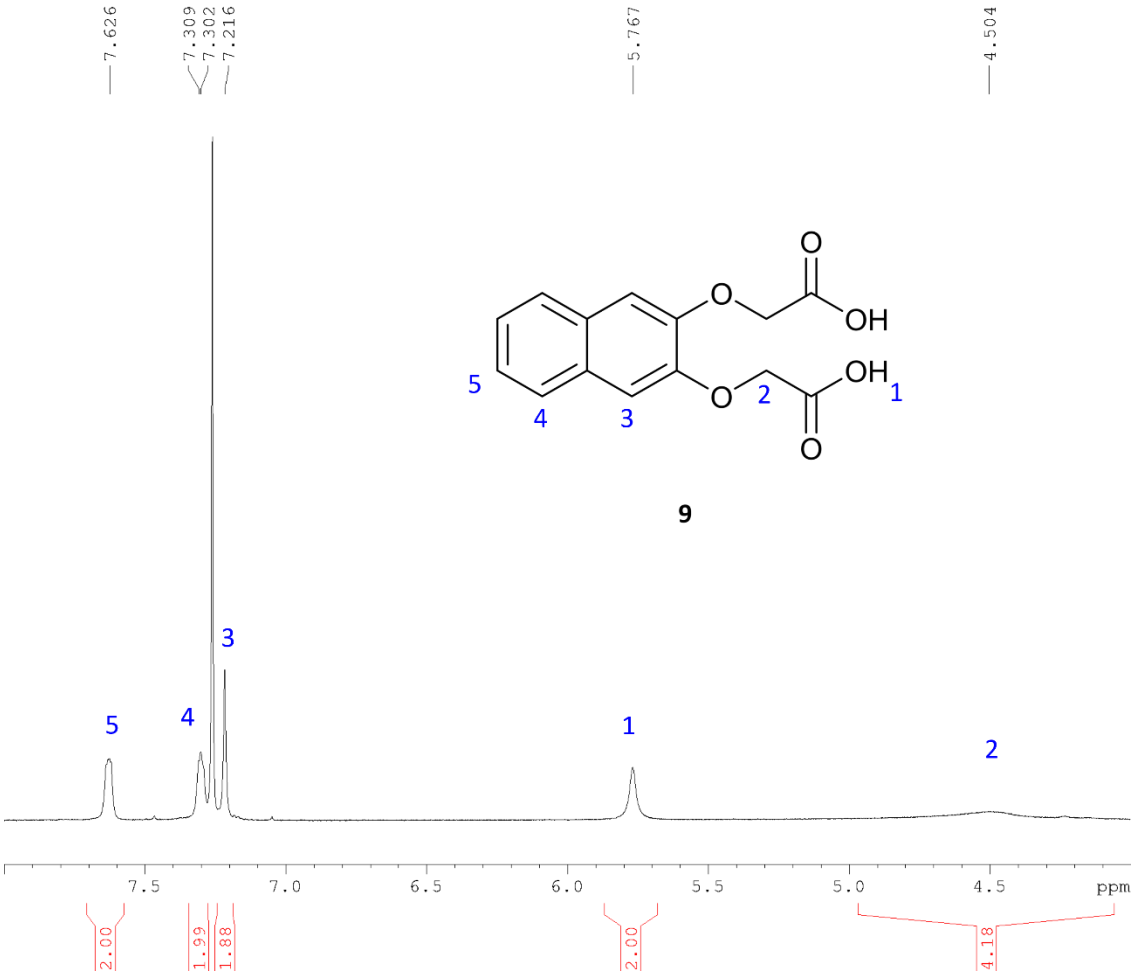

Figure A.14: ^{1}HNMR spectrum of **9**.

Figure A.15: ATR-FTIR spectrum of **9**.

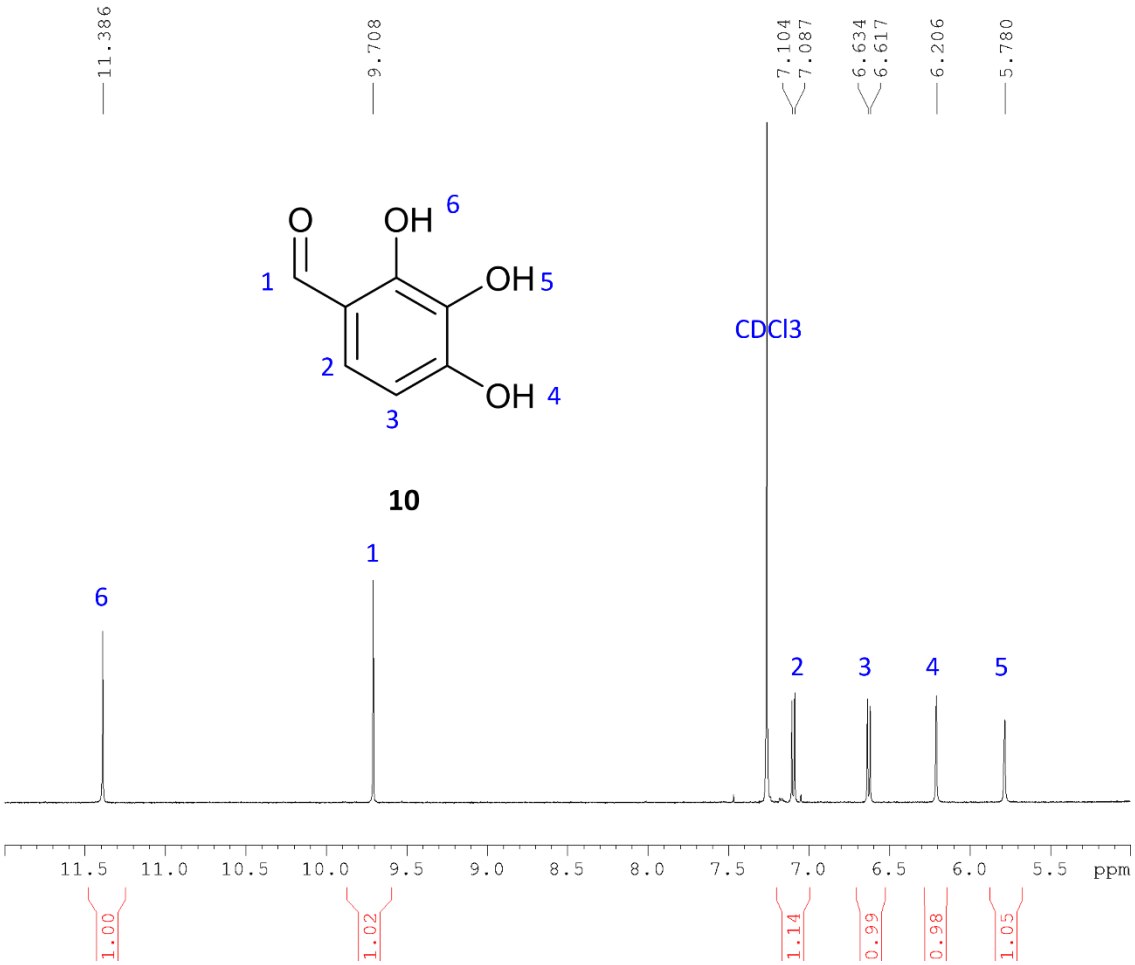

Figure A.16: ^{1}HNMR spectrum of **10**.

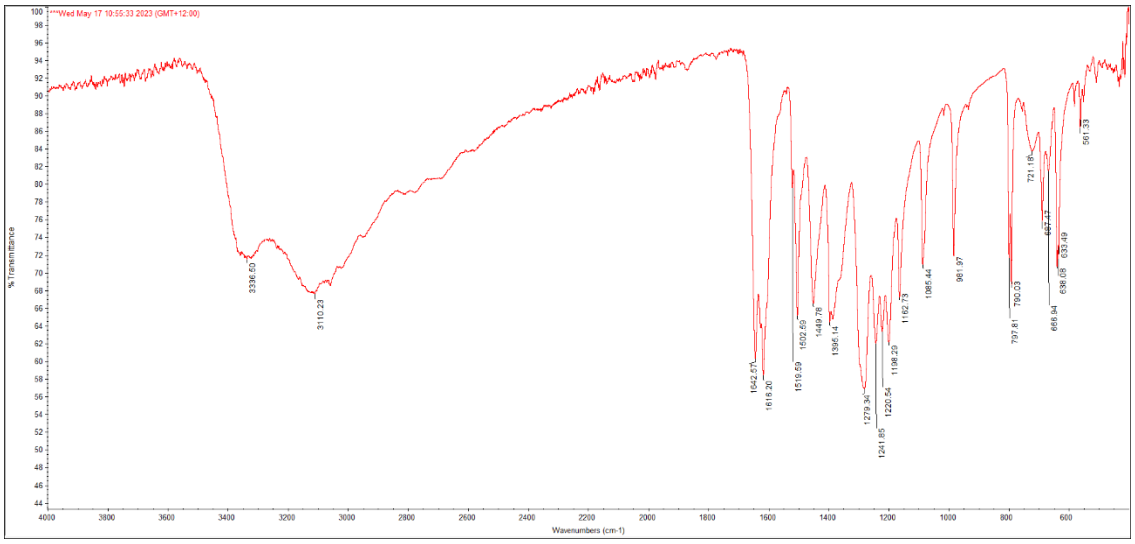

Figure A.17: ATR-FTIR spectrum of **10**.

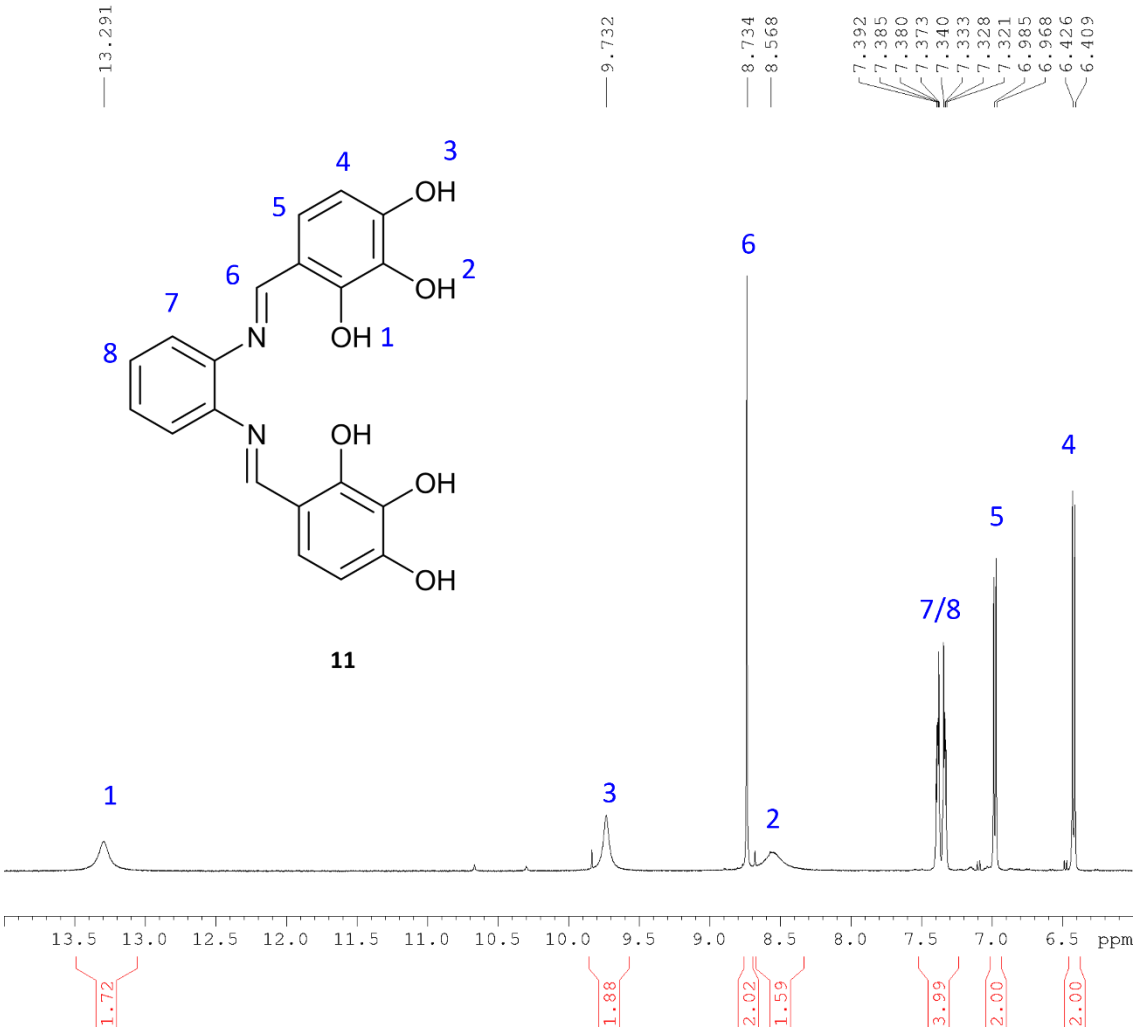

Figure A.18: ^{1}HNMR spectrum of **11**.

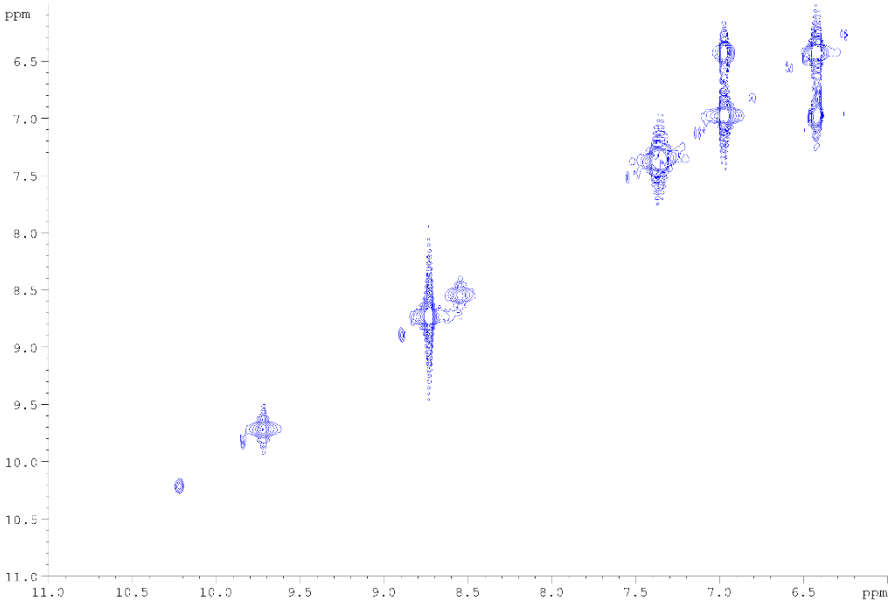

Figure A.19: COSY spectrum of **11**.

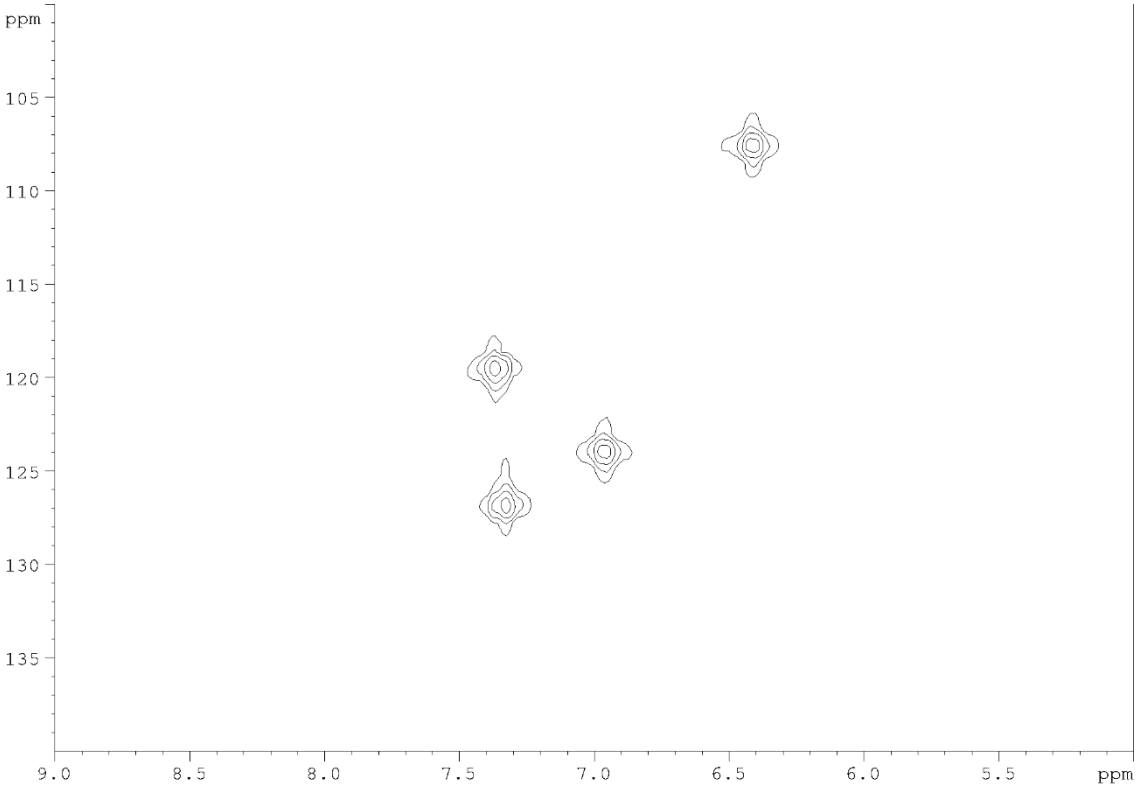

Figure A.20: HMQC spectrum of **11**.

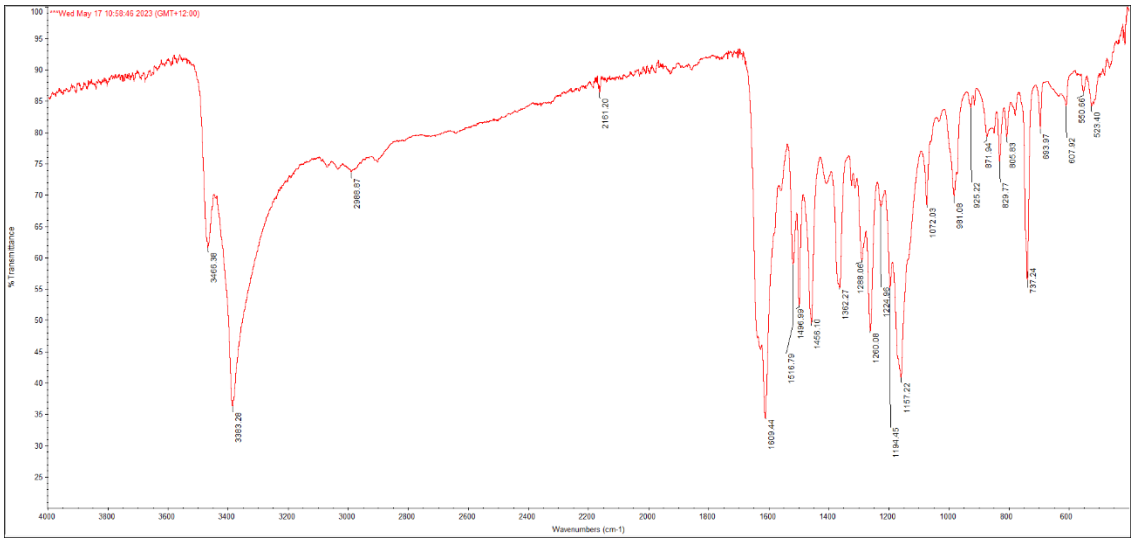

Figure A.21: ATR-FTIR spectrum of **11**..

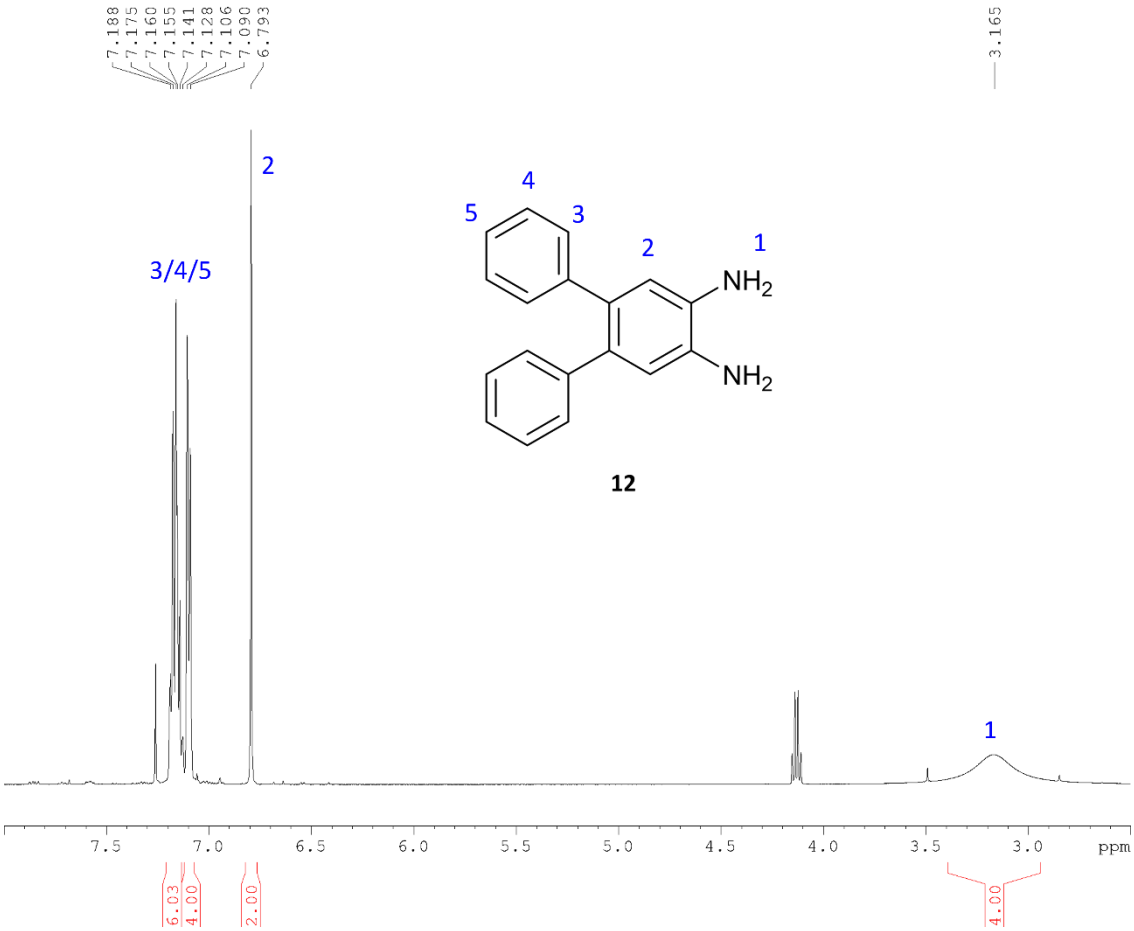

Figure A.22: ^{1}HNMR spectrum of **12**.

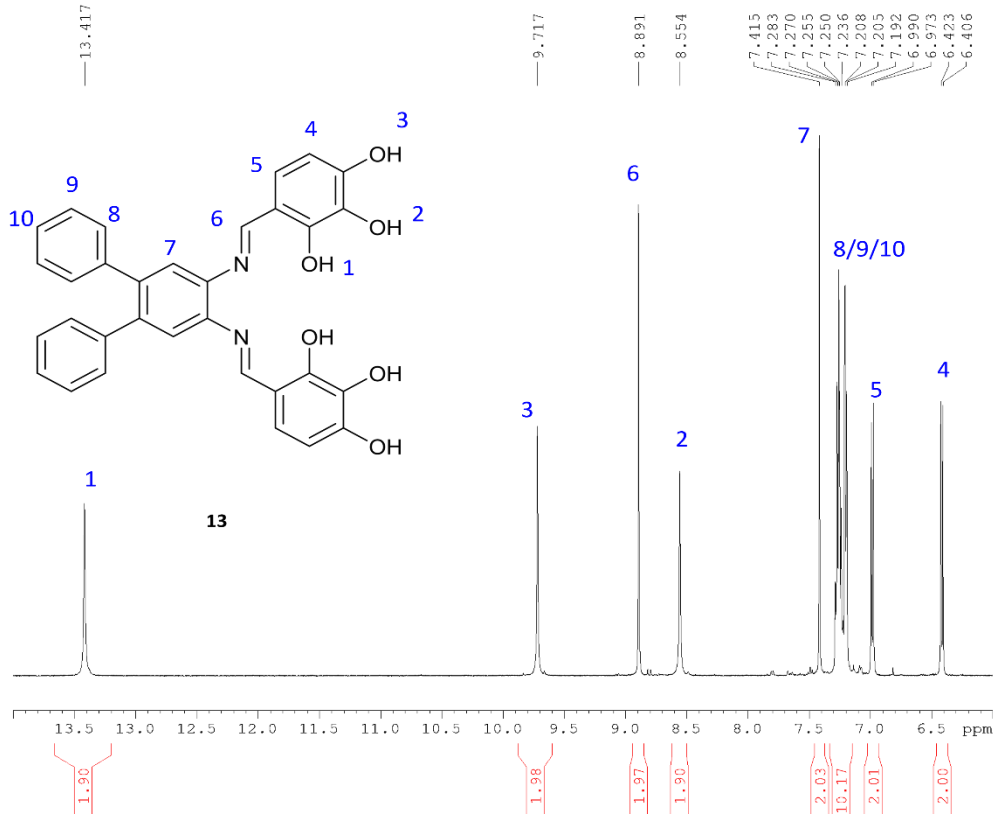

Figure A.23: [1]HNMR spectrum of **13**.

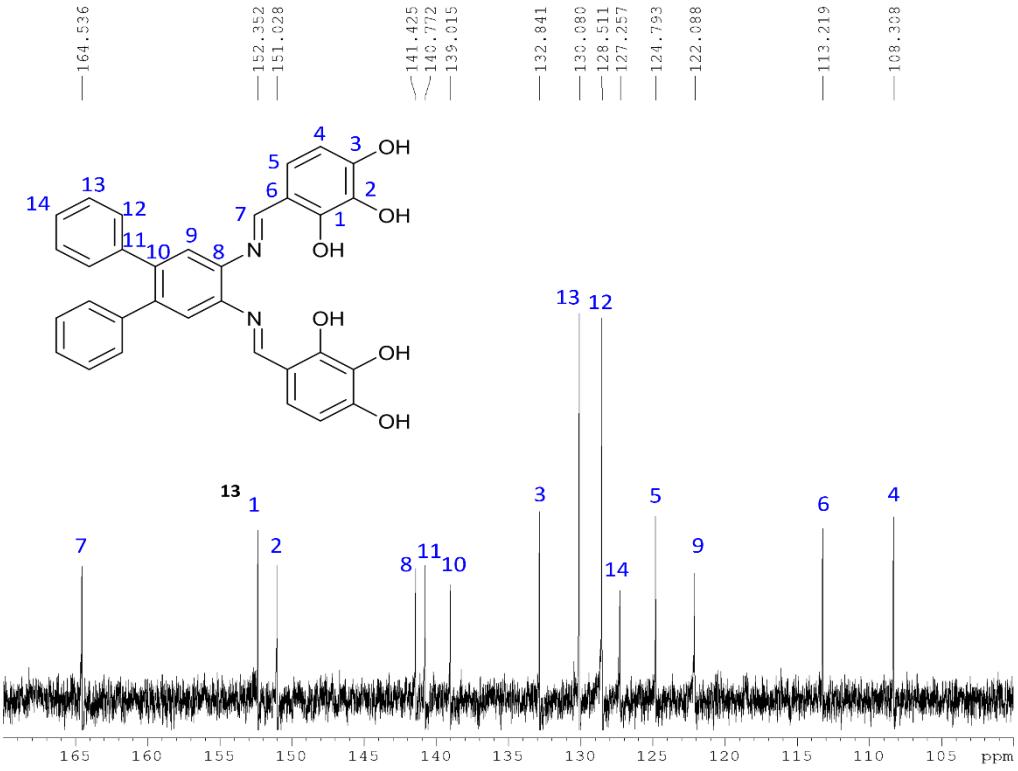

Figure A.24: [13]CNMR spectrum of **13**.

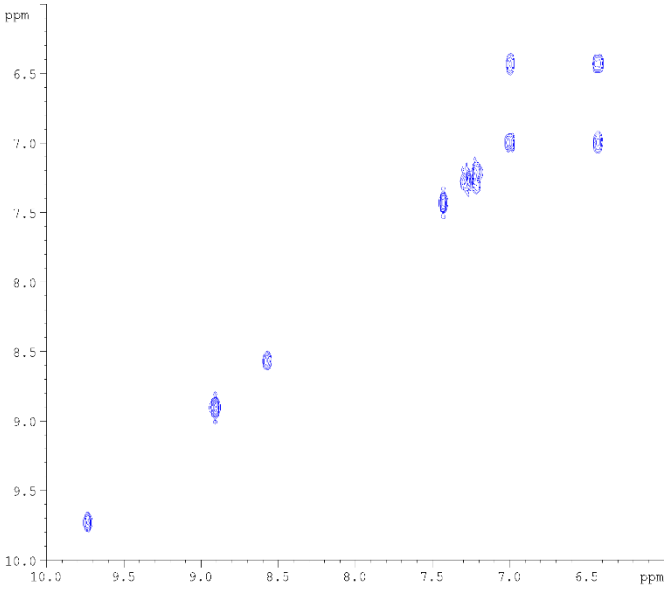

Figure A.25: COSY spectrum of **13**.

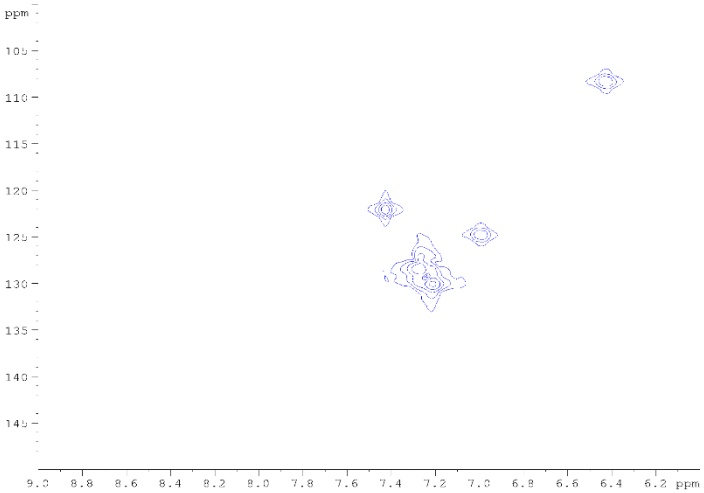

Figure A.26: HMQC spectrum of **13**.

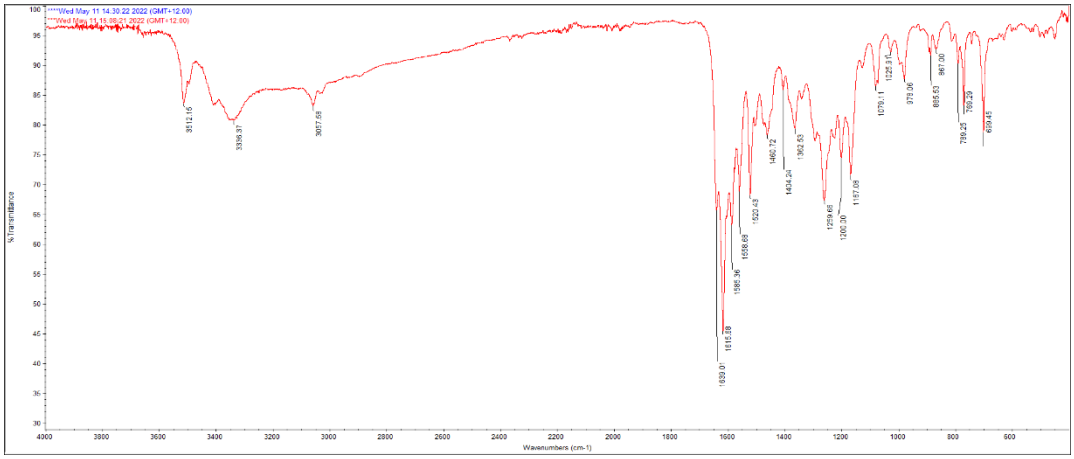

Figure A.27: ATR-FTIR spectrum of **13**.

Appendix B

Assorted Complex Spectra

Figures Figure B.1: ATR-FTIR spectrum of complex **C1.**–Figure B.14: ATR-FTIR spectrum of complex **C15.** show the ATR-FTIR of complexes **C1**-**C4** and **C6**-**C15**.

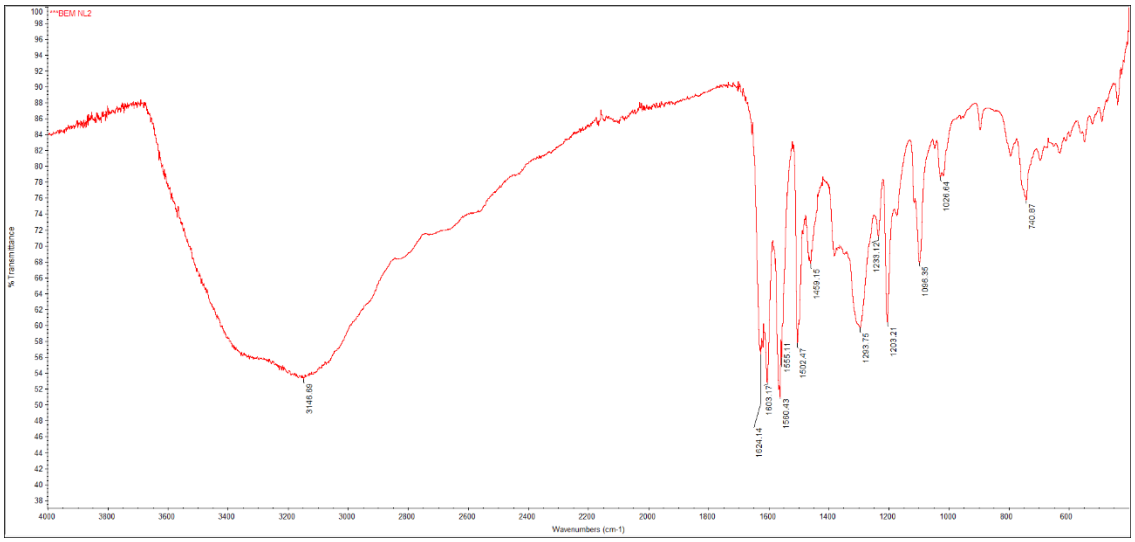

Figure B.1: ATR-FTIR spectrum of complex **C1**.

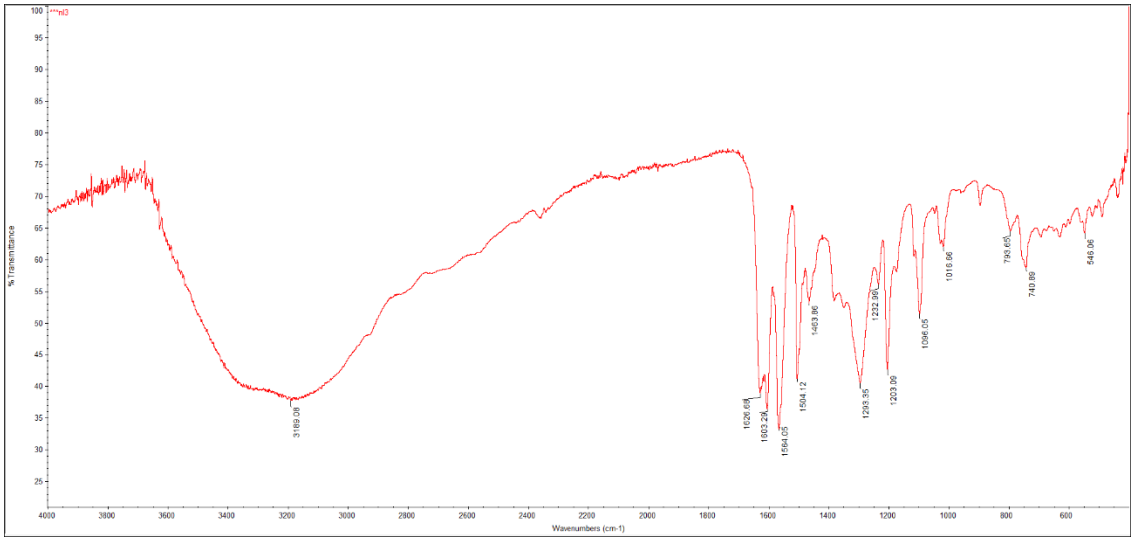

Figure B.2: ATR-FTIR spectrum of complex **C2**.

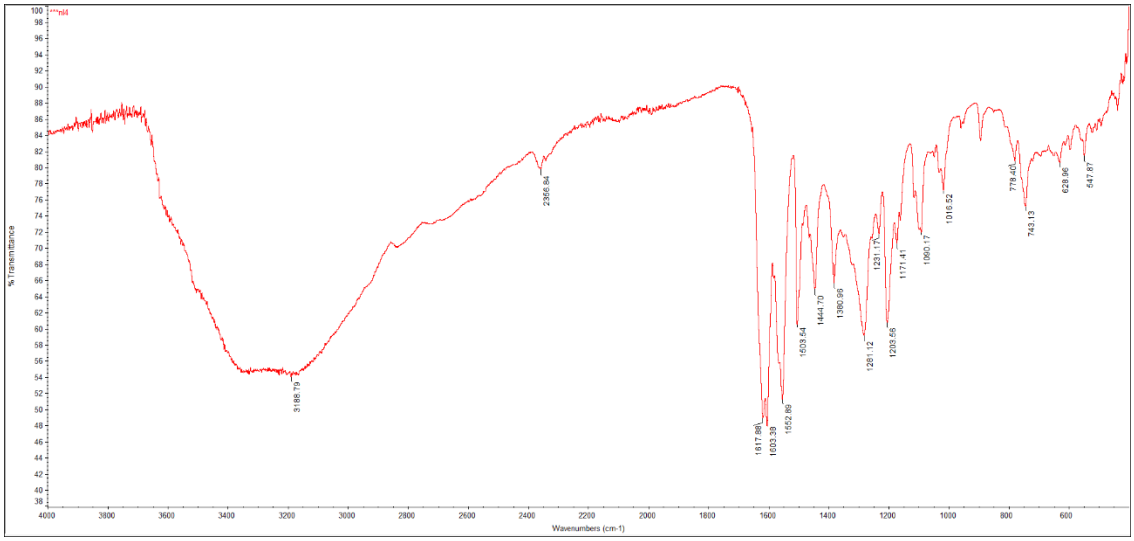

Figure B.3: ATR-FTIR spectrum of complex **C3**.

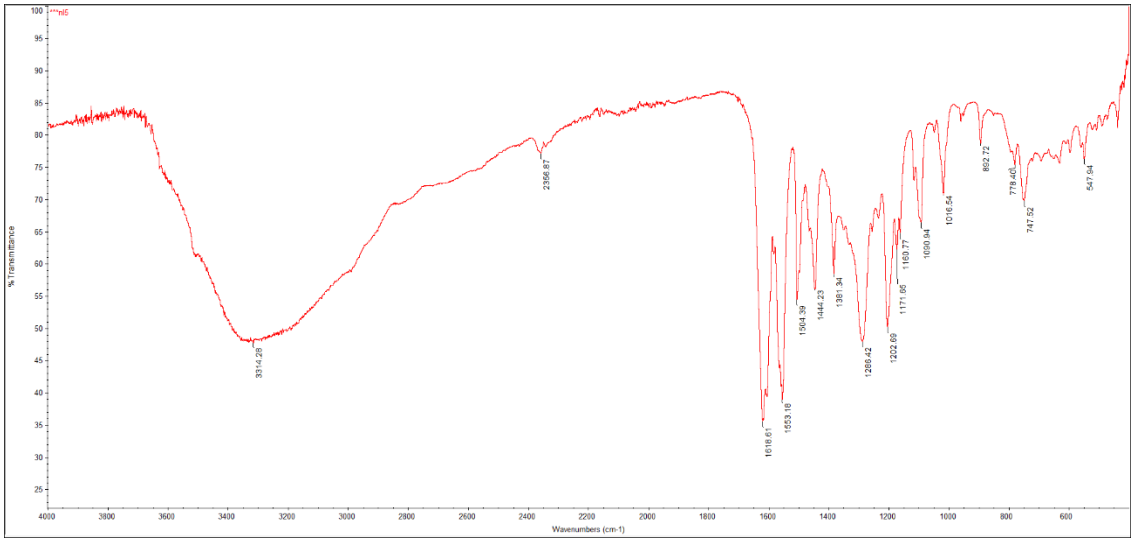

Figure B.4: ATR-FTIR spectrum of complex **C4**.

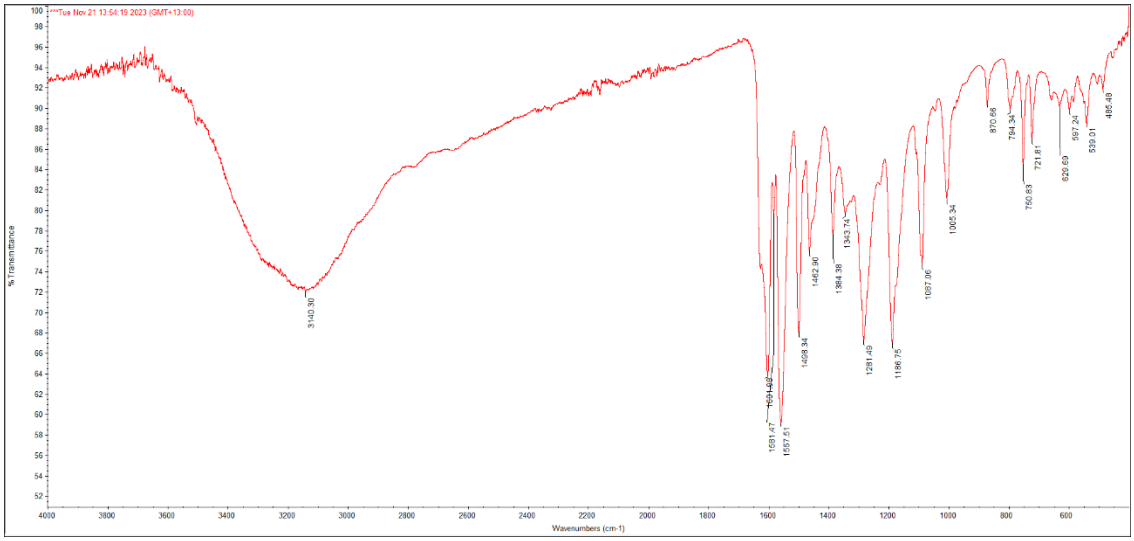

Figure B.5: ATR-FTIR spectrum of complex **C6**.

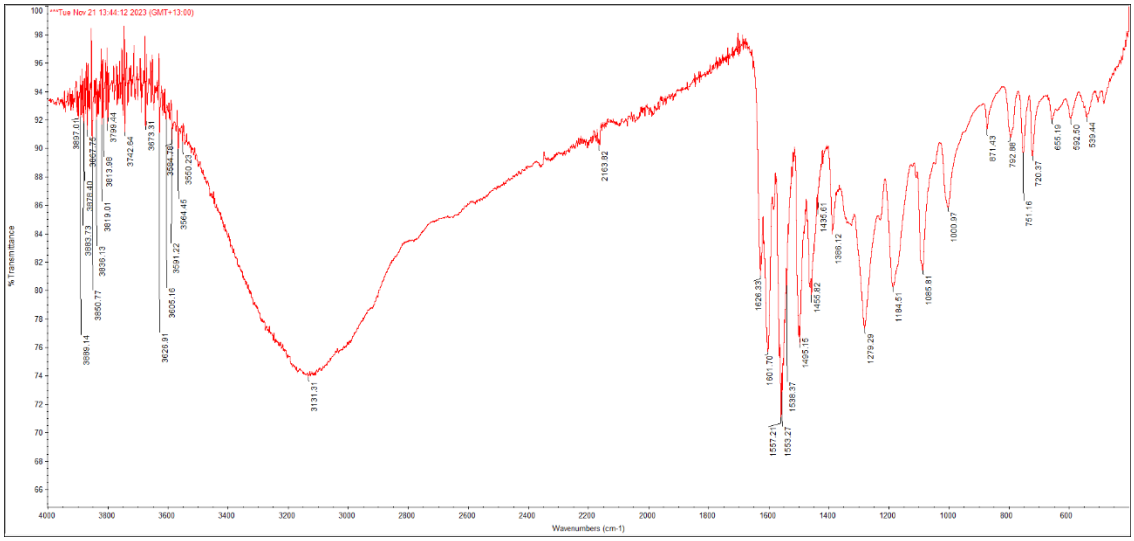

Figure B.6: ATR-FTIR spectrum of complex **C7**.

Figure B.7: ATR-FTIR spectrum of complex **C8**.

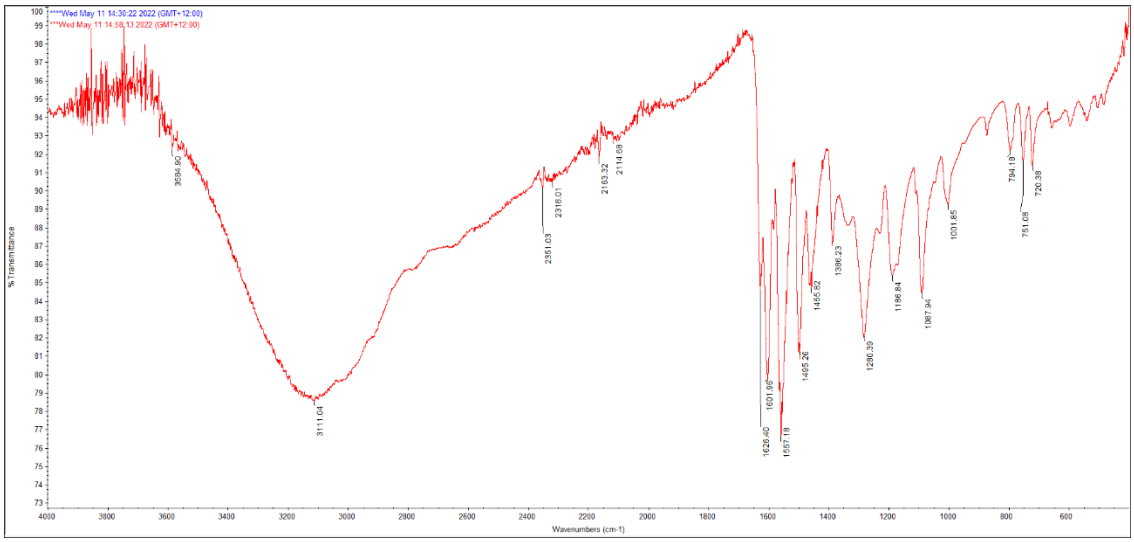

Figure B.8: ATR-FTIR spectrum of complex **C9**.

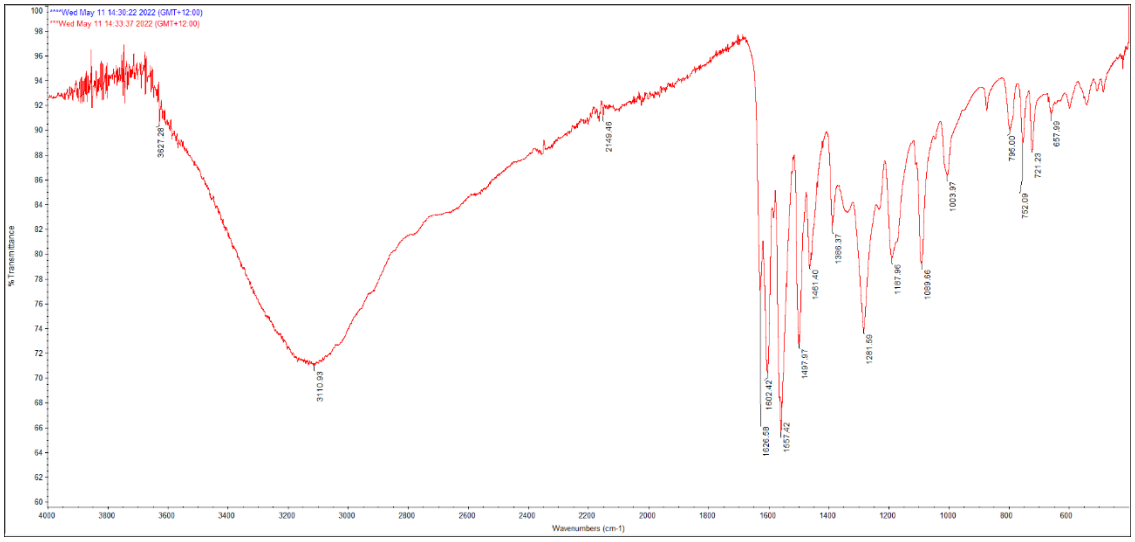

Figure B.9: ATR-FTIR spectrum of complex **C10**.

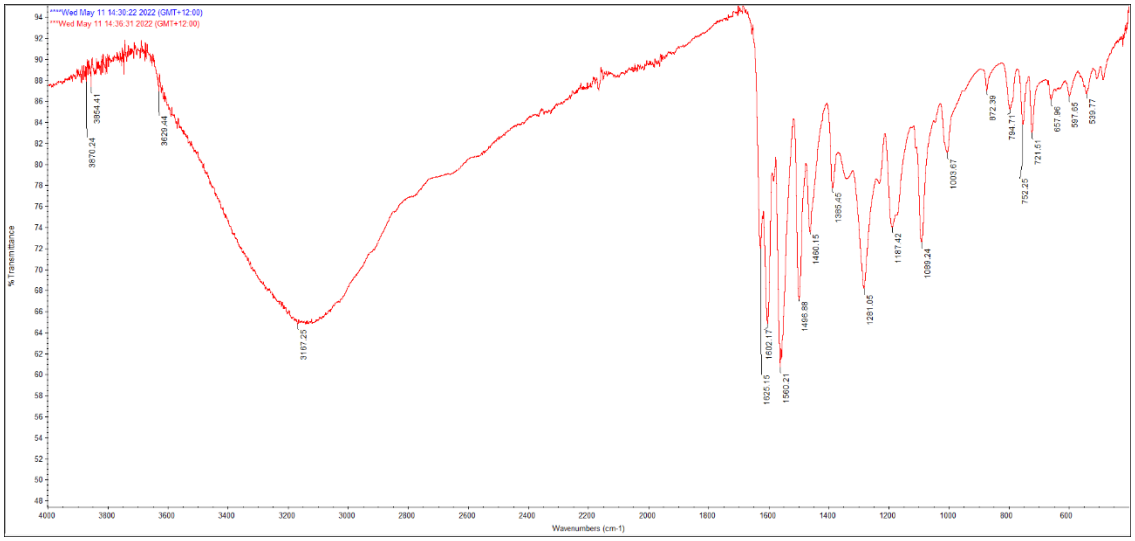

Figure B.10: ATR-FTIR spectrum of complex **C11**.

Figure B.11: ATR-FTIR spectrum of complex **C12**.

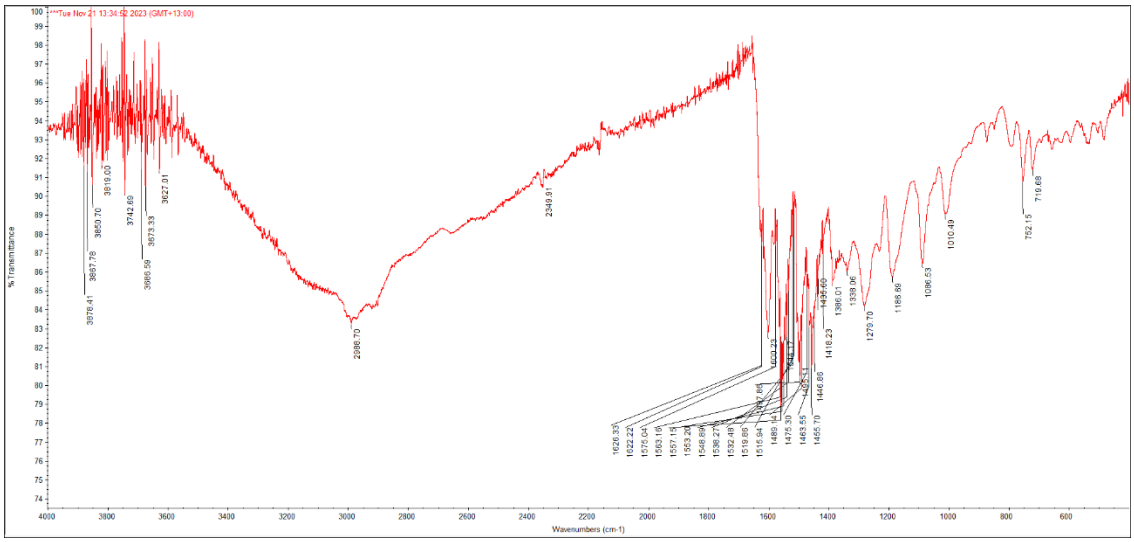

Figure B.12: ATR-FTIR spectrum of complex **C13**.

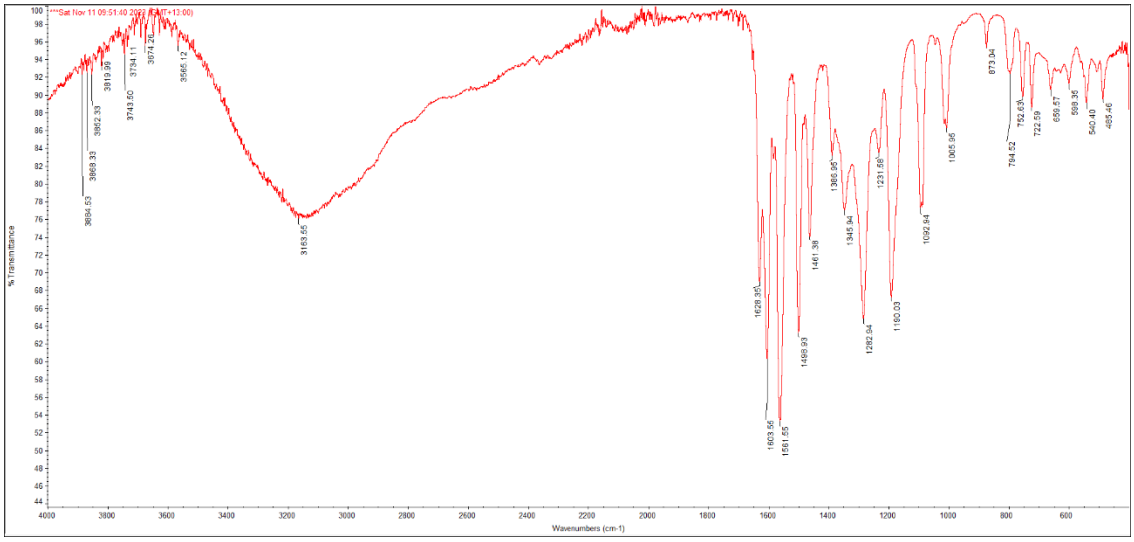

Figure B.13: ATR-FTIR spectrum of complex **C14**.

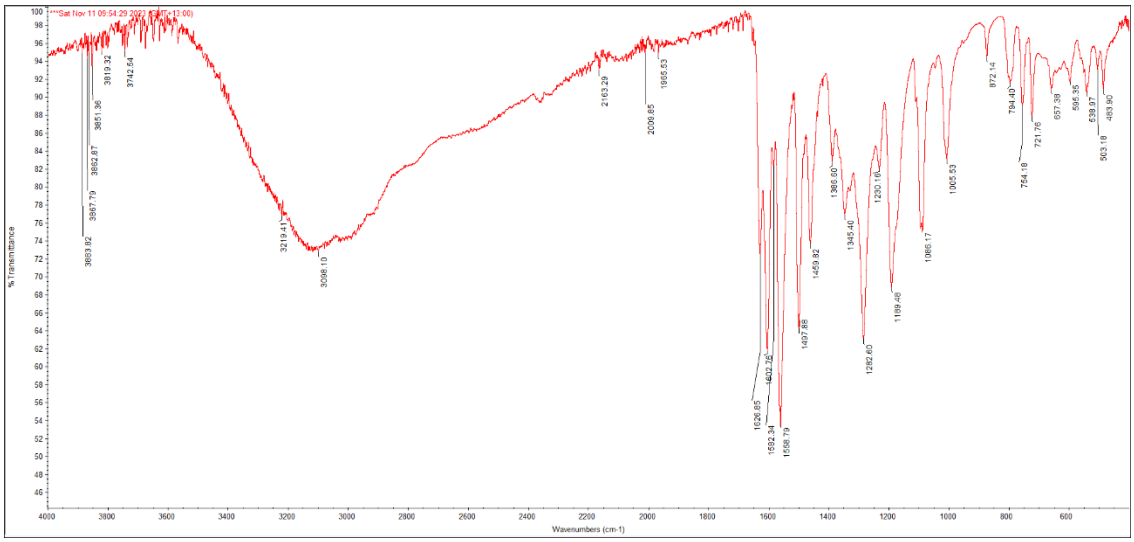

Figure B.14: ATR-FTIR spectrum of complex **C15**.

Appendix C

Assorted Tables

Table C1: Parameters of the Cole-Cole plot of **C9**			
T / K	χ_S / cm^3 mol^{-1}	χ_T / cm^3 mol^{-1}	α
3.0	1.26(6)	5.39(2)	0.34(1)
3.2	1.32(6)	5.080(9)	0.32(1)
3.4	1.34(6)	4.806(6)	0.30(1)
3.6	1.42(6)	4.554(4)	0.285(9)
3.8	1.4(1)	4.336(4)	0.28(1)
4.0	1.4(1)	4.143(3)	0.28(1)

Parameters are defined according to the following equation:

$$\chi_{(\omega)} = \chi_S + \frac{\chi_T - \chi_S}{1 + (i\omega\tau)^{1-\alpha}}$$

Table C2. Selected bond angles and M–Ln distances for complexes **C16** – **C22**							
	M1–Ln (Å)	M2–Ln (Å)	M1–O1–Ln (°)	M1–O2–Ln (°)	M2–O1–Ln (°)	M2–O2–Ln (°)	Ave. M–O–Ln (°)
C16	3.328(6)	-	105.2(3)	105.2(3)	-	-	105.2(3)
C17	3.4233(5)	3.4330(5)	107.9(1)	106.0(1)	107.4(1)	106.8(1)	107.0(1)
C18	3.421(1)	3.418(1)	106.3(2)	107.5(3)	107.2(3)	106.9(2)	107.0(3)
C19	3.3815(6)	3.3828(6)	106.7(1)	107.1(1)	106.4(1)	106.9(1)	106.8(1)
C20	-	-	-	-	-	-	-
C21	3.355(5)	3.3558(4)	107.3(6)	107.3(6)	108.1(6)	108.1(6)	107.7(6)
C22	3.443(3)	3.436(3)	107.8(4)	108.9(4)	109.2(3)	110.6(4)	109.1(4)

Table C3. Smallest Ln-Ln distances for complexes **C16 – C22**	
	Smallest Ln–Ln Distance (Å)
C16	9.561
C17	10.532
C18	10.882
C19	10.790
C20	8.088
C21	8.702
C22	10.779

Table C4: Number and type of intermolecular secondary interactions present in complexes **C1** – **C22**

	π-π stacking	Hydrogen bonding	Total
C1	8	4	12
C2	8	3	11
C3	8	4	12
C4	4	0	4
C5	2	4	6
C6	5	3	8
C7	5	3	8
C8	5	3	8
C9	5	3	8
C10	5	3	8
C11	5	3	8
C12	3	-	3
C13	6	-	6
C14	6	-	6
C15	6	-	6
C16	2	2	4
C17	5	3	8
C18	5	0	5
C19	3	0	3
C20	0	2	2
C21	2	2	4
C22	0	0	0

Appendix D

Crystal Structure and Refinement Data

Table D1. Crystal refinement data for complexes **C1** – **C3**

	C1	**C2**	**C3**
Empirical formula	$C_{44}H_{42}Cl_3DyN_4Ni_2O_{16}$	$C_{43.53}H_{39.28}Cl_3HoN_4Ni_2O_{15.5}$	$C_{44}H_{44}Cl_3ErN_4Ni_2O_{16}$
Formula weight/gmol^{-1}	1269.08	1255.19	1275.86
Temperature/K	100.00	100.00	100.00
Crystal system	triclinic	triclinic	triclinic
Space group	P-1	P-1	P-1
a/Å	10.3412(7)	10.2865(8)	10.2574(5)
b/Å	12.4587(8)	12.4612(11)	12.4423(5)
c/Å	19.0392(13)	19.0293(17)	18.9955(8)
α/°	95.777(4)	95.853(5)	95.075(2)
β/°	99.022(4)	99.146(5)	98.755(2)
γ/°	96.770(3)	96.852(5)	96.645(2)
Volume/Å^3	2387.9(3)	2372.7(4)	2366.03(18)
Z	2	2	2
ρ_{calc}/gcm^{-3}	1.765	1.757	1.791
μ/mm^{-1}	11.347	6.093	6.296
F(000)	1270.0	1253.0	1278.0
Crystal size/mm^3	? × ? × ?	0.15 × 0.02 × 0.02	0.19 × 0.06 × 0.05
Radiation	CuKα (λ = 1.54178)	CuKα (λ = 1.54178)	CuKα (λ = 1.54178)
2Θ range for data collection/°	4.734 to 136.49	4.74 to 136.476	7.194 to 136.47
Index ranges	-12 ≤ h ≤ 12, -14 ≤ k ≤ 14, -22 ≤ l ≤ 22	-12 ≤ h ≤ 12, -14 ≤ k ≤ 14, -22 ≤ l ≤ 22	-12 ≤ h ≤ 11, -14 ≤ k ≤ 14, -22 ≤ l ≤ 21
Reflections collected	18883	34020	10684
Independent reflections	8423 [R_{int} = 0.0894, R_{sigma} = 0.1248]	8352 [R_{int} = 0.0740, R_{sigma} = 0.0681]	7572 [R_{int} = 0.0445, R_{sigma} = 0.0740]
Data/restraints/parameters	8423/6/668	8352/6/669	7572/6/650
Goodness-of-fit on F^2	1.188	1.191	1.027
Final R indexes [$I \geq 2\sigma(I)$]	R_1 = 0.0984, wR_2 = 0.2736	R_1 = 0.0901, wR_2 = 0.2078	R_1 = 0.0653, wR_2 = 0.1653
Final R indexes [all data]	R_1 = 0.1489, wR_2 = 0.3098	R_1 = 0.1120, wR_2 = 0.2157	R_1 = 0.0845, wR_2 = 0.1802
Largest diff. peak/hole / e Å^{-3}	2.19/-4.04	1.50/-1.39	1.84/-2.81

Table D2. Crystal refinement data for complexes **C4** – **C6**

	C4	**C5**	**C6**
Empirical formula	$C_{42}H_{38}Cl_3N_4Ni_2O_{16}Tb$	$C_{65}H_{61}Cl_2Cu_3LaNaN_6O_{23}$	$C_{50}H_{62}Br_{2.8}Cu_2N_{4.2}O_{19.6}Y$
Formula weight/gmol^{-1}	1237.45	1718.93	1475.17
Temperature/K	100.00	100.00	100.00
Crystal system	monoclinic	triclinic	monoclinic
Space group	C2/c	P-1	$P2_1/n$
a/Å	21.342(2)	14.4129(9)	17.2422(17)
b/Å	17.818(2)	15.5664(10)	17.8148(19)
c/Å	15.5656(18)	17.8613(11)	18.357(2)
α/°	90	75.461(2)	90
β/°	103.855(3)	89.177(2)	99.915(6)
γ/°	90	75.355(2)	90
Volume/Å^3	5746.9(11)	3747.8(4)	5554.4(10)
Z	4	2	4
ρ_{calc}/gcm^{-3}	1.430	1.523	1.764
μ/mm^{-1}	8.512	6.655	5.293
F(000)	2472.0	1734.0	2973.0
Crystal size/mm^3	0.24 × 0.08 × 0.06	0.2 × 0.18 × 0.04	0.22 × 0.06 × 0.04
Radiation	CuKα (λ = 1.54178)	CuKα (λ = 1.54178)	CuKα (λ = 1.54178)
2Θ range for data collection/°	6.542 to 136.484	5.118 to 136.48	6.498 to 136.486
Index ranges	-25 ≤ h ≤ 25, -21 ≤ k ≤ 21, -18 ≤ l ≤ 18	-15 ≤ h ≤ 17, -18 ≤ k ≤ 18, -21 ≤ l ≤ 21	-20 ≤ h ≤ 20, -21 ≤ k ≤ 21, -19 ≤ l ≤ 22
Reflections collected	25581	37938	54611
Independent reflections	5188 [R_{int} = 0.0471, R_{sigma} = 0.0418]	12943 [R_{int} = 0.0341, R_{sigma} = 0.0359]	9766 [R_{int} = 0.0647, R_{sigma} = 0.0499]
Data/restraints/parameters	5188/6/322	12943/12/940	9766/67/768
Goodness-of-fit on F^2	1.047	1.034	1.134
Final R indexes [$I \geq 2\sigma(I)$]	R_1 = 0.0721, wR_2 = 0.2143	R_1 = 0.0414, wR_2 = 0.1162	R_1 = 0.0612, wR_2 = 0.1367
Final R indexes [all data]	R_1 = 0.0722, wR_2 = 0.2144	R_1 = 0.0417, wR_2 = 0.1166	R_1 = 0.0744, wR_2 = 0.1416
Largest diff. peak/hole / e Å^{-3}	2.96/-0.90	1.68/-1.19	2.38/-1.46

Table D3. Crystal refinement data for complexes **C7** – **C9**

	C7	**C8**	**C9**
Empirical formula	$C_{50}H_{62}Br_{2.6}Cu_2GdN_{4.4}O_{20.2}$	$C_{49.8}H_{61.2}Br_3Cu_2ErN_4O_{18.8}$	$C_{49}H_{58}Br_3Cu_2N_4O_{18}Tb$
Formula weight/gmol^{-1}	1539.93	1550.69	1516.72
Temperature/K	100.00	100.00	100.00
Crystal system	monoclinic	monoclinic	monoclinic
Space group	$P2_1/n$	$P2_1/n$	$P2_1/n$
a/Å	17.2699(12)	17.1422(8)	17.1318(10)
b/Å	17.8931(13)	17.7557(8)	17.8026(10)
c/Å	18.2873(13)	18.2694(8)	18.3083(11)
α/°	90	90	90
β/°	100.291(3)	99.757(3)	99.746(3)
γ/°	90	90	90
Volume/Å^3	5560.1(7)	5480.3(4)	5503.3(6)
Z	4	4	4
ρ_{calc}/gcm^{-3}	1.840	1.879	1.831
μ/mm^{-1}	11.371	6.858	10.295
F(000)	3070.0	3078.0	3008.0
Crystal size/mm^3	0.16 × 0.07 × 0.02	0.21 × 0.04 × 0.02	0.22 × 0.06 × 0.04
Radiation	CuKα (λ = 1.54178)	CuKα (λ = 1.54178)	CuKα (λ = 1.54178)
2Θ range for data collection/°	6.486 to 140.108	6.54 to 136.468	6.536 to 136.488
Index ranges	-21 ≤ h ≤ 21, -21 ≤ k ≤ 21, -21 ≤ l ≤ 22	-20 ≤ h ≤ 20, -21 ≤ k ≤ 21, -22 ≤ l ≤ 22	-20 ≤ h ≤ 20, -21 ≤ k ≤ 21, -22 ≤ l ≤ 22
Reflections collected	70820	66647	58688
Independent reflections	10527 [R_{int} = 0.0803, R_{sigma} = 0.0447]	10016 [R_{int} = 0.0786, R_{sigma} = 0.0480]	10025 [R_{int} = 0.0544, R_{sigma} = 0.0369]
Data/restraints/parameters	10527/49/767	10016/34/755	10025/0/728
Goodness-of-fit on F^2	1.104	1.054	1.071
Final R indexes [$I \geq 2\sigma(I)$]	R_1 = 0.0480, wR_2 = 0.1244	R_1 = 0.0676, wR_2 = 0.1752	R_1 = 0.0622, wR_2 = 0.1703
Final R indexes [all data]	R_1 = 0.0552, wR_2 = 0.1313	R_1 = 0.0834, wR_2 = 0.1868	R_1 = 0.0640, wR_2 = 0.1714
Largest diff. peak/hole / e Å^{-3}	1.38/-1.03	3.57/-1.31	2.29/-2.38

Table D4. Crystal refinement data for complexes **C10** – **C12**

	C10	**C11**	**C12**
Empirical formula	$C_{45.5}H_{46.8}Br_3Cu_2DyN_4O_{17.25}$	$C_{42}H_{38}Br_3Cu_2HoN_4O_{16}$	$C_{44.7}H_{43.7}Cl_{1.5}Cu_2N_{4.5}O_{21}Y$
Formula weight/gmol^{-1}	1454.98	1386.50	1249.10
Temperature/K	100.00	100.00	100.00
Crystal system	monoclinic	monoclinic	monoclinic
Space group	$P2_1/n$	$P2_1/n$	$P2_1/n$
a/Å	16.7741(17)	16.7861(11)	15.1725(15)
b/Å	17.8647(19)	17.7591(13)	20.884(2)
c/Å	17.9503(19)	17.8324(13)	17.1065(17)
α/°	90	90	90
β/°	98.471(6)	98.174(4)	91.657(5)
γ/°	90	90	90
Volume/Å^3	5320.4(10)	5261.9(6)	5418.0(9)
Z	4	4	4
ρ_{calc}/gcm^{-3}	1.816	1.750	1.531
μ/mm^{-1}	11.585	6.872	3.677
F(000)	2859.0	2704.0	2536.0
Crystal size/mm^3	0.2 × 0.15 × 0.1	0.15 × 0.12 × 0.04	0.24 × 0.1 × 0.08
Radiation	CuKα (λ = 1.54178)	CuKα (λ = 1.54178)	CuKα (λ = 1.54178)
2Θ range for data collection/°	6.734 to 136.49	6.768 to 136.486	6.68 to 130.166
Index ranges	-19 ≤ h ≤ 20, -21 ≤ k ≤ 20, -20 ≤ l ≤ 21	-19 ≤ h ≤ 20, -21 ≤ k ≤ 19, -21 ≤ l ≤ 21	-17 ≤ h ≤ 17, -24 ≤ k ≤ 24, -19 ≤ l ≤ 20
Reflections collected	58845	68174	50574
Independent reflections	9630 [R_{int} = 0.0520, R_{sigma} = 0.0333]	9618 [R_{int} = 0.1059, R_{sigma} = 0.0706]	9055 [R_{int} = 0.0557, R_{sigma} = 0.0405]
Data/restraints/parameters	9630/6/731	9618/12/662	9055/172/756
Goodness-of-fit on F^2	1.122	1.063	2.340
Final R indexes [$I \geq 2\sigma(I)$]	R_1 = 0.0720, wR_2 = 0.1825	R_1 = 0.1183, wR_2 = 0.3234	R_1 = 0.1645, wR_2 = 0.4761
Final R indexes [all data]	R_1 = 0.0747, wR_2 = 0.1839	R_1 = 0.1380, wR_2 = 0.3369	R_1 = 0.1713, wR_2 = 0.4849
Largest diff. peak/hole / e Å^{-3}	1.88/-1.97	3.62/-0.98	3.93/-1.45

Table D5. Crystal refinement data for complexes **C13** – **C15**

	C13	**C14**	**C15**
Empirical formula	$C_{41.5}H_{34}Cl_3Cu_2GdN_4O_{13.5}$	$C_{40}H_{26}Cl_3Cu_2ErN_4O_{12}$	$C_{47}H_{60}Cl_3Cu_2N_4O_{22}Tb$
Formula weight/gmol^{-1}	1195.41	1155.34	1425.34
Temperature/K	100.00	100.00	100.00
Crystal system	monoclinic	monoclinic	monoclinic
Space group	C2/c	I2/a	I2/a
a/Å	21.1391(14)	15.6011(9)	20.408(9)
b/Å	21.4691(13)	20.6965(11)	14.199(5)
c/Å	14.6883(11)	20.5583(15)	20.743(6)
α/°	90	90	90
β/°	112.882(4)	107.356(2)	101.288(17)
γ/°	90	90	90
Volume/Å^3	6141.5(7)	6335.8(7)	5895(4)
Z	4	4	4
ρ_{calc}/gcm^{-3}	1.293	1.211	1.606
μ/mm^{-1}	9.327	4.692	8.551
F(000)	2368.0	2268.0	2880.0
Crystal size/mm^3	0.13 × 0.04 × 0.02	0.11 × 0.1 × 0.07	0.25 × 0.07 × 0.05
Radiation	CuKα (λ = 1.54178)	CuKα (λ = 1.54178)	CuKα (λ = 1.54178)
2Θ range for data collection/°	6.126 to 136.476	6.206 to 133.186	7.592 to 130.164
Index ranges	-25 ≤ h ≤ 25, -25 ≤ k ≤ 25, -17 ≤ l ≤ 17	-18 ≤ h ≤ 18, -24 ≤ k ≤ 24, -24 ≤ l ≤ 24	-23 ≤ h ≤ 23, -12 ≤ k ≤ 16, -24 ≤ l ≤ 22
Reflections collected	30289	59783	19278
Independent reflections	5395 [R_{int} = 0.0829, R_{sigma} = 0.0597]	5486 [R_{int} = 0.0446, R_{sigma} = 0.0243]	4974 [R_{int} = 0.1614, R_{sigma} = 0.1325]
Data/restraints/parameters	5395/18/310	5486/0/301	4974/0/343
Goodness-of-fit on F^2	1.097	1.102	1.350
Final R indexes [I≥2σ(I)]	R_1 = 0.1213, wR_2 = 0.2618	R_1 = 0.0556, wR_2 = 0.1486	R_1 = 0.1364, wR_2 = 0.3691
Final R indexes [all data]	R_1 = 0.1386, wR_2 = 0.2726	R_1 = 0.0596, wR_2 = 0.1507	R_1 = 0.1919, wR_2 = 0.4062
Largest diff. peak/hole / e Å^{-3}	4.22/-1.79	1.45/-0.82	2.33/-1.31

Table D6. Crystal refinement data for complexes **C16** – **C18**

	C16	**C17**	**C18**
Empirical formula	$C_{22}H_{22}DyMgN_5O_{17}$	$C_{50}H_{62}Br_{2.6}Cu_2GdN_{4.4}O_{20.2}$	$C_{40}H_{34}Cu_2GdN_7O_{24}$
Formula weight/gmol^{-1}	815.25	1539.93	1281.07
Temperature/K	100.00	100.00	100.00
Crystal system	monoclinic	monoclinic	monoclinic
Space group	P2/n	$P2_1/n$	$P2_1/n$
a/Å	9.6141(11)	17.2591(13)	15.3187(19)
b/Å	15.5828(18)	17.9555(14)	20.812(3)
c/Å	10.2257(12)	18.2296(14)	16.653(2)
α/°	90	90	90
β/°	97.558(6)	100.244(2)	90.516(6)
γ/°	90	90	90
Volume/Å^3	1518.6(3)	5559.2(7)	5309.2(12)
Z	2	4	4
ρ_{calc}/gcm^{-3}	1.783	1.840	1.603
μ/mm^{-1}	14.136	11.373	9.649
F(000)	806.0	3070.0	2548.0
Crystal size/mm^3	0.535 × 0.276 × 0.234	0.19 × 0.14 × 0.06	0.19 × 0.14 × 0.06
Radiation	CuKα (λ = 1.54178)	CuKα (λ = 1.54178)	CuKα (λ = 1.54178)
2Θ range for data collection/°	10.41 to 136.462	6.5 to 136.402	6.798 to 136.488
Index ranges	-11 ≤ h ≤ 11, -18 ≤ k ≤ 18, -12 ≤ l ≤ 12	-20 ≤ h ≤ 20, -21 ≤ k ≤ 21, -21 ≤ l ≤ 21	-18 ≤ h ≤ 16, -25 ≤ k ≤ 25, -20 ≤ l ≤ 20
Reflections collected	10666	70878	59546
Independent reflections	2617 [R_{int} = 0.0598, R_{sigma} = 0.0544]	10147 [R_{int} = 0.0443, R_{sigma} = 0.0286]	9665 [R_{int} = 0.0584, R_{sigma} = 0.0404]
Data/restraints/parameters	2617/3/217	10147/50/787	9665/10/691
Goodness-of-fit on F^2	1.341	1.070	1.312
Final R indexes [$I \geq 2\sigma(I)$]	R_1 = 0.1079, wR_2 = 0.2712	R_1 = 0.0267, wR_2 = 0.0728	R_1 = 0.1013, wR_2 = 0.3001
Final R indexes [all data]	R_1 = 0.1092, wR_2 = 0.2734	R_1 = 0.0293, wR_2 = 0.0732	R_1 = 0.1147, wR_2 = 0.3172
Largest diff. peak/hole / e Å^{-3}	3.25/-2.28	0.84/-0.64	2.42/-1.15

Table D7. Crystal refinement data for complexes **C19** – **C22**

	C19	**C20**	**C21**	**C22**
Empirical formula	$C_{49}H_{55}Cu_2N_7O_{27}Y$	$C_{33}H_{26}CuN_2O_7$	$C_{64.4}H_{44.4}Cl_2Cu_2IN_4O_{12}Y$	$C_{66}H_{57}CaCl_2N_4Ni_2O_{14}$
Formula weight/gmol^{-1}	1389.99	626.10	1480.03	1358.55
Temperature/K	100.00	100.00	100.00	103.00
Crystal system	monoclinic	triclinic	monoclinic	triclinic
Space group	$P2_1/n$	P-1	C2/c	P-1
a/Å	15.1056(6)	10.180(2)	14.799(4)	11.1052(14)
b/Å	20.9357(8)	12.210(3)	47.466(12)	18.210(2)
c/Å	17.3629(7)	13.183(3)	13.233(4)	21.538(3)
α/°	90	103.241(9)	90	102.608(12)
β/°	92.6310(10)	105.732(9)	109.66(2)	90.020(8)
γ/°	90	95.302(9)	90	107.731(8)
Volume/Å^3	5485.2(4)	1514.4(6)	8754(4)	4038.1(9)
Z	4	2	4	2
ρ_{calc}/gcm^{-3}	1.683	1.373	1.123	1.117
μ/mm^{-1}	3.143	1.443	5.144	2.190
F(000)	2844.0	646.0	2955.0	1406.0
Crystal size/mm^3	0.45 × 0.07 × 0.06	0.2 × 0.2 × 0.17	0.1 × 0.1 × 0.04	0.13 × 0.05 × 0.04
Radiation	CuKα (λ = 1.54178)	CuKα (λ = 1.54178)	CuKα (λ = 1.54178)	CuKα (λ = 1.54178)
2Θ range for data collection/°	6.618 to 136.488	7.542 to 136.478	3.722 to 130.146	4.214 to 136.486
Index ranges	-18 ≤ h ≤ 18, -24 ≤ k ≤ 25, -20 ≤ l ≤ 20	-11 ≤ h ≤ 12, -14 ≤ k ≤ 14, -15 ≤ l ≤ 15	-17 ≤ h ≤ 17, -55 ≤ k ≤ 55, -15 ≤ l ≤ 15	-13 ≤ h ≤ 13, -21 ≤ k ≤ 18, -25 ≤ l ≤ 25
Reflections collected	91304	31309	47057	54745
Independent reflections	9956 [R_{int} = 0.1922, R_{sigma} = 0.0754]	5282 [R_{int} = 0.0432, R_{sigma} = 0.0340]	6928 [R_{int} = 0.1376, R_{sigma} = 0.1000]	14453 [R_{int} = 0.2753, R_{sigma} = 0.2983]
Data/restraints/parameters	9956/6/799	5282/0/394	6928/45/353	14453/0/691
Goodness-of-fit on F^2	1.091	1.109	2.092	1.010
Final R indexes [$I \geq 2\sigma(I)$]	R_1 = 0.0707, wR_2 = 0.1884	R_1 = 0.0527, wR_2 = 0.1476	R_1 = 0.2150, wR_2 = 0.5119	R_1 = 0.1652, wR_2 = 0.3854
Final R indexes [all data]	R_1 = 0.0739, wR_2 = 0.1893	R_1 = 0.0537, wR_2 = 0.1481	R_1 = 0.2400, wR_2 = 0.5324	R_1 = 0.2909, wR_2 = 0.4729
Largest diff. peak/hole / e Å^{-3}	1.85/-1.08	0.57/-0.62	2.73/-1.67	0.78/-0.67

Bibliography

1. D. Jiles, *Introduction to Magnetism and Magnetic Materials*, CRC Press, Boca Raton, 2016.
2. S. G. Vul'fson, *Molecular magnetochemistry*, Gordon and Breach Science Publishers, Amsterdam, 1998.
3. A. Zabala-Lekuona, J. M. Seco and E. Colacio, *Coord. Chem. Rev.*, 2021, **441**, 1-37.
4. A. Dey, J. Acharya and V. Chandrasekhar, *Chem. Asian. J.*, 2019, **14**, 4433-4453.
5. F. Neese and D. A. Pantazis, *Faraday Discuss.*, 2011, **148**, 229-238.
6. E. J. L. McInnes, *Angew. Chem., Int. Ed.*, 2016, **55**, 1959-1959.
7. F.-S. Guo, B. M. Day, Y.-C. Chen, M.-L. Tong, A. Mansikkamäki and R. A. Layfield, *Science*, 2018, **362**, 1400-1403.
8. C. Wang, Y.-S. Meng, S.-D. Jiang, B.-W. Wang and S. Gao, *Sci. China. Chem*, 2023, **66**, 683-702.
9. K. Yang, R. Sun, J. Zhao, C. Deng, B. Wang, S. Gao and W. Huang, *Inorg. Chem.*, 2023, **62**, 9892-9903.
10. X.-D. Huang, X.-F. Ma and L.-M. Zheng, *Angew. Chem., Int. Ed.*, 2023, **62**, e202300088.
11. R. Weller, M. Atanasov, S. Demeshko, T.-Y. Chen, I. Mohelsky, E. Bill, M. Orlita, F. Meyer, F. Neese and C. G. Werncke, *Inorg. Chem.*, 2023, **62**, 3153-3161.
12. T. Xue, Y.-S. Ding, D. Reta, Q.-W. Chen, X. Zhu and Z. Zheng, *Cryst. Growth Des*, 2023, **23**, 565-573.
13. D. Reta, J. G. C. Kragskow and N. F. Chilton, *J. Am. Chem. Soc.*, 2021, **143**, 5943-5950.
14. A. H. Vincent, Y. L. Whyatt, N. F. Chilton and J. R. Long, *J. Am. Chem. Soc.*, 2023, **145**, 1572-1579.
15. A. Chiesa, F. Cugini, R. Hussain, E. Macaluso, G. Allodi, E. Garlatti, M. Giansiracusa, C. A. P. Goodwin, F. Ortu, D. Reta, J. M. Skelton, T. Guidi, P. Santini, M. Solzi, R. De Renzi, D. P. Mills, N. F. Chilton and S. Carretta, *Phys. Rev. B*, 2020, **101**, 1-9.
16. A. Castro-Alvarez, Y. Gil, L. Llanos and D. Aravena, *Inorg. Chem. Front.*, 2020, **7**, 2478-2486.
17. M. Gregson, N. F. Chilton, A.-M. Ariciu, F. Tuna, I. F. Crowe, W. Lewis, A. J. Blake, D. Collison, E. J. L. McInnes, R. E. P. Winpenny and S. T. Liddle, *Chem. Sci.*, 2016, **7**, 155-165.
18. S. K. Langley, D. P. Wielechowski, V. Vieru, N. F. Chilton, B. Moubaraki, B. F. Abrahams, L. F. Chibotaru and K. S. Murray, *Angew. Chem., Int. Ed.*, 2013, **52**, 12014-12019.
19. F. S. Guo, B. M. Day, Y. C. Chen, M. L. Tong, A. Mansikkamäki and R. A. Layfield, *Science*, 2018, **362**, 1400-1403.
20. S. Gómez-Coca, A. Urtizberea, E. Cremades, P. J. Alonso, A. Camón, E. Ruiz and F. Luis, *Nat. Commun.*, 2014, **5**, 1-8.
21. R. Boča and C. Rajnák, *Coord. Chem. Rev.*, 2021, **430**, 1-14.
22. L. Bogani and W. Wernsdorfer, *Nat. Mater.*, 2008, **7**, 179-186.
23. M. N. Leuenberger and D. Loss, *Nature*, 2001, **410**, 789-793.
24. N. F. Chilton, *Annu. Rev. Mater. Res.*, 2022, **52**, 79-101.
25. J. Villain, F. Hartman-Boutron, R. Sessoli and A. Rettori, *Europhys. Lett.*, 1994, **27**, 159-164.
26. Z. Zhu, M. Guo, X.-L. Li and J. Tang, *Coord. Chem. Rev.*, 2019, **378**, 350-364.
27. R. Orbach and B. Bleaney, *Proc. R. Soc. London, Ser. A*, 1961, **264**, 458-484.
28. M. Briganti, F. Santanni, L. Tesi, F. Totti, R. Sessoli and A. Lunghi, *J. Am. Chem. Soc.*, 2021, **143**, 13633-13645.

29. A. Lunghi, F. Totti, S. Sanvito and R. Sessoli, *Chem. Sci.*, 2017, **8**, 6051-6059.
30. R. J. Blagg, L. Ungur, F. Tuna, J. Speak, P. Comar, D. Collison, W. Wernsdorfer, E. J. L. McInnes, L. F. Chibotaru and R. E. P. Winpenny, *Nat. Chem.*, 2013, **5**, 673-678.
31. K. R. Vignesh, S. K. Langley, K. S. Murray and G. Rajaraman, *Chem. Eur. J.*, 2017, **23**, 1654-1666.
32. M. J. Giansiracusa, A. K. Kostopoulos, D. Collison, R. E. P. Winpenny and N. F. Chilton, *Chem. Commun.*, 2019, **55**, 7025-7028.
33. L. Escalera-Moreno, J. J. Baldoví, A. Gaita-Ariño and E. Coronado, *Chem. Sci.*, 2018, **9**, 3265-3275.
34. K. S. Pedersen, J. Dreiser, H. Weihe, R. Sibille, H. V. Johannesen, M. A. Sørensen, B. E. Nielsen, M. Sigrist, H. Mutka, S. Rols, J. Bendix and S. Piligkos, *Inorg. Chem.*, 2015, **54**, 7600-7606.
35. Z. Zhu and J. Tang, *Nat. Sci. Rev.*, 2022, **9**, 1-3.
36. H.-D. Li, S.-G. Wu and M.-L. Tong, *Chem. Commun.*, 2023, **59**, 6159-6170.
37. S. T. Liddle and J. van Slageren, *Chem. Soc. Rev.*, 2015, **44**, 6655-6669.
38. H. Weihe and H. U. Güdel, *Inorg. Chem.*, 1997, **36**, 3632-3639.
39. T. Gupta, M. F. Beg and G. Rajaraman, *Inorg. Chem.*, 2016, **55**, 11201-11215.
40. W. Wernsdorfer, N. Aliaga-Alcalde, D. N. Hendrickson and G. Christou, *Nature*, 2002, **416**, 406-409.
41. R. Sessoli, D. Gatteschi, A. Caneschi and M. A. Novak, *Nature*, 1993, **365**, 141-143.
42. T. Lis, *Acta Cryst.*, 1980, **36**, 2042-2046.
43. M. A. Halcrow, *Chem. Soc. Rev.*, 2013, **42**, 1784-1795.
44. A. M. Ako, I. J. Hewitt, V. Mereacre, R. Clérac, W. Wernsdorfer, C. E. Anson and A. K. Powell, *Angew. Chem., Int. Ed.*, 2006, **45**, 4926-4929.
45. C. J. Milios, A. Vinslava, W. Wernsdorfer, S. Moggach, S. Parsons, S. P. Perlepes, G. Christou and E. K. Brechin, *J. Am. Chem. Soc.*, 2007, **129**, 2754-2755.
46. P. C. Bunting, M. Atanasov, E. Damgaard-Møller, M. Perfetti, I. Crassee, M. Orlita, J. Overgaard, J. van Slageren, F. Neese and J. R. Long, *Science*, 2018, **362**, eaat7319.
47. J. D. Rinehart and J. R. Long, *Chem. Sci.*, 2011, **2**, 2078-2085.
48. N. Ishikawa, M. Sugita, T. Ishikawa, S.-y. Koshihara and Y. Kaizu, *J. Am. Chem. Soc.*, 2003, **125**, 8694-8695.
49. N. F. Chilton, *Inorg. Chem.*, 2015, **54**, 2097-2099.
50. X. Tan, X. Ji and J.-M. Zheng, *Inorg. Chem. Commun.*, 2015, **60**, 27-32.
51. K. Liu, W. Shi and P. Cheng, *Coord. Chem. Rev.*, 2015, **289-290**, 74-122.
52. S. Osa, T. Kido, N. Matsumoto, N. Re, A. Pochaba and J. Mrozinski, *J. Am. Chem. Soc.*, 2004, **126**, 420-421.
53. J. L. W. Liu, J. Y. Huang, G. Z. Chen, Y. C. Jia, J. H. Ungur, L. Chibotaru, L. F. Chen, X. M. Tong, M. L., *Sci. Rep.*, 2015, **5**, 16621-16629.
54. S.-Y. Lin, Y.-N. Guo, Y. Guo, L. Zhao, P. Zhang, H. Ke and J. Tang, *Chem. Commun.*, 2012, **48**, 6924-6926.
55. X. Liu, C. Zhao, J. Wu, Z. Zhu and J. Tang, *Dalton. Trans.*, 2022, **51**, 16444-16447.
56. S.-Y. Lin, C. Wang, L. Zhao, J. Wu and J. Tang, *Dalton. Trans.*, 2015, **44**, 223-229.
57. S. Liu, Y. Gil, C. Zhao, J. Wu, Z. Zhu, X.-L. Li, D. Aravena and J. Tang, *Inorg. Chem. Front.*, 2022, **9**, 4982-4989.
58. Z. Zhu, C. Zhao, T. Feng, X. Liu, X. Ying, X.-L. Li, Y.-Q. Zhang and J. Tang, *J. Am. Chem. Soc.*, 2021, **143**, 10077-10082.
59. K.-X. Yu, J. G. C. Kragskow, Y.-S. Ding, Y.-Q. Zhai, D. Reta, N. F. Chilton and Y.-Z. Zheng, *Chem*, 2020, **6**, 1777-1793.
60. M. A. Palacios, J. Nehrkorn, E. A. Suturina, E. Ruiz, S. Gómez-Coca, K. Holldack, A. Schnegg, J. Krzystek, J. M. Moreno and E. Colacio, *Chem. Eur. J.*, 2017, **23**, 11649-11661.

61. P.-E. Car, M. Perfetti, M. Mannini, A. Favre, A. Caneschi and R. Sessoli, *Chem. Commun.*, 2011, **47**, 3751-3753.
62. G. Cucinotta, M. Perfetti, J. Luzon, M. Etienne, P.-E. Car, A. Caneschi, G. Calvez, K. Bernot and R. Sessoli, *Angew. Chem., Int. Ed.*, 2012, **51**, 1606-1610.
63. M.-E. Boulon, G. Cucinotta, J. Luzon, C. Degl'Innocenti, M. Perfetti, K. Bernot, G. Calvez, A. Caneschi and R. Sessoli, *Angew. Chem., Int. Ed.*, 2013, **52**, 350-354.
64. M. Briganti, G. F. Garcia, J. Jung, R. Sessoli, B. Le Guennic and F. Totti, *Chem. Sci.*, 2019, **10**, 7233-7245.
65. X.-W. Liu, Z. Wu, J.-T. Chen, L. Li, P. Chen and W.-B. Sun, *Inorg. Chem. Front.*, 2020, **7**, 1229-1238.
66. S. Petit, G. Pilet, D. Luneau, L. F. Chibotaru and L. Ungur, *Dalton. Trans.*, 2007, 4582-4588.
67. C.-I. Yang, K.-H. Cheng, S.-P. Hung, M. Nakano and H.-L. Tsai, *Polyhedron*, 2011, **30**, 3272-3278.
68. R. Mitsuhashi, S. Hosoya, T. Suzuki, Y. Sunatsuki, H. Sakiyama and M. Mikuriya, *Dalton. Trans.*, 2019, **48**, 395-399.
69. R. Mitsuhashi, S. Hosoya, T. Suzuki, Y. Sunatsuki, H. Sakiyama and M. Mikuriya, *RSC Adv.*, 2020, **10**, 43472-43479.
70. A. D. Fournet, K. J. Mitchell, W. Wernsdorfer, K. A. Abboud and G. Christou, *Inorg. Chem.*, 2017, **56**, 10706-10716.
71. Y.-S. Jiao, C.-Q. Jiao, Y.-S. Meng, X.-R. Liu, L. Zhao and T. Liu, *Inorg. Chem. Commun.*, 2018, **93**, 87-91.
72. C. Zhao, Z. Zhu, X.-L. Li and J. Tang, *Inorg. Chem. Front.*, 2022, **9**, 4049-4055.
73. G. Novitchi, W. Wernsdorfer, L. F. Chibotaru, J.-P. Costes, C. E. Anson and A. K. Powell, *Angew. Chem., Int. Ed.*, 2009, **48**, 1614-1619.
74. J.-P. Costes, S. Shova and W. Wernsdorfer, *Dalton. Trans.*, 2008, 1843-1849.
75. T. Hamamatsu, K. Yabe, M. Towatari, S. Osa, N. Matsumoto, N. Re, A. Pochaba, J. Mrozinski, J.-L. Gallani, A. Barla, P. Imperia, C. Paulsen and J.-P. Kappler, *Inorg. Chem.*, 2007, **46**, 4458-4468.
76. C. Aronica, G. Pilet, G. Chastanet, W. Wernsdorfer, J.-F. Jacquot and D. Luneau, *Angew. Chem., Int. Ed.*, 2006, **45**, 4659-4662.
77. S. Zhang, W. Mo, J. Zhang, Z. Zhang, B. Yin, D. Hu and S. Chen, *Inorg. Chem.*, 2019, **58**, 15330-15343.
78. F. Z. Chiboub Fellah, S. Boulefred, A. Chiboub Fellah, B. El Rez, C. Duhayon and J.-P. Sutter, *Inorg. Chim. Acta.*, 2016, **439**, 24-29.
79. A. B. Canaj, M. K. Singh, C. Wilson, G. Rajaraman and M. Murrie, *Chem. Commun.*, 2018, **54**, 8273-8276.
80. L. Gagliardi, R. Lindh and G. Karlström, *J. Chem. Phys.*, 2004, **121**, 4494-4500.
81. G. A. Ramakant, N. Ahmed, I. Tarannum, S. Mehta, M. Nandeshwar, A. Mondal, S. K. Singh and G. Prabusankar, *Cryst. Growth Des*, 2022, **22**, 6046-6055.
82. B. Yao, Y.-Q. Zhang, Y.-F. Deng, T. Li and Y.-Z. Zhang, *Inorg. Chem.*, 2022, **61**, 15392-15397.
83. H. Douib, K. Dhbaibi, B. Lefeuvre, V. Dorcet, T. Guizouarn and F. Pointillart, *Chirality*, 2023, **35**, 155-164.
84. Y. Gil, L. Llanos, P. Cancino, P. Fuentealba, A. Vega, E. Spodine and D. Aravena, *J. Phys. Chem.*, 2020, **124**, 5308-5320.
85. R. Herchel, P. Zoufalý and I. Nemec, *RSC Adv.*, 2019, **9**, 569-575.
86. M. Dolai, T. Mistri, A. Panja and M. Ali, *Inorg. Chim. Acta.*, 2013, **399**, 95-104.
87. G. E. Kostakis, I. J. Hewitt, A. M. Ako, V. Mereacre and A. K. Powell, *Phil. Trans. R. Soc. A.*, 2010, **368**, 1509-1536.

88. Sushila, R. Siddiqui, S. Patra, K. Shivam, A. Sil, B. Guchhait, H. Tian, R. Kataria, S. Goswami, P. Venugopalan and R. Patra, *Inorg. Chem.*, 2022, **61**, 11484-11496.
89. S. Schmitz, J. van Leusen, N. V. Izarova, Y. Lan, W. Wernsdorfer, P. Kogerler and K. Y. Monakhov, *Dalton. Trans.*, 2016, **45**, 16148-16152.
90. K. Y. Monakhov, W. Bensch and P. Kögerler, *Chem. Soc. Rev.*, 2015, **44**, 8443-8483.
91. H. Schiff, *Justus Liebigs Ann. Chem.*, 1866, **140**, 92-137.
92. V. K. Rao, S. S. Reddy, B. S. Krishna, K. R. M. Naidu, C. N. Raju and S. K. Ghosh, *Green Chemistry Letters and Reviews*, 2010, **3**, 217-223.
93. J. A. Klaus, T. M. Brooks, M. Zhou, A. J. Veinot, A. M. Warman, A. Palayew, P. T. Gormley, B. Ninh Khuong, C. M. Vogels, J. D. Masuda, F. J. Baerlocher and S. A. Westcott, *Transition Metal Chemistry*, 2017, **42**, 263-271.
94. C. M. Liu, D. Q. Zhang, X. Hao and D. B. Zhu, *Chem. Asian. J.*, 2014, **9**, 1847-1853.
95. A. Dey, J. Acharya and V. Chandrasekhar, *Chem. Asian. J.*, 2019, **14**, 4433-4453.
96. L. Rosado Piquer and E. C. Sanudo, *Dalton. Trans.*, 2015, **44**, 8771-8780.
97. H. Schiff, *Justus Liebigs Annalen der Chemie*, 1866, **140**, 92-137.
98. J. S. Casas, M. S. García-Tasende and J. Sordo, *Coord. Chem. Rev.*, 2000, **209**, 197-261.
99. J. A. Klaus, T. M. Brooks, M. Zhou, A. J. Veinot, A. M. Warman, A. Palayew, P. T. Gormley, B. Ninh Khuong, C. M. Vogels, J. D. Masuda, F. J. Baerlocher and S. A. Westcott, *Transit. Met. Chem.*, 2017, **42**, 263-271.
100. E. J. L. McInnes, *Angew. Chem., Int. Ed.*, 2016, **55**, 1959-1959.
101. M. Dolai, M. Ali, C. Rajnák, J. Titiš and R. Boča, *New J. Chem.*, 2019, **43**, 12698-12701.
102. A. Vráblová, M. Tomás, L. R. Falvello, Ľ. Dlháň, J. Titiš, J. Černák and R. Boča, *Dalton. Trans.*, 2019, **48**, 13943-13952.
103. S. Woodhouse, *Thesis*, 2019.
104. S. S. Woodhouse, T. N. Dais, E. H. Payne, M. K. Singh, E. K. Brechin and P. G. Plieger, *Dalton. Trans.*, 2021, **50**, 5318-5326.
105. H. Lund and J. Bjerrum, *Ber. Dtsch. Chem. Ges.*, 1931, **64**, 210-213.
106. G. Sheldrick, *Acta Cryst.*, 2015, **A71**, 3-8.
107. G. Sheldrick, *Acta Cryst.*, 2015, **C71**, 3-8.
108. O. V. Dolomanov, L. J. Bourhis, R. J. Gildea, J. A. K. Howard and H. Puschmann, *J. Appl. Cryst.*, 2009, **42**, 339-341.
109. Bruker *APEX4, SAINT and SADABS*, Bruker AXS Inc: Madison, Wisconsin, USA, 2021.
110. D. Pinkowicz, H. I. Southerland, C. Avendaño, A. Prosvirin, C. Sanders, W. Wernsdorfer, K. S. Pedersen, J. Dreiser, R. Clérac, J. Nehrkorn, G. G. Simeoni, A. Schnegg, K. Holldack and K. R. Dunbar, *J. Am. Chem. Soc.*, 2015, **137**, 14406-14422.
111. T.-T. Wang, H. Yan, Z.-W. Che and W.-B. Sun, *J. Mol. Struct.*, 2023, **1272**, 134179.
112. L. Wang, X. Yao, X. Zou, J. Li, W. Sun and G. Li, *CrystEngComm*, 2022, **24**, 1907-1916.
113. C.-M. Wang, Z. Wu, P. Chen, Y.-M. Tian and W.-B. Sun, *J. Mol. Struct.*, 2021, **1246**, 1-8.
114. S. S. Woodhouse, D. N. T. De Silva, G. B. Jameson, D. J. Cutler, S. Sanz, E. K. Brechin, C. G. Davies, G. N. L. Jameson and P. G. Plieger, *Dalton. Trans.*, 2019, **48**, 11872-11881.
115. D. N. T. De Silva, G. B. Jameson, A. P. S. Pannu, R. Pouhet, M. Wenzel and P. G. Plieger, *Dalton. Trans.*, 2015, **44**, 15949-15959.
116. R. Aldred, R. Johnston, D. Levin and J. Neilan, *J. Am. Chem. Soc.*, 1994, **13**, 1823-1831.
117. Q. Wang, C. Wilson, A. J. Blake, S. R. Collinson, P. A. Tasker and M. Schröder, *Tetrahedron Letters*, 2006, **47**, 8983-8987.
118. R. Jain, R. R. Jagdeeshwar and R. S. Mahender, *Novel process for the synthesis of phenoxyethyl derivatives*, WO2011101864, 2011
119. H. Sharghi, R. Khalifeh and A. R. S. Beni, *J. Iran. Chem. Soc.*, 2010, **7**, 275-288.
120. P. E. Reyes-Gutierrez, T. Kapal, B. Klepetarova, D. Saman, R. Pohl, Z. Zawada, E. Kuzmova, M. Hajek and F. Teply, *Sci. Rep.*, 2016, **6**, 23499.

121. L. Mei, L. S. Tai, F. H. Tao, S. Jie and L. Q. Rong, *Res. Chem. Intermed.*, 2012, **38**, 499-505.
122. M. N. Timofeeva, E. A. Petrova, E. A. Mel'gunova, A. Gil, M. A. Vicente and V. N. Panchenko, *Reac. Kinet. Mech. Cat.* , 2019, **127**, 41-52.
123. J. Zelazkova and J. Jampilek, presented in part at the The 15th International Electronic Conference on Synthetic Organic Chemistry, Basel, Switzerland, 2011.
124. H. Sakai, S. Shinto, Y. Araki, T. Wada, T. Sakanoue, T. Takenobu and T. Hasobe, *Chem. Eur. J.*, 2014, **20**, 10099-10109.
125. E. Costa-Villén, M. Font-Bardia, J. Mayans and A. Escuer, *Cryst. Growth. Des.*, 2024, **24**, 5806-5817.
126. H.-R. Wen, S.-J. Liu, X.-R. Xie, J. Bao, C.-M. Liu and J.-L. Chen, *Inorg. Chim. Acta.*, 2015, **435**, 274-282.
127. J. Mayans, Q. Saez, M. Font-Bardia and A. Escuer, *Dalton. Trans.*, 2019, **48**, 641-652.
128. R. Shannon, *Acta Cryst.*, 1976, **32**, 751-767.
129. J. B. Mann, *Hartree-Fock Wavefunctions and Radial Expactation Values: Hydrogen to Lawrencium*, Report LA-3691, Los Alamos Scientific Laboratory, USA, 1968.
130. M. Towatari, K. Nishi, T. Fujinami, N. Matsumoto, Y. Sunatsuki, M. Kojima, N. Mochida, T. Ishida, N. Re and J. Mrozinski, *Inorg. Chem.*, 2013, **52**, 6160-6178.
131. J. Goura, E. Colacio, J. M. Herrera, E. A. Suturina, I. Kuprov, Y. Lan, W. Wernsdorfer and V. Chandrasekhar, *Chem. Eur. J.*, 2017, **23**, 16621-16636.
132. L. Salmon, P. Thuéry, E. Rivière and M. Ephritikhine, *Inorg. Chem.*, 2006, **45**, 83-93.
133. J.-T. Chen, H. Yan, T.-t. Wang and W.-B. Sun, *J. Mol. Struct.*, 2024, **1311**, 138473.
134. P. Mahapatra, S. Ghosh, N. Koizumi, T. Kanetomo, T. Ishida, M. G. B. Drew and A. Ghosh, *Dalton. Trans.*, 2017, **46**, 12095-12105.
135. B. Cristóvão, D. Osypiuk, B. Miroslaw and A. Bartyzel, *Polyhedron*, 2018, **144**, 225-233.
136. H. Naeimi and Z. Babaei, *Lett. Org. Chem.*, 2015, **12**, 311-318.
137. K. Chai, W. Xia, H. Chen, W. Su, W. Xu and A. Su, *Mol. Cat.*, 2024, **561**, 114159.
138. J. Tang, Y. Cao, F. Ruan, F. Li, Y. Jin, M. N. Ha, X. Han and Q. Ke, *Ind. & Eng. Chem. Res.*, 2020, **59**, 9408-9413.
139. X. Yin, L. Deng, L. Ruan, Y. Wu, F. Luo, G. Qin, X. Han and X. Zhang, *Materials*, 2023, **16**, 1-30.
140. I. Castro, M. L. Calatayud, C. Yuste, M. Castellano, R. Ruiz-García, J. Cano, J. Faus, M. Verdaguer and F. Lloret, *Polyhedron*, 2019, **169**, 66-77.
141. F. Yang, Q. Zhou, G. Zeng, G. Li, L. Gao, Z. Shi and S. Feng, *Dalton. Trans.*, 2014, **43**, 1238-1245.
142. C. A. Hunter and J. K. M. Sanders, *J. Am. Chem. Soc.*, 1990, **112**, 5525-5534.